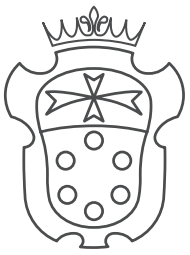

SCUOLA
NORMALE
SUPERIORE

Classe di Scienze

Corso di perfezionamento in
Metodi e Modelli per le Scienze Molecolari

XXXVI ciclo

Atomistic Models for Plasmonics: from Metal Nanostructures to Molecular Plasmonics

Supervisor

Prof.ssa Chiara Cappelli

Co-supervisor

Dr. Tommaso Giovannini

Candidato
Luca Nicoli

Anno accademico 2023–2024

Perso
dai sentieri che ho tracciato
prima ancora di averli percorsi.
Ed io,
smarrito,
mi trovo.

Contents

Abstract

This thesis presents a comprehensive theoretical framework for modeling the optical properties of plasmonic materials through the development of a family of classical atomistic electromagnetic multiscale models, referred to as Frequency-dependent Molecular Mechanics (ωMM). Building on the classical atomistic model of Frequency-dependent Fluctuating Charges (ωFQ), initially designed for Drude-like plasmonic materials, we have extended the ωFQ model to account for the unique characteristics of noble metals, resulting in the ωFQFμ approach. This new model incorporates interband electron transitions and has been extended to the simulation of bimetallic and alloyed nanostructures. Additionally, we have reformulated the ωMM approaches to operate in the real-time domain, enhancing their ability to study time-dependent optical behaviors. This work has further extended the ωMM family of models, coupling them in a multiscale fashion with both classical and Quantum Mechanical approaches to simulate the interactions of plasmonic materials with both non-absorbing and absorbing environments, respectively. The final models allow the study of phenomena such as refractive-index Localized Surface Plasmon Resonance and Surface-Enhanced Raman Spectroscopy.

Acronyms

Symbols

ω**FQ** Frequency-dependent Fluctuating Charges.

ω**FQF**μ Frequency-dependent Fluctuating Charges and Fluctuating Dipoles.

ω**FQF**μ**/FQ** Frequency-dependent Fluctuating Charges and Fluctuating Dipoles / Fluctuating Charges.

ω**MM** Frequency-dependent Molecular Mechanics.

B

BEM Boundary Element Method.

C

CPKS Coupled-Perturbed Kohn-Sham.

D

DIM Discrete Interaction Model.

E

EE electron-electron.

F

FDTD Finite Difference Time Domain.

FQ Fluctuating Charges.

L

LSP Localized Surface Plasmon.

LSPR Localized Surface Plasmon Resonance.

M

MNP Metal Nanoparticle.

N

NP nanoparticle.

P

PRF Plasmon Resonance Frequency.

PS Plasmonic System.

Q

QM Quantum Mechanics.

R

RPA Random Phase Approximation.

S

SERS Surface-Enhanced Raman Scattering.

SPP Surface Plasmon Polariton.

SPR Surface Plasmon Resonance.

T

TDDFT Time-Dependent Density Functional Theory.

TDDFTB/FQ Time-Dependent Density Functional Tight Binding / Fluctuating Charges.

Publications

This thesis is based on the following publications:

[Paper I] Giovannini, T., Bonatti, L., Lafiosca, P., **Nicoli, L.**, Castagnola, M., Illobre, P. G., Corni, S., & Cappelli, C., "Do we really need quantum mechanics to describe plasmonic properties of metal nanostructures?"

ACS Photonics 9 (2022): 3025-3034

`https://doi.org/10.1021/acsphotonics.2c00761`

[Paper II] **Nicoli, L.**, Lafiosca, P., Illobre, P. G., Bonatti, L., Giovannini, T., & Cappelli, C., "Fully atomistic modeling of plasmonic bimetallic nanoparticles: nanoalloys and core-shell systems"

Front. Photonics 4 (2023): 1199598

`https://doi.org/10.3389/fphot.2023.1199598`

[Paper III] Lafiosca, P., **Nicoli, L.**, Pipolo, S., Corni, S., Giovannini, T, & Cappelli, C., "Real-Time Formulation of Atomistic Electromagnetic Models for Plasmonics"

J. Phys. Chem. C (2024)

`https://doi.org/10.1021/acs.jpcc.4c04002`

[Paper IV] **Nicoli, L.**, Sodomaco, S., Lafiosca, P., Giovannini, T., & Cappelli, C., "Atomistic Multiscale Modeling of Colloidal Plasmonic Nanoparticles"

ACS Phys. Chem Au (2024)

`https://doi.org/10.1021/acsphyschemau.4c00052`

[Paper V] Lafiosca, P., **Nicoli, L.**, Bonatti, L., Giovannini, T., Corni, S., & Cappelli, C., "QM/classical modeling of surface enhanced Raman scattering based on atomistic electromagnetic models"

J. Chem. Theory Comput. 19 (2023): 3616-3633

`https://doi.org/10.1021/acs.jctc.3c00177`

List of publications not included in this thesis:

- Bonatti, L., **Nicoli, L.**, Giovannini, T. & Cappelli, C., "in-silico design of graphene plasmonic hot-spots"

  Nanoscale Adv. 4 (2022): 2294-2302.

  `https://doi.org/10.1039/D2NA00088A`

- **Nicoli, L.**, Giovannini, T., & Cappelli, C., "Assessing the quality of QM/MM approaches to describe vacuo-to-water solvatochromic shifts."

  J. Chem. Phys. 157 (2022): 214101

  `https://doi.org/10.1063/5.0118664`

Introduction

Plasmonic materials, typically composed of noble metals such as gold, silver, and aluminum, have gained significant attention in recent years for their ability to support Localized Surface Plasmon (LSP). LSPs are collective oscillations of electrons that occur at the interface between a metal nanoparticle (NP) and a dielectric medium excited by incident light. The unique properties of plasmonic materials arise from the LSP's capability to generate intense localized electric fields and hot electrons within the metal NPs, making them invaluable in a variety of advanced technological applications such as chemical sensing, photocatalysis, and photovoltaics.[1–6]

A variety of factors influence the plasmonic properties harnessed for these technologies. The choice of the material's composition is a crucial aspect.[7,8] While noble metals exhibit strong resonances in the visible to near-infrared range, materials like aluminum can resonate in the ultraviolet range. Furthermore, the morphology of the NPs, including size and shape, significantly affects the resonance frequency and intensity of the LSPs.[7] For example, spherical nanoparticles exhibit a single resonance mode, while elongated particles, such as nanorods, can support multiple modes.[9] The surrounding environment also plays a relevant role in modulating these resonances, potentially leading to Localized Surface Plasmon Resonance (LSPR) shift and the creation of hybrid plasmonic-molecular states.[1,2,10–12] Lastly, the architectural arrangement of plasmonic structures, such as interparticle spacing and orientation, critically affects electromagnetic coupling, electron tunneling, and the formation of hybridized plasmon modes, further modifying the optical response.[2,13]

Given the complex interplay of these factors, accurate *in-silico* modeling of plasmonic materials becomes essential for optimizing their functionality across various applications. Such modeling should allow researchers to pinpoint the influence of particle shape, size, material selection, and environmental interactions on the LSPR and its properties.

Many modeling techniques have been proposed throughout the years, ranging from fully Quantum Mechanics (QM) to classical electromagnetic models.[11,12,14–25] However, while accuracy is needed to model the multitude of factors that influence the LSPR, low computational cost is required to simulate systems spanning the wide range of dimensions of the LSP-based technologies (ranging from a few to hundreds of nm). All these requirements impose a severe modeling challenge. At the onset of my Ph.D., a comprehensive model accounting for the factors influencing the LSPR while maintaining a low computational cost was still lacking.

This Thesis, thus, provides a general theoretical framework, capable of modeling most of the parameters influencing the LSPR at a low computational cost. To achieve this, we have extended a classical atomistic electromagnetic model, namely Frequency-dependent Fluctuating Charges (ωFQ), creating a family of multiscale atomistic approaches called Frequency-dependent Molecular Mechanics (ωMM). The ωMM approaches are tailored to model both in time and the frequency domain the optical response of a general plasmonic substrate, accounting for its chemical composition and the interactions with its environment. The favorable computational scaling of the ωMM models allows to simulate realistic sized NPs, while the parameterization of the free ωMM parameters against *ab-initio* and experimental data guarantees the models' applicability in the quantum size regime.
The first chapter of this Thesis briefly presents the physics of the plasmonic excitations, highlighting their decaying mechanisms and time dynamics. This theoretical foundation is essential for introducing the subsequent chapter of the Thesis, which presents the main theoretical approaches for the simulation of the optical properties of plasmonic substrates that were available at the start of my Ph.D. Analyzing the limitations of these models will clarify to the reader the motivation of this thesis.

Chapter 1

Theory

The purpose of this Chapter is to introduce the theoretical concepts that are the basis of this Thesis. Section 1.1 will introduce the concept of plasmons in metals, i.e. a quasiparticle connected to the collective excitations of the electrons. Section 1.2 will quickly review the main processes with which plasmons interact with the environment (photons and molecules), and decays (intra- and interband mechanisms). Lastly, section 1.3 will briefly overview the time dynamics of the plasmon excitations.

1.1 Plasmons

Conduction electrons within a metal can be viewed as an interacting fermion gas, which behaves similarly to a classical plasma. Plasmas display organized or collective phenomena that manifest in two primary forms: screening and collective oscillations. The latter is associated with plasmons, which are the quanta of collective electron excitations supported by the quantum plasma that characterizes the interacting electron system.[26] Plasmons are defined when the plasmon wavelength is greater than the de Broglie wavelength of electrons at the Fermi level. Under this condition, known as the Random Phase Approximation (RPA), the quantum plasma exhibits collective behavior; otherwise, it is more accurately described as a collection of free individual particles.[26] The concept of plasmons originates from the study of an interacting electron gas, which is described by the following Hamiltonian:

$$\hat{H}_{\text{el.gas}} = \sum_i \frac{\mathbf{p}_i^2}{2m} + \frac{1}{2}\sum_{i\neq j} \frac{e^2}{4\pi\varepsilon|\mathbf{r}_i - \mathbf{r}_j|}, \tag{1.1}$$

where $\mathbf{p}_i$ is the momentum of the i-th electron, m is the electron mass, $\mathbf{r}_i$ and $\mathbf{r}_j$ are the positions of the i-th and j-th electrons, respectively; e is the elementary charge, and ε is the permittivity of the medium. The first term in Eq. 1.1 represents the kinetic energy of the electrons, while the second accounts for the Coulomb interaction between electrons. Using the RPA[27–30], the Hamiltonian can be rewritten as:

$$\hat{H}_{\text{el.gas}} = \hat{H}^0_{\text{el.gas}} + \hat{H}_{\text{el-el.scr}} + \hat{H}^{\text{pl}}_{\text{el.gas}} + \hat{H}_{\text{el-pl}}, \tag{1.2}$$

Where $\hat{H}^0_{\text{el.gas}}$, represents the kinetic energy of the electron gas, $\hat{H}_{\text{el-el.scr}}$, accounts for the screened Coulomb interaction between two electron, $\hat{H}^{\text{pl}}_{\text{el.gas}}$, describes the non-interacting plasmon gas, and $\hat{H}_{\text{el-pl}}$, represents the electron-plasmon interaction. Each term in Eq. 1.2 can be expressed in second quantization [31].
The kinetic energy of the electron gas $\hat{H}^0_{\text{el.gas}}$, reads:

$$\hat{H}^0_{\text{el.gas}} = \sum_{\mathbf{k}} \frac{\hbar^2 \mathbf{k}^2}{2m} c^\dagger_{\mathbf{k}} c_{\mathbf{k}}, \tag{1.3}$$

where $\hbar$ is the reduced Planck constant, $\mathbf{k}$ is the wavevector of an electron state, $c^\dagger_{\mathbf{k}}$ and $c_{\mathbf{k}}$ are the electron creation and annihilation operators, assuming a spherical and parabolic dispersion relation.

The screened Coulomb interaction between two electrons, $\hat{H}_{\text{el-el.scr}}$, reads:

$$\hat{H}_{\text{el-el.scr}} = \sum_{\mathbf{k}>\mathbf{q}_c} \frac{2\pi e^2}{\varepsilon|\mathbf{k}|} c^\dagger_{\mathbf{k}_\lambda+\mathbf{k}} c^\dagger_{\mathbf{k}_\mu-\mathbf{k}} c_{\mathbf{k}_\mu} c_{\mathbf{k}_\lambda}, \tag{1.4}$$

which describes the scattering of two electrons with initial momenta $\mathbf{k}_\lambda$ and $\mathbf{k}_\mu$, and final momenta $\mathbf{k}_\lambda+\mathbf{k}$ and $\mathbf{k}_\mu-\mathbf{k}$, respectively. The screening is incorporated through the cutoff wave vector $\mathbf{q}_c$, which separates short- and long-range components of the Coulomb interaction.

The the non-interacting plasmon gas Hamiltonian, $\hat{H}^{\text{pl}}_{\text{el.gas}}$, reads:

$$\hat{H}^{\text{pl}}_{\text{el.gas}} = \sum_{\mathbf{k}} \hbar\omega_k \left(a^\dagger_{\mathbf{k}} a_{\mathbf{k}} + \frac{1}{2} \right) \tag{1.5}$$

where $a^\dagger_{\mathbf{k}}$ and $a_{\mathbf{k}}$ are the plasmon creation and annihilation operators, and $\hbar\omega_k$ is the plasmon energy.

The electron-plasmon interaction, $\hat{H}_{\text{el-pl}}$, reads:

$$\hat{H}_{\text{el-pl}} = \sum_{\mathbf{k}<\mathbf{q}_c} \frac{2\pi e^2}{\varepsilon|\mathbf{q}|} \left(c^\dagger_{\mathbf{k}+\mathbf{q}} c_{\mathbf{k}} a_{\mathbf{q}} + a^\dagger_{-\mathbf{q}} c^\dagger_{\mathbf{k}+\mathbf{q}} c_{\mathbf{k}} \right), \tag{1.6}$$

where the processes of plasmon absorption and emission are accounted for in the summation. [32]

The plasmon Hamiltonian (Eq. 1.5) can be expressed as a function of the set of eigenmodes associated with the current distribution resulting from the collective free oscillations at each resonance frequency ω_k of the particle electron gas. [33] Mathematically, the plasmon modes are the eigenfunctions corresponding to purely imaginary eigenvalues of the dielectric function, whilst physically, they represent the potential associated with self-sustained charge-density oscillations [34].
Moreover, it is crucial to note that no external electric field has been included. Indeed, the existence of collective excitations in metals is fundamentally rooted in Quantum Field Theory. [35,36] This is justified by the fact that long-range electron interactions lead

to spontaneous symmetry breaking, specifically the breaking of the Galilei Boost.[37] Consequently, due to the generalized Goldstone theorem, this implies the existence of an elementary excitation (and its field, similar to Goldstone bosons for the standard Goldstone theorem) with finite energy, which are indeed the plasmons.[37]

1.2 Plasmons interactions

In the previous section, we introduced plasmonic excitation as a quasiparticle connected to the collective free oscillations of the electron gas, highlighting how plasmonic oscillations are inherently present in metals. In this section, we will introduce the main mechanisms of plasmon creation/annihilation, introducing some key concepts that will be fundamental for the Thesis.

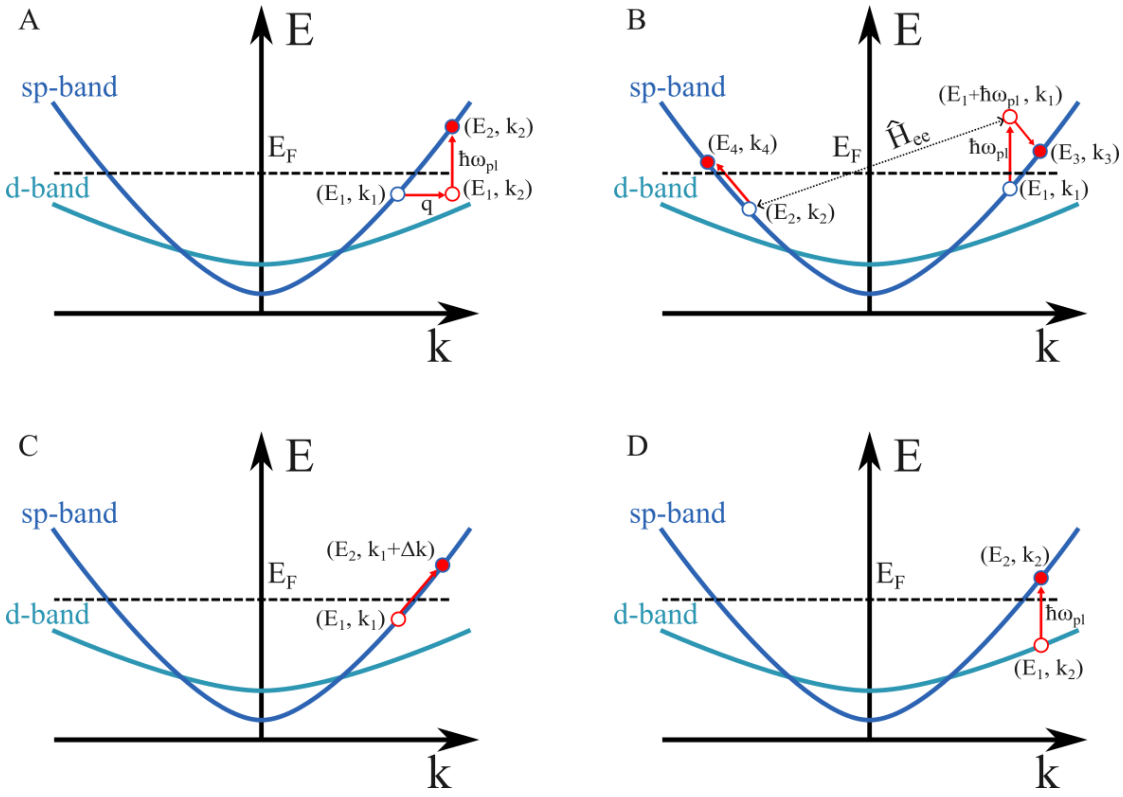

Figure 1.1: Four mechanisms responsible for plasmon scattering and electron-hole pair generation in metals. (A) An indirect transition facilitated by phonons, defects; (B) Electron-electron scattering, which generates two electron-hole pairs per LSP/SPP; (C) Landau damping, a surface collision-assisted transition; (D) Direct interband transition.

1.2.1 Photons

The plasmon-photon coupling gives rise to dressed plasmon modes also called Surface Plasmon Polariton (SPP).[38] Indeed, the term "plasmon" (or "quasi-electrostatic plasmonic modes"[38]) specifically denotes the oscillations of charge density in a free-electron plasma, whereas "plasmon polariton" describes a quasiparticle that results from the interaction between a plasmon and a photon from the electromagnetic field.[39] When SPP are confined to small metallic nanostructures, the collective oscillation of electrons becomes trapped or localized, giving rise to LSP. This localization occurs when the dimensions of the MNP are smaller than the wavelength of light.[40] The effect of the optical radiation is to shift the frequency of such collective hybrid modes with respect to the quasi-electrostatic plasmonic modes and to open SPP creation and annihilation channels.[38]
The Plasmon-Photon interaction Hamiltonian can be written as[33,41]:

$$H_{pl-pt} = ie\hbar\sqrt{\frac{\mathcal{N}V_p}{4mV_R\varepsilon}}\sum_w \left(e_w^{pt} b_{pt} a_w^\dagger - (\epsilon_w^{pt})^* b_{pt}^\dagger a_w\right) \tag{1.7}$$

Where i is the imaginary unit, $\mathcal{N}$ is the particle's carrier density, V_p is the volume of the metallic nanoparticle, V_R the normalizing volume of the electromagnetic field, $b_{pt}^\dagger$, and b_{pt} are the creation and annhilation operators of a photon with wavevector $\mathbf{k}_{pt}$ and polarization $\mathbf{e}_{pt}$, respectively. Moreover,

$$e_w^{pt} = C_{LF}\int_{V_p} d\mathbf{r}'\mathbf{e}^{pt}\cdot\mathbf{q}_w(\mathbf{r}')e^{i\mathbf{k_{pt}}\cdot\mathbf{r}'} \tag{1.8}$$

is a factor that gives the selection rules for the interaction of light with the plasmonic mode $\mathbf{q}_w(\mathbf{r})$ which can be viewed as the amplitude of a harmonic displacement. C_{LF} is a local field correction factor which accounts for the difference between the microscopic light field that couples to the plasmonic mode w and the incident macroscopic field $\mathbf{A}_{pt}$[41].

1.2.2 Intraband Mechanisms

Intraband mechanisms are a set of channels of plasmon annihilation that lead to the creation of electron-hole pairs in the conduction band. These transitions are optically forbidden since a substantial wavevector mismatch $\mathbf{\Delta k}$ needs to be compensated.[42]. There are three main mechanisms, depicted in Fig. 1.1A-C, that compensate for such momentum mismatch, namely: **phonon and defect scattering**, **electron-electron scattering**, and **Landau damping**. These mechanisms open channels for plasmon annihilation.

Phonon and defects scattering

The wavevector change for intraband transitions can be provided by a phonon or an impurity (defect) with wavevector $\mathbf{k}$, see Fig. 1.1A.
Phonon-assisted absorption can occur through two different pathways. In the first pathway (Fig. 1.1A), the electron initially scatters from the state $(E_1, \mathbf{k_1})$ to a virtual state $(E_1, \mathbf{k_2})$, assisted by a phonon. Following this, the plasmon is absorbed, and the electron transitions to its final state $(E_2, \mathbf{k_2})$. In the second pathway (not shown), the electron first absorbs the plasmon, reaching a virtual state $(E_2, \mathbf{k_1})$. The phonon then assists in the transition to the final state $(E_2, \mathbf{k_2})$ providing momentum conservation. The amplitudes of these two pathways will interfere.

This process, commonly referred to as 'Drude' or 'resistive' absorption, is usually phenomenologically described by a viscous friction force damping the motion of free carriers in the conduction band under the application of an electromagnetic field. The plasmon-phonon damping rate reads:[42,43]

$$\gamma_{ph}(\omega) = \langle \tau_{ep}^{-1}(E) \rangle_E \tag{1.9}$$

Where τ_{ep}^{-1} is the electron-phonon scattering rate and it is averaged in the energy E over $[E_F - \hbar\omega_{pl}, E_F + \hbar\omega_{pl}]$.

Electron-electron scattering

A notable mechanism for the decay of SPP involves electron-electron (EE) scattering[42,44] (Fig. 1.1B). In this mechanism, two electrons and two holes share the energy of the annhilated SPP. In condensed matter physics, the high density of states available for scattering makes multi-particle processes, including electron-electron scattering-assisted absorption of plasmons, significantly important.[43] At optical frequencies, Umklapp processes can be initialized[45,46]. In these processes, a photoexcited electron is promoted to an adjacent Brillouin zone, altering the momentum conservation relation, thus opening new decay channels for the plasmon. These processes involve the absorption of a plasmon with energy $\hbar\omega_{pl}$ and the elastic scattering of two electrons with different spins resulting in their simultaneous transition from the initial state $(E_1, \mathbf{k}_1; E_3, \mathbf{k}_3)$ to the final state $(E_2, \mathbf{k}_2; E_4, \mathbf{k}_4)$. Energy is conserved (elastic scattering), while for the momentum we have:

$$\mathbf{k}_1 + \mathbf{k}_2 - \mathbf{k}_3 - \mathbf{k}_4 = n\mathbf{g}, \tag{1.10}$$

where n is an integer and $\mathbf{g}$ is the reciprocal lattice vector.

The mechanism of EE scattering-assisted plasmon decay (see Fig 1.1B) can be synthesized as follows:[42,43] an electron $(E_1, \mathbf{k}_1)$ absorbs a plasmon quantum of energy transitioning to a virtual state $(E_1 + \hbar\omega_{pl}, \mathbf{k}_1)$. Umklapp EE scattering between this electron in the virtual state and another electron $(E_3, \mathbf{k}_3)$ in the conduction band leads to the final state $(E_2, \mathbf{k}_2; E_4, \mathbf{k}_4)$. There are four distinct interfering pathways for such processes, obtained by permuting the order of the particles excited and of the interactions occurring.

The EE scattering-assisted SPP damping rate is expressed as[42,47]

$$\gamma_{ee}(\omega) = \frac{1}{\tau_{ee}(\omega)} F_U(\omega), \tag{1.11}$$

where the EE scattering rate is approximated as[47]

$$\tau_{ee}(\omega)^{-1} \approx \frac{\pi}{24} \frac{E_F}{\hbar} \left(\frac{\hbar\omega}{E_F} \right)^2, \tag{1.12}$$

and $F_U(\omega)$ represents the fraction of total EE scattering events that are Umklapp processes.

Surface-assisted scattering (Landau damping)

Another plasmonic decay channel, particularly relevant for LSPs (Figure 1.1C) is described classically as surface collision-assisted decay[48,49], or in quantum terms as Landau damping (LD)[50,51]. Classically, when an electron collides with the surface, momentum can be transferred between the electron and the entire metal lattice, as during collisions with phonons or defects. This relaxes the momentum conservation rules, and the surface collision rate can be introduced as[52]

$$\gamma_{\text{sc}} \sim \frac{v_F}{d} \tag{1.13}$$

where d is the nanoparticle size.

Quantum mechanically, the plasmon annihilation is the result of the optical field's spatial localization and discontinuity at the surface of the nanoparticle. As the field is localized, its Fourier transform contains spectral components, some exceeding $\Delta k = \frac{\omega}{v_F}$, where v_F is the Fermi velocity. These spectral components enable momentum matching, allowing LSP annihilation without phonon or defect assistance.[42,43,51]

1.2.3 Interband Mechanisms

When the plasmon energies are comparable to the threshold for interband electron-hole pair production, plasmon-mediated vertical single-electron interband transitions become possible.[43,53–55] Such a mechanism is particularly relevant for noble metals where a single electron transition from the inner (4d or 5d) to the outer (5s or 6s) is excited (See Fig. 1.1D). The energy gap between the d shell and the Fermi level in the s shell, denoted as E_{ds}, is approximately 2 eV for Au and 3 eV for Ag.[39,43]

1.2.4 Molecule-Plasmon Interactions

When a molecule is placed near a plasmonic substrate, a plethora of possible plasmon-molecule interactions arise.[56,57] The dynamics of such interactions is highly influenced by the electronic structure of the molecule. When the energy of the LSP is far from that of molecular transitions, the result is a refractive index-induced shift in the plasmon resonance.[12,56] However, when molecules display significant light absorption near the LSPR, there is a strong resonant plasmon-molecule interaction that might even lead to the formation of hybridized states.[12,56]
In our discussion, we limit to account for the Plasmon-Molecule interaction Hamiltonian at the electric-dipole level of approximation, which can be written as:[41,58]

$$H_{pl-mol} = -\boldsymbol{\mu} \cdot \mathbf{E}_{LSP}(\mathbf{r}) = \sum_{w} \frac{e}{\varepsilon} \sqrt{\frac{\hbar \mathcal{N} V_p}{2m\omega_w}} \left(a_w^{\dagger} + a_w\right) \boldsymbol{\mu} \cdot \mathbf{G}_w(\mathbf{r}) \tag{1.14}$$

where ω_w is the frequency of the w-th plasmonic mode, $\mathbf{E}_{LSP}(\mathbf{r})$ is the electric field generated by the plasmonic nanostructure, $\boldsymbol{\mu}$ is the dipole moment of the molecule, and:

$$\mathbf{G}_w(\mathbf{r}) = C_{\mathrm{LF}} \nabla_{\mathbf{r}} \int_{V_{\mathbf{p}}} \mathrm{d}\mathbf{r}' \mathbf{q}_w\left(\mathbf{r}'\right) \cdot \nabla_{\mathbf{r}'} G_0\left(\mathbf{r}, \mathbf{r}'\right) \tag{1.15}$$

Where $G_0\left(\mathbf{r}, \mathbf{r}'\right)$ is a Green function that gives the field distribution outside the plasmonic nanoparticle, and C_{LF} is a local field correction factor defined in Sec. 1.2.1
Within the scope of this Thesis, Plasmon-Enhanced Molecular Spectroscopies such as Surface-Enhanced Raman Scattering (SERS) play a crucial role. SERS i.e., the huge Raman signal enhancement that a chromophore exhibits in the proximity of a plasmonic substrate is usually explained through two mechanisms: the *Electromagnetic Enhancement Mechanism* (EM), which originates from the interaction of the target molecule with the strong local field arising from the SPR induced on the PS, and the *Chemical Enhancement Mechanism* (CM) considered to be caused by the electron transfer between the PS and the target molecule.[59,60] The Hamiltonian in Eq. 1.14 has been proven to be sufficient to describe (EM) effects arising in plasmon-enhanced molecular spectroscopies such as SERS.[40,61] For this reason, in this Thesis, this approximation will be employed. Nevertheless, it is worth mentioning that the Molecule-Plasmon interaction Hamiltonian considered in this work (Eq. 1.14) does not account for further effects that arise in the metal–molecule interface and that require further modeling. For example, beginning with the charge-transfer phenomena that can occur between the metal substrate and the molecule, also leading to CM in SERS.[62] Moreover, plasmon-induced molecular excitation can lead to the desorption of the molecule or molecular dissociation, or adsorbates can alter the surface resistivity of metal substrates by causing scattering of metal electrons from adsorbate resonance states that are situated near the metal's Fermi level.[57] Furthermore, plasmons may decay non-radiatively by populating the resonance states, which are close to the metal Fermi level, leading to a reduction in the lifetime of plasmonic resonances and potentially exciting the adsorbate either vibrationally or electronically.[57]

1.3 Time evolution of plasmonic excitations

In this section, we will briefly review the lifecycle of a plasmon in a metal after its excitation. As for any excited state, the plasmon will eventually decay, through the mechanisms we just discussed. Thus, the Surface Plasmon Resonance (SPR) bandwidth is related to the dephasing time of coherent electron oscillations:[12,63]

$$\Gamma = \Gamma_{rad}(\omega) + \Gamma_{nr}(\omega) \tag{1.16}$$

The SPR linewidth includes both radiative (Γ_r) and non-radiative (Γ_{nr}) components. Radiative decay corresponds to elastically scattered light and it is strongly dependent on the incident frequency, whilst non-radiative decay encompasses the other plasmon relaxation processes:[12,61,64]

$$\Gamma_{nr} = \gamma_{ph} + \gamma_{e-e} + \gamma_{sc} + \gamma_{ib} + \gamma_{env} \tag{1.17}$$

Where γ_{ph}, γ_{e-e}, γ_{sc}, γ_{ib}, and γ_{env} are the plasmon-phonon, electron-electron, surface-assisted, interband-assisted, and plasmon-environment damping rates respectively.
To model the LSPR time dynamics, we will first introduce the Drude Theory of conduction and then move towards a formalization of the phenomenon through a quantum mechanical treatment.

1.3.1 The Drude Theory

Developed by Paul Drude in 1900, it is a seminal classical approach that describes the behavior of free electron gas in metallic systems, and it is still a cornerstone of plasmonic theory.

The Drude model is based on the following assumptions:

1. Metals are modeled as a collection of free electrons (also called a free electron gas) that move independently of each other under the influence of an electric field.

2. Electrons experience collisions with a characteristic average time between collisions, denoted by τ, which is constant.

3. Interband excitation mechanisms are neglected;

In the presence of an electric field $\mathbf{E}(t)$, the equation of motion for a single electron of charge $-e$ and mass m is given by:

$$m\frac{d\mathbf{v}}{dt} = -e\mathbf{E}(t) - \frac{m\mathbf{v}}{\tau} \tag{1.18}$$

Here, the second term represents the damping due to collisions with the lattice ions, where $\tau = \Gamma^{-1}$ is the average time between collisions (relaxation time), and Γ is a viscous friction coefficient. The solution to this differential equation decays exponentially in time, with a rate Γ which is connected to the free-electron scattering events.

A key result of the Drude model is the expression for the frequency-dependent **dielectric function** $\varepsilon(\omega)$, which is given by:

$$\varepsilon(\omega) = \varepsilon_\infty - \frac{\omega_p^2}{\omega(\omega + i\Gamma)} \tag{1.19}$$

where:

- ε_∞ is the high-frequency dielectric constant (accounting for bound electrons),
- $\omega_p = \sqrt{\frac{ne^2}{m\varepsilon_0}}$ is the **plasma frequency**, which characterizes the natural oscillation of the free electron gas, with n being the electron density,
- $\Gamma = \frac{1}{\tau}$ is the damping rate.

1.3.2 The Quantum Theory

The dynamics of a plasmonic system can be recast in the framework of open quantum systems.[65] The plasmonic Hamiltonian possesses a set of eigenstates that can mix, dephase, and decay due to the interaction with an external environment. The dynamics of the plasmonic open system S can be described by means of a quantum Markovian master equation in the Lindblad form:[65–68]

$$\frac{\partial \rho^S(t)}{\partial t} = -\frac{\mathrm{i}}{\hbar}\Big[H, \rho^S(t)\Big] - D[\rho^S(t)] \tag{1.20}$$

Where $\rho^S(t)$ is the reduced density matrix of the plasmonic system S, and $D[\rho^S(t)]$ is a dissipator that describes the influence of the environment on the system's state.

The plasmonic system S can be considered as a sum of S_l of independent, open subsystems:

$$S = \sum_{l=1} S_l \tag{1.21}$$

Each subsystem S_l is a two-level system, and the dynamics of the system S result from the independent dynamics of the systems S_l and are governed by the Lindblad equation Eq. 1.20:[65]

$$\rho^S(t) = \sum_l \rho^{S_l}(t) \tag{1.22}$$

Considering radiative and non-radiative processes, one can write the following master equation:[65]

$$\frac{\partial \rho^{S_l}(t)}{\partial t} = -\frac{\mathrm{i}}{\hbar}\Big[H, \rho^{S_l}\Big] - \frac{1}{2}\left(\Gamma_l^r + \Gamma_l^{nr}\right) \cdot \left(a_l^\dagger a_l + \rho^{S_l} a_l^\dagger a_l - -2a_l \rho^{S_l} a_l^\dagger\right) \tag{1.23}$$

Where $a_l^\dagger$ and a_l are the plasmon creator and annihilation operators previously defined, and Γ_l^r and Γ_l^{nr} are the spontaneous radiative and non-radiative rates of the $l-$th

mode, respectively. Such rates are connected to the interaction Hamiltonians defined in the previous section. Analogously to the classical Drude model, also the quantum theory predicts that the population of the plasmonic oscillatory states is damped exponentially with a rate that is connected to the plasmonic annihilation events:

$$\Gamma^{pop} = \Gamma^{r} + \Gamma^{nr} \tag{1.24}$$

Of course, differently from the classical theory, this quantum theory also predicts the plasmonic dephasing rate.

In this chapter, we have reviewed the fundamental aspects of plasmonic oscillations in metals. We first introduced the concept of 'quasi-electrostatic plasmon' modes, which are the self-sustained charge-density oscillations in metals, and that are well-defined within the RPA. Next, we introduced the main mechanisms of plasmon creation and annihilation, highlighting how the coupling with the optical radiation generates a dressed-plasmon mode, called SPP or LSP when the dimension of the MNP are smaller than the wavelength of light. We have also discussed both the intraband and interband plasmon damping mechanisms, as well as the interaction of a plasmonic mode with an external molecule. Lastly, we have briefly reviewed the plasmon temporal dynamics showing how both the phenomenological Drude model and a more accurate open quantum system approach predict an exponential damping of the excitations. The decay rate is connected to the mechanisms of plasmon annihilation.
In the next chapter, we will focus on the computational modelling of plasmonic excitations and substrates.

Chapter 2

Computational modelling of plasmonic systems

The purpose of this Chapter is to introduce the reader to the main challenges of the computational modeling of plasmonic materials, specifically at the beginning of my PhD. Section 2.1 briefly reviews what Plasmonic System (PS) are, what they are used for, and why their computational modeling is so relevant. Next, we briefly review the models for the simulation of the optical properties of PS based on quantum mechanical (Section 2.2) and classical electromagnetic models (Section 2.3). Within this framework, we will dedicate the entire section 2.4 to the description of the classical ωFQ model, which is the basement on top of which I built the contributions reported in this Thesis, and that are briefly reviewed in section 2.5.

2.1 Plasmonic Systems

Plasmonic systems are materials that sustain a LSP. Classic examples of such materials include nanoparticles of noble metals like silver and gold,[69] though more recent interest has grown in materials such as graphene,[70,71] semiconductors,[72,73] and refractory materials.[74] The plasmonic properties of a PS depend heavily on a variety of factors, each playing a unique role.[2,12] First, the material composition determines the resonance wavelength; for example, gold nanoparticles resonate in the visible range, while gold-silver alloys show a blue-shift of the LSPR.[8] Secondly, the morphology, i.e. the size and shape of the NP, also significantly influences the resonance frequency and intensity of the LSP. While spherical NPs exhibit a single resonance mode, rod-shaped particles show multiple modes.[9] The environment around the plasmonic material greatly impacts the resonance, shifting the LSPR or creating hybrid plasmonic-molecular states.[2,12] Lastly, the architecture of the PS plays a crucial role. Indeed, depending on the number of NPs forming the PS, the interparticle spacing and orientation in such assemblies critically determine the electromagnetic coupling and can produce hybridized plasmon modes, further modifying the optical response.[2]

PS have a broad range of applications across various fields.[75,76] One prominent application is in chemical and biological sensing, where their high sensitivity to environmental changes makes them ideal for use in LSP biosensors.[2,77–81] These sensors detect molecular binding events on the sensor surface by measuring shifts in the LSPR due to the change of its surrounding refractive index, allowing for highly precise detection of biomolecules[82]. In spectroscopy, plasmonic materials are the substrate for Surface-Enhanced Raman Spectroscopy (SERS), where their localized field enhancements amplify Raman signals from surface-bound molecules, enabling the detection of trace amounts of chemicals and biomarkers.[83–86] Additionally, plasmonic nanoparticles play an important role in enhancing light absorption in photovoltaic cells by scattering and trapping light within the active layer, thus increasing overall efficiency.[6,87]

For all these reasons, accurate modeling of plasmonic materials is essential for designing and optimizing these systems to enhance their functionality in diverse applications.[88] Given the complex interactions between light and nanoscale materials, predicting the behavior of plasmonic materials without computational models is challenging. Modeling allows researchers to optimize the optical responses of these materials by simulating how various factors—such as particle shape, size, material selection, and environmental influences—affect the localized surface plasmon resonance. Furthermore, accurate modeling reduces experimental costs by enabling pre-experimental predictions that can narrow down feasible designs, reducing the need for extensive physical testing. This predictive capacity is crucial for applications requiring highly specific configurations, e.g. for SERS. Modeling thus serves as a cornerstone for the development of advanced plasmonic technologies, enabling the engineering of more efficient, application-specific, and cost-effective plasmonic systems.[19]

The following section introduces the main theoretical approaches for simulating the optical response of PS.

2.2 Quantum Mechanical Models

A potential strategy to simulate the optical properties of PS, involves utilizing *ab initio* methods via quantum techniques.[19] Among the various approaches, Time-Dependent Density Functional Theory (TDDFT) in its linear response (LR)-TDDFT approximation is commonly used.[89,90] (LR)-TDDFT is based on the Casida formalism and the excitation spectrum ω is derived by solving the following eigenvalue equation:

$$\begin{bmatrix} \mathbf{A} & \mathbf{B} \\ \mathbf{B}^* & \mathbf{A}^* \end{bmatrix} \begin{bmatrix} \mathbf{X} \\ \mathbf{Y} \end{bmatrix} = \omega \begin{bmatrix} 1 & 0 \\ 0 & -1 \end{bmatrix} \begin{bmatrix} \mathbf{X} \\ \mathbf{Y} \end{bmatrix} \tag{2.1}$$

where $X_{ia} = P_{ia}^{(1)}$, and $Y_{ia} = P_{ai}^{(1)}$ are the coefficients of the first order expansion of the system's density evaluated on the basis of the virtual a, b and occupied i, j Kohn-Sham (KS) molecular orbitals (MOs), while the matrices read:

$$\begin{aligned} A_{ai,bj} &= (\varepsilon_a - \varepsilon_i)\delta_{ab}\delta_{ij} + K_{ai,bj} \\ B_{ai,bj} &= K_{ai,jb} \end{aligned} \tag{2.2}$$

Where ε are orbital energies, and $\mathbf{K}$ is the coupling matrix in the adiabatic approximation, defined as:[91]

$$K_{pq,rs} = \int \mathrm{d}\mathbf{r}\mathrm{d}\mathbf{r}' \psi_p^*(\mathbf{r})\psi_q(\mathbf{r}) \left(\frac{1}{|\mathbf{r} - \mathbf{r}'|} + \frac{\delta^2 E_{\mathrm{xc}}}{\delta\rho(\mathbf{r})\delta\rho(\mathbf{r}')} \right) \psi_s^*(\mathbf{r}')\psi_r(\mathbf{r}'), \tag{2.3}$$

where E_{xc} is the total exchange-correlation functional. It is important to note that TDDFT usually disregards retardation effects, though some strategies have been introduced to incorporate them.[92] Additionally, these methods are typically limited to handling relatively small systems, and in recent years, significant efforts have been dedicated to creating approximate TDDFT-based methods capable of simulating larger PS systems.[19] These advancements include simplified versions of the Casida equation like PolTDDFT,[14,15] minimal auxiliary basis sets (TDDFT-as),[93] real-time TDDFT (RT-TDDFT),[16–18] as well as tight-binding methodologies such as TDDFT+TB[94–96] and TDDFTB.[97,98]

TDDFT has proven to be the workhorse to accurately study the plasmonic response of small metal clusters, due to its ability to integrate quantum effects within the plasmonic response.[11,16–19,99–101] However, the high accuracy of TDDFT comes at a large computational cost, thus limiting its applicability to small PS systems, which typically consist of around a thousand atoms and measure less than 5 nm in size.[102]

To go beyond this limitation, which hinders the applicability of TDDFT in a predictive manner for realistic-sized PS, classical models can be invoked.

2.3 Classical Models

Classical models are widely employed to simulate the optical properties of PS materials.[12,20–25] Classical models do not explicitly consider the quantum nature of the substrate and can be divided in two main classes: continuum models, and atomistic models. Continuum models describe the plasmonic substrate as a dielectric medium, endowed with a complex permittivity $\epsilon(\omega)$. Example of such models are the Mie theory, Finite Difference Time Domain (FDTD), and Boundary Element Method (BEM).
Mie theory describes the optical properties of homogeneous spherical particles in a non-absorbing medium, based on Maxwell's equations and the multipole expansion of electromagnetic fields. The incident and internal fields are expanded in regular multipole fields within the particle, while the external scattered field is expanded in outgoing spherical waves. The boundary conditions at the particle's surface allow for the determination of unknown coefficients and the particle's optical response.[12,103,104] Although widely adopted to study plasmonic NP, Mie's theory cannot be applied to complex shapes or assemblies, and other models need to be invoked.[12]
FDTD involves numerically integrating Maxwell's equations in the time domain within a finite space containing an object of arbitrary geometry and composition. The PS geometry is discretized using a grid mesh (Yee cells), and the space and time derivatives of the electric and magnetic fields are approximated by a finite-difference scheme to minimize computational errors and ensure stability.[12,105] FDTD is a very flexible and versatile approach and has been extensively used to study PS.[21,22,106]
The BEM models the PS response to the external electromagnetic field through charges distributed on the particle's surface and interfaces.[107–110] By enforcing boundary conditions, surface-integral equations are derived and solved numerically after discretizing the surface into representative tesserae. BEM's primary advantages include low computational and storage demands, making it suitable for simulating complex non-spherical nanoparticles that other methods may struggle to handle.[12] BEM had been widely employed and extended to simulate complex tasks, such as real-time dynamics[111], quantum-tunneling in nanojunctions[112], quantum-cavity molecular-coupling[113], and more.
Nevertheless, the lack of atomistic detail, hinders the possibility of BEM, but in general of all continuum models, to properly handle systems with atomically defined features, such as complex multimetallic-systems.
To solve this issue, atomistic classical models can be used. In this case, each atom of the substrate is considered and usually is endowed with a polarizable multipolar expansion (charges, dipoles, ...).[23–25] Such quantities interact with the external optical field and their response is tailored to mimic the plasmonic resonance.
Within this class of models fall the family of Discrete Interaction Model (DIM)[23,114,115] and the ωFQ[24], which is crucial to this Thesis and thus will be discussed separately in the next section.
The DIM family of models, attributes a frequency-dependent polarizability and/or capacity to each atom, with these parameters obtained through accurate ab initio calculations[114].

The starting point of the DIM is its Lagrangian:[25]

$$\begin{aligned} L[\{\mu,q\},\lambda] =& E[\{\mu,q\}] - \lambda\left(q^{\text{tot}} - \sum_i^N q_i\right) \\ =& \frac{1}{2}\sum_i^N q_i \mathbf{c}_{ii}^{-1} q_i + \frac{1}{2}\sum_i^N \sum_{j\neq i}^N q_i \mathbf{T}_{ij}^{(0)} q_j \\ &+ \frac{1}{2}\sum_i^N \mu_i \alpha_{ii}^{-1} \mu_i - \frac{1}{2}\sum_i^N \sum_{j\neq i}^N \mu_i \mathbf{T}_{ij}^{(2)} \mu_j \\ &+ \sum_i^N q_i \mathbf{V}^{\text{ext}} - \sum_i^N \mu_i \mathbf{E}^{\text{ext}} \\ &- \sum_i^N \sum_{j\neq i}^N \mu_i \mathbf{T}_{ij}^{(1)} q_j - \lambda\left(q^{\text{tot}} - \sum_i^N q_i\right) \end{aligned} \tag{2.4}$$

Where, q_i is the fluctuating charge associated with the i-th atom, μ_i represents the fluctuating dipole assigned to the i-th atom, c_{ii} denotes the self-interaction tensor of the i-th charge, a_{ii} indicates the self-interaction tensor of the i-th dipole, while $T_{ij}^{(0)}$, $T_{ij}^{(1)}$, and $T_{ij}^{(2)}$ refer to the electrostatic interaction tensors. Additionally, V_{ext} is the external scalar potential, E_{ext} is the external electric field that is time-independent, q_{tot} represents the total charge of the nanoparticle, l is the Lagrangian multiplier, and N signifies the total number of atoms.
Minimizing Eq. 2.4 with respect to the charges yields a set of linear equations, which can be solved to determine the atomic charges and dipoles. The NP polarizability is then obtained from the sum of the atomic polarizabilities, and the PS optical properties can thus be derived.[116] The DIM is a pioneering family of models that had been enlarged to account for several phenomena influencing the plasmonic response of metal NPs. These advancements include accounting for the effect of an external environment adding a classical (cd-DIM)[117–119] or QM (QM/DIM) type of coupling[120–123]; accounting for the size effects of quantum-sized NPs (ex-DIM)[118].
In the next sections, I will introduce the ωFQ classical atomistic electromagnetic model, which serves as the foundation for the further developments I pursued during my thesis, briefly mentioning the key differences with respect to the DIM model.

2.4 Frequency-dependent Fluctuating Charges force field (ωFQ)

The ωFQ model is a classical atomistic approach used to describe how nanostructured materials respond to an external oscillating electric field, denoted as $\mathbf{E}^{\text{ext}}(t)$. Each atom within the plasmonic substrate is represented by a fluctuating charge q_p, which responds to the external perturbation. Given our focus on the surface plasmonic resonance phenomenon, the charges q_p are treated as time-dependent variables and represent the plasmonic density. Assuming that our plasmonic substrate behaves as a closed system, and by applying the microscopic continuity equation, an equation of motion for the charges can be derived, expressed as:[24]

$$\frac{\mathrm{d}q_p}{\mathrm{d}t} = \sum_q \mathcal{A}_{pq} \left(n_q \langle \mathbf{p} \rangle_{pq} \cdot \hat{\mathbf{l}}_{qp} - n_p \langle \mathbf{p} \rangle_{pq} \cdot \hat{\mathbf{l}}_{pq} \right) \tag{2.5}$$

where n_p denotes the effective electron density at each atom site, and $\langle \mathbf{p} \rangle_{pq}$ is the momentum of an electron averaged across all trajectories connecting atoms p and q. Here, $\hat{\mathbf{l}}_{pq} = -\hat{\mathbf{l}}_{qp}$ is the unit vector that links atoms p and q. The term $\mathcal{A}_{pq}$ represents an effective area that regulates the charge exchange between these atoms. Eq. 2.5 is based on the assumption that the total charge remains constant, while any charge fluctuations at atom p correspond to charge inflow or outflow with respect to other atoms in the system.

In the original ωFQ model formulation, it is assumed that the system is chemically homogeneous. Hence, we can express $n_p = n_q = n_0$, where n_0 represents the unperturbed effective electron density for each atom. This simplifies Eq. 2.5 to:

$$\frac{\mathrm{d}q_p}{\mathrm{d}t} = 2n_0 \sum_q \mathcal{A}_{pq} \langle \mathbf{p} \rangle_{pq} \cdot \hat{\mathbf{l}}_{qp} \tag{2.6}$$

A fundamental aspect of the ωFQ model is its depiction of the charge redistribution mechanism between atoms based on the Drude model of conductivity, expressed by the following equation:[124]

$$\frac{\mathrm{d}\mathbf{p}_p}{\mathrm{d}t} = \mathbf{E}_p(t) - \frac{\mathbf{p}_p}{\tau}, \tag{2.7}$$

Where $\mathbf{p}_p$ is the momentum of the electron associated with atom p, τ represents the relaxation time associated with scattering events, and $\mathbf{E}_p(t)$ denotes the *total* electric field acting on the $p-$th atomic site.

Assuming the external electromagnetic field is monochromatic and oscillates with frequency ω, we can reformulate eq. (2.5) and eq. (2.7) in the frequency domain to obtain:[24]

$$-\mathrm{i}\omega q_p(\omega) = 2n_0 \sum_q \mathcal{A}_{pq} \frac{\langle \mathbf{E}(\omega) \rangle_{pq} \cdot \hat{\mathbf{l}}_{qp}}{1/\tau - \mathrm{i}\omega}. \tag{2.8}$$

To finalize the ωFQ equation, we incorporate two modifications. First, we rewrite the total electric field averaged over the trajectories connecting p and q, in terms of the

atomic properties of the system. This is done by assuming that

$$\langle \mathbf{E}(\omega) \rangle \cdot \hat{\mathbf{l}}_{qp} \approx \frac{\mu_q^{\mathrm{el}} - \mu_p^{\mathrm{el}}}{l_{pq}}, \tag{2.9}$$

where l_{pq} is the distance between atoms p and q, and μ_p^{el} is the electrochemical potential of atom p, given by:

$$\mu_p^{\mathrm{el}} = \sum_r T_{pr}^{\mathrm{qq}} q_r(\omega) + V_p^{\mathrm{ext}}. \tag{2.10}$$

Where T_{pr}^{qq} is a charge-charge interaction kernel, and V_p^{ext} is the external electrostatic potential on the $p-$th site.

Secondly, to prevent unphysical charge transfer between atoms that are too distant from one another, each term in Eq. 2.8 is weighted by a factor of $1 - f(l_{pq})$, where f is a Fermi-like damping function dependent solely on the interatomic distance, defined as:

$$f(l_{pq}) = \frac{1}{1 + \exp\left[-d\left(\frac{l_{pq}}{s \cdot l_{pq}^0} - 1\right)\right]}, \tag{2.11}$$

with l_{pq}^0 being the equilibrium distance between atoms p and q in the bulk material, and d and s are parameters that determine the inflection point and steepness of the curve.

By integrating these two modifications, we can express the final working equation of the ωFQ model as:

$$\sum_q \left[\sum_r K_{pr}(\omega)(T_{qr}^{\mathrm{qq}} - T_{pr}^{\mathrm{qq}}) + \mathrm{i}\omega\delta_{pq} \right] q_q(\omega) = \sum_q (V_p^{\mathrm{ext}} - V_q^{\mathrm{ext}}) K_{pq}(\omega), \tag{2.12}$$

where we define the so-called Drude-tunneling matrix as:

$$K_{pq}(\omega) = \frac{2n_0}{1/\tau - \mathrm{i}\omega} \frac{\mathcal{A}_{pq}[1 - f(l_{pq})]}{l_{pq}}, \quad p \neq r, \tag{2.13}$$

with the diagonal elements being zero. The inclusion of the Fermi damping function in eq. (2.13) provides a phenomenological description of quantum tunneling for small interatomic distances l_{pq}.

Eq. 2.12 can be recast in matrix form as:

$$\mathbf{A}^{qq}(\omega) \cdot \mathbf{q}(\omega) = \mathbf{f}^{ext}(\omega) \tag{2.14}$$

Solving the system in eq. (2.14) allows to obtain a set of complex-valued charges $\mathbf{q}(\omega)$ that illustrate the plasmonic substrate's response to the incoming monochromatic radiation field at frequency ω. From these charges, we can compute the complex-valued frequency-dependent polarizability as:

$$\alpha_{\gamma\beta}(\omega) = \sum_p q_p^{\gamma}(\omega)\beta_p \qquad \gamma, \beta = x, y, z, \tag{2.15}$$

where the external optical field is linearly polarized along direction γ, and β_p represents the β component of the Cartesian position of atom p. Consequently, the absorption cross-section can be calculated as:

$$\sigma_{\text{abs}}(\omega) = \frac{4\pi}{3c}\omega \,\text{tr}\left[\text{Im}\left\{\boldsymbol{\alpha}(\omega)\right\}\right], \tag{2.16}$$

where c denotes the speed of light, and $tr[\text{Im}\left\{\boldsymbol{\alpha}(\omega)\right\}]$ is the trace of the imaginary component of the system's polarizability.

It is now useful to quickly address the differences between the ωFQ and the DIM models. In both cases, each atom within the nanostructure is assigned a multipolar expansion charge (ωFQ) and/or dipole moment (DIM) to represent the oscillating electronic density of the plasmonic system in response to an external electric field. Despite their structural similarities, these two model families differ in their theoretical foundations and applicable contexts:

- The ωFQ model is based on the Drude model of conduction[124] and classical electrodynamics. This endows the ωFQ model with a deep physical meaning since the charges are subjected to a viscous-like friction force, connected directly to the intraband plasmon damping mechanisms. In contrast, the DIM incorporates the plasmonic characteristics of the substrate through a phenomenological framework that utilizes frequency-dependent atomic parameters (such as capacitance and polarizability, particularly in its advanced form, the CPIM).[23,114]

- The ωFQ model accounts for quantum tunneling effects between adjacent nanoparticles by exponentially modifying Drude conductance based on the distances between atoms. This consideration is especially significant for nanoaggregates and nanojunctions, where plasmonic hot spots are formed[24]. Recently, the DIM has been adapted to describe the surface effects of nanoparticles within the quantum-size regime, utilizing a set of coordination-dependent parameters[117–119].

- The ωFQ model stands out as the only atomistic classical approach that can accurately describe graphene plasmonics by rewriting its working equation (Eq. 2.6) in terms of essential physical parameters like Fermi energy, relaxation time, and two-dimensional electron density[125–127]. Notably, the ωFQ model can effectively reproduce experimental data for realistic structures with complex geometries consisting of hundreds of nanometers in size (over 1 million atoms).

2.5 My contributions

Each of the methods presented in the previous sections has its advantages, limitations, and specific range of applicability. The absence, at the onset of my Ph.D., of a unified model that could be adaptable to study various systems is the core motivation behind this Thesis. Indeed, the scientific literature was still lacking a model that would be: (1) atomistic, (2) composition-dependent, (3) formulated both in time and frequency domains, (4) capable of including quantum effects, such as electron tunneling (crucial in nanojunctions), (5) capable of accounting for environmental effects depending whether the environment is absorbing or non-absorbing; while (6) keeping an affordable computational cost. Thus, the central focus of this work had been to develop a family of computational models, based on the classical atomistic electromagnetic model ωFQ, and capable of fulfilling the aforementioned requirements.
At the outset of my PhD, the ωFQ model had recently been introduced to simulate the optical properties of sodium nanoparticles with subnanometer gaps.[24,128] ωFQ had also been extended to 2D materials,[125] and employed to study graphene substrates.[126] However, as stated in the previous section, ωFQ is limited to Drude-like homogeneous plasmonic materials and does not account for any interaction of the plasmon with its surrounding environment. Throughout my PhD, I thus contributed to extending the ωFQ model into a more general framework of a family of atomistic electromagnetic models, namely ωMM. The contributions of this Thesis to this research field are as follows:

- **Extension to *d*-metals**: The original formulation of the ωFQ model aimed to simulate metal nanoparticles in a frequency range where interband transitions can be ignored. The ωFQ method is extended into the ωFQFμ method to describe materials containing *d*-electrons. [**Paper I**]

- **Extension to complex metallic chemical compositions**: The standard formulation of ωFQ and ωFQFμ was at first limited to homogeneous systems. Thanks to their atomistic nature, the models are extended to account for variations in the chemical composition of the plasmonic material. [**Paper II**]

- **Real-time dynamics**: The ωMM models are reformulated in the time-domain to study the real-time dynamics of plasmonic excitation in noble metal nanoparticles. [**Paper III**]

- **Interaction with the environment**: In the framework of plasmon-molecule interactions, the family of ωMM models are coupled with both classical and QM models to simulate refractive-index induced PRF shifts [**Paper IV**] and SERS [**Paper V**] respectively.

Chapter 3

Overview of attached publications

In the ωFQ model, intraband transitions are modeled through the Drude model of free electrons. However, ωFQ cannot adequately describe interband transitions that occur between a fully occupied band (e.g., formed by the d orbitals of the metal) and a partially empty band (e.g., formed by s, p orbitals). To fill this gap, in **[Paper I]** we extend the ωFQ model, introducing the possibility of excitation of interband transitions. This is achieved by partitioning the experimental frequency-dependent permittivity into two components: the Drude contribution and the intraband contribution. The Drude contribution is modeled using the ωFQ method with a set of charges assigned to each atom of the plasmonic substrate, while the intraband contribution defines a set of atomic frequency-dependent electric dipoles via an interband polarizability. The resulting Frequency-dependent Fluctuating Charges and Fluctuating Dipoles (ωFQFμ) method is thus applicable to d-metal nanoparticles, allowing for the decomposition of intraband and interband contributions to the plasmonic densities. Notably, this method can replicate the results of TDDFT calculations and capture all typical "quantum" size effects, including the sign and magnitude of the plasmon shift and the gradual loss of the plasmon resonance in gold.

In **[Paper II]** we further extend ωFQFμ generalizing the working equations to multimetallic systems. To this end, we propose an empirical formula for the interband polarizability of bimetallic systems, based on applying the harmonic mean of the homogeneous interband polarizabilities weighted by the chemical composition of the local environment of each atom. This method has been parametrized using *ab initio* calculations and validated against experimental data, demonstrating both its accuracy and versatility in simulating silver-gold alloyed nanoparticles.

In **[Paper III]**, we recast the ωMM class of models in the real-time domain. This is achieved by applying a Fourier anti-transform to the working equations of the ωFQ and ωFQFμ models and approximating the interband polarizability as a sum of Drude-Lorentz oscillators (DL). The obtained time-dependent equations of motion of metal charges and dipoles are then solved with a second-order velocity Verlet algorithm. Incorporating real-time dynamics extends the capabilities of the ωMM class of models, pro-

viding a framework for studying the time-dependent optical behavior of metal nanoparticles.

In [**Paper IV**], we tackle the problem of the interaction of the PS with a non-absorbing environment, in particular focusing on colloidal plasmonic NPs. To model such systems, we couple ωFQFμ, to the classical Fluctuating Charges (FQ) model. The resulting Frequency-dependent Fluctuating Charges and Fluctuating Dipoles / Fluctuating Charges (ωFQFμ/FQ) approach incorporates interactions between the radiation, the NP, and surrounding solvent molecules, considering the mutual effects between the plasmonic substrate and the solvent. The ωFQFμ/FQ method is validated against reference Time-Dependent Density Functional Tight Binding / Fluctuating Charges (TDDFTB/FQ) calculations, showing excellent accuracy, especially in predicting shifts in plasmon resonance frequencies for structures smaller than the quantum-size limit.

In [**Paper V**], we further extend the treatment of environmental effects considering the interaction of a PS with an absorbing environment. This is achieved by coupling the ωMM class of models with a QM Hamiltonian, for the simulation of SERS. In this work, the electric polarizability of the QM region is computed by solving the modified Coupled-Perturbed Kohn-Sham (CPKS) equations, including the local field operator linked to the plasmonic substrate. Following this, the SERS signal is obtained by numerically differentiating the electric polarizability with respect to the normal mode coordinates of the QM region. The resulting QM/ωFQ and QM/ωFQFμ methods are applied to simulate SERS spectra for pyridine and methotrexate adsorbed on different PS, highlighting how the atomistic structure and chemical nature of the plasmonic substrate are critical in determining the enhancement factors. Additionally, simulated spectra are compared with experimental data.

Chapter 4

Attached publications

I. Do We Really Need Quantum Mechanics to Describe Plasmonic Properties of Metal Nanostructures?

ACS Photonics

pubs.acs.org/journal/apchd5

Article

Do We Really Need Quantum Mechanics to Describe Plasmonic Properties of Metal Nanostructures?

Tommaso Giovannini,* Luca Bonatti, Piero Lafiosca, Luca Nicoli, Matteo Castagnola, Pablo Grobas Illobre, Stefano Corni, and Chiara Cappelli*

Cite This: *ACS Photonics* 2022, 9, 3025−3034

Read Online

ACCESS | Metrics & More | Article Recommendations | Supporting Information

ABSTRACT: Optical properties of metal nanostructures are the basis of several scientific and technological applications. When the nanostructure characteristic size is of the order of few nm or less, it is generally accepted that only a description that explicitly describes electrons by quantum mechanics can reproduce faithfully its optical response. For example, the plasmon resonance shift upon shrinking the nanostructure size (red-shift for simple metals, blue-shift for *d*-metals such as gold and silver) is universally accepted to originate from the quantum nature of the system. Here we show instead that an atomistic approach based on classical physics, ωFQFμ (frequency dependent fluctuating charges and fluctuating dipoles), is able to reproduce all the typical "quantum" size effects, such as the sign and the magnitude of the plasmon shift, the progressive loss of the plasmon resonance for gold, the atomistically detailed features in the induced electron density, and the non local effects in the nanoparticle response. To support our findings, we compare the ωFQFμ results for Ag and Au with literature time-dependent DFT simulations, showing the capability of fully classical physics to reproduce these TDDFT results. Only electron tunneling between nanostructures emerges as a genuine quantum mechanical effect, that we had to include in the model by an ad hoc term.

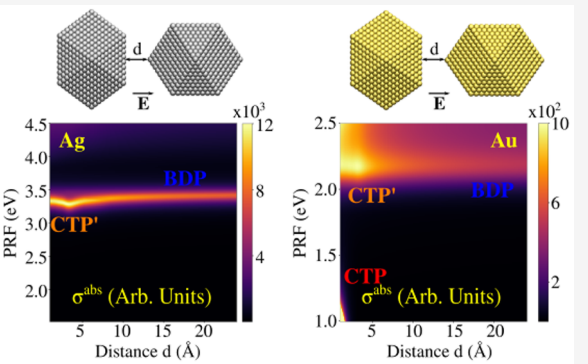

KEYWORDS: *atomistic, interband, gold, silver, tunneling, field enhancement*

1. INTRODUCTION

The recent progress in nanoscience has allowed to experimentally reach the atomistic detail in the geometrical arrangement of metal nanoaggregates.[1−5] This has paved the way for many technological applications, including the creation of local hot-spots featuring enormously enhanced electric field, that has allowed single molecule detection, and even submolecular resolutions, when coupled to surface enhanced spectral techniques.[6−13] A deep understanding of the peculiarities of these structures may benefit of an unavoidable interplaying between theory and experiments. At subnanometric scales such as for atomistically defined needles/tips, quantum effects play an important role in the plasmonic response and therefore need to be considered.[14−23] As a result, a unified theoretical approach to describe the plasmonic properties of metal nanoaggregates under different regimes needs to consistently take into account the physical phenomena underlying the quantum and classical response.[19,24,25]

Large-size nanoparticles are typically described by means of classical electrodynamics, such as the Mie theory,[26] the Discrete Dipole Approximation (DDA),[27] the electromagnetic Finite Difference Time Domain (FDTD),[28] or the Boundary Element Method (BEM).[29−34]

Nonlocal corrections can be considered by exploiting spatially dependent dielectric function based models[35] or hydrodynamic models,[36−38] which are also able to account for the electron spill-out effect that determines the near-field generated in plasmonic hot-spots of *d*-metals.[39−41] However, these models substantially discard atomistic details, which could become relevant when studying surface-assisted spectroscopic properties.[42] It is also worth noting that electron spill-out and nonlocal effects can effectively be treated by means of surface response functions, which would need to be specified for different surface planes.[43,44] Limitations of these approaches for nanoparticles have recently been discussed.[45] In this context, ab initio modeling, at the Time-Dependent Density Functional Theory (TDDFT) level, is still considered the most accurate approach to deal with these effects;[46−50] however, it can only treat relatively small metal nanoparticles (NP; with diameter < 5 nm); therefore, real-size systems

Received: May 20, 2022
Published: September 1, 2022

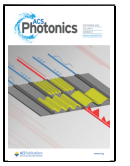

https://doi.org/10.1021/acsphotonics.2c00761
ACS Photonics 2022, 9, 3025−3034

cannot be afforded due to the prohibitively large computational cost. Such a situation naturally leads to the conclusion that an explicit quantum mechanical treatment of electrons, such as DFT and TDDFT, is mandatory to provide a realistic picture of plasmonic phenomena in this size regime. Such a conclusion is not really challenged by the existing classical atomistic approaches to nanoplasmonics,[51−57] that, while delivering accurate results, are based on fitting very general classical response expressions on TDDFT calculations, retaining therefore the physical basis of the latter.

In this paper, we explore whether a classical atomistic method based on essentially classical ingredients (Drude conduction mechanism and classical polarizabilities to reproduce interband polarization) can reproduce the optical response of complex plasmonic nanostructures. To this goal, we propose a physically robust approach to describe the plasmonic properties of sizable metal nanoaggregates characterized by the presence of interband transitions. Together with collective electronic excitations, they determine the plasmonic response of noble metal nanoparticles. The model is based on the recently developed ωFQ method,[32,58−61] in which each metal atom is endowed with a net charge, which varies as a response of the external electric field. The charge-exchange between atoms is governed by the Drude mechanism. As an element of mere quantum mechanical origin that we found essential to add to our classical atomistic picture, the Drude charge exchange is modulated by quantum tunneling, which guarantees a correct description of the optical response for subnanometric junctions.[15,16,18,20,22,58,62,63] Although the method has been successfully applied to sodium nanostructures and graphene-based materials,[58,59] the basic formulation of ωFQ overlooks interband contributions, thus, it is unsuitable to describe the plasmonic properties of nanostructures based on *d*-metals.[64−68] Here, we substantially extend ωFQ so to assign each metal atom with an atomic complex-valued polarizability (i.e., a complex-valued dipole moment), appropriately tuned to model interband effects. The resulting approach is called ωFQFμ (frequency-dependent fluctuating charges and fluctuating dipoles) by analogy with a parent polarizable approach, which has been proposed by some of the present authors to treat completely different chemical systems.[69−71] The theoretical basis of the approach stems from the evidence that *d*-states can efficiently be treated as polarizable shells placed at lattice positions.[67]

Notice that ωFQFμ was developed from a different perspective compared to other classical atomistic approaches.[51−54] Indeed, ωFQFμ is built from textbook bulk metal physics rather than fitting of generic polarizability and capacity frequency-dependent expressions. This provides practical benefits as well. In fact, Drude-tunneling and interband regimes are perfectly decoupled in the two terms that depend on ωFQs[58] and ωFμs, thus allowing for a fine, physically guided, tuning of the plasmonic response. In the following, we show that ωFQFμ is able to correctly reproduce the plasmonic properties of Ag and Au nanostructures as a function of size and shape, and also their plasmonic response when forming subnanometer junctions. Remarkably, the favorable scaling of the method permits to afford large systems (more than 10^4 atoms), which cannot be treated at the quantum-mechanical level. Also, the ability of ωFQFμ to fully retain the atomistic detail is crucial to reproduce not only the plasmonic response but also near-field enhancements, which play a key-role in near-field enhanced spectroscopies.[72,73]

2. THEORETICAL MODEL

ωFQFμ is a fully atomistic, classical approach which substantially extends ωFQ, which assigns to each metal atom a time dependent charge. Under the action of a time dependent external electric field, metal atoms exchange charge via the Drude conduction mechanism, which is further assisted by quantum tunneling, which limits the charge transfer among nearest neighboring atoms and makes the interaction decrease with the typical exponential decay.[58] In particular, ωFQ charge equation of motion in the frequency domain (ω) reads:[58]

$$-i\omega q_i(\omega) = \frac{2n_0\tau}{1-i\omega\tau}\sum_j [1-f(l_{ij})]\frac{\mathcal{A}_{ij}}{l_{ij}}(\phi_j^{el}-\phi_i^{el}) = \sum_j K_{ij}(\phi_j^{el}-\phi_i^{el}) \quad (1)$$

where $q_i(\omega)$, a complex-valued quantity, is the Fourier component at the frequency ω of the oscillating atomic charge on atom *i*. n_0 is the metal density, τ the friction time, $\mathcal{A}_{ij}$ is the effective area connecting *i*th and *j*th atoms, and l_{ij} is their distance. ϕ^{el} is the electrochemical potential acting on each metal atom, which takes into account the interactions between the different atoms and their interaction with the external electric field, which oscillates at frequency ω. $f(l_{ij})$ is a Fermi-like function mimicking quantum tunneling:[58]

$$f(l_{ij}) = \frac{1}{1+\exp\left[-d\left(\frac{l_{ij}}{s\cdot l_{ij}^0}-1\right)\right]} \quad (2)$$

where l_{ij}^0 is the equilibrium atom−atom distance, whereas *d* and *s* are dimensionless parameters that determine the sharpness and the center of the Fermi function $f(l_{ij})$, respectively. Their values can be determined by comparing computed results with reference ab initio data (see also Section S1 in the Supporting Information (SI)). In eq 1, Drude and tunneling terms are collected in the **K** matrix. The parameters entering ωFQ all have a clear microscopic physical meaning. Therefore, their values can be either chosen by an independent experiment or fitted to reproduce higher level results, and then the soundness of their values can be judged. We took the latter perspective, as discussed in the SI.

Due to its physical foundations, ωFQ cannot describe the specificity of metals featuring *d*-electrons, which contribute to interband transitions and that substantially affect the plasmon response.[64−68] Therefore, we here extend ωFQ into a novel method, ωFQFμ, in which each atom is assigned a charge and an additional source of polarization, that is, an atomic polarizability (to which an induced dipole moment is associated). The presence of the dipole moments is included in eq 1 by taking into account the interaction between charges and dipoles in the electrochemical potential. The induced dipole moments $\boldsymbol{\mu}_i$ are instead obtained by solving the following set of linear equations:

$$\boldsymbol{\mu}_i = \alpha_i^{\omega}(\mathbf{E}_i^{ext} + \mathbf{E}_i^{\mu} + \mathbf{E}_i^{q}) \quad (3)$$

where, $\mathbf{E}^{ext}$, $\mathbf{E}^{\mu}$, and $\mathbf{E}^{q}$ are the external electric field and those generated by the other dipole moments and charges, respectively. α^{ω} is the atomic complex polarizability, which is introduced to describe interband transitions. Remarkably, α^{ω} can easily be obtained by extracting interband contributions

https://doi.org/10.1021/acsphotonics.2c00761
ACS Photonics 2022, 9, 3025−3034

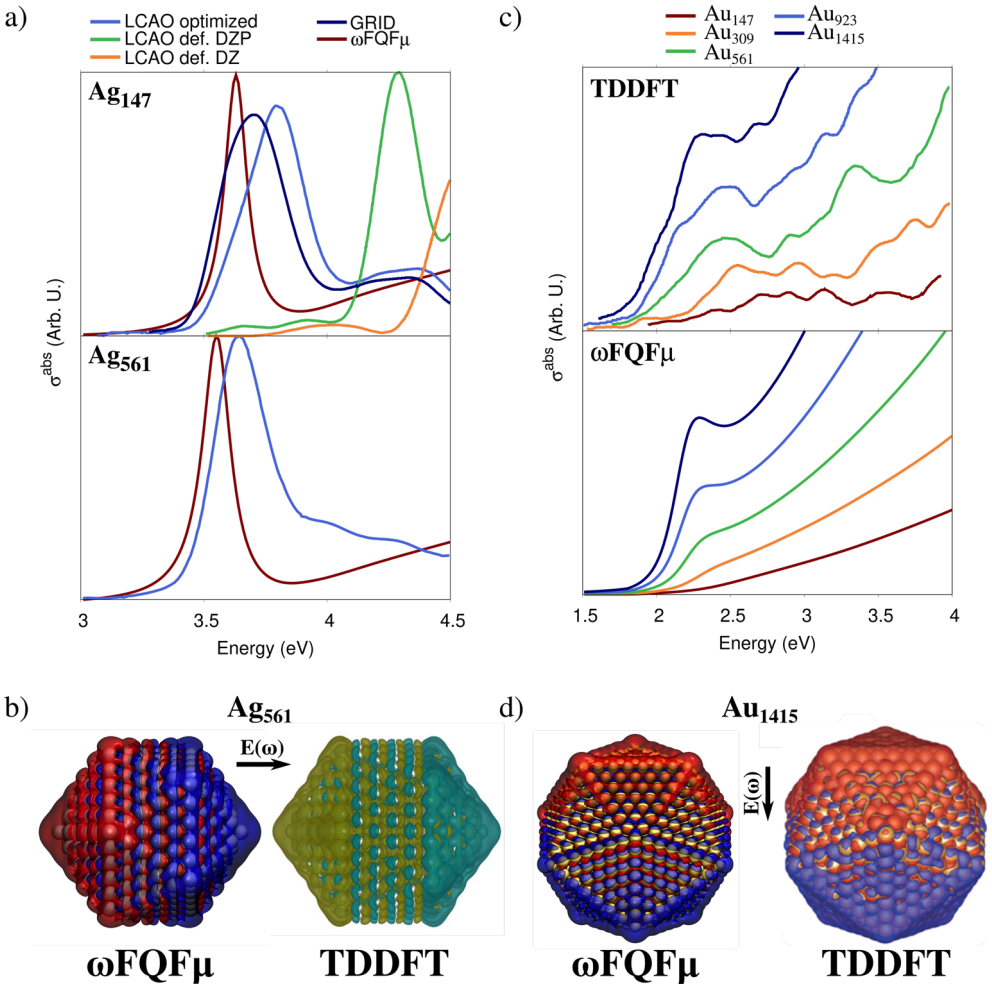

Figure 1. (a) Computed ωFQFμ and TDDFT σ^{abs} for Ag_{147} (~0.8 nm radius) and Ag_{561} (~1.4 nm radius). TDDFT results are reproduced from ref 87 and obtained by exploiting different basis sets (LCAO optimized, def. DZ (double-ζ), def. DZP (double-ζ polarized)) and on a real-space grid (GRID). (b) ωFQFμ and TDDFT[87] plasmon densities for Ag_{561}. TDDFT plasmon densities adapted with permission from ref 87. Copyright 2015 APS Publications. (c) ωFQFμ and TDDFT[88] σ^{abs} for Au_{147}–Au_{1415} (~1.9 nm radius). (d) ωFQFμ and TDDFT[88] plasmon densities for Au_{1415}. TDDFT plasmon densities adapted with permission from ref 88. Copyright 2014 ACS Publications. ωFQFμ isovalues are set to 0.002 and 0.0005 au for Ag and Au, respectively.

from the experimental permittivity function (see Section S1 in the SI), with no need to introduce a posteriori adjustable parameters.

To effectively couple charges and dipoles, that is, to simultaneously account for Drude and interband transitions, eqs 1 and 3 need to be solved simultaneously. By explicitly indicating all terms, the problem can be recast as the following set of linear equations:

$$\sum_{j=1}^{N}\left(\sum_{k=1}^{N} K_{ik}(T_{kj}^{qq} - T_{ij}^{qq}) + i\omega\delta_{ij}\right)q_j + \sum_{j=1}^{N}\left(\sum_{k=1}^{N} K_{ik}(T_{kj}^{q\mu} - T_{ij}^{q\mu})\right)\boldsymbol{\mu}_j = \sum_{k=1}^{N} K_{ik}(V_i^{ext} - V_k^{ext}) \quad (4)$$

$$\sum_{j\neq i}^{N} T_{ij}^{\mu q} q_j + \sum_{j\neq i}^{N} T_{ij}^{\mu\mu}\boldsymbol{\mu}_j + \frac{1}{\alpha_i^{\omega}}\boldsymbol{\mu}_i = \mathbf{E}_i^{ext} \quad (5)$$

where T^{qq}, $T^{q\mu}$, and $T^{\mu\mu}$ define charge–charge, charge–dipole, dipole–dipole interactions, respectively. By imposing $T^{\mu\mu}$ diagonal elements to correspond to $1/\alpha^{\omega}$, eqs 4 and 5 can be written in a compact matrix formulation as

$$\begin{pmatrix} \mathbf{A}^{qq} & \mathbf{A}^{q\mu} \\ \mathbf{T}^{\mu q} & \mathbf{T}^{\mu\mu} \end{pmatrix}\begin{pmatrix} \mathbf{q} \\ \boldsymbol{\mu} \end{pmatrix} = \begin{pmatrix} \mathbf{f}^{q} \\ \mathbf{f}^{\mu} \end{pmatrix} \quad (6)$$

where the complex $\mathbf{A}$ matrices include interaction kernels and the K_{ij} terms (see Section S1 in the SI for more details). The right-hand side of eq 6 accounts for external polarization sources, that is, the electric potential and field calculated at atomic positions:

$$f_i^{q} = \sum_j K_{ij}(V_i^{ext} - V_j^{ext})$$

$$\mathbf{f}_i^{\mu} = \mathbf{E}_i^{ext}$$

Notably, any kind of plasmonic materials can be modeled by ωFQFμ because it integrates all relevant physical ingredients (i.e., Drude conduction, electrostatics, quantum tunneling and interband transition) via eq 1 and eq 3. Also, once complex-

https://doi.org/10.1021/acsphotonics.2c00761
ACS Photonics 2022, 9, 3025−3034

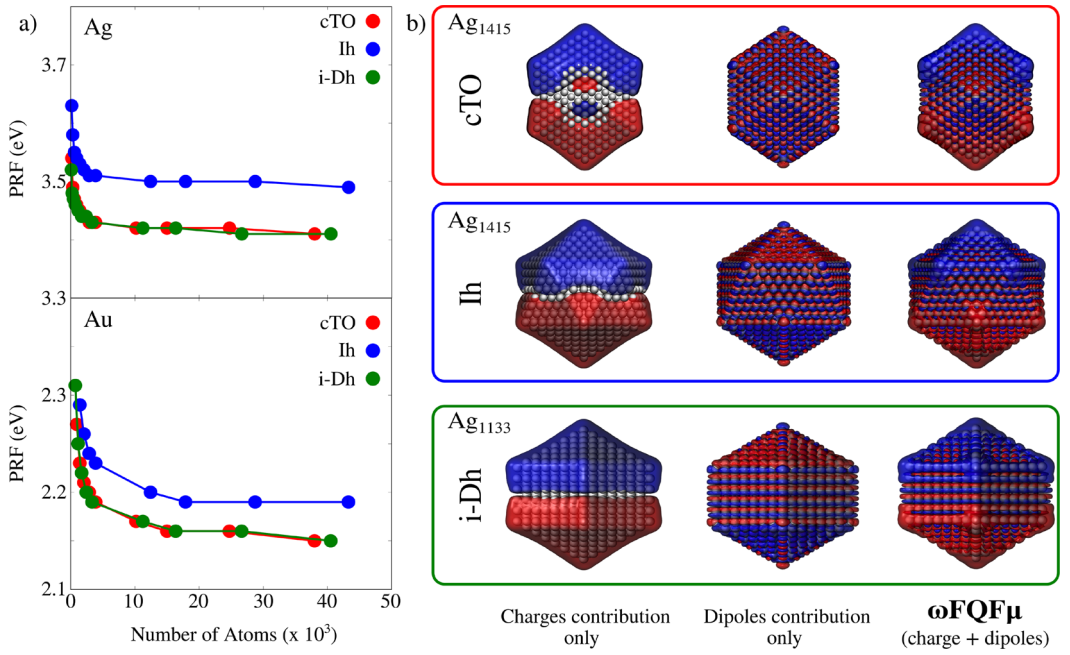

Figure 2. (a) Ag and Au PRF for cTO, Ih, and i-Dh NPs as a function of the number of atoms. (b) Ag densities calculated at the PRF for cTO (top), Ih (middle), and i-Dh (bottom) geometries. Charge and dipole contributions are plotted together with ωFQFμ plasmon densities. Isovalues are 0.002 and 0.0005 au for Ag and Au, respectively.

valued charges and dipoles are computed, the absorption cross section σ^{abs} and the induced electric field can easily be calculated (see Section S1 in the SI for more details).

To conclude this section, it is worth noting that other atomistic, classical models, belonging to the Discrete Interaction Model (DIM) class, have been proposed to describe the plasmonic response of noble-metal nanoparticles.[54,74] Among them, the coordination-dependent−Discrete Interaction Model (cd-DIM)[74] is able to properly describe the size dependency of the Plasmon Resonance Frequency (PRF) for Ag NPs and the plasmonic response of Ag dimers, which is governed by quantum tunneling. Within this model, both effects arise from a modification of the coordination of surface atoms and the consequent modification of the atomic polarizability that is considered to be a parametrized function of the coordination number. In our approach the first effect genuinely originates from the screening effect of *d*-electrons, which is physically modeled by the presence of the α^{ω} term. A correct description of the plasmonic response of dimers arises from the phenomenological introduction of the quantum tunneling via the Fermi function in eq 2.

3. RESULTS AND DISCUSSION

3.1. Optical Response of Metal Nanoparticles: ωFQFμ versus TDDFT Results. Here the capability of ωFQFμ at describing typical plasmonic response properties of single metal nanoparticles is discussed.[75] Although the model is completely general, it is here applied to Ag and Au nanoparticles (NP), for which α^{ω} values are obtained from the permittivity functions reported by Etchegoin et al. in ref 76 and fitted in ref 77 (see also Section S1 in the SI). For both metals, we first consider NPs with three different geometrical arrangements, namely, truncated cuboctahedron (cTO), icosahedral (Ih), and ino-decahedron (i-Dh), which are all characterized by atomistically defined edges.[54] Their plasmonic properties are studied as a function of the size (from a minimum of 85 atoms, ∼5 Å radius, to a maximum of 43287 atoms, ∼65 Å radius).[78−80] Note that geometry relaxation is not considered, because it only slightly affects optical responses.[23,81−86]

Although sizable NPs cannot be afforded by ab initio methods, they can indeed be treated by ωFQFμ,[60] at a reasonable computational time (on average, 59 min on Intel(R) Xeon(R) Gold 5120 CPU @ 2.20 GHz, 28 processors, for each frequency given in input for the structure composed of 43287 atoms). As an example of the performance of ωFQFμ, Kuisma et al.[87] have reported that the calculation of the optical spectrum of Ag_{561} (∼1.4 nm radius) in Ih geometry with the time-propagation (TP) approach to TDDFT requires a wall time of 42.0 h with 512 cores.[87] For the same system, ωFQFμ only requires 25 s on the aforementioned platform. Remarkably, ωFQFμ and reference TDDFT data are very similar (see Figure 1a, bottom panel). Slight discrepancies in the PRF and band broadening among the two models can be justified by considering that TDDFT results substantially vary as a function of the basis set; this is demonstrated by the data shown in Figure 1a (top panel), which are taken from ref 87. Clearly, reference ab initio data display large variability of almost 1 eV when moving from linear combinations of atomic orbitals (LCAO) with different basis sets to real space grid calculation (GRID) results. We also remark that the width of peaks is chosen arbitrarily in TDDFT calculations.

A similar comparison can be performed for Au Ih NPs. TDDFT absorption cross sections reproduced from ref 88 and calculated at the ωFQFμ level are reported in Figure 1c,d. Also, in this case, ωFQFμ can correctly reproduce PRF trends as a function of the NP size and the relative intensities of the bands for the different NPs.

One of the most peculiar features of noble metal NPs and, in general, of *d*-metals is that the PRF blue shifts as the size of the

https://doi.org/10.1021/acsphotonics.2c00761
ACS Photonics 2022, 9, 3025−3034

system decreases, in contrast to what happens for simple metals (and correctly reproduced by ωFQ[58]). The physical origin of this blue-shift has been studied in the past.[67] The screening of the Coulomb interaction among conduction electrons (that determines the plasmon frequency) by the localized *d*-electron core interplays with conduction electrons spill-out at the cluster surface. In short, the *d*-electron core screens electron−electron repulsion, thus decreasing the *d*-metal plasmon frequency compared to what is expected on the basis of the free-electron density of the metal. At the surface, conduction electrons spill out of the structure; in ωFQ and ωFQFμ, the finite size of each atomic distribution accounts for this effect. In parallel, the *d*-electron core, which is localized on the metal atom (described by a point dipole in ωFQFμ) cannot effectively screen the electron−electron repulsion. As a result, the plasmon frequency moves back to the nonscreened, free-electron value. Remarkably, ωFQFμ can indeed describe this mechanism because it provides the right result for the right reason. In fact, if the *d*-electron core response is artificially switched-off (i.e., $\alpha^{\omega} \rightarrow 0$ in eq 3), the plasmon frequency (which is overall increased), red shifts for metal nanoparticles, as it is expected based on spill-out effects only.[58,82] This is demonstrated by the plots reported in Figure S3 in the SI.

The dependence of computed PRFs on the number of atoms is reported in Figure 2a for different geometries; the plots clearly demonstrate that ωFQFμ can indeed correctly reproduce the previously reported trends. Also, the linear fit of Ag Ih PRFs as a function of the inverse of the NP diameter permits to linearly extrapolate PRF = 3.47 eV for an infinite diameter. This value is in almost perfect agreement with the mesoscopic limit of 3.43 eV, as obtained at the quasi-static FDTD (QSFDTD) level,[87] and in excellent agreement with the extrapolated ab initio value of 3.35 eV (see also Figure S4 in the SI).[87]

The investigation of plasmon densities (i.e., the imaginary part of the charge density induced by a monochromatic electromagnetic field oscillating at the PRF) is of fundamental importance for correctly characterizing the plasmon resonance. Computed densities at the PRF for the largest structures in each geometrical arrangement are depicted in Figure 2b. In all cases, they represent a dipolar plasmon. Our result can be compared with reference ab initio data for Ag_{561} (∼1.4 nm radius, see Figure 1b) and Au_{1415} (∼1.9 nm radius, see Figure 1d). In both cases, the agreement is almost perfect.

For the purpose of a deeper theoretical analysis, ωFQFμ can also be used to decouple the contributions of Drude and interband transitions to the total plasmon density. Charge and dipole contributions are graphically depicted in Figure 2b for selected Ag NPs (see Figure S5 in the SI for Au NPS). Clearly, the two plasmon densities are associated with dipole moments in opposite directions. This finding remarks the screening role of the *d*-electrons response.[41,67] As explained above, this results in the typical blue shift observed for *d*-metals.

To further demonstrate the ability of ωFQFμ to correctly take into account screening effects in *d*-metal NPs, we can compare density distributions in inner regions. Computed ωFQFμ and TDDFT densities for Au_{1415} Ih NP (∼1.9 nm radius), in the central region of the cluster (defined for $-2 < z < 2$ Å), are depicted in Figure 3. Notice that densities are computed at the corresponding PRFs, which only differ by 0.01 eV. Coherently with the results reported in Figure 1d, positive and negative charges are located at the top and bottom surface regions, respectively. However, ωFQFμ and TDDFT densities are mainly characterized by a local charge distribution around each Au atom, which is polarized along an opposite direction with respect to the polarization of the surface density. Such a behavior is related to screening effects, which are correctly taken into account by our atomistic, yet classical model.

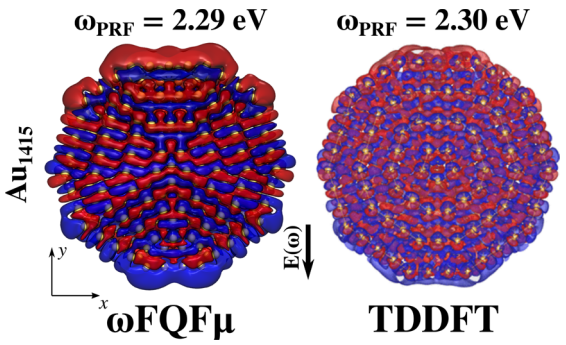

Figure 3. ωFQFμ and TDDFT[88] Au_{1415} (∼1.9 nm radius) plasmon densities in the central region of the cluster ($-2 < z < 2$ Å). TDDFT plasmon densities adapted with permission from ref 88. Copyright 2014 ACS Publications.

In Figure 4a,b the total enhanced electric field ($|\mathbf{E}|/|\mathbf{E}_0|$, where $\mathbf{E}_0$ is the external electric field intensity) at the PRF is reported. Such quantity (elevated to the fourth power) is related to field enhancement factors that are measured in SERS experiments.[10] The dependence of $|\mathbf{E}|/|\mathbf{E}_0|$ factors as a function of the number of atoms and the NPs radius is reported in Figure 4a and b, respectively. Notice that enhancement factors are computed at a distance of 3 Å from the tip of each structure; according to many previous reports, it corresponds to the typical adsorption distance of molecular systems.[89] $|\mathbf{E}|/|\mathbf{E}_0|$ color maps at the PRF for each geometrical arrangement are graphically displayed in Figures 4c. As expected, $|\mathbf{E}|/|\mathbf{E}_0|$ maximum values correspond to tips, and are reported for cTO geometries (for both gold and silver), where edges are the sharpest. Interestingly, for all arrangements, $|\mathbf{E}|/|\mathbf{E}_0|$ follows a $\sqrt[3]{N}$ trend (N being the number of atoms) and, thus, a linear trend with respect to NP radius, because the difference in the electric potential linearly increases with the NP intrinsic size. Remarkably, ωFQFμ is also able to quantify the differences between Ag and Au NPs, being the latter associated with much lower enhancement factors as compared to the former, as expected in this frequency range.

As a final comment, it is remarkable that ωFQFμ is able to describe nonlocal effects. To demonstrate that, we artificially changed the total electric potential and field acting on a specific atom placed at the surface or at the centroid of Ag_{147} (∼0.8 nm radius) and Ag_{3871} (∼2.7 nm radius) structures in the Ih configuration. As a result, independently of the atom position, not only charge and the dipole of the perturbed atom are modified, but also those of other atoms (see Figure S6 in the SI).

3.2. Subnanometer Junctions. In this section we will show that ωFQFμ has the potential to describe hot-spots in subnanometer junctions in a physically consistent manner. This is possible due to the account for quantum tunneling (eq 1), which dominates the plasmon response in these systems. To showcase ωFQFμ performances, we study Ag_{2869}/Au_{2869} (∼2.6 nm radius) cTO dimers. In particular, we select two different morphologies obtained by approaching two NPs so to obtain surface−tip or surface−surface geometrical arrange-

https://doi.org/10.1021/acsphotonics.2c00761
ACS Photonics 2022, 9, 3025−3034

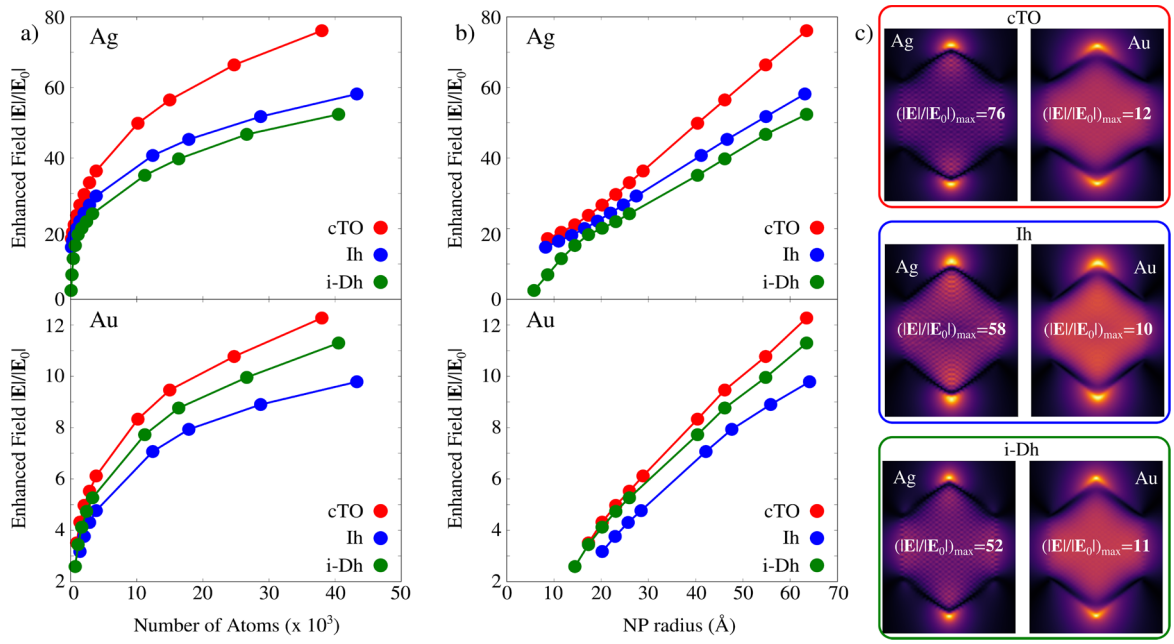

Figure 4. Ag and Au enhanced electric field $|E|/|E_0|$ calculated at 3 Å from the tips for cTO, Ih, and i-Dh NPs as a function of the number of atoms (a) and NP radius (b). (c) Ag and Au $|E|/|E_0|$ color maps for cTO (top), Ih (middle), and i-Dh (bottom) geometries.

ments (see Figures 5 and 6).[90] Note that for both structures the structural relaxation effects are not taken into account,

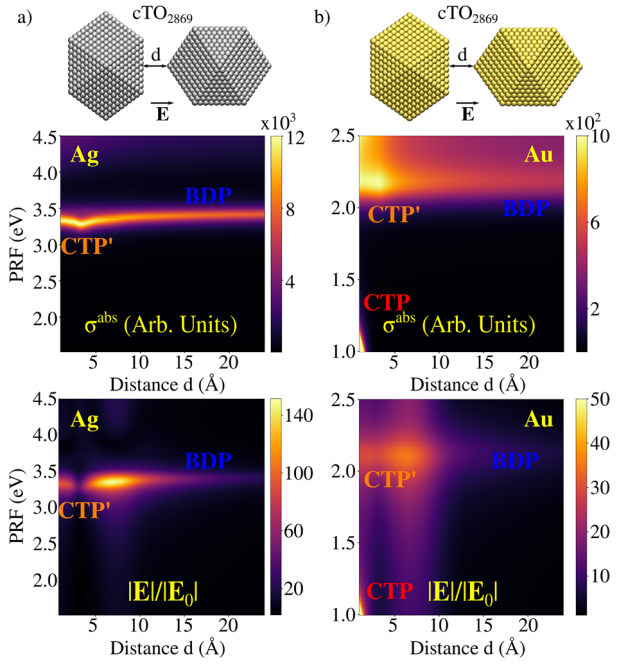

Figure 5. Ag (a) and Au (b) cTO_{2869} dimers in surface−tip geometrical arrangement. Color maps of σ^{abs} and $|E|/|E_0|$ as a function of the PRF and the distance between the two NPs are reported in the middle and bottom panels, respectively.

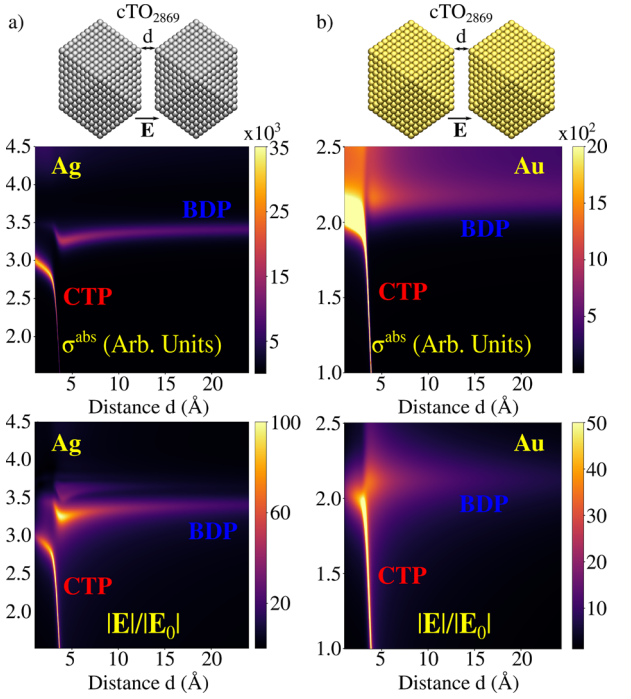

Figure 6. Ag (a) and Au (b) cTO_{2869} dimers in surface−surface geometrical arrangement. Color maps of σ^{abs} and $|E|/|E_0|$ as a function of the PRF and the distance between the two NPs are reported in middle and bottom panels, respectively.

similarly to previous studies.[81] However, to study the effects of structural relaxation we have modeled surface roughness as derived from an atomic adjustment on the surface of one of the two cTO NPs in the surface−surface arrangement (see Figure S7 in the SI).

For the ideal cTO dimers, we investigate both σ^{abs} and $|E|/|E_0|$ calculated at the gap's center as a function of the distance d between the two monomers, in the range 1−24 Å. Computed spectra (Figure 5a,b) are characterized by a high energy peak (∼3.5 eV for Ag and ∼2.2 eV for Au), which red-shifts as d decreases. However, a clear discontinuity occurs at around 4 Å, where quantum tunneling plays a relevant role; in fact, such a distance is close to the Ag−Ag and Au−Au equilibrium distances.

https://doi.org/10.1021/acsphotonics.2c00761
ACS Photonics 2022, 9, 3025−3034

For Au dimers, a second peak at lower energies is visible (d < 2 Å, PRF < 1.5 eV), which blue-shifts as d decreases (see Figure 5b). This band is not present for Ag, because its PRF falls below the investigated frequency range. Highest energy PRF corresponds to the typical Boundary Dipolar Plasmon, BDP, whereas the low-energy peak is associated with a Charge Transfer Plasmon, CTP, where a dipole moment arises in the whole structure (see Figures S8 and S9 in the SI). Note that for distances at which the CT mechanism takes place (for d < 4 Å), the high energy peak is associated with a high-order charge transfer plasmon, usually called CTP′. The clear discontinuity highlighted in σ^{abs} plots is also evident in the case of the computed $|\mathbf{E}|/|\mathbf{E}_0|$ values, which are reported as a color map as a function of the distance in Figure 5, bottom panels. For Ag, the maximum $|\mathbf{E}|/|\mathbf{E}_0|$ is depicted before the two NPs enter in the CT regime, whereas the opposite holds for the Au dimer, for which it corresponds to the CTP peak.

The surface−surface arrangements show similar plasmonic features, independently of the metal nature (see Figure 6a,b). In fact, both spectra are characterized by the presence of two bands when d < 4 Å: a CTP and a CTP′ peak (very low in intensity for Ag and fused with CTP for Au), which blue-shift or red-shift as d decreases, respectively. For d > 4 Å spectra are instead dominated by the BDP mode. The associated $|\mathbf{E}|/|\mathbf{E}_0|$ factors are plotted as a function of the distance in Figure 6, bottom panels. The computed values are of the same order of magnitude as for the previous case. Also, the maximum enhancement for Ag is shown at about 3.3 eV, for a distance of about 4 Å, that is, when CT effects start to dominate the plasmonic response. For Au, the maximum $|\mathbf{E}|/|\mathbf{E}_0|$ occurs at lower distances ($d \sim 3$ Å), however it is associated with the CTP′ plasmonic mode, differently from the tip−substate arrangement. Interestingly, in case of Ag, a clear additional region of enhancement is displayed at energies larger than 3.5 eV, for d > 4 Å. This region is associated with a high-order plasmon, which is indeed dark in the σ^{abs}.

Finally, note that, for both studied geometries, the maximum $|\mathbf{E}|/|\mathbf{E}_0|$ is 3−5 times larger than the corresponding factor obtained for the Ag monomer and even 10 times for Au.

4. SUMMARY AND CONCLUSIONS

We have discussed the prediction of a classical physics based model for nanoplasmonics, ωFQFμ. ωFQFμ is a general atomistic approach to describe the plasmonic features of complex metal nanostructures characterized by interband transitions. In the model, which is formulated in the frequency domain, each atom of the structure is endowed with both a complex-valued charge and dipole, which are determined by solving response equations to an external monochromatic electric field. The two polarization sources conceptually describe the two fundamental mechanisms occurring in d-metals, that is, Drude conduction (charges) and d-electrons polarization (dipoles). Remarkably, charges and dipoles mutually interact; therefore, all physical features of metal nanostructures are considered. ωFQFμ is fully classical, therefore nanostructures of realistic size can be computed with accuracy comparable to full ab initio calculations, but with enormously lower computational cost. Note that the interband polarizability in eq 3 arises from the quantum nature of the system; however, in our approach it is modeled without explicitly considering the quantum nature of the constituting atoms.

From a conceptual point of view, demonstrating that ωFQFμ is able to reproduce the findings of a fully quantum description of the system is clearly questioning the notion that an explicit quantum mechanical treatment is needed to describe the change in plasmonic properties upon shrinking of the nanostructure size. From the results presented in this work, it turns out that only quantum tunneling (relevant for nanoaggregates and nanojunction) is inaccessible by such classical physics, and we had in fact to phenomenologically include the tunneling in ωFQFμ. It is finally worth noting that another relevant quantum effect, Landau damping, is not included in this classical modeling and would in principle require adding a phenomenological correction to ωFQFμ.

From a computational perspective, the developed method paves the way for an investigation of the plasmonic properties of realistic metal nanoparticles, characterized by complex shapes that require an atomistic detail.

■ ASSOCIATED CONTENT

Supporting Information

The Supporting Information is available free of charge at https://pubs.acs.org/doi/10.1021/acsphotonics.2c00761.

Details on ωFQFμ equations and parametrization; Computational details; Ag and Au single NPs absorption cross sections and comparison with reference data; Demonstration of ωFQFμ nonlocality; Plasmon densities for Ag/Au cTO_{2869} dimers (PDF)

■ AUTHOR INFORMATION

Corresponding Authors

Tommaso Giovannini − *Scuola Normale Superiore, 56126 Pisa, Italy;* orcid.org/0000-0002-5637-2853; Email: tommaso.giovannini@sns.it

Chiara Cappelli − *Scuola Normale Superiore, 56126 Pisa, Italy;* orcid.org/0000-0002-4872-4505; Email: chiara.cappelli@sns.it

Authors

Luca Bonatti − *Scuola Normale Superiore, 56126 Pisa, Italy*

Piero Lafiosca − *Scuola Normale Superiore, 56126 Pisa, Italy*

Luca Nicoli − *Scuola Normale Superiore, 56126 Pisa, Italy*

Matteo Castagnola − *Scuola Normale Superiore, 56126 Pisa, Italy*

Pablo Grobas Illobre − *Scuola Normale Superiore, 56126 Pisa, Italy;* orcid.org/0000-0003-2544-9712

Stefano Corni − *Dipartimento di Scienze Chimiche, Università di Padova, 35131 Padova, Italy; Istituto di Nanoscienze del Consiglio Nazionale delle Ricerche CNR-NANO, 41125 Modena, Italy;* orcid.org/0000-0001-6707-108X

Complete contact information is available at: https://pubs.acs.org/10.1021/acsphotonics.2c00761

Funding

This work has received funding from the European Research Council (ERC) under the European Union's Horizon 2020 Research and Innovation Program (Grant Agreement No. 818064). S.C. gratefully acknowledge the European Union's Horizon 2020 FET Project ProID (No. 964363) for funding.

Notes

The authors declare no competing financial interest.

https://doi.org/10.1021/acsphotonics.2c00761
ACS Photonics 2022, 9, 3025−3034

■ ACKNOWLEDGMENTS

We gratefully acknowledge the Center for High Performance Computing (CHPC) at SNS for providing the computational infrastructure.

■ REFERENCES

(1) Junno, T.; Deppert, K.; Montelius, L.; Samuelson, L. Controlled manipulation of nanoparticles with an atomic force microscope. *Appl. Phys. Lett.* **1995**, *66*, 3627−3629.
(2) Ishida, T.; Murayama, T.; Taketoshi, A.; Haruta, M. Importance of size and contact structure of gold nanoparticles for the genesis of unique catalytic processes. *Chem. Rev.* **2020**, *120*, 464−525.
(3) Sau, T. K.; Rogach, A. L. Nonspherical noble metal nanoparticles: colloid-chemical synthesis and morphology control. *Adv. Mater.* **2010**, *22*, 1781−1804.
(4) Liz-Marzán, L. M. Tailoring surface plasmons through the morphology and assembly of metal nanoparticles. *Langmuir* **2006**, *22*, 32−41.
(5) Grzelczak, M.; Pérez-Juste, J.; Mulvaney, P.; Liz-Marzán, L. M. Shape control in gold nanoparticle synthesis. *Chem. Soc. Rev.* **2008**, *37*, 1783−1791.
(6) Willets, K. A.; Van Duyne, R. P. Localized surface plasmon resonance spectroscopy and sensing. *Annu. Rev. Phys. Chem.* **2007**, *58*, 267−297.
(7) Zhang, R.; Zhang, Y.; Dong, Z.; Jiang, S.; Zhang, C.; Chen, L.; Zhang, L.; Liao, Y.; Aizpurua, J.; Luo, Y.; Yang, J. L.; Hou, J. G. Chemical mapping of a single molecule by plasmon-enhanced Raman scattering. *Nature* **2013**, *498*, 82−86.
(8) Jiang, S.; Zhang, Y.; Zhang, R.; Hu, C.; Liao, M.; Luo, Y.; Yang, J.; Dong, Z.; Hou, J. Distinguishing adjacent molecules on a surface using plasmon-enhanced Raman scattering. *Nat. Nanotechnol.* **2015**, *10*, 865−869.
(9) Chiang, N.; Chen, X.; Goubert, G.; Chulhai, D. V.; Chen, X.; Pozzi, E. A.; Jiang, N.; Hersam, M. C.; Seideman, T.; Jensen, L.; Van Duyne, R. P. Conformational contrast of surface-mediated molecular switches yields Ångstrom-scale spatial resolution in ultrahigh vacuum tip-enhanced Raman spectroscopy. *Nano Lett.* **2016**, *16*, 7774−7778.
(10) Langer, J.; et al. Present and Future of Surface-Enhanced Raman Scattering. *ACS Nano* **2020**, *14*, 28−117.
(11) Benz, F.; Schmidt, M. K.; Dreismann, A.; Chikkaraddy, R.; Zhang, Y.; Demetriadou, A.; Carnegie, C.; Ohadi, H.; De Nijs, B.; Esteban, R.; et al. Single-molecule optomechanics in "picocavities. *Science* **2016**, *354*, 726−729.
(12) Yang, B.; Chen, G.; Ghafoor, A.; Zhang, Y.; Zhang, Y.; Zhang, Y.; Luo, Y.; Yang, J.; Sandoghdar, V.; Aizpurua, J.; et al. Sub-nanometre resolution in single-molecule photoluminescence imaging. *Nat. Photonics* **2020**, *14*, 693−699.
(13) Liu, P.; Chulhai, D. V.; Jensen, L. Single-Molecule Imaging Using Atomistic Near-Field Tip-Enhanced Raman Spectroscopy. *ACS Nano* **2017**, *11*, 5094−5102.
(14) Teperik, T. V.; Nordlander, P.; Aizpurua, J.; Borisov, A. G. Quantum effects and nonlocality in strongly coupled plasmonic nanowire dimers. *Opt. Express* **2013**, *21*, 27306−27325.
(15) Zhu, W.; Esteban, R.; Borisov, A. G.; Baumberg, J. J.; Nordlander, P.; Lezec, H. J.; Aizpurua, J.; Crozier, K. B. Quantum mechanical effects in plasmonic structures with subnanometre gaps. *Nat. Commun.* **2016**, *7*, 11495.
(16) Urbieta, M.; Barbry, M.; Zhang, Y.; Koval, P.; Sánchez-Portal, D.; Zabala, N.; Aizpurua, J. Atomic-Scale Lightning Rod Effect in Plasmonic Picocavities: A Classical View to a Quantum Effect. *ACS Nano* **2018**, *12*, 585−595.
(17) Savage, K. J.; Hawkeye, M. M.; Esteban, R.; Borisov, A. G.; Aizpurua, J.; Baumberg, J. J. Revealing the quantum regime in tunnelling plasmonics. *Nature* **2012**, *491*, 574−577.
(18) Marinica, D.; Kazansky, A.; Nordlander, P.; Aizpurua, J.; Borisov, A. G. Quantum plasmonics: nonlinear effects in the field enhancement of a plasmonic nanoparticle dimer. *Nano Lett.* **2012**, *12*, 1333−1339.
(19) Esteban, R.; Borisov, A. G.; Nordlander, P.; Aizpurua, J. Bridging quantum and classical plasmonics with a quantum-corrected model. *Nat. Commun.* **2012**, *3*, 825.
(20) Esteban, R.; Zugarramurdi, A.; Zhang, P.; Nordlander, P.; García-Vidal, F. J.; Borisov, A. G.; Aizpurua, J. A classical treatment of optical tunneling in plasmonic gaps: extending the quantum corrected model to practical situations. *Faraday Discuss.* **2015**, *178*, 151−183.
(21) Campos, A.; Troc, N.; Cottancin, E.; Pellarin, M.; Weissker, H.-C.; Lermé, J.; Kociak, M.; Hillenkamp, M. Plasmonic quantum size effects in silver nanoparticles are dominated by interfaces and local environments. *Nat. Phys.* **2019**, *15*, 275−280.
(22) Scholl, J. A.; García-Etxarri, A.; Koh, A. L.; Dionne, J. A. Observation of quantum tunneling between two plasmonic nanoparticles. *Nano Lett.* **2013**, *13*, 564−569.
(23) Barbry, M.; Koval, P.; Marchesin, F.; Esteban, R.; Borisov, A.; Aizpurua, J.; Sánchez-Portal, D. Atomistic near-field nanoplasmonics: reaching atomic-scale resolution in nanooptics. *Nano Lett.* **2015**, *15*, 3410−3419.
(24) Baumberg, J. J.; Aizpurua, J.; Mikkelsen, M. H.; Smith, D. R. Extreme nanophotonics from ultrathin metallic gaps. *Nat. Mater.* **2019**, *18*, 668−678.
(25) Chen, X.; Liu, P.; Jensen, L. Atomistic electrodynamics simulations of plasmonic nanoparticles. *J. Phys. D Appl. Phys.* **2019**, *52*, 363002.
(26) Mie, G. Beiträge zur Optik trüber Medien, speziell kolloidaler Metallösungen. *Ann. Phys.-Berlin* **1908**, *330*, 377−445.
(27) Draine, B. T.; Flatau, P. J. Discrete-dipole approximation for scattering calculations. *J. Opt. Soc. Am. A* **1994**, *11*, 1491−1499.
(28) Taflove, A.; Hagness, S. C.; Piket-May, M. *Computational Electromagnetics: The Finite-Difference Time-Domain Method*; Elsevier: Amsterdam, The Netherlands, 2005.
(29) Myroshnychenko, V.; Carbó-Argibay, E.; Pastoriza-Santos, I.; Pérez-Juste, J.; Liz-Marzán, L. M.; García de Abajo, F. J. Modeling the optical response of highly faceted metal nanoparticles with a fully 3D boundary element method. *Adv. Mater.* **2008**, *20*, 4288−4293.
(30) García de Abajo, F. J.; Howie, A. Retarded field calculation of electron energy loss in inhomogeneous dielectrics. *Phys. Rev. B* **2002**, *65*, 115418.
(31) Mennucci, B.; Corni, S. Multiscale modelling of photoinduced processes in composite systems. *Nat. Rev. Chem.* **2019**, *3*, 315−330.
(32) Bonatti, L.; Gil, G.; Giovannini, T.; Corni, S.; Cappelli, C. Plasmonic Resonances of Metal Nanoparticles: Atomistic vs Continuum Approaches. *Front. Chem.* **2020**, *8*, 340.
(33) Marcheselli, J.; Chateau, D.; Lerouge, F.; Baldeck, P.; Andraud, C.; Parola, S.; Baroni, S.; Corni, S.; Garavelli, M.; Rivalta, I. Simulating Plasmon Resonances of Gold Nanoparticles with Bipyramidal Shapes by Boundary Element Methods. *J. Chem. Theory Comput.* **2020**, *16*, 3807−3815.
(34) Coccia, E.; Fregoni, J.; Guido, C.; Marsili, M.; Pipolo, S.; Corni, S. Hybrid theoretical models for molecular nanoplasmonics. *J. Chem. Phys.* **2020**, *153*, 200901.
(35) Luo, Y.; Fernandez-Dominguez, A.; Wiener, A.; Maier, S. A.; Pendry, J. Surface plasmons and nonlocality: a simple model. *Phys. Rev. Lett.* **2013**, *111*, 093901.
(36) Ciraci, C.; Pendry, J. B.; Smith, D. R. Hydrodynamic model for plasmonics: a macroscopic approach to a microscopic problem. *ChemPhysChem* **2013**, *14*, 1109−1116.
(37) Raza, S.; Bozhevolnyi, S. I.; Wubs, M.; Mortensen, N. A. Nonlocal optical response in metallic nanostructures. *J. Phys.: Condens. Matter* **2015**, *27*, 183204.
(38) Ciraci, C.; Della Sala, F. Quantum hydrodynamic theory for plasmonics: Impact of the electron density tail. *Phys. Rev. B* **2016**, *93*, 205405.
(39) Toscano, G.; Raza, S.; Jauho, A.-P.; Mortensen, N. A.; Wubs, M. Modified field enhancement and extinction by plasmonic nanowire dimers due to nonlocal response. *Opt. Express* **2012**, *20*, 4176−4188.
(40) David, C.; García de Abajo, F. J. Surface plasmon dependence on the electron density profile at metal surfaces. *ACS Nano* **2014**, *8*, 9558−9566.

https://doi.org/10.1021/acsphotonics.2c00761
ACS Photonics 2022, 9, 3025−3034

(41) Toscano, G.; Straubel, J.; Kwiatkowski, A.; Rockstuhl, C.; Evers, F.; Xu, H.; Asger Mortensen, N.; Wubs, M. Resonance shifts and spill-out effects in self-consistent hydrodynamic nanoplasmonics. *Nat. Commun.* **2015**, *6*, 1−11.
(42) Bonatti, L.; Nicoli, L.; Giovannini, T.; Cappelli, C. In silico design of graphene plasmonic hot-spots. *Nanoscale Adv.* **2022**, *4*, 2294−2302.
(43) Gonçalves, P.; Christensen, T.; Rivera, N.; Jauho, A.-P.; Mortensen, N. A.; Soljačić, M. Plasmon−emitter interactions at the nanoscale. *Nat. Commun.* **2020**, *11*, 1−13.
(44) Echarri, A. R.; Gonçalves, P.; Tserkezis, C.; de Abajo, F. J. G.; Mortensen, N. A.; Cox, J. D. Optical response of noble metal nanostructures: quantum surface effects in crystallographic facets. *Optica* **2021**, *8*, 710−721.
(45) Babaze, A.; Ogando, E.; Stamatopoulou, P. E.; Tserkezis, C.; Mortensen, N. A.; Aizpurua, J.; Borisov, A. G.; Esteban, R. Quantum surface effects in the electromagnetic coupling between a quantum emitter and a plasmonic nanoantenna: time-dependent density functional theory vs. semiclassical Feibelman approach. *Opt. Express* **2022**, *30*, 21159−21183.
(46) Zhu, M.; Aikens, C. M.; Hollander, F. J.; Schatz, G. C.; Jin, R. Correlating the crystal structure of a thiol-protected Au25 cluster and optical properties. *J. Am. Chem. Soc.* **2008**, *130*, 5883−5885.
(47) Rossi, T. P.; Zugarramurdi, A.; Puska, M. J.; Nieminen, R. M. Quantized evolution of the plasmonic response in a stretched nanorod. *Phys. Rev. Lett.* **2015**, *115*, 236804.
(48) Weissker, H.-C.; Mottet, C. Optical properties of pure and core-shell noble-metal nanoclusters from TDDFT: The influence of the atomic structure. *Phys. Rev. B* **2011**, *84*, 165443.
(49) Marchesin, F.; Koval, P.; Barbry, M.; Aizpurua, J.; Sánchez-Portal, D. Plasmonic response of metallic nanojunctions driven by single atom motion: quantum transport revealed in optics. *ACS Photonics* **2016**, *3*, 269−277.
(50) Sinha-Roy, R.; Garcia-Gonzalez, P.; Weissker, H.-C.; Rabilloud, F.; Fernandez-Dominguez, A. I. Classical and ab Initio Plasmonics Meet at Sub-nanometric Noble Metal Rods. *ACS Photonics* **2017**, *4*, 1484−1493.
(51) Morton, S. M.; Jensen, L. A discrete interaction model/quantum mechanical method for describing response properties of molecules adsorbed on metal nanoparticles. *J. Chem. Phys.* **2010**, *133*, 074103.
(52) Morton, S. M.; Jensen, L. A discrete interaction model/quantum mechanical method to describe the interaction of metal nanoparticles and molecular absorption. *J. Chem. Phys.* **2011**, *135*, 134103.
(53) Jensen, L. L.; Jensen, L. Electrostatic interaction model for the calculation of the polarizability of large noble metal nanoclusters. *J. Phys. Chem. C* **2008**, *112*, 15697−15703.
(54) Jensen, L. L.; Jensen, L. Atomistic electrodynamics model for optical properties of silver nanoclusters. *J. Phys. Chem. C* **2009**, *113*, 15182−15190.
(55) Zakomirnyi, V. I.; Rinkevicius, Z.; Baryshnikov, G. V.; Sørensen, L. K.; Ågren, H. Extended discrete interaction model: plasmonic excitations of silver nanoparticles. *J. Phys. Chem. C* **2019**, *123*, 28867−28880.
(56) Rinkevicius, Z.; Li, X.; Sandberg, J. A.; Mikkelsen, K. V.; Ågren, H. A hybrid density functional theory/molecular mechanics approach for linear response properties in heterogeneous environments. *J. Chem. Theory Comput.* **2014**, *10*, 989−1003.
(57) Zakomirnyi, V. I.; Rasskazov, I. L.; Sørensen, L. K.; Carney, P. S.; Rinkevicius, Z.; Ågren, H. Plasmonic nano-shells: atomistic discrete interaction versus classic electrodynamics models. *Phys. Chem. Chem. Phys.* **2020**, *22*, 13467−13473.
(58) Giovannini, T.; Rosa, M.; Corni, S.; Cappelli, C. A classical picture of subnanometer junctions: an atomistic Drude approach to nanoplasmonics. *Nanoscale* **2019**, *11*, 6004−6015.
(59) Giovannini, T.; Bonatti, L.; Polini, M.; Cappelli, C. Graphene plasmonics: Fully atomistic approach for realistic structures. *J. Phys. Chem. Lett.* **2020**, *11*, 7595−7602.
(60) Lafiosca, P.; Giovannini, T.; Benzi, M.; Cappelli, C. Going Beyond the Limits of Classical Atomistic Modeling of Plasmonic Nanostructures. *J. Phys. Chem. C* **2021**, *125*, 23848−23863.
(61) Yamada, A. Classical electronic and molecular dynamics simulation for optical response of metal system. *J. Chem. Phys.* **2021**, *155*, 174118.
(62) Duan, H.; Fernández-Domínguez, A. I.; Bosman, M.; Maier, S. A.; Yang, J. K. Nanoplasmonics: classical down to the nanometer scale. *Nano Lett.* **2012**, *12*, 1683−1689.
(63) Scholl, J. A.; Koh, A. L.; Dionne, J. A. Quantum plasmon resonances of individual metallic nanoparticles. *Nature* **2012**, *483*, 421−427.
(64) Pinchuk, A.; Kreibig, U.; Hilger, A. Optical properties of metallic nanoparticles: influence of interface effects and interband transitions. *Surf. Sci.* **2004**, *557*, 269−280.
(65) Pinchuk, A.; Von Plessen, G.; Kreibig, U. Influence of interband electronic transitions on the optical absorption in metallic nanoparticles. *J. Phys. D: Appl. Phys.* **2004**, *37*, 3133.
(66) Balamurugan, B.; Maruyama, T. Evidence of an enhanced interband absorption in Au nanoparticles: size-dependent electronic structure and optical properties. *Appl. Phys. Lett.* **2005**, *87*, 143105.
(67) Liebsch, A. Surface-plasmon dispersion and size dependence of Mie resonance: silver versus simple metals. *Phys. Rev. B* **1993**, *48*, 11317.
(68) Santiago, E. Y.; Besteiro, L. V.; Kong, X.-T.; Correa-Duarte, M. A.; Wang, Z.; Govorov, A. O. Efficiency of hot-electron generation in plasmonic nanocrystals with complex shapes: surface-induced scattering, hot spots, and interband transitions. *ACS Photonics* **2020**, *7*, 2807−2824.
(69) Giovannini, T.; Puglisi, A.; Ambrosetti, M.; Cappelli, C. Polarizable QM/MM approach with fluctuating charges and fluctuating dipoles: the QM/FQFμ model. *J. Chem. Theory Comput.* **2019**, *15*, 2233−2245.
(70) Giovannini, T.; Riso, R. R.; Ambrosetti, M.; Puglisi, A.; Cappelli, C. Electronic transitions for a fully polarizable qm/mm approach based on fluctuating charges and fluctuating dipoles: linear and corrected linear response regimes. *J. Chem. Phys.* **2019**, *151*, 174104.
(71) Giovannini, T.; Egidi, F.; Cappelli, C. Molecular spectroscopy of aqueous solutions: a theoretical perspective. *Chem. Soc. Rev.* **2020**, *49*, 5664−5677.
(72) Verma, P. Tip-enhanced Raman spectroscopy: technique and recent advances. *Chem. Rev.* **2017**, *117*, 6447−6466.
(73) Zhang, W.; Yeo, B. S.; Schmid, T.; Zenobi, R. Single molecule tip-enhanced Raman spectroscopy with silver tips. *J. Phys. Chem. C* **2007**, *111*, 1733−1738.
(74) Chen, X.; Moore, J. E.; Zekarias, M.; Jensen, L. Atomistic electrodynamics simulations of bare and ligand-coated nanoparticles in the quantum size regime. *Nat. Commun.* **2015**, *6*, 8921.
(75) Ringe, E.; McMahon, J. M.; Sohn, K.; Cobley, C.; Xia, Y.; Huang, J.; Schatz, G. C.; Marks, L. D.; Van Duyne, R. P. Unraveling the effects of size, composition, and substrate on the localized surface plasmon resonance frequencies of gold and silver nanocubes: a systematic single-particle approach. *J. Phys. Chem. C* **2010**, *114*, 12511−12516.
(76) Etchegoin, P. G.; Le Ru, E.; Meyer, M. An analytic model for the optical properties of gold. *J. Chem. Phys.* **2006**, *125*, 164705.
(77) Johnson, P. B.; Christy, R.-W. Optical constants of the noble metals. *Phys. Rev. B* **1972**, *6*, 4370.
(78) Johnson, H. E.; Aikens, C. M. Electronic structure and TDDFT optical absorption spectra of silver nanorods. *J. Phys. Chem. A* **2009**, *113*, 4445−4450.
(79) Bae, G.-T.; Aikens, C. M. Time-dependent density functional theory studies of optical properties of Ag nanoparticles: octahedra, truncated octahedra, and icosahedra. *J. Phys. Chem. C* **2012**, *116*, 10356−10367.
(80) Cottancin, E.; Celep, G.; Lermé, J.; Pellarin, M.; Huntzinger, J.; Vialle, J.; Broyer, M. Optical properties of noble metal clusters as a

https://doi.org/10.1021/acsphotonics.2c00761
ACS Photonics 2022, 9, 3025−3034

function of the size: comparison between experiments and a semi-quantal theory. *Theor. Chem. Acc.* **2006**, *116*, 514−523.
(81) Chen, X.; Jensen, L. Morphology dependent near-field response in atomistic plasmonic nanocavities. *Nanoscale* **2018**, *10*, 11410−11417.
(82) Kreibig, U.; Vollmer, M. *Optical Properties of Metal Clusters*; Springer Science & Business Media, 2013; Vol. 25.
(83) Novo, C.; Gomez, D.; Perez-Juste, J.; Zhang, Z.; Petrova, H.; Reismann, M.; Mulvaney, P.; Hartland, G. V. Contributions from radiation damping and surface scattering to the linewidth of the longitudinal plasmon band of gold nanorods: a single particle study. *Phys. chem. Chem. Phys.* **2006**, *8*, 3540−3546.
(84) Juvé, V.; Cardinal, M. F.; Lombardi, A.; Crut, A.; Maioli, P.; Pérez-Juste, J.; Liz-Marzán, L. M.; Del Fatti, N.; Vallée, F. Size-dependent surface plasmon resonance broadening in nonspherical nanoparticles: single gold nanorods. *Nano Lett.* **2013**, *13*, 2234−2240.
(85) Foerster, B.; Joplin, A.; Kaefer, K.; Celiksoy, S.; Link, S.; Sönnichsen, C. Chemical interface damping depends on electrons reaching the surface. *ACS Nano* **2017**, *11*, 2886−2893.
(86) Douglas-Gallardo, O. A.; Soldano, G. J.; Mariscal, M. M.; Sánchez, C. G. Effects of oxidation on the plasmonic properties of aluminum nanoclusters. *Nanoscale* **2017**, *9*, 17471−17480.
(87) Kuisma, M.; Sakko, A.; Rossi, T. P.; Larsen, A. H.; Enkovaara, J.; Lehtovaara, L.; Rantala, T. T. Localized surface plasmon resonance in silver nanoparticles: Atomistic first-principles time-dependent density-functional theory calculations. *Phys. Rev. B* **2015**, *91*, 115431.
(88) Iida, K.; Noda, M.; Ishimura, K.; Nobusada, K. First-principles computational visualization of localized surface plasmon resonance in gold nanoclusters. *J. Phys. Chem. A* **2014**, *118*, 11317−11322.
(89) Payton, J. L.; Morton, S. M.; Moore, J. E.; Jensen, L. A hybrid atomistic electrodynamics−quantum mechanical approach for simulating surface-enhanced raman scattering. *Acc. Chem. Res.* **2014**, *47*, 88−99.
(90) Kim, M.; Kwon, H.; Lee, S.; Yoon, S. Effect of nanogap morphology on plasmon coupling. *ACS Nano* **2019**, *13*, 12100−12108.

https://doi.org/10.1021/acsphotonics.2c00761
ACS Photonics 2022, 9, 3025−3034

II. Fully atomistic modeling of plasmonic bimetallic nanoparticles: nanoalloys and core-shell systems

frontiers | Frontiers in Photonics

TYPE Original Research
PUBLISHED 16 June 2023
DOI 10.3389/fphot.2023.1199598

OPEN ACCESS

EDITED BY
Stefania D'Agostino,
National Research Council (CNR), Italy

REVIEWED BY
Cristian Ciracì,
Italian Institute of Technology (IIT), Italy
Maxim A. Yurkin,
Institute of Chemical Kinetics and Combustion (RAS), Russia

*CORRESPONDENCE
Tommaso Giovannini,
tommaso.giovannini@sns.it
Chiara Cappelli,
chiara.cappelli@sns.it

RECEIVED 03 April 2023
ACCEPTED 07 June 2023
PUBLISHED 16 June 2023

CITATION
Nicoli L, Lafiosca P, Grobas Illobre P, Bonatti L, Giovannini T and Cappelli C (2023), Fully atomistic modeling of plasmonic bimetallic nanoparticles: nanoalloys and core-shell systems. *Front. Photonics* 4:1199598. doi: 10.3389/fphot.2023.1199598

Fully atomistic modeling of plasmonic bimetallic nanoparticles: nanoalloys and core-shell systems

Luca Nicoli[1], Piero Lafiosca[1], Pablo Grobas Illobre[1], Luca Bonatti[1], Tommaso Giovannini[1]* and Chiara Cappelli[1,2]*

[1]Classe di Scienze, Scuola Normale Superiore, Pisa, Italy, [2]European Laboratory for Non-Linear Spectroscopy (LENS), Florence, Italy

The recently developed ωFQFμ model (*ACS Photonics*, 9, 3,025–3,034) is extended to bimetallic nanoparticles, such as nanoalloys and core-shell systems. The method finds its grounds in basic physical concepts, such as Drude conduction theory, electrostatics, interband transitions, and quantum tunneling. The approach, which is parametrized on *ab initio* simulations of Ag-Au nanoalloys, is challenged against complex Ag-Au nanostructures (spheres, nanorods, and core-shell nanoparticles). Remarkable agreement with available experimental data is found, thus demonstrating the reliability of the newly developed approach.

KEYWORDS

atomistic, alloys, core-shell, plasmonics, gold, silver, bimetallic

1 Introduction

Metal nanoparticles (NPs) exhibit unique optical properties, which are mainly due to the formation of surface plasmons, i.e., collective excitations of conductive electrons. (Moskovits, 1985; Nie and Emory, 1997; Maier, 2007; Anker et al., 2008; Atwater and Polman, 2010; Santhosh et al., 2016). At the plasmon resonance frequency (PRF) such surface plasmons exhibit a resonant behavior, which gives rise to a huge enhancement of the electric field in the proximity of the NP surface. This phenomenon is exploited to increase the detection limit of common analytical techniques. (Kneipp et al., 1997; Maier et al., 2003; Muehlschlegel et al., 2005; Lim et al., 2010; Giannini et al., 2011; Neuman et al., 2018). PRF can be tuned by varying the NP shape, dimension, and chemical composition (Ag, Au, Al, . . .). As an alternative, bimetallic nanoalloys or core-shell NPs can be used. Such systems are constituted by two different metal elements, e.g., Ag-Au, Au-Cu, Cu-Ag (Xiang et al., 2008; Wang et al., 2009; Huang et al., 2015; Gong and Leite, 2016; Cao et al., 2018; Ma et al., 2020; Awada et al., 2021). In this case, the PRF can be tuned not only by modifying the aforementioned variables (size, shape, . . .) but also the relative concentration of the two metals.

Many theoretical approaches have been developed to describe the plasmonic properties of single metal NPs(Corni and Tomasi, 2001; 2002a; Aizpurua et al., 2003; Myroshnychenko et al., 2008; Hohenester and Trügler, 2012; Ciraci et al., 2013; Ciraci and Della Sala, 2016; Giovannini et al., 2019b; Bonatti et al., 2020; Coccia et al., 2020; Baghramyan et al., 2021; Giannone et al., 2021; Della Sala, 2022; Della Sala et al., 2022), among which is worth mentioning quantum hydrodynamic models, which are able to describe both nonlocal and

electron spill-out effects (Ciraci et al., 2013; Raza et al., 2015; Ciraci and Della Sala, 2016). However, the most widely exploited methods are based on classical physics, (Corni and Tomasi, 2002b; Hao et al., 2007; Jensen and Jensen, 2008; Jensen and Jensen, 2009; Pérez-González et al., 2010; Halas et al., 2011; Ciracì et al., 2012; Chen et al., 2015), such as the Mie Theory (Mie, 1908), the finite difference time domain (FDTD) (Shuford et al., 2006), the Discrete Dipole Approximation (DDA) (Draine and Flatau, 1994) or exploit a continuum representation of the NP by means of the Boundary Element Method (BEM) (Corni and Tomasi, 2001; García de Abajo and Howie, 2002; Hohenester and Trügler, 2012; Hohenester, 2015). All the classical approaches mentioned above rely on defining a suitable permittivity function ε. Clearly, in the case of bimetallic systems, ε-dependent methods are not flexible enough to treat *a priori* any chemical composition and need to resort to experimentally measured ε values for specific alloy concentrations or to approximations, which may not be physically justified (such as a linear combination of the ε values of the two metals) (Peña-Rodríguez and Pal, 2011a; Verbruggen et al., 2013; Ma et al., 2015; Putra et al., 2017; Kuddah et al., 2020; Newmai et al., 2022).

Atomistic approaches appear as the most natural choice to overcome this problem. Full *ab initio* methods can be exploited, however, their prohibitive computational cost limits their application to relatively small systems (Barcaro et al., 2011; López Lozano et al., 2013; Barcaro et al., 2014; Barcaro et al., 2015; Olobardi et al., 2019; Asadi-Aghbolaghi et al., 2020; Danielis et al., 2021). For this reason, classical atomistic approaches have been developed, (Jensen and Jensen, 2008; Jensen and Jensen, 2009; Chen et al., 2015; Zakomirnyi et al., 2019; Zakomirnyi et al., 2020), however they have only marginally been applied to the description of bimetallic NPs (Sørensen et al., 2021).

In this work, we extend ωFQFμ (Giovannini et al., 2022) to simulate the optical properties of bimetallic NPs, with special emphasis on Ag-Au nanoalloys and core-shell systems. ωFQFμ is a fully atomistic, classical, approach, which assigns each atom of the metal nanoalloy with an electric charge and an electric dipole moment, which vary as a response to an externally applied electric field. The theoretical foundations of ωFQFμ lay in Drude's theory of conduction, classical electrodynamics, interband transitions, and quantum tunneling. In fact, the Drude mechanism of charge exchange is modeled through the equation of motion of the electric charges (Giovannini et al., 2019b; Bonatti et al., 2020; Giovannini et al., 2020; Lafiosca et al., 2021; Bonatti et al., 2022), while interband contributions are taken into account by means of effective interband polarizability (Giovannini et al., 2022) introduced to mimic d-shell polarizability (Liebsch, 1993). Also, quantum tunneling effects, which play a crucial role in nanojunctions and nanoaggregates (Esteban et al., 2012; Giovannini et al., 2019b), are described by tuning charge exchange through a phenomenological function. Therefore, ωFQFμ conceptually differs from other approaches which are based on classical physics only.

The manuscript is organized as follows. In the next section, the formulation of ωFQFμ for bimetallic systems is presented. After a brief section presenting the computational details, the method is tested against the reproduction of the plasmonic properties of alloyed spherical NPs, alloyed nanorods, and spherical core-shell systems. Conclusions and a sketch of the future perspectives of the approach end the manuscript.

2 Materials and methods

2.1 Theoretical model

In this section, we extend ωFQFμ (Giovannini et al., 2022) to describe the optical properties of bimetallic systems. To this end, we follow the derivation reported in (Giovannini et al., 2019b) and (Giovannini et al., 2022). In ωFQFμ, the fluctuations of the electronic density of a plasmonic substrate composed of N atoms emerging as a response to the external electric field are represented by a set of N discrete fluctuating complex-valued charges q_i and N fluctuating complex-valued dipoles $\boldsymbol{\mu}_i$, which are located at atomic positions. The equation of motion of charges q originates from the continuity equation (Giovannini et al., 2019b) (atomic units are used throughout the paper):

$$\begin{aligned}\frac{\mathrm{d}q_i}{\mathrm{d}t} &= \sum_{ij} A_{ij}\left(n_j\langle\mathbf{p}_j\rangle_i\cdot\hat{\mathbf{l}}_{ji} - n_i\langle\mathbf{p}_i\rangle_j\cdot\hat{\mathbf{l}}_{ij}\right)\\ &= \sum_{ij}\left(A_j n_j\langle\mathbf{p}_j\rangle_i\cdot\hat{\mathbf{l}}_{ji} - A_i n_i\langle\mathbf{p}_i\rangle_j\cdot\hat{\mathbf{l}}_{ij}\right)\end{aligned} \tag{1}$$

where n_i is the electron density on atom i, $\langle\mathbf{p}_i\rangle_j$ is the momentum of the electron associated with atom i averaged over all the trajectories towards atom j. $\hat{\mathbf{l}}_{ij} = -\hat{\mathbf{l}}_{ji}$ is the unit vector connecting i and j. A_{ij} is the effective area dividing ith and jth atoms, and its value modulates the charge exchange between each atom pair. By following (Giovannini et al., 2019b; Giovannini et al., 2020; Giovannini et al., 2022), A_{ij} is approximated as an atomic parameter (A_i).The electron momentum $\mathbf{p}_i$ can be estimated by means of the Drude model of conductance (Bade, 1957) as follows:

$$\frac{\mathrm{d}\mathbf{p}_i}{\mathrm{d}t} = \mathbf{E}_i(t) - \frac{\mathbf{p}_i}{\tau_i} \tag{2}$$

where $\mathbf{E}_i(t)$ is the electric field acting on the ith atom and τ_i is the relaxation time associated with scattering events. Assuming the external uniform monochromatic electric field $\mathbf{E}^{\mathrm{ext}}(t) = \mathbf{E}^{\mathrm{ext}}(\omega)\exp(-\mathrm{i}\omega t)$ oscillates at frequency ω, we can reformulate Eqs 1, 2 in the frequency domain, i.e.:

$$-\mathrm{i}\omega q_i = \sum_j\left(A_j n_j\frac{\langle\mathbf{E}_j(\omega)\rangle_i\cdot\hat{\mathbf{l}}_{ji}}{1/\tau_j - \mathrm{i}\omega} - A_i n_i\frac{\langle\mathbf{E}_i(\omega)\rangle_j\cdot\hat{\mathbf{l}}_{ij}}{1/\tau_i - \mathrm{i}\omega}\right) \tag{3}$$

Following the original derivation reported in (Giovannini et al., 2019b), we can write:

$$\langle\mathbf{E}_i(\omega)\rangle_j\cdot\hat{\mathbf{l}}_{ij} \approx \frac{\phi_j - \phi_i}{l_{ij}} \tag{4}$$

where ϕ_i is the chemical potential of atom i and $l_{ij} = l_{ji}$ is the distance between ith and jth atoms. By this, Eq. 3 becomes:

$$-\mathrm{i}\omega q_i = \sum_j\left(\frac{A_j n_j\left(1 - f_{ji}\left(l_{ij}\right)\right)}{1/\tau_j - \mathrm{i}\omega} + \frac{A_i n_i\left(1 - f_{ij}\left(l_{ij}\right)\right)}{1/\tau_i - \mathrm{i}\omega}\right)\frac{\phi_i - \phi_j}{l_{ij}} \tag{5}$$

where quantum tunneling effects are expressed in terms of a Fermi-like function f_{ij} (l_{ij}), which reads:

$$f_{ij}\left(l_{ij}\right)=\frac{1}{1+\exp\left[-d_{ij}\left(\frac{l_{ij}}{s_{ij}\cdot l_{ij}^{0}}-1\right)\right]} \tag{6}$$

where l_{ij}^{0} is the equilibrium distance between atoms i and j, and the parameters d_{ij} and s_{ij} determine the shape of the damping function. Notice that the inclusion of a phenomenological description of quantum tunneling is needed to correctly describe the optical response of plasmonic subnanometer junctions and hot-spots (Esteban et al., 2012; Esteban et al., 2015; Scholl et al., 2013; Giovannini et al., 2019b; Bonatti et al., 2022; Giovannini et al., 2022). Indeed, in the case of plasmonic nanoaggregates, charge transfer plasmons (CT) may occur. In ωFQFμ, the charge exchange among different NPs is governed by Drude and tunneling mechanisms, and the total system charge is conserved (see Eq. 5), allowing for a physically consistent description of such plasmonic modes. To make the notation more compact, the following terms are introduced (Lafiosca et al., 2021):

$$w_i(\omega)=\frac{2n_i}{1/\tau_i-\mathrm{i}\omega} \tag{7}$$

$$K_{ij}=A_i\frac{1-f_{ij}\left(l_{ij}\right)}{l_{ij}} \tag{8}$$

$$z_i(\omega)=-\frac{\mathrm{i}\omega}{w_i(\omega)} \tag{9}$$

Dividing Eq. 5 by $w_i(\omega)$, we obtain:

$$z_i(\omega)q_i=\frac{1}{2}\sum_j\left(K_{ij}+\frac{w_j(\omega)}{w_i(\omega)}K_{ji}\right)\left(\phi_i-\phi_j\right) \tag{10}$$

where the chemical potential ϕ_i can be written as:

$$\phi_i=\sum_k T_{ik}^{\mathrm{qq}}q_k+\sum_k T_{ik}^{\mathrm{q\mu}}\boldsymbol{\mu}_k+V_i^{\mathrm{ext}} \tag{11}$$

The first and the second terms in Eq. 11 are the electric potential generated by the charges and the dipoles of the system, mediated by the interaction tensors $\mathbf{T}^{\mathrm{qq}}$ and $\mathbf{T}^{\mathrm{q\mu}}$ (see (Giovannini et al., 2019a) for their definitions). V_i^{ext} is the electric potential associated with the external electric field. By plugging Eq. 11 into Eq. 10, the linear equations ruling charge evolution are obtained, i.e.:

$$\begin{aligned}\mathbf{Z}(\omega)\mathbf{q}=&\frac{1}{2}\left(\bar{\mathbf{K}}+\bar{\mathbf{H}}(\omega)\right)\mathbf{T}^{\mathrm{qq}}\mathbf{q}+\frac{1}{2}\left(\bar{\mathbf{K}}+\bar{\mathbf{H}}(\omega)\right)\mathbf{T}^{\mathrm{q\mu}}\boldsymbol{\mu}\\&+\frac{1}{2}\left(\bar{\mathbf{K}}+\bar{\mathbf{H}}(\omega)\right)\mathbf{V}\end{aligned} \tag{12}$$

where the following matrices are introduced:

$$H_{ij}(\omega)=\frac{w_j(\omega)}{w_i(\omega)}K_{ji} \tag{13}$$

$$\bar{K}_{ij}=K_{ij}-\sum_k K_{ik}\delta_{ij} \tag{14}$$

$$Z_{ij}=z_i\delta_{ij} \tag{15}$$

$$\bar{H}_{ij}=H_{ij}-\sum_k H_{ik}\delta_{ij} \tag{16}$$

The electric dipoles $\boldsymbol{\mu}_i$, which are introduced to properly model interband contributions, are obtained by solving the following set of linear equations:

$$\boldsymbol{\mu}_i=\alpha_i(\omega)\left[\mathbf{E}_i^{\mathrm{ext}}(\omega)+\mathbf{E}_i^{q}(\omega)+\mathbf{E}_i^{\mu}(\omega)\right] \tag{17}$$

where $\alpha_i(\omega)$ is the frequency-dependent polarizability of the ith atom, related to interband terms, which multiplies the total electric field acting on the ith dipole, composed by the external field $\mathbf{E}_i^{\mathrm{ext}}$, the field generated by the fluctuating charges, $\mathbf{E}_i^{q}$, and the field generated by the fluctuating dipoles, $\mathbf{E}_i^{\mu}$. If the system is homogeneous, α_i is calculated as reported in (Giovannini et al., 2022):

$$\alpha_i(\omega)\equiv\alpha_A^{\mathrm{IB}}(\omega)=\frac{\varepsilon_A^{\mathrm{IB}}(\omega)}{4\pi n_A} \tag{18}$$

where $\varepsilon_A^{\mathrm{IB}}$ is the interband contribution to the frequency-dependent permittivity function and n_A is the number density of atoms of the chemical element A. $\varepsilon^{\mathrm{IB}}$ is calculated by subtracting the Drude term from the frequency-dependent permittivity.

If the system is heterogeneous, the link between the macroscopic, bulk dynamical permittivity $\varepsilon^{\mathrm{IB}}(\omega)$ and the microscopic, atomistic frequency-dependent interband polarizability $\alpha_i(\omega)$ is not straightforward. Let us focus on bimetallic systems, composed of two chemical elements A and B. We assume the interband polarizability of the ith atom belonging to the A moiety to be a function of the local composition of the system, i.e., $\alpha_{A,i}^{\mathrm{IB,alloy}}(N_{A,i},N_{B,i})$, where $N_{A,i}$ and $N_{B,i}$ are the number of nearest neighbors of A and B type, respectively. The simplest approach is to model $\alpha_{A,i}^{\mathrm{IB,\,alloy}}$ as the weighted average of α_A^{IB} and α_B^{IB}. Therefore, the interband frequency-dependent polarizability of the ith atom of species A in the alloy composed by materials A and B is defined as follows:

$$\alpha_i(\omega)\equiv\alpha_{A,i}^{\mathrm{IB,alloy}}(\omega)=\left(\frac{\frac{N_{A,i}+1}{\alpha_A^{\mathrm{IB}}(\omega)}+\frac{N_{B,i}}{\alpha_B^{\mathrm{IB}}(\omega)}}{N_{A,i}+N_{B,i}+1}\right)^{-1} \tag{19}$$

Notice that, possible alternative approaches, e.g., to resort to arithmetic averages have been investigated. However, the weighted harmonic mean indeed gives the best numerical results (see Supplementary Figure S1 and Sec. S1 in the Supplementary Materials – SM).

Starting from Eq. 17, the final expression for the electric dipoles becomes (Giovannini et al., 2022):

$$\boldsymbol{\mu}_i=\alpha_i(\omega)\left[\mathbf{E}_i^{\mathrm{ext}}+\sum_k\mathbf{T}_{ik}^{\mu q}q_k+\sum_k\mathbf{T}_{ik}^{\mu\mu}\boldsymbol{\mu}_k\right] \tag{20}$$

where the field generated by the multipoles is mediated by the interaction tensors $\mathbf{T}^{\mu q}$ and $\mathbf{T}^{\mu\mu}$, defined according to (Giovannini et al., 2019a).

The coupled charge-dipole equations can finally be written in a compact notation as follows:

$$\begin{aligned}&\begin{bmatrix}\frac{1}{2}\left(\bar{\mathbf{K}}+\bar{\mathbf{H}}(\omega)\right)\mathbf{T}^{\mathrm{qq}}-\mathbf{Z}(\omega) & \frac{1}{2}\left(\bar{\mathbf{K}}+\bar{\mathbf{H}}(\omega)\right)\mathbf{T}^{\mathrm{q\mu}}\\ \mathbf{T}^{\mu q} & \mathbf{T}^{\mu\mu}-\mathbf{Z}^{\mathrm{IB}}(\omega)\end{bmatrix}\begin{bmatrix}\mathbf{q}\\ \boldsymbol{\mu}\end{bmatrix}\\&=\begin{bmatrix}\frac{1}{2}\left(\bar{\mathbf{K}}+\bar{\mathbf{H}}(\omega)\right)\mathbf{V}^{\mathrm{ext}}\\ -\mathbf{E}^{\mathrm{ext}}\end{bmatrix}\end{aligned} \tag{21}$$

where $\mathbf{Z}^{\mathrm{IB}}$ is a diagonal matrix, of which the elements $Z_i^{\mathrm{IB}}(\omega)=-1/\alpha_i(\omega)$ are defined according to Eq. 19. Notice that in the case of homogenous systems, i.e., $A=B$, the standard ωFQFμ equations presented by Giovannini et al. (2022) are recovered. From the values of charges and dipoles, the complex polarizability $\bar{\alpha}$ can be

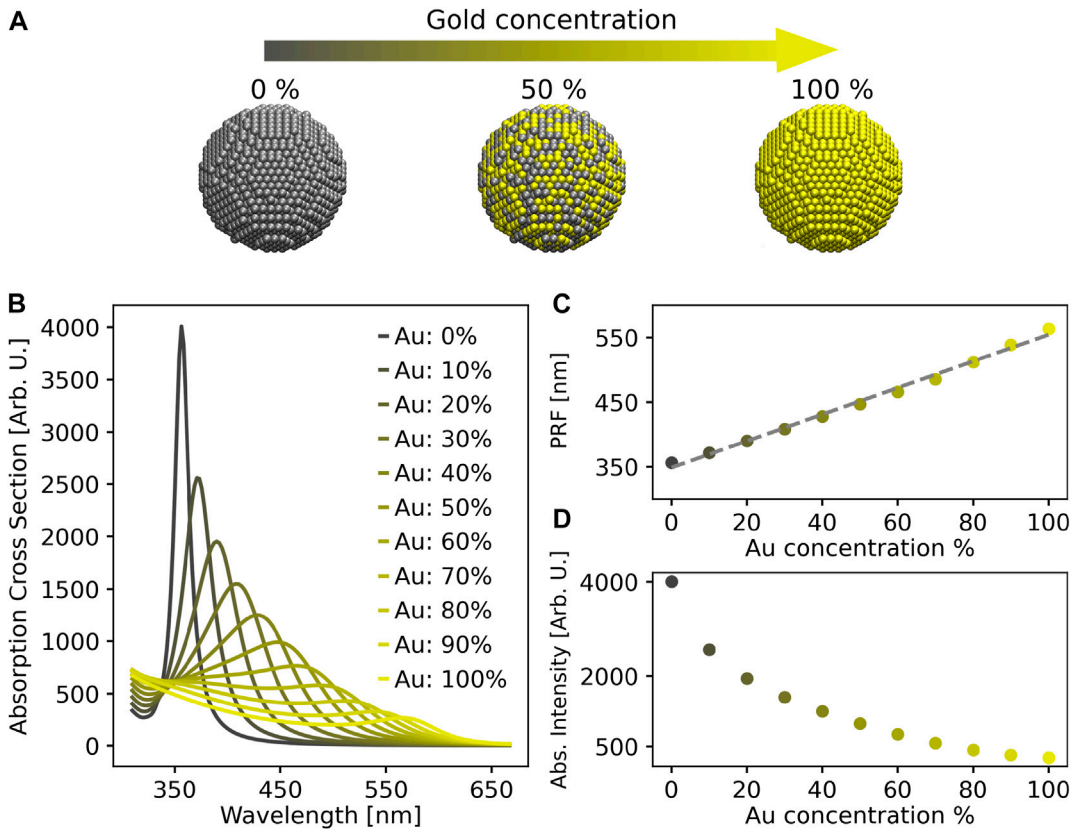

FIGURE 1
(A) Graphical depiction of spherical NP structures. ωFQFμ absorption cross-section **(B)**, Plasmon Resonance Frequency (PRF) **(C)**, and absorption intensity **(D)** as a function of Au concentration.

computed, from which the absorption cross section σ^{abs} can be calculated:

$$\bar{\alpha}(\omega)_{kl} = \frac{\partial \bar{d}_k(\omega)}{\partial E_l(\omega)} = \sum_i q_{i,k}(\omega) \cdot \frac{k_i}{E_l(\omega)} - \sum_i \mu_{i,k}(\omega) \tag{22}$$

$$\sigma^{\text{abs}} = \frac{4\pi}{3c}\omega \ \text{tr}\left(\text{Im}\left(\bar{\alpha}(\omega)\right)\right) \tag{23}$$

In the previous equations $\mathbf{d}$ is the total complex dipole moment, i runs over NP atoms, k represents x, y, z positions of the ith atom, and l runs over x, y, z directions of the external electric field. c is the speed of light and $\text{Im}(\bar{\alpha})$ is the imaginary part of the complex polarizability $\bar{\alpha}$.

2.2 Computational details

The developed ωFQFμ approach is challenged to reproduce the optical response of several Ag-Au nanostructures. In particular, we first consider Ag-Au spherical nanoalloys with diameter D = 5.2 nm (4,347 atoms) and Ag-Au nanorods with D = 2.5 nm and length L = 10 nm (2,560 atoms), which are generated by using Atomic Simulation Environment (ASE) Python module v. 3.17 (Larsen et al., 2017). A lattice constant of 4.08 Å (Haynes, 2014) and a Face-Centered Cubic (FCC) packing are exploited. For both spheres and nanorods, ten alloy compositions are considered by starting from pure Ag structures and increasing the percentage of Au atoms, which randomly replace Ag atoms (from 0% to 100%, with a constant step of 10%). To gain statistical significance, for each Au percentage, ten nanoalloy structures are generated by randomly replacing the proper fraction of Ag with Au, similarly to the strategy followed in previous studies (Sørensen et al., 2021). As a further example, core-shell spherical systems, which are constituted by an inner Au sphere (D = 5.0 nm, 3,851 atoms) surrounded by an outer Ag shell (D = 6.25 nm, 3,698 atoms), are investigated.

ωFQFμ equations are solved by using a stand-alone Fortran 95 package. ωFQFμ parameters (see Eqs 5, 6, 18) for Ag and Au atoms are taken from (Giovannini et al., 2022). In particular, Drude and interband parameters are recovered from Ag and Au experimental permittivity functions (Etchegoin et al., 2006). The parameters d_{ij} = 12.0 and s_{ij} = 0.95 entering Eq. 6 are obtained by fitting ωFQFμ results for i = Ag and j = Au (and *vice versa*) on reference time-dependent density functional theory + tight binding (TD-DFT + TB) (Asadi-Aghbolaghi et al., 2020) absorption spectra of Ag-Au clusters (see Sec. S2 in the SM).

3 Results and discussion

3.1 Spherical nanoparticles and nanorods

The modeling of the dependence of the absorption cross-section σ^{abs} of a spherical NP on the Au concentration has received much

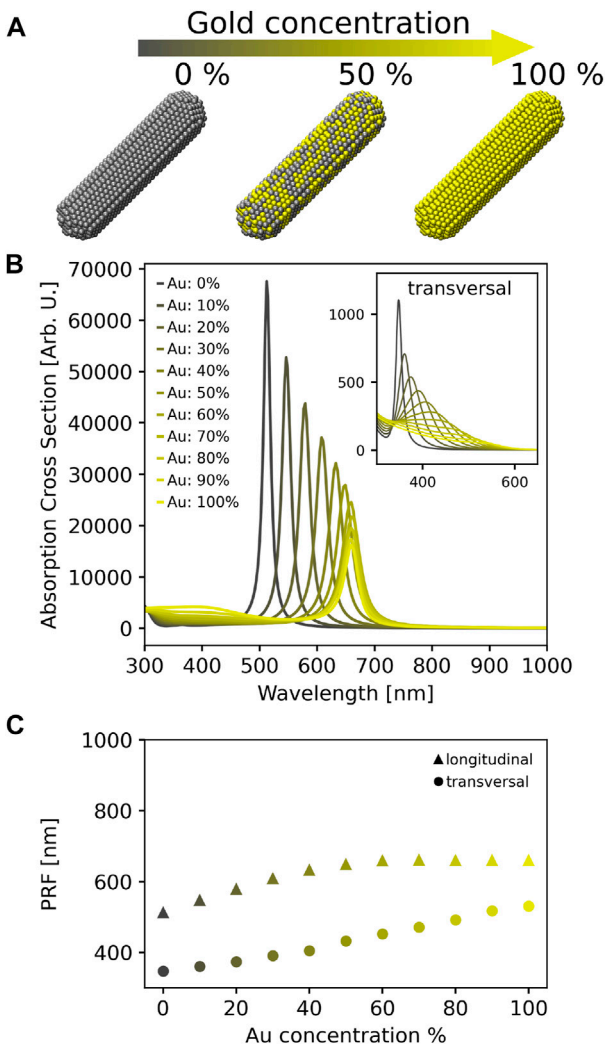

FIGURE 2
(A) Graphical depiction of nanorod structures. L = 10 nm and AR = 4. ωFQFμ absorption cross section **(B)** and Plasmon Resonance Frequency (PRF) **(C)** as a function of Au concentration. Both transversal (see inset in **(B)**) and longitudinal modes are considered.

attention in the literature (Papavassiliou, 1976; Link et al., 1999; Rioux et al., 2014; Ristig et al., 2015). In particular, a simple linear combination of Ag and Au permittivity functions combined with the Mie theory cannot reproduce the linear behavior of the plasmon red-shift upon increasing Au concentration which is experimentally observed (Link et al., 1999). This issue can be solved by following the strategy proposed by Rioux et al. (2014), who have developed an analytical and rigorous model to predict a composition-dependent complex dielectric function of Ag-Au alloys, based on critical point analysis of the band-structure of Ag and Au. By coupling such modeling to the Mie theory, the correct trend is followed for spherical nanoalloys. It is worth noting that such a strategy might be exploited within the more refined, yet continuum, BEM method, thus overcoming the limitations of this approach in describing the plasmonic properties of nanoalloys. However, while the methodology proposed by Rioux et al. (2014) is rigorous from the theoretical point of view, its extension to different alloy compositions, and to alloys of different chemical nature rather than Au and Ag is far from trivial, due to the high (about 30) number of parameters that would need to be fitted to obtain the composition dependent dielectric function.

Computed ωFQFμ values for σ^{abs} of a spherical NP with different Au concentrations are reported in (see Figure 1). In all cases, spectra are characterized by a main peak (associated with the dipolar mode, see Supplementary Figure S2 in the SM), which redshifts and lowers in intensity as the Au concentration increases. By plotting the PRF (in nm) as a function of the percentage of Au (see Figure 1C), a linear trend is observed ($R^2 \sim 1.00$). This behavior perfectly follows Vegard's law, which reads:

$$\lambda^{Vegard}(x) = (1-x)\lambda_{Ag} + x\lambda_{Au} \tag{24}$$

where x is the percentage of Au atoms. Such a linear dependence of the absorption wavelength on Au percentage is reported by many experimental works (Papavassiliou, 1976; Link et al., 1999; Rioux et al., 2014; Ristig et al., 2015). The slope (2.06 nm/% Au) of the line fitted on ωFQFμ results is in good agreement with experimental data (Link et al., 1999) (~ 1.35 nm/% Au). Furthermore, by moving from pure Ag to pure Au NPs, the intensity of the plasmon band exponentially decreases (R^2 = 0.99, see Figure 1D), thus perfectly reproducing experimental findings (Link et al., 1999).

We note that, remarkably, other classical atomistic approaches may fail at reproducing the experimentally reported linear trend in wavelength and the exponentially decreasing intensity (Sørensen et al., 2021). Differently, ωFQFμ can correctly reproduce all the plasmonic properties of these structures, which is a key result of this paper.

We now move to discuss the plasmonic properties of Ag-Au alloy nanorods. Also in this case, we study the dependence of the absorption frequency on the Au concentration, which varies from 0% (pure Ag nanorod) to 100% (pure Au nanorod), with a constant step of 10%. ωFQFμ absorption cross sections, which are reported in Figure 2B, are clearly dominated by an intense peak which redshifts and decreases in intensity as the gold concentration increases. This peak is associated with the longitudinal dipolar mode (see also Supplementary Figure S3 in the SM). From a comparison with spherical NPs (see Figure 1B), we note that the dipolar peak moves to lower energies, independently of the chemical composition of the alloy nanorod. Also, in this case, additional bands can be appreciated in the region between 350 and 500 nm. There, octupolar plasmons arise (Bonatti et al., 2020), together with transversal dipolar modes. The associated bands associated are graphically depicted as an inset in Figure 2B, and redshift and lower in intensity as the Au concentration increases.

The PRFs (in nm) of both the longitudinal and transversal dipolar modes as a function of the Au percentage are graphically depicted in Figure 2C. The transversal mode follows the linear trend (circles, R^2 = 0.99) predicted by Vegard's law (see Eq. 24), while for the longitudinal plasmon, an evident deviation from the linear regime is observed, especially for Au concentrations larger than 40%. Our findings are in agreement with the experimental measurements reported by Bok et al. (2009), where for the transversal peak a linear trend is measured. Also, the experimental slope (1.47 nm/%Au) correlates significantly well with our calculations (1.92 nm/%Au). Differently, the longitudinal absorption wavelength is reported to be rather independent of the chemical composition for Au percentages > 40%, while a slight

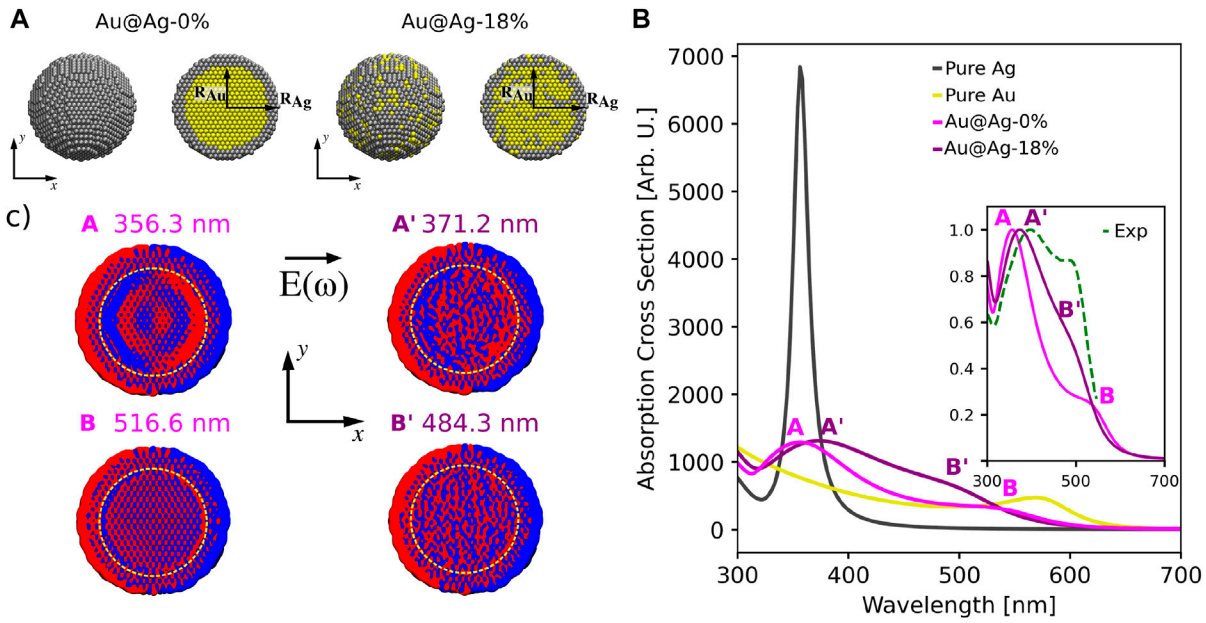

FIGURE 3
(A) Graphical depiction of Au@Ag-0% and Au@Ag-18% core-shell nanospheres (D = 6.25 nm). **(B)** Computed Au@Ag-0% and Au@Ag-18% absorption cross sections (data for pure Ag and Au structures are also reported, D = 6.25 nm). The normalized experimental spectrum reproduced from Peña-Rodríguez and Pal (2011b) is depicted in the inset, together with the normalized ωFQFμ Au@Ag-0% and Au@Ag-18% absorption cross sections. **(C)** Plasmon density computed at A, B (Au@Ag-0%) and A′, B′ (Au@Ag-18%) frequencies (isovalue = 0.0001 a. u.). The yellow dotted circle highlights the interface between the gold core and the silver shell.

blueshift is expected by increasing the Ag concentration Bok et al. (2009). Note that a DDA description is able to reproduce the composition dependence of the longitudinal mode but fails at describing the linear trend of the transversal peak (Bok et al., 2009). This is probably related to the exploited linear combination of Ag and Au permittivity functions. Remarkably, ωFQFμ correctly models both behaviors.

These findings can be explained by considering that the longitudinal dipolar mode falls at energies that are reasonably far from interband transition regions of both Ag and Au. In this regime, Drude free electrons play a dominant role (Link et al., 1999; Bok et al., 2009) and the good agreement with experiments reported by both DDA (Bok et al., 2009) and ωFQFμ show that the permittivity function in this region can be reasonably approximated as a linear combination of Ag and Au Drude contributions. Differently, the transversal plasmon mode absorbs at much higher energies, where interband effects cannot be neglected (Kreibig et al., 1995). This proves the reliability of ωFQFμ, which, differently from other models (Draine and Flatau, 1994), describes the plasmonic resonance by means of both electric charges and dipoles, modeling the intraband and interband mechanisms, respectively.

3.2 Au@Ag core-shell NPs

ωFQFμ is not limited to the description of nanoalloys, but can generally describe bimetallic nanostructures. To showcase its applicability, we consider pure core-shell (Au@Ag-0%) spherical NPs with a diameter D of 6.25 nm (3,698 atoms, see Figure 3A), constituted by a Au core (D_{Au} = 5 nm), and an external Ag shell (external D_{Ag} = 6.25 nm, D_{Au}/D_{Ag} = 0.8). In addition, to show the flexibility of ωFQFμ, the effect of alloying such structures, which has been experimentally realized (Ristig et al., 2015; Blommaerts et al., 2019), is also taken into account, by randomly replacing 18% of the core Au atoms with Ag, and viceversa for the Ag shell (Au@Ag-18%, see Figure 3A).

Computed ωFQFμ absorption cross sections in the visible range for both core-shell systems are reported in Figure 3B, together with reference spectra for Ag and Au spherical NPs with D = 6.25 nm. Similarly to Figure 1B, Ag and Au reference absorption spectra are characterized by a main peak, located at about 360 nm and 570 nm for Ag and Au, respectively. The spectrum of the pure Au@Ag-0% core-shell is instead dominated by two peaks A and B, in agreement with (Peña-Rodríguez and Pal, 2011a; Chen et al., 2012; Gao et al., 2014), which fall at about 356 nm (A) and 517 nm (B). To deeply investigate the nature of the plasmons associated with these two bands, we graphically report in Figure 3C, left panel, the electron densities at the excitation energies for pure Au@Ag-0% core-shell (on a slice in the xy plane). As it can be appreciated, both peaks are associated with a global dipolar plasmon. However, they differ for the electron distribution in both the Au core and the interface between the two regions (see yellow dashed line in Figure 3C). Indeed, for peak A a huge charge accumulation at the interface is reported, while for peak B, the boundary between the Ag shell and the Au core is only partially marked. This is due to the fact that our model allows for charge exchange between the two layers, which is for instance not accounted for by other classical descriptions (Szántó et al., 2021). However, such a charge transfer is limited by the different tunneling barriers between the two metals, as introduced in Eq. 6, and by the different chemical nature

(chemical hardness, polarizability, Drude parameters, ...). As a consequence, charge accumulation at the Ag-Au interface is expected.

Similarly, the Au@Ag-18% absorption cross section (see Figure 3B) is characterized by two main peaks A′ and B′, which are blue- and red-shifted as compared to their counterparts in Au@Ag-0% system. Such a behavior can be justified by considering that by increasing the alloying degree up to 50%, a fully alloyed Ag-Au spherical NP is obtained. Therefore, in this situation, a single band is expected at about 450 nm (see also Figure 1B). The plasmonic nature of the electron densities computed at the A′ and B′ frequencies is graphically reported in Figure 3C, right panel. A global dipolar plasmon is observed. However, by also comparing with Au@Ag-0%, charge accumulation at the core-shell boundary is still present, but less pronounced, in particular for B′. This confirms the above speculation: indeed, by increasing the alloying degree, a decrease in the potential barrier at the interface is obtained.

To conclude the discussion on Au@Ag core-shell systems, we compare our results with experimental absorption cross sections reported by Peña-Rodríguez and Pal (2011b) (see inset in Figure 3B), who studied the plasmonic response of Au@Ag core-shell spherical NPs with D = 44.2 nm and characterized by D_{Au}/D_{Ag} = 0.81 (comparable with our simulations). As it can be noticed, the experimental spectrum is characterized by two main peaks at about 400 nm and 497 nm. This is in very good agreement with our calculations, thus further demonstrating the reliability of our model. In fact, only a slight discrepancy in relative intensities, probably due to different experimental conditions (size of the NP, solvent, ...), is observed.

4 Conclusion

ωFQFμ has been extended to the description of bimetallic metal nanoalloys and core-shell NPs, and has been applied to spherical alloyed NPs and nanorods, for which alternative methods proposed in the literature fail, due to incorrect modeling of interband contributions. Remarkably, ωFQFμ correctly reproduces experimental trends, also in the case of core-shell systems; this is a direct consequence of the atomistic nature of the approach, which permits a physically consistent picture of the local environment of each specific atom.

ωFQFμ is general enough to describe any kind of bimetallic system; for instance, it can be applied to complex geometrical arrangements, such as subnanometer junctions, which form when two NPs approach each other. Such complex nanostructures require appropriate treatment of interband transitions and reliable modeling of quantum tunneling effects. The effect of alloying in subnanometer junctions has been only marginally investigated, due to the lack of theoretical approaches to correctly describe the plasmonic properties of alloys and generic bimetallic systems. ωFQFμ can indeed be applied to these systems and this investigation will be the topic of future studies. Also, ωFQFμ can be extended to generic multi-metallic nanostructures, through the generalization of Eq. 19 followed by a specification of the quantities entering Eq. 6.

As a final technological perspective, relevant for instance in sensing applications, the approach can be potentially applied to compute spectral properties of molecules adsorbed on bimetallic systems, by generalizing previous studies on homogenous substrates (Payton et al., 2013; Lafiosca et al., 2023). In this way, Surface-Enhanced spectroscopic signals can be simulated by retaining an atomistic description of the plasmonic substrate, which plays a crucial role in bimetallic systems, as it is demonstrated in this work.

Data availability statement

The raw data supporting the conclusion of this article will be made available by the authors, without undue reservation.

Author contributions

LN, PL, and TG developed the theoretical methodology. LN, PL, and PG ran ωFQFμ calculations. TG, LN, and PL implemented the method into the stand-alone Fortran95 code for ωFQFμ calculations. LN, PL, PG, LB, and TG analyzed data and wrote the original draft manuscript. TG and CC discussed and supervised the whole project. CC acquired the funding and finalized the manuscript (final version). All authors contributed to the article and approved the submitted version.

Funding

This work has received funding from the European Research Council (ERC) under the European Union's Horizon 2020 research and innovation program (grant agreement N. 818064). CC acknowledges funding from PNRR MUR project PE0000023-NQSTI.

Acknowledgments

We gratefully acknowledge the Center for High-Performance Computing (CHPC) at SNS for providing the computational infrastructure.

Conflict of interest

The authors declare that the research was conducted in the absence of any commercial or financial relationships that could be construed as a potential conflict of interest.

Publisher's note

Supplementary material

The Supplementary Material for this article can be found online at: https://www.frontiersin.org/articles/10.3389/fphot.2023.1199598/full#supplementary-material

References

Aizpurua, J., Hanarp, P., Sutherland, D., Käll, M., Bryant, G. W., and García de Abajo, F. J. (2003). Optical properties of gold nanorings. *Phys. Rev. Lett.* 90, 057401. doi:10.1103/physrevlett.90.057401

Anker, J. N., Hall, W. P., Lyandres, O., Shah, N. C., Zhao, J., and Van Duyne, R. P. (2008). Biosensing with plasmonic nanosensors. *Nat. Mater.* 7, 442–453. doi:10.1038/nmat2162

Asadi-Aghbolaghi, N., Ruger, R., Jamshidi, Z., and Visscher, L. (2020). Td-dft+ tb: An efficient and fast approach for quantum plasmonic excitations. *J. Phys. Chem. C* 124, 7946–7955. doi:10.1021/acs.jpcc.0c00979

Atwater, H. A., and Polman, A. (2010). Plasmonics for improved photovoltaic devices. *Nat. Mater.* 9, 205–213. doi:10.1038/nmat2629

Awada, C., Dab, C., Grimaldi, M. G., Alshoaibi, A., and Ruffino, F. (2021). High optical enhancement in au/ag alloys and porous au using surface-enhanced Raman spectroscopy technique. *Sci. Rep.* 11, 4714. doi:10.1038/s41598-021-84093-0

Bade, W. (1957). Drude-model calculation of dispersion forces. i. general theory. *J. Chem. Phys.* 27, 1280–1284. doi:10.1063/1.1743991

Baghramyan, H. M., Della Sala, F., and Ciracì, C. (2021). Laplacian-level quantum hydrodynamic theory for plasmonics. *Phys. Rev. X* 11, 011049. doi:10.1103/physrevx.11.011049

Barcaro, G., Broyer, M., Durante, N., Fortunelli, A., and Stener, M. (2011). Alloying effects on the optical properties of ag–au nanoclusters from tddft calculations. *J. Phys. Chem. C* 115, 24085–24091. doi:10.1021/jp2087219

Barcaro, G., Sementa, L., Fortunelli, A., and Stener, M. (2014). Optical properties of pt and ag–pt nanoclusters from tddft calculations: Plasmon suppression by pt poisoning. *J. Phys. Chem. C* 118, 28101–28108. doi:10.1021/jp508824w

Barcaro, G., Sementa, L., Fortunelli, A., and Stener, M. (2015). Optical properties of nanoalloys. *Phys. Chem. Chem. Phys.* 17, 27952–27967. doi:10.1039/c5cp00498e

Blommaerts, N., Vanrompay, H., Nuti, S., Lenaerts, S., Bals, S., and Verbruggen, S. W. (2019). Unraveling structural information of turkevich synthesized plasmonic gold–silver bimetallic nanoparticles. *Small* 15, 1902791. doi:10.1002/smll.201902791

Bok, H.-M., Shuford, K. L., Kim, S., Kim, S. K., and Park, S. (2009). Multiple surface plasmon modes for gold/silver alloy nanorods. *Langmuir* 25, 5266–5270. doi:10.1021/la803900w

Bonatti, L., Gil, G., Giovannini, T., Corni, S., and Cappelli, C. (2020). Plasmonic resonances of metal nanoparticles: Atomistic vs. continuum approaches. *Front. Chem.* 8, 340. doi:10.3389/fchem.2020.00340

Bonatti, L., Nicoli, L., Giovannini, T., and Cappelli, C. (2022). *In silico* design of graphene plasmonic hot-spots. *Nanoscale Adv.* 4, 2294–2302. doi:10.1039/d2na00088a

Cao, M., Liu, Q., Chen, M., Chen, L., Yang, D., Hu, H., et al. (2018). Fully alloying auag nanorods in a photothermal nano-oven: Superior plasmonic property and enhanced chemical stability. *ACS Omega* 3, 18623–18629. doi:10.1021/acsomega.8b03020

Chen, Y., Wu, H., Li, Z., Wang, P., Yang, L., and Fang, Y. (2012). The study of surface plasmon in au/ag core/shell compound nanoparticles. *Plasmonics* 7, 509–513. doi:10.1007/s11468-012-9336-6

Chen, X., Moore, J. E., Zekarias, M., and Jensen, L. (2015). Atomistic electrodynamics simulations of bare and ligand-coated nanoparticles in the quantum size regime. *Nat. Commun.* 6, 8921. doi:10.1038/ncomms9921

Ciraci, C., and Della Sala, F. (2016). Quantum hydrodynamic theory for plasmonics: Impact of the electron density tail. *Phys. Rev. B* 93, 205405. doi:10.1103/physrevb.93.205405

Ciracì, C., Hill, R., Mock, J., Urzhumov, Y., Fernández-Domínguez, A., Maier, S., et al. (2012). Probing the ultimate limits of plasmonic enhancement. *Science* 337, 1072–1074. doi:10.1126/science.1224823

Ciraci, C., Pendry, J. B., and Smith, D. R. (2013). Hydrodynamic model for plasmonics: A macroscopic approach to a microscopic problem. *ChemPhysChem* 14, 1109–1116. doi:10.1002/cphc.201200992

Coccia, E., Fregoni, J., Guido, C., Marsili, M., Pipolo, S., and Corni, S. (2020). Hybrid theoretical models for molecular nanoplasmonics. *J. Chem. Phys.* 153, 200901. doi:10.1063/5.0027935

Corni, S., and Tomasi, J. (2001). Enhanced response properties of a chromophore physisorbed on a metal particle. *J. Chem. Phys.* 114, 3739–3751. doi:10.1063/1.1342241

Corni, S., and Tomasi, J. (2002a). Excitation energies of a molecule close to a metal surface. *J. Chem. Phys.* 117, 7266–7278. doi:10.1063/1.1507579

Corni, S., and Tomasi, J. (2002b). Surface enhanced Raman scattering from a single molecule adsorbed on a metal particle aggregate: A theoretical study. *J. Chem. Phys.* 116, 1156–1164. doi:10.1063/1.1428349

Danielis, N., Vega, L., Fronzoni, G., Stener, M., Bruix, A., and Neyman, K. M. (2021). Agpd, aupd, and aupt nanoalloys with ag-or au-rich compositions: Modeling chemical ordering and optical properties. *J. Phys. Chem. C* 125, 17372–17384. doi:10.1021/acs.jpcc.1c04222

Della Sala, F., Pachter, R., and Sukharev, M. (2022). Advances in modeling plasmonic systems. *J. Chem. Phys.* 157, 190401. doi:10.1063/5.0130790

Della Sala, F. (2022). Orbital-free methods for plasmonics: Linear response. *J. Chem. Phys.* 157, 104101. doi:10.1063/5.0100797

Draine, B. T., and Flatau, P. J. (1994). Discrete-dipole approximation for scattering calculations. *J. Opt. Soc. Am. A* 11, 1491–1499. doi:10.1364/josaa.11.001491

Esteban, R., Borisov, A. G., Nordlander, P., and Aizpurua, J. (2012). Bridging quantum and classical plasmonics with a quantum-corrected model. *Nat. Commun.* 3, 825. doi:10.1038/ncomms1806

Esteban, R., Zugarramurdi, A., Zhang, P., Nordlander, P., García-Vidal, F. J., Borisov, A. G., et al. (2015). A classical treatment of optical tunneling in plasmonic gaps: Extending the quantum corrected model to practical situations. *Faraday Discuss.* 178, 151–183. doi:10.1039/c4fd00196f

Etchegoin, P. G., Le Ru, E., and Meyer, M. (2006). An analytic model for the optical properties of gold. *J. Chem. Phys.* 125, 164705. doi:10.1063/1.2360270

Gao, C., Hu, Y., Wang, M., Chi, M., and Yin, Y. (2014). Fully alloyed ag/au nanospheres: Combining the plasmonic property of ag with the stability of au. *J. Am. Chem. Soc.* 136, 7474–7479. doi:10.1021/ja502890c

García de Abajo, F. J., and Howie, A. (2002). Retarded field calculation of electron energy loss in inhomogeneous dielectrics. *Phys. Rev. B* 65, 115418. doi:10.1103/physrevb.65.115418

Giannini, V., Fernández-Domínguez, A. I., Heck, S. C., and Maier, S. A. (2011). Plasmonic nanoantennas: Fundamentals and their use in controlling the radiative properties of nanoemitters. *Chem. Rev.* 111, 3888–3912. doi:10.1021/cr1002672

Giannone, G., Smiga, S., D'Agostino, S., Fabiano, E., and Della Sala, F. (2021). Plasmon couplings from subsystem time-dependent density functional theory. *J. Phys. Chem. A* 125, 7246–7259. doi:10.1021/acs.jpca.1c05384

Giovannini, T., Puglisi, A., Ambrosetti, M., and Cappelli, C. (2019a). Polarizable qm/mm approach with fluctuating charges and fluctuating dipoles: The qm/fq$f\mu$ model. *J. Chem. Theory Comput.* 15, 2233–2245. doi:10.1021/acs.jctc.8b01149

Giovannini, T., Rosa, M., Corni, S., and Cappelli, C. (2019b). A classical picture of subnanometer junctions: An atomistic drude approach to nanoplasmonics. *Nanoscale* 11, 6004–6015. doi:10.1039/c8nr09134j

Giovannini, T., Bonatti, L., Polini, M., and Cappelli, C. (2020). Graphene plasmonics: Fully atomistic approach for realistic structures. *J. Phys. Chem. Lett.* 11, 7595–7602. doi:10.1021/acs.jpclett.0c02051

Giovannini, T., Bonatti, L., Lafiosca, P., Nicoli, L., Castagnola, M., Illobre, P. G., et al. (2022). Do we really need quantum mechanics to describe plasmonic properties of metal nanostructures? *ACS Photonics* 9, 3025–3034. doi:10.1021/acsphotonics.2c00761

Gong, C., and Leite, M. S. (2016). Noble metal alloys for plasmonics. *ACS Photonics* 3, 507–513. doi:10.1021/acsphotonics.5b00586

Halas, N. J., Lal, S., Chang, W.-S., Link, S., and Nordlander, P. (2011). Plasmons in strongly coupled metallic nanostructures. *Chem. Rev.* 111, 3913–3961. doi:10.1021/cr200061k

Hao, F., Nehl, C. L., Hafner, J. H., and Nordlander, P. (2007). Plasmon resonances of a gold nanostar. *Nano Lett.* 7, 729–732. doi:10.1021/nl062969c

Haynes, W. (2014). *CRC handbook of chemistry and physics*. Boca Raton: CRC Press.

Hohenester, U., and Trügler, A. (2012). MNPBEM – a Matlab toolbox for the simulation of plasmonic nanoparticles. *Comput. Phys. Commun.* 183, 370–381. doi:10.1016/j.cpc.2011.09.009

Hohenester, U. (2015). Quantum corrected model for plasmonic nanoparticles: A boundary element method implementation. *Phys. Rev. B* 91, 205436. doi:10.1103/physrevb.91.205436

Huang, J., Zhu, Y., Liu, C., Zhao, Y., Liu, Z., Hedhili, M. N., et al. (2015). Fabricating a homogeneously alloyed auag shell on au nanorods to achieve strong, stable, and tunable surface plasmon resonances. *Small* 11, 5214–5221. doi:10.1002/smll.201501220

Jensen, L. L., and Jensen, L. (2008). Electrostatic interaction model for the calculation of the polarizability of large noble metal nanoclusters. *J. Phys. Chem. C* 112, 15697–15703. doi:10.1021/jp804116z

Jensen, L. L., and Jensen, L. (2009). Atomistic electrodynamics model for optical properties of silver nanoclusters. *J. Phys. Chem. C* 113, 15182–15190. doi:10.1021/jp904956f

Kneipp, K., Wang, Y., Kneipp, H., Perelman, L. T., Itzkan, I., Dasari, R. R., et al. (1997). Single molecule detection using surface-enhanced Raman scattering (sers). *Phys. Rev. Lett.* 78, 1667–1670. doi:10.1103/physrevlett.78.1667

Kreibig, U., Vollmer, M., Kreibig, U., and Vollmer, M. (1995). "Theoretical considerations," in *Optical properties of metal clusters*, 13–201.

Kuddah, M., Putra, M., and Djuhana, D. (2020). "The incident electrical field angle effect in localized surface plasmon resonance (lspr) of bimetallic ag-au nanorod using mnpbem simulation," in IOP Conference Series: Materials Science and Engineering (IOP Publishing), 012058.

Lafiosca, P., Giovannini, T., Benzi, M., and Cappelli, C. (2021). Going beyond the limits of classical atomistic modeling of plasmonic nanostructures. *J. Phys. Chem. C* 125, 23848–23863. doi:10.1021/acs.jpcc.1c04716

Lafiosca, P., Nicoli, L., Bonatti, L., Giovannini, T., Corni, S., and Cappelli, C. (2023). Qm/classical modeling of surface enhanced Raman scattering based on atomistic electromagnetic models. *J. Chem. Theory Comput.* doi:10.1021/acs.jctc.3c00177

Larsen, A. H., Mortensen, J. J., Blomqvist, J., Castelli, I. E., Christensen, R., Dułak, M., et al. (2017). The atomic simulation environment—A python library for working with atoms. *J. Phys. Condens. Matter* 29, 273002. doi:10.1088/1361-648x/aa680e

Liebsch, A. (1993). Surface-plasmon dispersion and size dependence of mie resonance: Silver versus simple metals. *Phys. Rev. B* 48, 11317–11328. doi:10.1103/physrevb.48.11317

Lim, D.-K., Jeon, K.-S., Kim, H. M., Nam, J.-M., and Suh, Y. D. (2010). Nanogap-engineerable Raman-active nanodumbbells for single-molecule detection. *Nat. Mater.* 9, 60–67. doi:10.1038/nmat2596

Link, S., Wang, Z. L., and El-Sayed, M. (1999). Alloy formation of gold-silver nanoparticles and the dependence of the plasmon absorption on their composition. *J. Phys. Chem. B* 103, 3529–3533. doi:10.1021/jp990387w

López Lozano, X., Mottet, C., and Weissker, H.-C. (2013). Effect of alloying on the optical properties of ag–au nanoparticles. *J. Phys. Chem. C* 117, 3062–3068. doi:10.1021/jp309957y

Ma, Y.-W., Zhang, L.-H., Wu, Z.-W., Yi, M.-F., Zhang, J., and Jian, G.-S. (2015). The study of tunable local surface plasmon resonances on au-ag and ag-au core-shell alloy nanostructure particles with dda method. *Plasmonics* 10, 1791–1800. doi:10.1007/s11468-015-9997-z

Ma, J., Liu, X., Wang, R., Zhang, J., Jiang, P., Wang, Y., et al. (2020). Bimetallic core–shell nanostars with tunable surface plasmon resonance for surface-enhanced Raman scattering. *ACS Appl. Nano Mater.* 3, 10885–10894. doi:10.1021/acsanm.0c02144

Maier, S. A., Kik, P. G., Atwater, H. A., Meltzer, S., Harel, E., Koel, B. E., et al. (2003). Local detection of electromagnetic energy transport below the diffraction limit in metal nanoparticle plasmon waveguides. *Nat. Mater.* 2, 229–232. doi:10.1038/nmat852

Maier, S. A. (2007). *Plasmonics: Fundamentals and applications*. Springer Science & Business Media.

Mie, G. (1908). Beiträge zur optik trüber medien, speziell kolloidaler metallösungen. *Ann. Phys.-Berlin* 330, 377–445. doi:10.1002/andp.19083300302

Moskovits, M. (1985). Surface-enhanced spectroscopy. *Rev. Mod. Phys.* 57, 783–826. doi:10.1103/revmodphys.57.783

Muehlschlegel, P., Eisler, H.-J., Martin, O. J., Hecht, B., and Pohl, D. (2005). Resonant optical antennas. *Science* 308, 1607–1609. doi:10.1126/science.1111886

Myroshnychenko, V., Rodríguez-Fernández, J., Pastoriza-Santos, I., Funston, A. M., Novo, C., Mulvaney, P., et al. (2008). Modelling the optical response of gold nanoparticles. *Chem. Soc. Rev.* 37, 1792–1805. doi:10.1039/b711486a

Neuman, T., Esteban, R., Casanova, D., García-Vidal, F. J., and Aizpurua, J. (2018). Coupling of molecular emitters and plasmonic cavities beyond the point-dipole approximation. *Nano Lett.* 18, 2358–2364. doi:10.1021/acs.nanolett.7b05297

Newmai, M. B., Verma, M., Dahiya, A., and Kumar, P. S. (2022). Monomer driven growth of catalytically active agau plasmonic nanoalloys. *J. Phys. Chem. Solids*161, 110371. doi:10.1016/j.jpcs.2021.110371

Nie, S., and Emory, S. R. (1997). Probing single molecules and single nanoparticles by surface-enhanced Raman scattering. *Science* 275, 1102–1106. doi:10.1126/science.275.5303.1102

Olobardi, S., Vega, L., Fortunelli, A., Stener, M., Vines, F., and Neyman, K. M. (2019). Optical properties and chemical ordering of ag–pt nanoalloys: A computational study. *J. Phys. Chem. C* 123, 25482–25491. doi:10.1021/acs.jpcc.9b07382

Papavassiliou, G. C. (1976). Surface plasmons in small au-ag alloy particles. *J. Phys. F. Met. Phys.* 6, L103–L105. doi:10.1088/0305-4608/6/4/004

Payton, J. L., Morton, S. M., Moore, J. E., and Jensen, L. (2013). A hybrid atomistic electrodynamics–quantum mechanical approach for simulating surface-enhanced Raman scattering. *Acc. Chem. Res.* 47, 88–99. doi:10.1021/ar400075r

Peña-Rodríguez, O., and Pal, U. (2011a). Au@ ag core–shell nanoparticles: Efficient all-plasmonic fano-resonance generators. *Nanoscale* 3, 3609–3612. doi:10.1039/c1nr10625b

Peña-Rodríguez, O., and Pal, U. (2011b). Enhanced plasmonic behavior of bimetallic (ag-au) multilayered spheres. *Nanoscale Res. Lett.* 6, 279. doi:10.1186/1556-276X-6-279

Pérez-González, O., Zabala, N., Borisov, A., Halas, N., Nordlander, P., and Aizpurua, J. (2010). Optical spectroscopy of conductive junctions in plasmonic cavities. *Nano Lett.* 10, 3090–3095. doi:10.1021/nl1017173

Putra, M., Djuhana, D., Fauzia, V., Harmoko, A., and Imawan, C. (2017). "A numerical study of the sensitivity of surface plasmon resonance bimetallic silver-gold alloys using boundary element method," in IOP Conference Series: Materials Science and Engineering (IOP Publishing), 012016.

Raza, S., Bozhevolnyi, S. I., Wubs, M., and Mortensen, N. A. (2015). Nonlocal optical response in metallic nanostructures. *J. Phys. Condens. Matter* 27, 183204. doi:10.1088/0953-8984/27/18/183204

Rioux, D., Vallières, S., Besner, S., Muñoz, P., Mazur, E., and Meunier, M. (2014). An analytic model for the dielectric function of au, ag, and their alloys. *Adv. Opt. Mater.* 2, 176–182. doi:10.1002/adom.201300457

Ristig, S., Prymak, O., Loza, K., Gocyla, M., Meyer-Zaika, W., Heggen, M., et al. (2015). Nanostructure of wet-chemically prepared, polymer-stabilized silver–gold nanoalloys (6 nm) over the entire composition range. *J. Mater. Chem. B* 3, 4654–4662. doi:10.1039/c5tb00644a

Santhosh, K., Bitton, O., Chuntonov, L., and Haran, G. (2016). Vacuum rabi splitting in a plasmonic cavity at the single quantum emitter limit. *Nat. Commun.* 7, 11823. doi:10.1038/ncomms11823

Scholl, J. A., García-Etxarri, A., Koh, A. L., and Dionne, J. A. (2013). Observation of quantum tunneling between two plasmonic nanoparticles. *Nano Lett.* 13, 564–569. doi:10.1021/nl304078v

Shuford, K. L., Ratner, M. A., Gray, S. K., and Schatz, G. C. (2006). Finite-difference time-domain studies of light transmission through nanohole structures. *Appl. Phys. B* 84, 11–18. doi:10.1007/s00340-006-2218-x

Sørensen, L. K., Utyushev, A. D., Zakomirnyi, V. I., and Ågren, H. (2021). Atomistic description of plasmonic generation in alloys and core shell nanoparticles. *Phys. Chem. Chem. Phys.* 23, 173–185. doi:10.1039/d0cp04854b

Szántó, G., Csarnovics, I., and Bonyár, A. (2021). Numerical investigation of the refractive index sensitivity of au/ag core-shell nanostructures for sensing applications. *Sens. Bio-Sens.* 32, 100414. doi:10.1016/j.sbsr.2021.100414

Verbruggen, S. W., Keulemans, M., Martens, J. A., and Lenaerts, S. (2013). Predicting the surface plasmon resonance wavelength of gold–silver alloy nanoparticles. *J. Phys. Chem. C* 117, 19142–19145. doi:10.1021/jp4070856

Wang, C., Peng, S., Chan, R., and Sun, S. (2009). Synthesis of auag alloy nanoparticles from core/shell-structured ag/au. *Small* 5, 567–570. doi:10.1002/smll.200801169

Xiang, Y., Wu, X., Liu, D., Li, Z., Chu, W., Feng, L., et al. (2008). Gold nanorod-seeded growth of silver nanostructures: From homogeneous coating to anisotropic coating. *Langmuir* 24, 3465–3470. doi:10.1021/la702999c

Zakomirnyi, V. I., Rinkevicius, Z., Baryshnikov, G. V., Sørensen, L. K., and Ågren, H. (2019). Extended discrete interaction model: Plasmonic excitations of silver nanoparticles. *J. Phys. Chem. C* 123, 28867–28880. doi:10.1021/acs.jpcc.9b07410

Zakomirnyi, V. I., Rasskazov, I. L., Sørensen, L. K., Carney, P. S., Rinkevicius, Z., and Ågren, H. (2020). Plasmonic nano-shells: Atomistic discrete interaction versus classic electrodynamics models. *Phys. Chem. Chem. Phys.* 22, 13467–13473. doi:10.1039/d0cp02248a

III. Real-Time Formulation of Atomistic Electromagnetic Models for Plasmonics

THE JOURNAL OF PHYSICAL CHEMISTRY C
A JOURNAL OF THE AMERICAN CHEMICAL SOCIETY

pubs.acs.org/JPCC

Article

Real-Time Formulation of Atomistic Electromagnetic Models for Plasmonics

Piero Lafiosca, Luca Nicoli, Silvio Pipolo, Stefano Corni, Tommaso Giovannini,* and Chiara Cappelli*

Cite This: https://doi.org/10.1021/acs.jpcc.4c04002

Read Online

ACCESS | Metrics & More | Article Recommendations | Supporting Information

ABSTRACT: Investigating nanoplasmonics using time-dependent approaches permits shedding light on the dynamic optical properties of plasmonic structures, which are intrinsically connected with their potential applications in photochemistry and photoreactivity. This work proposes a real-time (RT) extension of our recently developed fully atomistic approaches ωFQ and ωFQFμ. These methods successfully reproduce quantum size effects in metal nanoparticles, including plasmon shifts for both simple and *d*-metals, even below the quantum size limit. Also, thanks to their atomistic nature and the phenomenological inclusion of quantum tunneling effects, they can effectively describe the optical response of subnanometer junctions. By incorporating real-time dynamics, the approach provides an efficient framework for studying the time-dependent optical behavior of metal nanostructures, including the decoherence of plasmon excitations.

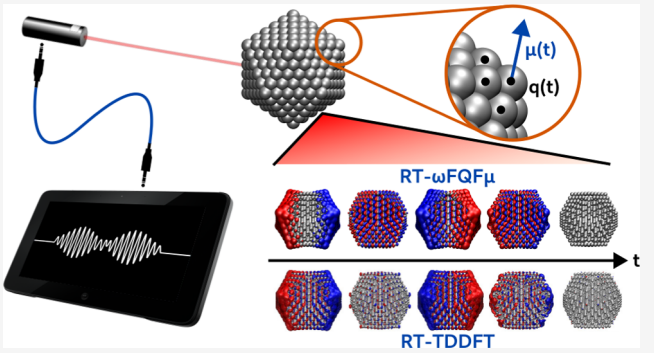

1. INTRODUCTION

Under the action of external radiation, the conductive electrons of plasmonic nanomaterials, such as noble metal nanoparticles, can be excited, giving rise to the so-called localized surface plasmons (LSP).[1−3] Such plasmons are excited at the plasmon resonance frequency (PRF), which generally shows a high tunability as a function of the size, shape, and chemical composition of the nanostructure.[4−7] Such a property, together with the capability of plasmonic materials to absorb a huge amount of energy and the huge enhancement of the electric near field, makes plasmonic materials based on noble metals a unique platform for a plethora of technological applications, ranging from sensing[7−14] to photocatalysis.[15−24]

In this context, an in-depth understanding of the dynamics of the optical response of plasmonic structures is vital for elucidating the mechanisms underlying the photophysics and photochemistry of such systems.[25−27] From the experimental point of view, this can be achieved by resorting to time-resolved spectroscopies.[28,29] To rationalize the experimental findings, theoretical approaches able to describe the time evolution of the optical response need to be exploited.[30−33] The most common theoretical methods generally rely on solving classical Maxwell's Equations or purely quantum mechanical (QM) methods. Classical approaches, such as the Boundary Element Method (BEM)[34−36] or the Finite-Difference Time-Domain (FDTD) method,[37,38] are powerful tools for modeling nanoscale optical systems, however, they typically overlook tunneling effects and the atomistic details that are essential for an accurate description of structures defined at the subnanometer levels,[39−48] such as nanojunctions or picocavities.[20] On the other hand, QM-based approaches, headed by Real-Time Time-Dependent Density Functional Theory (RT-TDDFT), TDDFT[30,49−56] and Real-Time Time-Dependent Density Functional Tight-Binding (RT-TDDFTB),[57−59] provide a first-principle description of the nanostructure response by retaining the atomistic nature of the system. However, they are computationally prohibitive for large nanosystems and are generally exploited to describe systems composed at most of a few thousand atoms.

To overcome the drawbacks of classical and QM-based approaches, we have recently developed two methods, namely frequency-dependent fluctuating charges (ωFQ)[60−65] and frequency-dependent fluctuating charges and fluctuating dipoles (ωFQFμ).[66,67] Such methods describe the nanostructure at the full atomistic level and model its optical response by integrating the Drude conduction theory, classical electrodynamics, quantum mechanical tunneling, and interband effects. In particular, in ωFQ, each atom of the nanosystem is endowed with a charge that dynamically responds to the external field as regulated by the Drude conduction model.[60,68] In this way, intraband effects are incorporated into the model.

Received: June 16, 2024
Revised: September 6, 2024
Accepted: September 23, 2024

To describe *d*-metal nanostructures, we have extended ωFQ by introducing ωFQFμ, where each atom is additionally endowed with a complex polarizability, modeling *d* shell polarizability and interband effects.[66] In both approaches, we also introduce a phenomenological description of quantum tunneling effects regulating the charge exchange between neighbor atoms.[44,45] Both ωFQ and ωFQFμ can reproduce reference *ab initio* and experimental data, including plasmon shifts for both simple and noble metals, and atomistically defined nanojunctions, even below the quantum size limit.[60,66] In other words, they feature accuracy comparable to QM-based approaches, at a much lower computational cost.

In this work, we extend the ωFQ and ωFQFμ models to the real-time (RT) regime, enabling the simulation of the time evolution of plasmonic excitations as driven by light pulses of arbitrary profiles. The resulting RT-ωFQ and RT-ωFQFμ approaches permit the study of the dynamics of the optical response of metal nanostructures, including the decoherence of plasmon excitations. The approaches can describe the response dynamics under short impulses (in the as/fs time scale) and continuous waves (CW) using the same theoretical framework. This is particularly relevant since CW irradiation is often exploited in plasmonic catalysis.[15,25] We validate the novel approaches by comparing our results with reference *ab initio* TDDFT data for sodium and silver nanostructures. Our method thus offers a comprehensive and efficient tool for studying the dynamics of optical response of metal nanostructures, bridging the gap between classical and QM descriptions, and paving the way for advanced applications in nanophotonics.

The manuscript is organized as follows. In the next section, we report the theoretical derivation of RT-ωFQ and RT-ωFQFμ. The methods are then applied to simulate the time evolution of the optical response of a sodium dimer, displaying a single-atom junction, and a silver icosahedral nanoparticle. The summary and conclusions end the manuscript.

2. METHODS

In this section, we first briefly recall the theoretical foundations of the fully atomistic ωFQ and ωFQFμ approaches for nanoplasmonics. We then present and discuss their extension to the time domain.

2.1. ωFQ and ωFQFμ Models. ωFQ is a fully atomistic, classical model that endows each atom of the nanostructure with a frequency-dependent charge.[60] When an external electric oscillating field is applied to the system, the charge exchange between the atoms is governed by the Drude conduction model. Such an interaction exponentially vanishes by phenomenologically incorporating quantum tunneling mechanisms limiting the charge transfer among the nearest neighboring atoms.[60] By considering a monochromatic field oscillating at frequency ω, ωFQ charges $q_i(\omega)$ are computed by solving the following equation[60]

$$-\mathrm{i}\omega q_i(\omega) = \frac{2n_0\tau}{1-\mathrm{i}\omega\tau}\sum_j^N [1-f(l_{ij})]\frac{\mathcal{A}_{ij}}{l_{ij}}(\phi_j^{el}-\phi_i^{el}) = \frac{2n_0\tau}{1-\mathrm{i}\omega\tau}\sum_j^N K_{ij}(\phi_j^{el}-\phi_i^{el}) \quad (1)$$

where N is the number of atoms, τ is the friction time, n_0 is the numerical density of the material, $\mathcal{A}_{ij}$ is the effective area connecting *i*-th and *j*-th atoms, and l_{ij} is their distance. ϕ_i^{el} is the electrochemical potential on each atom regulating the dynamical polarization of the system. This takes into account the interactions between the atoms and their interaction with the external electric field. Finally, $f(l_{ij})$ is a Fermi-like function mimicking quantum tunneling[60]

$$f(l_{ij}) = \frac{1}{1+\exp\left[-d\left((l_{ij}/s\cdot l_{ij}^0)-1\right)\right]} \quad (2)$$

where l_{ij}^0 is the atom−atom equilibrium distance, whereas d and s determine the sharpness and the center of the damping function, respectively. The parameters entering eq 1 have a microscopic physical meaning and can be extracted from the experimental permittivity or determined by comparing computed results with reference *ab initio* calculations.[60,62]

Equation 1 can be recast in a compact way as the following linear system[69]

$$[\mathbf{A}^{qq} - z_q(\omega)\mathbf{I}_N]\mathbf{q}(\omega) = -\mathbf{f}^q(\omega) \quad (3)$$

where $\mathbf{I}_N$ is the $N \times N$ identity matrix, while $\mathbf{A}^{qq}$, $z_q(\omega)$ and $\mathbf{f}_q(\omega)$ read[69]

$$\mathbf{A}^{qq} = (\mathbf{K}-\mathbf{P})\mathbf{T}^{qq}$$
$$z_q(\omega) = \frac{1}{2n_0}\left(-\omega^2 - \mathrm{i}\omega\frac{1}{\tau}\right)$$
$$\mathbf{f}^q(\omega) = (\mathbf{K}-\mathbf{P})\mathbf{V}^{\mathrm{ext}}(\omega) \quad (4)$$

where $\mathbf{T}^{qq}$ is the charge−charge interaction kernel[60,70] and $\mathbf{V}^{\mathrm{ext}}(\omega)$ is the potential associated with the external field evaluated at the position of each atom. The matrix $\mathbf{P}$ takes the following form[69]

$$P_{ij} = \sum_k K_{ik}\delta_{ij} \quad (5)$$

ωFQ is a fully atomistic approach that models the optical response of nanostructure materials by accounting for intraband mechanisms only, via the Drude conduction model. Therefore, the approach cannot describe metals featuring interband transitions, such as noble metal nanostructures.[71−75] To model these systems, we have recently developed ωFQFμ,[66] which extends ωFQ by assigning to each atom of the nanosystem an additional source of polarization, i.e., an atomic polarizability and an associated induced dipole $\boldsymbol{\mu}_i$. The electric potential produced by the dipoles is included in eq 1 as an external potential acting on the charges in the electrochemical potential ϕ^{el}. The dipoles $\boldsymbol{\mu}_i$ are calculated by solving the following set of linear equations[66]

$$\boldsymbol{\mu}_i = \alpha^{\mathrm{IB}}(\omega)(\mathbf{E}_i^q + \mathbf{E}_i^\mu + \mathbf{E}_i^{\mathrm{ext}}) \quad (6)$$

where $\mathbf{E}^q$ and $\mathbf{E}^\mu$ are the electric fields generated by the charge and the other dipole moments, respectively, while $\mathbf{E}^{\mathrm{ext}}$ is the external electric field. $\alpha^{\mathrm{IB}}(\omega)$ is the atomic complex polarizability describing interband transitions, which can be easily obtained by extracting interband contributions from the experimental permittivity function.[66]

The equations defining charges and dipoles responses can be coupled together resulting in the following linear system[66]

$$\left[\begin{pmatrix}\mathbf{A}^{qq} & \mathbf{A}^{q\mu}\\ \mathbf{T}^{\mu q} & \mathbf{T}^{\mu\mu}\end{pmatrix} - \begin{pmatrix}z_q(\omega)\mathbf{I}_N & \mathbf{0}\\ \mathbf{0} & z_\mu(\omega)\mathbf{I}_{3N}\end{pmatrix}\right]\begin{pmatrix}\mathbf{q}(\omega)\\ \boldsymbol{\mu}(\omega)\end{pmatrix} = \begin{pmatrix}-\mathbf{f}^q(\omega)\\ \mathbf{f}^\mu(\omega)\end{pmatrix} \quad (7)$$

https://doi.org/10.1021/acs.jpcc.4c04002
J. Phys. Chem. C XXXX, XXX, XXX−XXX

where $\mathbf{T}^{\mu q}$ and $\mathbf{T}^{\mu\mu}$ are the dipole-charge and dipole−dipole interaction kernels,[66,70,76] while $\mathbf{A}^{q\mu}$, $z_\mu(\omega)$ and $\mathbf{f}^\mu(\omega)$ are defined as[66]

$$\begin{aligned}\mathbf{A}^{q\mu} &= (\mathbf{K} - \mathbf{P})\mathbf{T}^{q\mu}\\ z_\mu(\omega) &= -\frac{1}{\alpha^{\mathrm{IB}}(\omega)}\\ \mathbf{f}^\mu(\omega) &= \mathbf{E}^{\mathrm{ext}}(\omega)\end{aligned} \tag{8}$$

where $\mathbf{T}^{q\mu} = [\mathbf{T}^{\mu q}]^\dagger$ is the charge-dipole interaction kernel.[66,70,76]

2.2. Real-Time Extension of ωFQ and ωFQFμ Models. In this section, we extend both ωFQ and ωFQFμ to the time domain by proposing their real-time extension. Let us first focus on ωFQ. Explicating the definition of $z_q(\omega)$ in eq 3, we obtain

$$\left(-\frac{\omega^2}{2n_0} - \frac{\mathrm{i}\omega}{2n_0\tau}\right)\mathbf{q}(\omega) = \mathbf{A}^{qq}\mathbf{q}(\omega) + \mathbf{f}^q(\omega) \tag{9}$$

By considering the following definition of the Fourier transform

$$\begin{aligned}\mathcal{F}[f](\omega) &= \int_{-\infty}^{\infty} \mathrm{d}t\, \mathrm{e}^{\mathrm{i}\omega t} f(t)\\ \mathcal{F}^{-1}[f](t) &= \frac{1}{2\pi}\int_{-\infty}^{\infty} \mathrm{d}\omega\, \mathrm{e}^{-\mathrm{i}\omega t} f(\omega)\end{aligned} \tag{10}$$

we can rewrite eq 9 in the time domain by applying $\mathcal{F}^{-1}$ to both sides

$$\frac{1}{2n_0}\ddot{\mathbf{q}}(t) + \frac{1}{2n_0\tau}\dot{\mathbf{q}}(t) = \mathbf{A}^{qq}\mathbf{q}(t) + \mathbf{f}^q(t) \tag{11}$$

where we exploited the following properties of the Fourier transform

$$\begin{aligned}\dot{\mathbf{q}}(t) &= \frac{1}{2\pi}\int_{-\infty}^{\infty} \mathrm{d}\omega\, \mathrm{e}^{-\mathrm{i}\omega t}(-\mathrm{i}\omega)\mathbf{q}(\omega)\\ \ddot{\mathbf{q}}(t) &= \frac{1}{2\pi}\int_{-\infty}^{\infty} \mathrm{d}\omega\, \mathrm{e}^{-\mathrm{i}\omega t}(-\omega^2)\mathbf{q}(\omega)\end{aligned} \tag{12}$$

Equation 11 represents the dynamical evolution of a set of coupled forced damped oscillators with the same mass $\frac{1}{2n_0}$ and the same damping parameter $\frac{1}{\tau}$, under the time-dependent force $\mathbf{f}_q(t)$ that depends on the electric potential generated on each charge at the time t. Equation 11 defines the RT-ωFQ approach, which has also been formulated in refs 77,78.

By moving to ωFQFμ, eq 7 can be rewritten explicating $z_q(\omega)$ and $z_\mu(\omega)$ as follows

$$\left(-\frac{\omega^2}{2n_0} - \frac{\mathrm{i}\omega}{2n_0\tau}\right)\mathbf{q}(\omega) = \mathbf{A}^{qq}\mathbf{q}(\omega) + \mathbf{A}^{q\mu}\boldsymbol{\mu}(\omega) + \mathbf{f}^q(\omega) \tag{13}$$

$$\boldsymbol{\mu}(\omega) = \alpha^{\mathrm{IB}}(\omega)[-\mathbf{T}^{\mu q}\mathbf{q}(\omega) - \mathbf{T}^{\mu\mu}\boldsymbol{\mu}(\omega) + \mathbf{f}^\mu(\omega)] \tag{14}$$

Before applying the inverse Fourier transform, it is convenient to rewrite eq 14 to avoid the convolution in the time domain in terms of interband polarizability. To this end, we approximate the interband polarizability $\alpha^{\mathrm{IB}}(\omega)$ as a sum of Drude−Lorentz oscillators (DL), similarly to what has been proposed in FDTD[37,38] and BEM[79] frameworks

$$\alpha^{\mathrm{IB}}(\omega) \approx \alpha^{\mathrm{IB}}_{\mathrm{fit}}(\omega) = \sum_p^M \frac{A_p}{\omega_p^2 - \omega^2 - \mathrm{i}\omega\gamma_p} \tag{15}$$

where M is the total number of DL oscillators, each of them defined in terms of the parameters A_p, ω_p, and γ_p. We can split eq 14 by partitioning $\boldsymbol{\mu}(\omega)$ as DL-dependent terms $\boldsymbol{\mu}_p(\omega)$ such that

$$\boldsymbol{\mu}(\omega) = \sum_p^M \boldsymbol{\mu}_p(\omega) \tag{16}$$

$$\begin{aligned}\boldsymbol{\mu}_p(\omega) = \frac{A_p}{\omega_p^2 - \omega^2 - \mathrm{i}\omega\gamma_p}[&-\mathbf{T}^{\mu q}\mathbf{q}(\omega) - \mathbf{T}^{\mu\mu}\boldsymbol{\mu}(\omega)\\ &+ \mathbf{f}^\mu(\omega)]\end{aligned} \tag{17}$$

At this point, the original ωFQFμ problem in eqs 13 and 14 can be recast in $M + 1$ equations in the frequency domain, i.e.

$$\begin{aligned}\left(-\frac{\omega^2}{2n_0} - \frac{\mathrm{i}\omega}{2n_0\tau}\right)\mathbf{q}(\omega) &= \mathbf{A}^{qq}\mathbf{q}(\omega) + \mathbf{A}^{q\mu}\boldsymbol{\mu}(\omega) + \mathbf{f}^q(\omega)\\ \frac{\omega_p^2 - \omega^2 - \mathrm{i}\omega\gamma_p}{A_p}\boldsymbol{\mu}_p(\omega) &= -\mathbf{T}^{\mu q}\mathbf{q}(\omega) - \mathbf{T}^{\mu\mu}\boldsymbol{\mu}(\omega) + \mathbf{f}^\mu(\omega)\end{aligned} \tag{18}$$

By applying $\mathcal{F}^{-1}$ Fourier transform to both charges and dipoles expressions in eq 18, we finally obtain the $M + 1$ differential equations defining the RT-ωFQFμ model

$$\frac{1}{2n_0}\ddot{\mathbf{q}}(t) + \frac{1}{2n_0\tau}\dot{\mathbf{q}}(t) = \mathbf{A}^{qq}\mathbf{q}(t) + \mathbf{A}^{q\mu}\boldsymbol{\mu}(t) + \mathbf{f}^q(t) \tag{19}$$

$$\begin{aligned}\tfrac{1}{A_p}\ddot{\boldsymbol{\mu}}_p(t) + \tfrac{\gamma_p}{A_p}\dot{\boldsymbol{\mu}}_p(t) &= -\mathbf{T}^{\mu q}\mathbf{q}(t) - \mathbf{T}^{\mu\mu}\boldsymbol{\mu}(t)\\ &\quad + \mathbf{f}^\mu(t) - \tfrac{\omega_p^2}{A_p}\boldsymbol{\mu}_p(t)\end{aligned} \tag{20}$$

where we have exploited again the properties recalled in eq 12.

2.3. Numerical Propagation Scheme. To propagate RT-ωFQ and RT-ωFQFμ in time, we exploit a second-order velocity Verlet algorithm in the presence of a friction term.[80] Note that such a procedure has been previously exploited to deal with similar problems in the context of continuum approaches.[79] Let us consider a general coordinate system $\mathbf{x}(t)$ described by the following differential equation

$$\ddot{\mathbf{x}}(t) = \mathbf{F}(t) - \gamma\dot{\mathbf{x}}(t) \tag{21}$$

where $\mathbf{F}$ is the mass-normalized force acting on each coordinate and γ is the friction coefficient. By using a fixed step Δt, the second-order velocity Verlet algorithm scheme expresses $\mathbf{x}(t)$ and the associated velocity $\dot{\mathbf{x}}(t)$ as

$$\begin{aligned}\mathbf{x}(t + \Delta t) &= \mathbf{x}(t) + \Delta t\left(1 - \gamma\frac{\Delta t}{2}\right)\dot{\mathbf{x}}(t) + \frac{\Delta t^2}{2}\mathbf{F}(t)\\ \dot{\mathbf{x}}(t + \Delta t) &= \left(1 - \gamma\Delta t + \gamma^2\frac{\Delta t^2}{2}\right)\dot{\mathbf{x}}(t)\\ &\quad + \frac{\Delta t}{2}(1 - \gamma\Delta t)\mathbf{F}(t) + \frac{\Delta t}{2}\mathbf{F}(t + \Delta t)\end{aligned} \tag{22}$$

https://doi.org/10.1021/acs.jpcc.4c04002
J. Phys. Chem. C XXXX, XXX, XXX−XXX

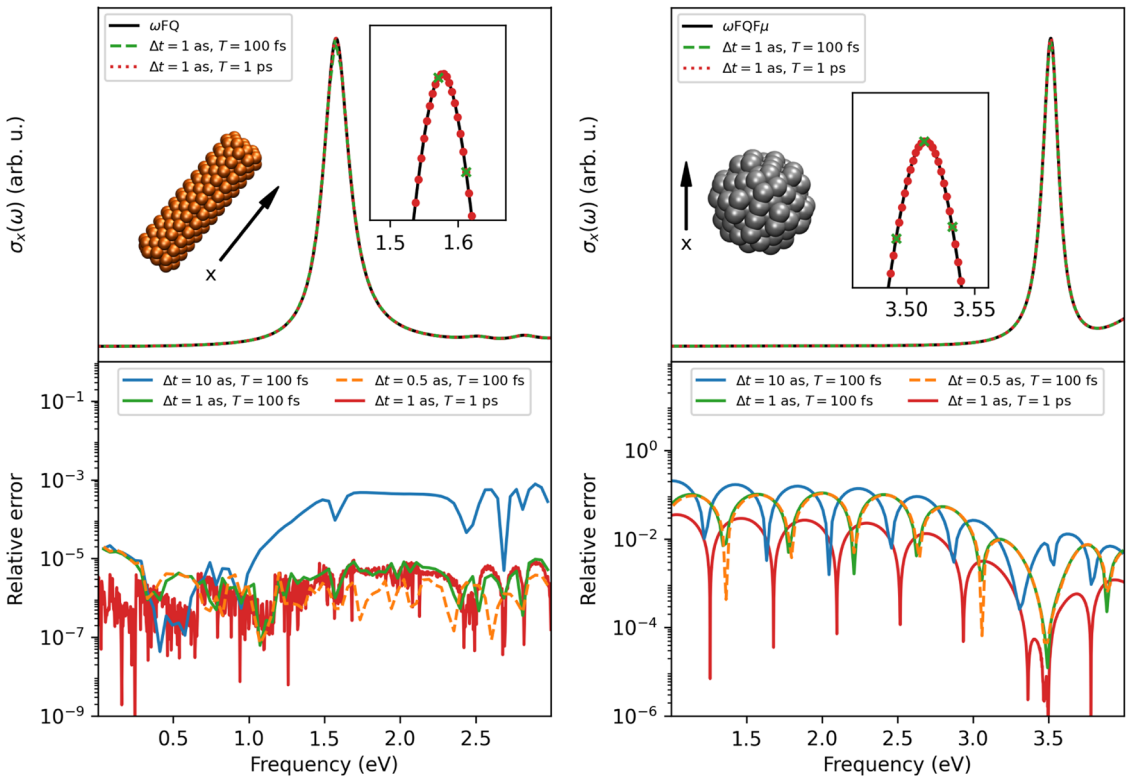

Figure 1. (Left) RT-ωFQ and ωFQ absorption cross section (σ_x) of a Na_{261} nanorod as polarized along the x axis. RT-ωFQ results are obtained by varying the parameters of the time evolution (Δt and T) under the action of the external pulse in eq 30. Relative RT-ωFQ-ωFQ errors are reported in the bottom panel. (Right) RT-ωFQFμ and ωFQFμ absorption cross section (σ_x) of a Ag_{164} spherical NP as polarized along the x axis. RT-ωFQFμ results are obtained by varying the parameters of the time evolution (Δt and T) under the action of the external pulse in eq 30. Relative RT-ωFQ-ωFQ errors are reported in the bottom panel.

Equation 22 can be specified for RT-ωFQ and RT-ωFQFμ by defining the mass-normalized time-dependent force acting on charges and dipoles from eqs 19 and 20

$$\mathbf{F}^q(t) = 2n_0[\mathbf{A}^{qq}\mathbf{q}(t) + \mathbf{A}^{q\mu}\boldsymbol{\mu}(t) + \mathbf{f}^q(t)] \tag{23}$$

$$\mathbf{F}^\mu_p(t) = A_p[-\mathbf{T}^{\mu q}\mathbf{q}(t) - \mathbf{T}^{\mu\mu}\boldsymbol{\mu}(t) + \mathbf{f}^\mu(t)] - \omega_p^2\boldsymbol{\mu}_p(t) \tag{24}$$

Note that for RT-ωFQ, only the forces acting on charges are calculated by discarding $\mathbf{A}^{q\mu}\,\boldsymbol{\mu}(t)$ in eq 23.

The second-order velocity Verlet algorithm scheme in eq 22 can finally be specified for the time-propagation of RT-ωFQ as follows

$$\mathbf{q}(t+\Delta t) = \mathbf{q}(t) + \Delta t\left(1 - \frac{\Delta t}{2\tau}\right)\dot{\mathbf{q}}(t) + \frac{\Delta t^2}{2}\mathbf{F}^q(t) \tag{25}$$

$$\dot{\mathbf{q}}(t+\Delta t) = \left(1 - \frac{\Delta t}{\tau} + \frac{\Delta t^2}{2\tau^2}\right)\dot{\mathbf{q}}(t) + \frac{\Delta t}{2}\left(1 - \frac{\Delta t}{\tau}\right)\mathbf{F}^q(t) + \frac{\Delta t}{2}\mathbf{F}^q(t+\Delta t) \tag{26}$$

In RT-ωFQFμ, the dipoles' time-propagation can be obtained similarly as

$$\boldsymbol{\mu}_p(t+\Delta t) = \boldsymbol{\mu}_p(t) + \Delta t\left(1 - \gamma_p\frac{\Delta t}{2}\right)\dot{\boldsymbol{\mu}}_p(t) + \frac{\Delta t^2}{2}\mathbf{F}^\mu(t) \tag{27}$$

$$\dot{\boldsymbol{\mu}}_p(t+\Delta t) = \left(1 - \gamma_p\Delta t + \gamma_p^2\frac{\Delta t^2}{2}\right)\dot{\boldsymbol{\mu}}_p(t) + \frac{\Delta t}{2}(1 - \gamma_p\Delta t)\mathbf{F}^\mu(t) + \frac{\Delta t}{2}\mathbf{F}^\mu(t+\Delta t) \tag{28}$$

2.4. Computational Details. RT-ωFQ and RT-ωFQFμ equations are solved by using a stand-alone Fortran 95 package. The numerical integration of charges and dipoles is performed by propagating eqs 25−28 from $t = 0$ and by assuming zero initial conditions, which naively correspond to the stationary solution in the absence of external field. ωFQ and ωFQFμ parameters for Na and Ag nanostructures are recovered from refs 60,66 respectively.

For RT-ωFQFμ, the interband polarizability α^{IB} in eq 15 is fitted to experimental data by resorting to the Basin-hopping stochastic global optimization algorithm.[81] The Ag interband polarizability (see ref 66 for its definition) is fitted with a different number of DL oscillators ($M = 4, 5, 6, 7$) by minimizing the residual error

$$\text{res} = \int_{\omega_{\min}}^{\omega_{\max}} d\omega|\alpha^{IB}(\omega) - \alpha^{IB}_{fit}(\omega)| \tag{29}$$

where α^{IB}_{fit} is the fitted permittivity that depends on the parameters A_p, ω_p, and γ_p. For each value of M, the optimal parameters are obtained by selecting the best α^{IB}_{fit} from 100 Basin-hopping simulations. Each Basin-hopping simulation is started by setting random values of ω_p extracted in the range between $\omega_{min} = 1$ eV and $\omega_{max} = 7$ eV, A_p and γ_p equal to 1 for each $p = 1, \cdots, M$. The fitting procedure is implemented in

https://doi.org/10.1021/acs.jpcc.4c04002
J. Phys. Chem. C XXXX, XXX, XXX−XXX

Python by resorting to the `lmfit` package,[82] which exploits the Basin-hopping algorithm as implemented in the `scipy` library.[83] Note that for $M = 6, 7$ the fitting procedure returns some values of $\omega_p \approx 0$ which can potentially generate numerical issues in the time propagation. However, these values can be safely discarded because $\alpha_{\mathrm{fit}}^{\mathrm{IB}}$ is correctly reproduced in the experimental frequency region of interest (vide infra). Three sets of parameters with $M = 4, 5, 6$ are finally generated. The numerical values of A_p, ω_p, and γ_p are reported in Table S1 in the Supporting Information − SI.

3. RESULTS AND DISCUSSION

In this section, RT-ωFQ and RT-ωFQFμ approaches are first validated by comparing the absorption spectra as calculated by Fourier-transform the time-dependent responses or by using ωFQ and ωFQFμ defined in the frequency domain. RT-ωFQ and RT-ωFQFμ robustness is further demonstrated by simulating the time-resolved spectral signal of a Sodium dimer characterized by an atomistically defined junction and the dynamical response of an Icosahedral Silver NP and comparing our results with reference *ab initio* data.

3.1. Validation of the Propagation Scheme. RT-ωFQ and RT-ωFQFμ are validated by computing the optical response of a Sodium cylindrical nanorod (Na_{261}, length 4.968 nm, diameter 1.242 nm, described at the RT-ωFQ level), and a silver spherical NP (Ag_{164}, diameter 1.634 nm, described at the RT-ωFQFμ level). The considered nanostructures are graphically depicted in Figure 1. For both systems, we apply an external electric field described as the following Gaussian-type kick pulse linearly polarized along the $\hat{\mathbf{x}}$ axis

$$\mathbf{E}_{\Delta t}^{\mathrm{ext}}(t) = E_0 \exp\left[-\frac{(t-t_0)^2}{2(\sigma\Delta t)^2}\right]\hat{\mathbf{x}}, \quad 0 < t < T \tag{30}$$

where $t_0 = 5$ fs, $\sigma = 0.1$, while Δt and T are the time-step and the total evolution time exploited in the time propagation. The Gaussian width depends on Δt in order to have a uniform sampling by varying the time step.

The longitudinal absorption cross-section σ_k along the axis $k = x, y, z$ is computed as

$$\sigma_k(\omega) = \frac{4\pi\omega}{c}\mathrm{Im}[\alpha_{kk}(\omega)] \tag{31}$$

where ω is the frequency, c is the speed of light and $\alpha_{kk}(\omega)$ is the frequency-dependent polarizability element, which is obtained from the time-propagation dynamics as follows

$$\alpha_{kk}^{\mathrm{RT}-\omega\mathrm{FQ}}(\omega) = \frac{\int \mathrm{d}t\left[\sum_i^N q_i(t) r_{i,k}\right]\mathrm{e}^{\mathrm{i}\omega t}}{\int \mathrm{d}t E_k^{\mathrm{ext}}(t)\mathrm{e}^{\mathrm{i}\omega t}}$$

$$\alpha_{kk}^{\mathrm{RT}-\omega\mathrm{FQF}\mu}(\omega) = \frac{\int \mathrm{d}t\left[\sum_i^N q_i(t) r_{i,k} + \mu_{i,k}(t)\right]\mathrm{e}^{\mathrm{i}\omega t}}{\int \mathrm{d}t E_k^{\mathrm{ext}}(t)\mathrm{e}^{\mathrm{i}\omega t}} \tag{32}$$

where q_i is the charge of the i-th atom, whereas $r_{i,k}$, $\mu_{i,k}$ and E_k are the $k = x, y, z$ Cartesian components of the position and the electric dipole of atom i, and the external electric field. The Fourier transform in eq 32 is numerically computed by resorting to the Fast Fourier Transform as implemented in the `scipy` package.[83]

RT-ωFQ and RT-ωFQFμ longitudinal absorption cross sections of the Na_{261} nanorod and Ag_{164} spherical NP are reported in Figure 1 (top panel), where they are compared to the corresponding $\sigma_x(\omega)$ calculated by exploiting the reference ωFQ and ωFQFμ models, respectively. The relative error on $\sigma_x(\omega)$ obtained from RT-ωFQ(Fμ) with respect to ωFQ(Fμ) is reported in the bottom panel of Figure 1. In the case of (RT-)ωFQFμ calculations, the fitted interband permittivity $\alpha_{\mathrm{fit}}^{\mathrm{IB}}$ obtained with $M = 6$ (see Table S1 in the SI) is used for both RT-ωFQFμ and ωFQFμ, thus ensuring the same optical response of the system in the two cases.

To validate our integration scheme, the absorption cross-section is calculated by varying the integration time step Δt (0.5, 1, 10 as) and the total simulation time T (100 fs, 1 ps). By first inspecting Figure 1, we note that the numerical results obtained from real-time simulations are qualitatively consistent with the reference values calculated in the frequency domain, perfectly reproducing all the features of the absorption spectrum for both ωFQ and ωFQFμ. This is valid for both $T = 100$ fs and $T = 1$ ps, for which the most accurate results are obtained as a higher density of data points is acquired (see inset of Figure 1, top panel).

For a more quantitative analysis, we investigate the relative error obtained for RT-ωFQ and RT-ωFQFμ by taking their frequency-domain counterparts as a reference. Such an analysis is performed for the same input frequencies in both the real-time and frequency-domain calculations. The numerical results are depicted in Figure 1, bottom panel, by varying the numerical parameters of the integration scheme (Δt, T) to quantify their impact on the numerical stability of the simulation. By first focusing on RT-ωFQ (left), we observe that a large Δt (10 as $T = 100$ fs) is generally associated with the largest errors, in particular in correspondence of the maxima in the absorption spectrum, i.e., for frequencies >1.5 eV. Differently, all calculations performed by using a smaller time-step (0.5, 1 as $T = 100$ fs), are associated with a substantial reduction of relative errors for all frequencies and are overall consistent with each other. Interestingly, elongating the total time of the simulation does not significantly affect the numerical errors in the region of the spectrum characterized by absorption peaks.

The relative errors computed for RT-ωFQFμ are inherently higher than those reported for RT-ωFQ by almost 2 orders of magnitude on average. In this case, reducing the time step of the integration does not substantially reduce the relative errors. The most accurate results are obtained by increasing the precision of the Fast Fourier Transform, i.e., by elongating the time simulation of the real-time propagation ($T = 1$ ps), which is associated with an increase in the number of sampled frequencies. This is particularly evident in the significant regions of the spectrum (frequency >3 eV), where the relative errors are comparable to those reported by RT-ωFQ. The relatively large errors can thus be attributed to limitations in numerical precision.

The discussed analysis validates the accuracy of our implementation and the exploited second-order procedure. In all the following calculations, the time step $\Delta t = 1$ ps is exploited because it guarantees the best compromise between computational cost and accuracy.

3.2. Sodium NP Dimer: Single-Atom Junction. As a first test case to analyze the performance of RT-ωFQ, we consider two Na_{380} icosahedral NPs that are connected by a monatomic junction (see inset in Figure 2). Such structure is extracted from a dynamical simulation of the retraction process of two fused Na_{380} NPs, which has been studied at the full *ab initio* level by Marchesin et al.[84] and at the ωFQ level in ref 60.

https://doi.org/10.1021/acs.jpcc.4c04002
J. Phys. Chem. C XXXX, XXX, XXX−XXX

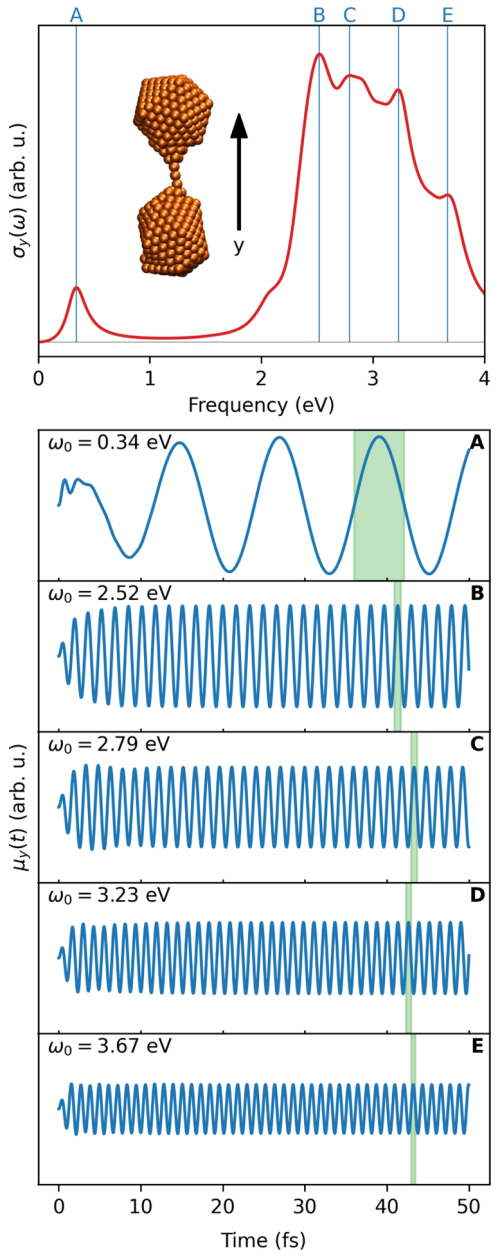

Figure 2. (Top) ωFQ absorption cross section of Na_{380} dimer as polarized along the y axis. (Bottom) RT-ωFQ total dipole moment induced in the y direction as a function of time for A, B, C, D, and E peaks highlighted in the top panel.

The breaking process gradually occurs: the monatomic junction first arises, and then the dimer dissociates as the distance increases. This study focuses on the monatomic junction because we have recently shown that tunneling effects are essential to reproduce the *ab initio* reference data.[60,84] As such, this system represents a perfect test case to show the capabilities of the newly developed RT-ωFQ for studying the dynamics of the optical response of atomistically defined NPs.

In fact, the simulated absorption cross-section along the longitudinal axis of the NP dimer (y) at the ωFQ level is characterized by two main bands.[60] Such plasmon peaks are associated with two peculiar charge-transfer (CT) plasmonic excitations. The band occurring at 0.34 eV (see A peak in Figure 2) is characterized by a dipolar plasmon in the whole dimer structure. For this reason, it is generally named Charge-Transfer Plasmon (CTP).[85−87] The second band dominates the spectrum and is especially broad (2−4 eV), resulting from the convolution of many absorption peaks. This behavior is commonly identified in most NP dimers.[41,84,88−90] The associated plasmon shows an overall multipolar character (generally dipolar character by looking at the single nanoparticles), and it is generally called CTP'. The large inhomogeneous broadening reported for the CTP' band is due to transitions with different nodal structure at the atomic scale, but corresponding to plasmons of similar nature (see B, C, D, and E peaks in Figure 2), similarly to what has been reported for other stretched sodium NPs.[60,88]

To study the plasmon dynamics in the time domain, we resort to RT-ωFQ. We exploit an external cosinusoidal electric field along the dimer axis (y)

$$\mathbf{E}^{\text{ext}}(t) = E_0 \cos(\omega_0 t)\hat{\mathbf{y}} \tag{33}$$

Differently from Section 3.1, the used functional form resembles a continuous wave (CW) illumination of the nanostructure. This demonstrates the flexibility of our approach to describing different excitations, which can better represent the experimental conditions.[15,25] The real-time simulation is carried out by using $E_0 = 10^{-6}$ au (≈ 50 μV/Å), $\Delta t = 1$ as, and $T = 50$ fs. In Figure 2, the time propagation of the total dipole moment along the dimer axis μ_y is plotted by setting ω_0 (see eq 33 in resonance with A, B, C, D, and E absorption frequencies). The numerical values are normalized with respect to the dipole moments computed at resonance with A absorption, for which the largest μ_y is reported. By looking at Figure 2, we note that the stationary solution is reached for all external frequencies after about 20 fs. In such a time regime, the total dipole moment oscillates in phase with the external field at the forcing frequency, which increases moving from the A to the E band. Remarkably, the relaxation time is similar for each external frequency, since it is intrinsically related to the scattering time assigned to sodium atoms (τ, see eq 1). Furthermore, the relative amplitudes of the dipole moments associated with the diverse plasmon excitations are directly connected with the imaginary part of the polarizability of the system, which in turn is related to the absorption cross section reported in Figure 2 through eq 31. This is why the largest amplitudes are reported for ω_0 in resonance with the A peak, and the relative amplitudes decrease by increasing the external frequency, following the trends highlighted by the absorption spectrum.

Our real-time model also allows for graphically investigating the dynamical oscillation of the induced charge density. A similar study has also been performed at the *ab initio* level as derived from TDDFT calculations, assuming a periodic oscillation equal to $2\pi/\omega_0$.[84] RT-ωFQ gives direct access to this analysis, allowing an in-depth investigation of the dynamics of the plasmon. In this case, we focus on plasmonic dynamics once the system enters the stationary condition. Such a time evolution is depicted in Figure 3 for the CTP peak at 0.34 eV (all the other time evolution are graphically depicted in Figures S2−S5 in the SI). As can be noticed, the single-atom junction behaves as an accumulation point for electron conduction, limiting the charge transfer between the two structures. Such a structure is associated with a substantial reduction of the electron current across the single-atom junction at both the ωFQ and TDDFT levels.[60,84] We finally remark that the plasmon dynamics in Figure 3 qualitatively

https://doi.org/10.1021/acs.jpcc.4c04002
J. Phys. Chem. C XXXX, XXX, XXX−XXX

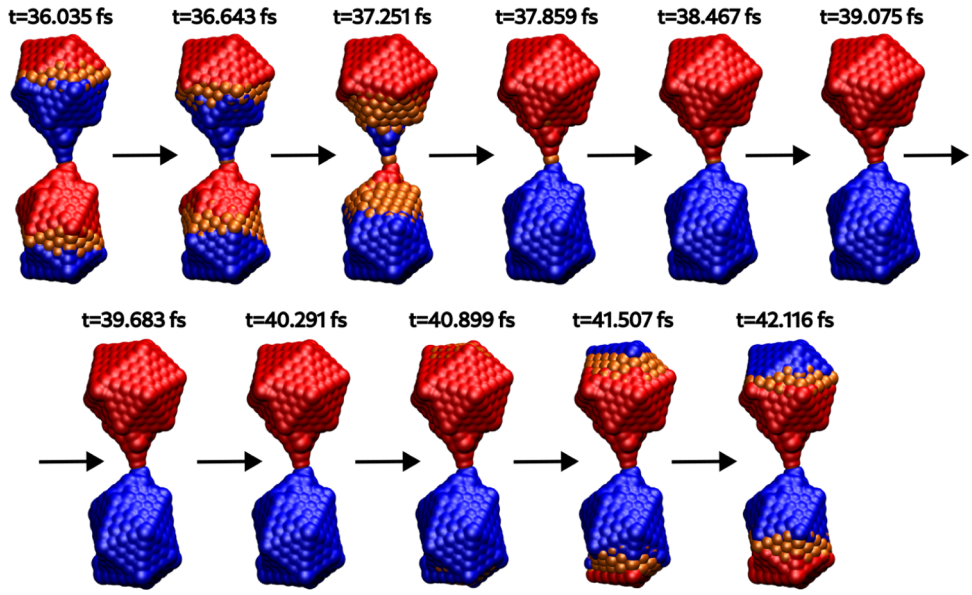

Figure 3. RT-ωFQ time evolution of the induced charge density of Na_{380} dimer excited using a monochromatic field oscillating at 0.34 eV (A peak in Figure 2, top panel). The induced charge density oscillation is reported for the time region highlighted in green in Figure 2, bottom panel. The density isovalue is set to 0.001 au.

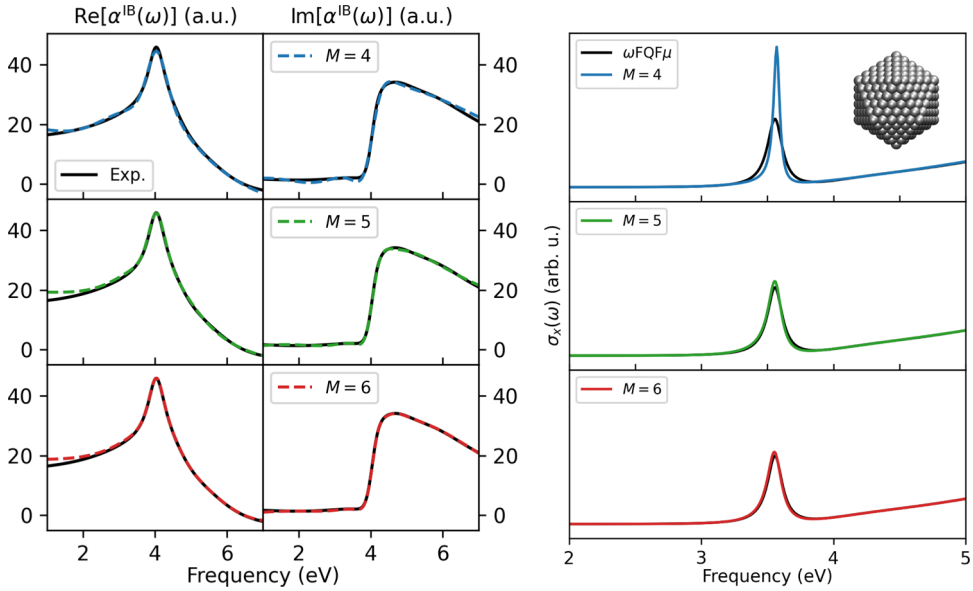

Figure 4. (Left) Fitting of the experimental interband polarizability $\alpha^{IB}(\omega)$ by using M = 4, 5, 6 DL oscillators (see eq 15). (Right) RT-ωFQFμ absorption cross section using α^{IB} as fitted using M = 4, 5, 6 DL oscillators. ωFQFμ reference spectrum as calculated by using the experimental α^{IB} is also reported for comparison's sake.

reproduces the TDDFT behavior[84] at a much lower computational cost.

To conclude our analysis, it is possible to monitor the charge transfer dynamics through the single-atom junction by calculating the total charge accumulated on each monomer at each time step. The partitioning of the Sodium dimer and the total charge on a monomer as obtained for a monochromatic field with ω_0 in resonance with A, B, C, D and E absorption frequencies are reported in Figure S6 in the SI. As it can be seen from the evolution of $Q(t)$ as normalized with respect to the maximum charge obtained at ω_0 = 0.34 eV (see Figure S6, right side), the total charge accumulated on the red monomer oscillates in phase with the total dipole at the frequency of the probing field. We can also quantify the CTP character of each plasmonic peak by inspecting the amplitude of $Q(t)$. In particular, the A peak at ω_0 = 0.34 eV shows a strong CTP character, while the other plasmonic excitations have a predominant BDP character, in accordance with the induced charge density evolution reported in Figures 3 and S2−S5 in the SI. It is worth remarking that the presence of the atomic link between the sodium monomers is not a necessary condition to allow for the charge-transfer between the subsystems, as it has been shown in the frequency domain with the ωFQ(Fμ) models.[60,66]

3.3. Icosahedral Ag NP. Let us now consider the intricate case of *d*-metal nanostructures, for which a proper description of interband transitions is crucial to reproduce the correct experimental optical properties.[66] As explained in Section 2.2,

https://doi.org/10.1021/acs.jpcc.4c04002
J. Phys. Chem. C XXXX, XXX, XXX−XXX

in order to study the dynamics of ωFQFμ plasmonic response, we approximate the interband polarizability $\alpha^{IB}(\omega)$ as a sum of M DL oscillators. The number M of DL oscillators is chosen to ensure the accurate reproduction of the interband polarizability. To select the minimum number of DL required for this purpose, in Figure 4 (left) we report α^{IB}_{fit} as fitted by exploiting 4, 5, and 6 DL oscillators For all cases, the reproduction of the experimental polarizability is particularly satisfactory, especially for frequencies larger than 4 eV. Some larger discrepancies are instead observed for smaller frequencies (1−4 eV), because $\alpha^{IB}(\omega)$ imaginary part is close to zero, and the DL functional form is not ideal in this case. The numerical fitting values are reported in Table S1 in SI. Note however that in such a region the optical response is dominated by intraband transitions, thus the effect of interband transitions is expected to be small. It is also worth pointing out that some amplitudes A_p are negative (as also obtained in ref 79), however, the overall sign of the interband polarizability is positive.

To further evaluate the accuracy of the fitting procedure, in Figure 4 (right), the absorption cross-section of an Ih Ag NP constituted of 561 atoms (Ag_{561}, radius ∼1.4 nm) is computed at the RT-ωFQFμ level (Δt = 1 as, T = 500 fs) by exploiting $\alpha^{IB}(\omega)$ fitted using M = 4, 5, 6 DL oscillators. ωFQFμ spectrum calculated in the frequency domain by using the experimental interband polarizability is taken as a reference (black line in Figure 4, right). The results clearly show that an accurate reproduction of the ωFQFμ spectrum is achieved when M > 4 DL oscillators are exploited in the fitting procedure. In fact, M = 4 (top panel) provides an overall good description of the ωFQFμ spectrum, however, the maximum intensity of the plasmon peak (at about 3.56 eV) and its width are wrongly predicted (the intensity is almost twice the reference, the width is smaller). Indeed, our results remark on the crucial importance of a proper modeling of the interband transitions to reproduce the optical properties of noble metal NPs, highlighting how small differences in the interband polarizability can drastically affect the optical response. As a final comment, it is worth pointing out that the outlined discrepancies are associated with the diverse description of the interband polarizability. This is demonstrated by the perfect agreement between ωFQFμ and RT-ωFQFμ spectra computed by using the same permittivity function (see Figure S1 in the SI).

To further demonstrate the reliability and robustness of our newly developed RT-ωFQFμ approach, we simulate the time evolution of the plasmonic excitation of Ag_{561} Ih NP under the effect of the following ultrafast Gaussian light pulse

$$\mathbf{E}^{ext}(t) = E_0 \cos(\omega_0(t - t_0))e^{-(t-t_0)^2/(2\sigma^2)}\hat{\mathbf{x}} \quad (34)$$

where E_0 = 51 μV/Å and σ = 2.121 fs. ω_0 is set to the PRF (3.56 eV). The parameters are chosen to match the *ab initio* RT-TDDFT study performed by Rossi et al.[30] on the same structure. Their *ab initio* results are thus taken as a reference for challenging RT-ωFQFμ. A graphical depiction of the exploited impulse is given in Figure 5, where the computed RT-ωFQFμ dipole as a function of time is also reported. The light pulse triggers a plasmonic response by generating a pronounced dipole moment within the system, which arises after a few femtoseconds (see Figure 5a). As the system evolves in time, specifically when t approaches 13 fs, the system undergoes a dephasing process. The coherence of the plasmon

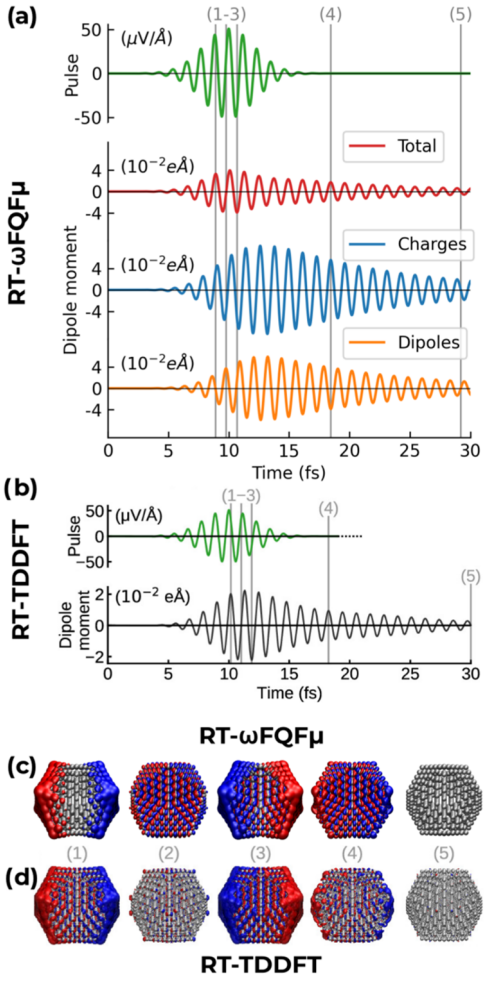

Figure 5. (a, b) RT-ωFQFμ (a) and RT-TDDFT[30] (b) time evolution of the plasmon excitation of Ag_{561} Ih NP excited using a monochromatic Gaussian pulse (top panel). In panel (a), the total RT-ωFQFμ response (red) is also decomposed in charge (blue) and dipole (orange) components. (c, d) RT-ωFQFμ (c) and RT-TDDFT[30] (d) plasmon densities at specific times (1−5) as depicted in panels (a, b), respectively. The isovalue is set to 0.035. RT-TDDFT data in panels b and d are reproduced from ref 30. Available under a CC-BY 4.0 license. Copyright 2020 American Chemical Society.

oscillations deteriorates, leading to a gradual decay of the dipole moment. The picture outlined by RT-ωFQFμ perfectly matches the reference *ab initio* RT-TDDFT time evolution (see Figure 5b). The agreement between the classical and quantum methods is excellent, not only qualitatively, but also quantitatively. In fact, only minor discrepancies are observed. The time delay of the plasmonic response for RT-ωFQFμ is smaller than RT-TDDFT as highlighted by vertical 1−3 bar in Figure 5a,b. In addition, RT-ωFQFμ predicts a larger induced dipole moment, but of the same order of magnitude (∼0.035 vs ∼0.022 eÅ). This result is particularly remarkable, especially considering the classical nature of RT-ωFQFμ and the associated low computational cost.

To quantify the effective decay timing τ associated with the dephasing mechanisms, we fit the RT-ωFQFμ and RT-TDDFT curves by using $e^{-t/\tau}$ functional form. The resulting RT-ωFQFμ τ is 9.6 fs, showing a typical localized surface plasmon decay time. This is in very good agreement with the reference *ab initio* fitted τ value (7.8 fs). Therefore, RT-ωFQFμ can be as accurate as RT-TDDFT in describing the

https://doi.org/10.1021/acs.jpcc.4c04002
J. Phys. Chem. C XXXX, XXX, XXX−XXX

plasmonic time evolution and decay, even for nanostructures below the quantum size limit, where it is commonly accepted that an explicit quantum description is necessary. The small numerical discrepancy can be due to the fact that RT-ωFQFμ does not account for electron-surface scattering damping mechanisms[66,91,92] thus modifying the final numerical value of τ.

The fitted τ substantially differs from the Drude scattering time exploited to model intraband mechanisms in our RT-ωFQFμ calculations (~39 fs). Such a finding suggests that interband effects play a nontrivial role in determining the time evolution of the response of the plasmonic decay. This is expected since interband transitions determine the optical response of noble nanostructures as demonstrated in Figure 4. In fact, the interband relaxation in Ag nanostructures is governed by the inverse of γ_p in eq 20 (see also Table S1 in the SI). For $M = 6$ DL oscillators, the scattering times $(1/\gamma_p)$ range from 4.5 as to 30.5 as. Therefore, intra and interband decay mechanisms nontrivially interplay, resulting in the fitted τ value. To deepen on this point, in Figure 5a, the RT-ωFQFμ time evolution of the total dipole moment is decomposed in its charge and dipole contributions. In fact, our classical approach allows for dissecting the contributions from delocalized and d electrons. This is possible thanks to the formulation of RT-ωFQFμ in terms of charges and dipoles with a clear physical meaning being directly associated with intra and interband mechanisms, respectively.[66] Figure 5a shows that charges and dipole dynamics are inherently connected, generally oscillating in counter phase for the whole duration of the plasmonic excitation (especially for $t > 13$ fs). Also, note that both charge and dipole decay with the same effective time, although the time scattering related to the two underlying mechanisms is defined in two different time scales. This is not surprising considering that charges and dipoles act as coupled oscillators in our model (see eqs 19 and 20). However, their dynamics nontrivially couple, thus resulting in the total dipole moment time evolution which has been previously discussed.

To further investigate this point, we analyze the time evolution of the plasmonic response by plotting the plasmon densities at relevant times (see 1−5, in Figure 5a,b), which are given in Figure 5c. The RT-TDDFT plasmon densities, reproduced from ref 30, are given in Figure 5d as a reference. The plasmonic excitation is characterized by electron density oscillations, which can be dissected into two main components. The first component is a surface-to-surface element, predominantly associated with delocalized valence electrons and intraband mechanisms. These electrons exhibit collective behavior and mainly determine the overall electron density oscillations. The second component arises from atom-localized contributions, which are linked to the screening effect due to interband transitions originating from the d-band. The plasmon decay (plots 4−5 in Figure 5c) is directly correlated with the diminishing surface-to-surface electron density oscillations, marking the end of the collective plasmonic activity. The intricate interplay between the delocalized valence electrons and the localized d-band electrons therefore forms the basis of the observed electron density oscillations. By comparing RT-ωFQFμ and RT-TDDFT, we note that such an interplay is correctly reproduced by our classical RT-ωFQFμ approach, thanks to the proper inclusion of intraband and interband decay mechanisms.

To conclude, we note that the stationary solution of a single damped harmonic oscillator with natural frequency ω_0 driven by a monochromatic field is characterized by a phase of $\pi/2$ when the frequency of the field approaches ω_0. However, the total dipole moment dynamics as calculated at both the RT-ωFQFμ and RT-TDDFT levels reported in Figure 5 are associated with a phase different from $\pi/2$ despite the field pulse being centered at the PRF in both simulations. Several effects come into play in determining the phase of the total dipole. First, the field pulse is not monochromatic and the pulse duration is shorter than the plasmonic relaxation time, therefore our system is not in a stationary state. Second, the total induced dipole moment contains the response from all plasmonic excitations (not only the one in resonance with the external field) which contribute differently to the global phase. Finally, in RT-ωFQFμ, the nanostructure is modeled as a set of coupled damped oscillators that are not individually in resonance with the external field at the PRF.

To have a better insight into this behavior, we investigate the total dipole phase in the Na_{380} dimer analyzed in Section 3.2 under the action of the monochromatic field linearly polarized along the y direction with frequency ω_0 equal to the A, B, C, D, and E frequencies reported in the absorption spectrum (see Figure 2). The Na_{380} dimer is modeled using the RT-ωFQ method, in which all the charges share the same "effective mass" and friction coefficients (see eq 11), therefore simplifying our analysis. The field amplitude and the induced dipole are reported in Figure S7 (left) in the SI. For each time evolution, we extract the phase factor between the induced dipole (blue line) and the field amplitude (red line). We can see that the phase factor is close to $\pi/2$ but there is a non-negligible difference. Note that such a discrepancy is not associated with numerical issues since similar results are obtained with a smaller time step or longer simulations. Furthermore, in Figure S7 in the SI (right) we report the phase distribution of each charge $q_i(t)$ induced by a monochromatic field with $\omega_0 = 0.34$ eV (peak A in Figure 2). The phase accumulated on each charge nontrivially varies depending on the position and the local surroundings. Therefore, the phase of the total induced dipole is a rather complicated function whose value cannot be estimated *a priori*. To conclude, the single-damped oscillator model may fail in the description of the dynamic response of plasmonic nanostructures, thus highlighting the role of accurate modeling of these systems.

4. CONCLUSIONS

In this work we have presented two novel approaches, namely RT-ωFQ and RT-ωFQFμ, to describe the time evolution of plasmonic excitations in simple and noble metal nanoparticles. The developed methods are the real-time extension of ωFQ and ωFQFμ, which have been previously developed in the frequency domain. Such models provide an accurate fully atomistic modeling of plasmonic nanoparticles, by properly describing intra and interband effects and also tunneling mechanisms. Our real-time extension can handle short impulses (in the as/fs time scale) and CW within the same theoretical formulation.

RT-ωFQ and RT-ωFQFμ are first numerically validated taking the frequency-domain counterparts' results as reference. Then the models have been tested against two different challenging nanostructures: a sodium dimer characterized by a single atom junction, and an Ih Ag NP. To show the flexibility of our implementation, the first system is studied under CW illumination, while a Gaussian pulse is used to excite the Ag NP. As a result, while in the first case, after a transient, the total

https://doi.org/10.1021/acs.jpcc.4c04002
J. Phys. Chem. C XXXX, XXX, XXX−XXX

dipole moment of the nanostructure oscillates in phase with the external CW field, Ag NP total dipole moment is first excited and then fast decays in the fs time scale. In the latter, we directly compared with *ab initio* RT-TDDFT, demonstrating a qualitative and even quantitative agreement between our classical and the quantum approach. As a consequence, our approach can serve as a powerful approach for simulating the plasmonic response dynamics even for NP size below the quantum size limit. We note that we can further increase the agreement between our approach and full quantum treatments by including electron surface scattering damping decay mechanisms, which can serve as an additional decay channel.[91]

The development of RT-ωFQ and RT-ωFQFμ paves the way for the investigation of the decoherence of the plasmonic response in nanostructures of sizes considerably larger than those that can be treated at the purely quantum level, without losing accuracy. Also, the model has the potential to be coupled to a QM description of molecular systems adsorbed on metal nanostructures,[77] as previously done in the frequency domain[93,94] or by using diverse electrodynamical approaches.[79,95−98] Such an extension will be the topic of future papers.

■ ASSOCIATED CONTENT

Supporting Information

The Supporting Information is available free of charge at https://pubs.acs.org/doi/10.1021/acs.jpcc.4c04002.

Numerical values of A_p, ω_p, and γ_p for M = 4, 5, 6 DLs. Graphical depiction of plasmon time evolution for B, C, D, and E peaks depicted in Figure 3. Charge transfer dynamics for A peak depicted in Figure 3. Time propagation and dipole phase for Na_{380} for A, B, C, D, and E peaks depicted in Figure 3 (PDF)

■ AUTHOR INFORMATION

Corresponding Authors

Tommaso Giovannini − *Department of Physics, University of Rome Tor Vergata, 00133 Rome, Italy;* orcid.org/0000-0002-5637-2853; Email: tommaso.giovannini@uniroma2.it

Chiara Cappelli − *Scuola Normale Superiore, 56126 Pisa, Italy;* orcid.org/0000-0002-4872-4505; Email: chiara.cappelli@sns.it

Authors

Piero Lafiosca − *Scuola Normale Superiore, 56126 Pisa, Italy;* orcid.org/0000-0002-3967-0736

Luca Nicoli − *Scuola Normale Superiore, 56126 Pisa, Italy;* orcid.org/0000-0002-4808-3381

Silvio Pipolo − *UCCS Unité de Catalyse et Chimie du Solide, Université de Lille, Université d'Artois UMR 8181, F-59000 Lille, France*

Stefano Corni − *Dipartimento di Scienze Chimiche, Università di Padova, 35131 Padova, Italy; Istituto di Nanoscienze del Consiglio Nazionale delle Ricerche CNR-NANO, 41125 Modena, Italy;* orcid.org/0000-0001-6707-108X

Complete contact information is available at: https://pubs.acs.org/10.1021/acs.jpcc.4c04002

Funding

This work has received funding from the European Research Council (ERC) under the European Union's Horizon 2020 research and innovation program (grant agreement No. 818064). S.C. thanks the Horizon 2020 EU grant ProID (grant agreement No. 964363) for funding.

Notes

The authors declare no competing financial interest.

■ ACKNOWLEDGMENTS

We thank Giulia Dall'Osto for the discussions on the dielectric function fitting. We gratefully acknowledge the Center for High-Performance Computing (CHPC) at SNS for providing the computational infrastructure.

■ REFERENCES

(1) Pitarke, J. M.; Silkin, V.; Chulkov, E.; Echenique, P. Theory of surface plasmons and surface-plasmon polaritons. *Rep. Prog. Phys.* **2007**, *70*, 1.

(2) Giannini, V.; Fernández-Domínguez, A. I.; Heck, S. C.; Maier, S. A. Plasmonic nanoantennas: fundamentals and their use in controlling the radiative properties of nanoemitters. *Chem. Rev.* **2011**, *111*, 3888−3912.

(3) Halas, N. J.; Lal, S.; Chang, W.-S.; Link, S.; Nordlander, P. Plasmons in strongly coupled metallic nanostructures. *Chem. Rev.* **2011**, *111*, 3913−3961.

(4) Kelly, K. L.; Coronado, E.; Zhao, L. L.; Schatz, G. C. The optical properties of metal nanoparticles: the influence of size, shape, and dielectric environment. *J. Phys. Chem. B* **2003**, *107*, 668−677.

(5) Liz-Marzán, L. M. Tailoring surface plasmons through the morphology and assembly of metal nanoparticles. *Langmuir* **2006**, *22*, 32−41.

(6) Ringe, E.; McMahon, J. M.; Sohn, K.; Cobley, C.; Xia, Y.; Huang, J.; Schatz, G. C.; Marks, L. D.; Van Duyne, R. P. Unraveling the effects of size, composition, and substrate on the localized surface plasmon resonance frequencies of gold and silver nanocubes: a systematic single-particle approach. *J. Phys. Chem. C* **2010**, *114*, 12511−12516.

(7) Langer, J.; Jimenez de Aberasturi, D.; Aizpurua, J.; Alvarez-Puebla, R. A.; Auguié, B.; Baumberg, J. J.; Bazan, G. C.; Bell, S. E. J.; Boisen, A.; Brolo, A. G.; et al. Present and Future of Surface-Enhanced Raman Scattering. *ACS Nano* **2020**, *14*, 28−117.

(8) Willets, K. A.; Van Duyne, R. P. Localized surface plasmon resonance spectroscopy and sensing. *Annu. Rev. Phys. Chem.* **2007**, *58*, 267−297.

(9) Zhang, R.; Zhang, Y.; Dong, Z.; Jiang, S.; Zhang, C.; Chen, L.; Zhang, L.; Liao, Y.; Aizpurua, J.; Luo, Y.; et al. Chemical mapping of a single molecule by plasmon-enhanced Raman scattering. *Nature* **2013**, *498*, 82−86.

(10) Jiang, S.; Zhang, Y.; Zhang, R.; Hu, C.; Liao, M.; Luo, Y.; Yang, J.; Dong, Z.; Hou, J. Distinguishing adjacent molecules on a surface using plasmon-enhanced Raman scattering. *Nat. Nanotechnol.* **2015**, *10*, 865−869.

(11) Chiang, N.; Chen, X.; Goubert, G.; Chulhai, D. V.; Chen, X.; Pozzi, E. A.; Jiang, N.; Hersam, M. C.; Seideman, T.; Jensen, L.; Van Duyne, R. P. Conformational contrast of surface-mediated molecular switches yields Ångstrom-scale spatial resolution in ultrahigh vacuum tip-enhanced Raman spectroscopy. *Nano Lett.* **2016**, *16*, 7774−7778.

(12) Benz, F.; Schmidt, M. K.; Dreismann, A.; Chikkaraddy, R.; Zhang, Y.; Demetriadou, A.; Carnegie, C.; Ohadi, H.; De Nijs, B.; Esteban, R.; et al. Single-molecule optomechanics in "picocavities". *Science* **2016**, *354*, 726−729.

(13) Yang, B.; Chen, G.; Ghafoor, A.; Zhang, Y.; Zhang, Y.; Zhang, Y.; Luo, Y.; Yang, J.; Sandoghdar, V.; Aizpurua, J.; et al. Sub-nanometre resolution in single-molecule photoluminescence imaging. *Nat. Photonics* **2020**, *14*, 693−699.

(14) Liu, P.; Chulhai, D. V.; Jensen, L. Single-Molecule Imaging Using Atomistic Near-Field Tip-Enhanced Raman Spectroscopy. *ACS Nano* **2017**, *11*, 5094−5102.

(15) Yuan, Y.; Zhou, L.; Robatjazi, H.; Bao, J. L.; Zhou, J.; Bayles, A.; Yuan, L.; Lou, M.; Lou, M.; Khatiwada, S.; et al. Earth-abundant photocatalyst for H2 generation from NH3 with light-emitting diode illumination. *Science* **2022**, *378*, 889−893.
(16) Ezendam, S.; Herran, M.; Nan, L.; Gruber, C.; Kang, Y.; Gröbmeyer, F.; Lin, R.; Gargiulo, J.; Sousa-Castillo, A.; Cortés, E. Hybrid plasmonic nanomaterials for hydrogen generation and carbon dioxide reduction. *ACS Energy Lett.* **2022**, *7*, 778−815.
(17) Baldi, A.; Askes, S. H. Pulsed Photothermal Heterogeneous Catalysis. *ACS Catal.* **2023**, *13*, 3419−3432.
(18) Herran, M.; Sousa-Castillo, A.; Fan, C.; Lee, S.; Xie, W.; Döblinger, M.; Auguié, B.; Cortés, E. Tailoring plasmonic bimetallic nanocatalysts toward sunlight-driven H2 production. *Adv. Funct. Mater.* **2022**, *32*, No. 2203418.
(19) Yuan, L.; Zhou, J.; Zhang, M.; Wen, X.; Martirez, J. M. P.; Robatjazi, H.; Zhou, L.; Carter, E. A.; Nordlander, P.; Halas, N. J. Plasmonic Photocatalysis with Chemically and Spatially Specific Antenna−Dual Reactor Complexes. *ACS Nano* **2022**, *16*, 17365−17375.
(20) Baumberg, J. J. Picocavities: a primer. *Nano Lett.* **2022**, *22*, 5859−5865.
(21) Li, S.; Miao, P.; Zhang, Y.; Wu, J.; Zhang, B.; Du, Y.; Han, X.; Sun, J.; Xu, P. Recent advances in plasmonic nanostructures for enhanced photocatalysis and electrocatalysis. *Adv. Mater.* **2021**, *33*, No. 2000086.
(22) Gargiulo, J.; Berté, R.; Li, Y.; Maier, S. A.; Cortés, E. From optical to chemical hot spots in plasmonics. *Acc. Chem. Res.* **2019**, *52*, 2525−2535.
(23) Mukherjee, S.; Libisch, F.; Large, N.; Neumann, O.; Brown, L. V.; Cheng, J.; Lassiter, J. B.; Carter, E. A.; Nordlander, P.; Halas, N. J. Hot electrons do the impossible: plasmon-induced dissociation of H2 on Au. *Nano Lett.* **2013**, *13*, 240−247.
(24) Clavero, C. Plasmon-induced hot-electron generation at nanoparticle/metal-oxide interfaces for photovoltaic and photocatalytic devices. *Nat. Photonics* **2014**, *8*, 95−103.
(25) Robatjazi, H.; Bao, J. L.; Zhang, M.; Zhou, L.; Christopher, P.; Carter, E. A.; Nordlander, P.; Halas, N. J. Plasmon-driven carbon−fluorine (C (sp 3)−F) bond activation with mechanistic insights into hot-carrier-mediated pathways. *Nat. Catal.* **2020**, *3*, 564−573.
(26) Zhan, C.; Moskovits, M.; Tian, Z.-Q. Recent progress and prospects in plasmon-mediated chemical reaction. *Matter* **2020**, *3*, 42−56.
(27) Dong, Y.; Hu, C.; Xiong, H.; Long, R.; Xiong, Y. Plasmonic Catalysis: New Opportunity for Selective Chemical Bond Evolution. *ACS Catal.* **2023**, *13*, 6730−6743.
(28) Cortés, E.; Grzeschik, R.; Maier, S. A.; Schlücker, S. Experimental characterization techniques for plasmon-assisted chemistry. *Nat. Rev. Chem.* **2022**, *6*, 259−274.
(29) Sa, J.; Wach, A.; Szlachetko, J.; Maximenko, A.; Sobol, T.; Partyka-Jankowska, E.; Bacellar, C.; Cirelli, C.; Johnson, P.; Castillo, R. G.et al. Dynamics of Plasmon-Induced Hot Carrier Creation in Colloidal Gold 2024 DOI: 10.21203/rs.3.rs-3799527/v1.
(30) Rossi, T. P.; Erhart, P.; Kuisma, M. Hot-carrier generation in plasmonic nanoparticles: The importance of atomic structure. *ACS Nano* **2020**, *14*, 9963−9971.
(31) Liu, J. G.; Zhang, H.; Link, S.; Nordlander, P. Relaxation of plasmon-induced hot carriers. *ACS Photonics* **2018**, *5*, 2584−2595.
(32) Sánchez, C. G.; Berdakin, M. Plasmon-induced hot carriers: An atomistic perspective of the first tens of femtoseconds. *J. Phys. Chem. C* **2022**, *126*, 10015−10023.
(33) Wu, X.; van der Heide, T.; Wen, S.; Frauenheim, T.; Tretiak, S.; Yam, C.; Zhang, Y. Molecular dynamics study of plasmon-mediated chemical transformations. *Chem. Sci.* **2023**, *14*, 4714−4723.
(34) Myroshnychenko, V.; Rodríguez-Fernández, J.; Pastoriza-Santos, I.; Funston, A. M.; Novo, C.; Mulvaney, P.; Liz-Marzan, L. M.; de Abajo, F. J. G. Modelling the optical response of gold nanoparticles. *Chem. Soc. Rev.* **2008**, *37*, 1792−1805.
(35) Hohenester, U.; Trügler, A. MNPBEM−A Matlab toolbox for the simulation of plasmonic nanoparticles. *Comput. Phys. Commun.* **2012**, *183*, 370−381.
(36) de Abajo, F. J. G.; Howie, A. Retarded field calculation of electron energy loss in inhomogeneous dielectrics. *Phys. Rev. B* **2002**, *65*, No. 115418.
(37) Hao, F.; Nordlander, P. Efficient dielectric function for FDTD simulation of the optical properties of silver and gold nanoparticles. *Chem. Phys. Lett.* **2007**, *446*, 115−118.
(38) Sehmi, H. S.; Langbein, W.; Muljarov, E. Optimizing the Drude-Lorentz model for material permittivity: Method, program, and examples for gold, silver, and copper. *Phys. Rev. B* **2017**, *95*, No. 115444.
(39) Teperik, T. V.; Nordlander, P.; Aizpurua, J.; Borisov, A. G. Quantum effects and nonlocality in strongly coupled plasmonic nanowire dimers. *Opt. Express* **2013**, *21*, 27306−27325.
(40) Zhu, W.; Esteban, R.; Borisov, A. G.; Baumberg, J. J.; Nordlander, P.; Lezec, H. J.; Aizpurua, J.; Crozier, K. B. Quantum mechanical effects in plasmonic structures with subnanometre gaps. *Nat. Commun.* **2016**, *7*, No. 11495.
(41) Urbieta, M.; Barbry, M.; Zhang, Y.; Koval, P.; Sánchez-Portal, D.; Zabala, N.; Aizpurua, J. Atomic-Scale Lightning Rod Effect in Plasmonic Picocavities: A Classical View to a Quantum Effect. *ACS Nano* **2018**, *12*, 585−595.
(42) Savage, K. J.; Hawkeye, M. M.; Esteban, R.; Borisov, A. G.; Aizpurua, J.; Baumberg, J. J. Revealing the quantum regime in tunnelling plasmonics. *Nature* **2012**, *491*, 574−577.
(43) Marinica, D.; Kazansky, A.; Nordlander, P.; Aizpurua, J.; Borisov, A. G. Quantum plasmonics: nonlinear effects in the field enhancement of a plasmonic nanoparticle dimer. *Nano Lett.* **2012**, *12*, 1333−1339.
(44) Esteban, R.; Borisov, A. G.; Nordlander, P.; Aizpurua, J. Bridging quantum and classical plasmonics with a quantum-corrected model. *Nat. Commun.* **2012**, *3*, No. 825.
(45) Esteban, R.; Zugarramurdi, A.; Zhang, P.; Nordlander, P.; García-Vidal, F. J.; Borisov, A. G.; Aizpurua, J. A classical treatment of optical tunneling in plasmonic gaps: extending the quantum corrected model to practical situations. *Faraday Discuss.* **2015**, *178*, 151−183.
(46) Campos, A.; Troc, N.; Cottancin, E.; Pellarin, M.; Weissker, H.-C.; Lermé, J.; Kociak, M.; Hillenkamp, M. Plasmonic quantum size effects in silver nanoparticles are dominated by interfaces and local environments. *Nat. Phys.* **2019**, *15*, 275−280.
(47) Scholl, J. A.; García-Etxarri, A.; Koh, A. L.; Dionne, J. A. Observation of quantum tunneling between two plasmonic nanoparticles. *Nano Lett.* **2013**, *13*, 564−569.
(48) Barbry, M.; Koval, P.; Marchesin, F.; Esteban, R.; Borisov, A.; Aizpurua, J.; Sánchez-Portal, D. Atomistic near-field nanoplasmonics: reaching atomic-scale resolution in nanooptics. *Nano Lett.* **2015**, *15*, 3410−3419.
(49) Domenis, N.; Grobas Illobre, P.; Marsili, M.; Stener, M.; Toffoli, D.; Coccia, E. Time Evolution of Plasmonic Features in Pentagonal Ag Clusters. *Molecules* **2023**, *28*, 5671.
(50) Herring, C. J.; Montemore, M. M. Recent Advances in Real-Time Time-Dependent Density Functional Theory Simulations of Plasmonic Nanostructures and Plasmonic Photocatalysis. *ACS Nanosci. Au* **2023**, *3*, 269−279.
(51) Kuisma, M.; Sakko, A.; Rossi, T. P.; Larsen, A. H.; Enkovaara, J.; Lehtovaara, L.; Rantala, T. T. Localized surface plasmon resonance in silver nanoparticles: Atomistic first-principles time-dependent density-functional theory calculations. *Phys. Rev. B* **2015**, *91*, No. 115431.
(52) Ding, F.; Guidez, E. B.; Aikens, C. M.; Li, X. Quantum coherent plasmon in silver nanowires: A real-time TDDFT study. *J. Chem. Phys.* **2014**, *140*, No. 244705.
(53) Senanayake, R. D.; Lingerfelt, D. B.; Kuda-Singappulige, G. U.; Li, X.; Aikens, C. M. Real-time TDDFT investigation of optical absorption in gold nanowires. *J. Phys. Chem. C* **2019**, *123*, 14734−14745.

https://doi.org/10.1021/acs.jpcc.4c04002
J. Phys. Chem. C XXXX, XXX, XXX−XXX

(54) Baseggio, O.; Fronzoni, G.; Stener, M. A new time dependent density functional algorithm for large systems and plasmons in metal clusters. *J. Chem. Phys.* **2015**, *143*, No. 024106.
(55) Baseggio, O.; De Vetta, M.; Fronzoni, G.; Stener, M.; Sementa, L.; Fortunelli, A.; Calzolari, A. Photoabsorption of icosahedral noble metal clusters: An efficient TDDFT approach to large-scale systems. *J. Phys. Chem. C* **2016**, *120*, 12773−12782.
(56) Sinha-Roy, R.; Garcia-Gonzalez, P.; Weissker, H.-C.; Rabilloud, F.; Fernandez-Dominguez, A. I. Classical and ab Initio Plasmonics Meet at Sub-nanometric Noble Metal Rods. *ACS Photonics* **2017**, *4*, 1484−1493.
(57) Ilawe, N. V.; Oviedo, M. B.; Wong, B. M. Real-time quantum dynamics of long-range electronic excitation transfer in plasmonic nanoantennas. *J. Chem. Theory Comput.* **2017**, *13*, 3442−3454.
(58) Ilawe, N. V.; Oviedo, M. B.; Wong, B. M. Effect of quantum tunneling on the efficiency of excitation energy transfer in plasmonic nanoparticle chain waveguides. *J. Mater. Chem. C* **2018**, *6*, 5857−5864.
(59) D'Agostino, S.; Rinaldi, R.; Cuniberti, G.; Della Sala, F. Density functional tight binding for quantum plasmonics. *J. Phys. Chem. C* **2018**, *122*, 19756−19766.
(60) Giovannini, T.; Rosa, M.; Corni, S.; Cappelli, C. A classical picture of subnanometer junctions: an atomistic Drude approach to nanoplasmonics. *Nanoscale* **2019**, *11*, 6004−6015.
(61) Bonatti, L.; Gil, G.; Giovannini, T.; Corni, S.; Cappelli, C. Plasmonic Resonances of Metal Nanoparticles: Atomistic vs. Continuum Approaches. *Front. Chem.* **2020**, *8*, 340.
(62) Giovannini, T.; Bonatti, L.; Polini, M.; Cappelli, C. Graphene plasmonics: Fully atomistic approach for realistic structures. *J. Phys. Chem. Lett.* **2020**, *11*, 7595−7602.
(63) Bonatti, L.; Nicoli, L.; Giovannini, T.; Cappelli, C. In silico design of graphene plasmonic hot-spots. *Nanoscale Adv.* **2022**, *4*, 2294−2302.
(64) Zanotto, S.; Bonatti, L.; Pantano, M. F.; Miseikis, V.; Speranza, G.; Giovannini, T.; Coletti, C.; Cappelli, C.; Tredicucci, A.; Toncelli, A. Strain-induced plasmon confinement in polycrystalline graphene. *ACS Photonics* **2023**, *10*, 394−400.
(65) Yamada, A. Classical electronic and molecular dynamics simulation for optical response of metal system. *J. Chem. Phys.* **2021**, *155*, No. 174118.
(66) Giovannini, T.; Bonatti, L.; Lafiosca, P.; Nicoli, L.; Castagnola, M.; Illobre, P. G.; Corni, S.; Cappelli, C. Do we really need quantum mechanics to describe plasmonic properties of metal nanostructures? *ACS Photonics* **2022**, *9*, 3025−3034.
(67) Nicoli, L.; Lafiosca, P.; Grobas Illobre, P.; Bonatti, L.; Giovannini, T.; Cappelli, C. Fully atomistic modeling of plasmonic bimetallic nanoparticles: nanoalloys and core-shell systems. *Front. Photonics* **2023**, *4*, No. 1199598.
(68) Bade, W. L. Drude-Model Calculation of Dispersion Forces. I. General Theory. *J. Chem. Phys.* **1957**, *27*, 1280−1284.
(69) Lafiosca, P.; Giovannini, T.; Benzi, M.; Cappelli, C. Going Beyond the Limits of Classical Atomistic Modeling of Plasmonic Nanostructures. *J. Phys. Chem. C* **2021**, *125*, 23848−23863.
(70) Mayer, A. Formulation in terms of normalized propagators of a charge-dipole model enabling the calculation of the polarization properties of fullerenes and carbon nanotubes. *Phys. Rev. B* **2007**, *75*, No. 045407.
(71) Pinchuk, A.; Kreibig, U.; Hilger, A. Optical properties of metallic nanoparticles: influence of interface effects and interband transitions. *Surf. Sci.* **2004**, *557*, 269−280.
(72) Pinchuk, A.; Von Plessen, G.; Kreibig, U. Influence of interband electronic transitions on the optical absorption in metallic nanoparticles. *J. Phys. D: Appl. Phys.* **2004**, *37*, 3133.
(73) Balamurugan, B.; Maruyama, T. Evidence of an enhanced interband absorption in Au nanoparticles: size-dependent electronic structure and optical properties. *Appl. Phys. Lett.* **2005**, *87*, No. 143105.
(74) Liebsch, A. Surface-plasmon dispersion and size dependence of Mie resonance: silver versus simple metals. *Phys. Rev. B* **1993**, *48*, No. 11317.
(75) Santiago, E. Y.; Besteiro, L. V.; Kong, X.-T.; Correa-Duarte, M. A.; Wang, Z.; Govorov, A. O. Efficiency of hot-electron generation in plasmonic nanocrystals with complex shapes: surface-induced scattering, hot spots, and interband transitions. *ACS Photonics* **2020**, *7*, 2807−2824.
(76) Giovannini, T.; Puglisi, A.; Ambrosetti, M.; Cappelli, C. Polarizable QM/MM approach with fluctuating charges and fluctuating dipoles: the QM/FQFμ model. *J. Chem. Theory Comput.* **2019**, *15*, 2233−2245.
(77) Huang, X.; Zhang, W.; Liang, W. Time-dependent Kohn- Sham electron dynamics coupled with nonequilibrium plasmonic response via atomistic electromagnetic model. *J. Chem. Phys.* **2024**, *160*, No. 214106.
(78) Huang, X.; Liang, W. Real-Time Simulation of Ultrafast Electronic Dynamics of Nanoscale Systems Involving an Organic Molecule and a Nanoparticle Dimer. *J. Phys. Chem. Lett.* **2024**, *15*, 6592−6597.
(79) Dall'Osto, G.; Gil, G.; Pipolo, S.; Corni, S. Real-time dynamics of plasmonic resonances in nanoparticles described by a boundary element method with generic dielectric function. *J. Chem. Phys.* **2020**, *153*, No. 184114.
(80) Vanden-Eijnden, E.; Ciccotti, G. Second-order integrators for Langevin equations with holonomic constraints. *Chem. Phys. Lett.* **2006**, *429*, 310−316.
(81) Wales, D. J.; Doye, J. P. Global optimization by basin-hopping and the lowest energy structures of Lennard-Jones clusters containing up to 110 atoms. *J. Phys. Chem. A* **1997**, *101*, 5111−5116.
(82) Newville, M.; Otten, R.; Nelson, A.; Stensitzki, T.; Ingargiola, A.; Allan, D.; Fox, A.; Carter, F.; Michał; Osborn, R.; et al. *lmfit/lmfit-py: 1.3.2*, version 1.3.2, 2024 DOI: 10.5281/zenodo.598352.
(83) Virtanen, P.; Gommers, R.; Oliphant, T. E.; Haberland, M.; Reddy, T.; Cournapeau, D.; Burovski, E.; Peterson, P.; Weckesser, W.; Bright, J.; et al. SciPy 1.0: Fundamental Algorithms for Scientific Computing in Python. *Nat. Methods* **2020**, *17*, 261−272.
(84) Marchesin, F.; Koval, P.; Barbry, M.; Aizpurua, J.; Sánchez-Portal, D. Plasmonic response of metallic nanojunctions driven by single atom motion: quantum transport revealed in optics. *ACS Photonics* **2016**, *3*, 269−277.
(85) Liu, L.; Wang, Y.; Fang, Z.; Zhao, K. Plasmon hybridization model generalized to conductively bridged nanoparticle dimers. *J. Chem. Phys.* **2013**, *139*, No. 064310.
(86) Pérez-González, O.; Zabala, N.; Aizpurua, J. Optical characterization of charge transfer and bonding dimer plasmons in linked interparticle gaps. *New J. Phys.* **2011**, *13*, No. 083013.
(87) Duan, H.; Fernández-Domínguez, A. I.; Bosman, M.; Maier, S. A.; Yang, J. K. Nanoplasmonics: classical down to the nanometer scale. *Nano Lett.* **2012**, *12*, 1683−1689.
(88) Rossi, T. P.; Zugarramurdi, A.; Puska, M. J.; Nieminen, R. M. Quantized evolution of the plasmonic response in a stretched nanorod. *Phys. Rev. Lett.* **2015**, *115*, No. 236804.
(89) Varas, A.; García-González, P.; Feist, J.; García-Vidal, F.; Rubio, A. Quantum plasmonics: from jellium models to ab initio calculations. *Nanophotonics* **2016**, *5*, 409−426.
(90) Zhang, P.; Feist, J.; Rubio, A.; García-González, P.; García-Vidal, F. Ab initio nanoplasmonics: The impact of atomic structure. *Phys. Rev. B* **2014**, *90*, No. 161407.
(91) Khurgin, J. B.; Levy, U. Generating hot carriers in plasmonic nanoparticles: when quantization does matter? *ACS Photonics* **2020**, *7*, 547−553.
(92) Khurgin, J.; Tsai, W.-Y.; Tsai, D. P.; Sun, G. Landau damping and limit to field confinement and enhancement in plasmonic dimers. *ACS Photonics* **2017**, *4*, 2871−2880.
(93) Lafiosca, P.; Nicoli, L.; Bonatti, L.; Giovannini, T.; Corni, S.; Cappelli, C. Qm/classical modeling of surface enhanced Raman scattering based on atomistic electromagnetic models. *J. Chem. Theory Comput.* **2023**, *19*, 3616−3633.

https://doi.org/10.1021/acs.jpcc.4c04002
J. Phys. Chem. C XXXX, XXX, XXX−XXX

(94) Grobas Illobre, P.; Lafiosca, P.; Guidone, T.; Mazza, F.; Giovannini, T.; Cappelli, C. Multiscale Modeling of Surface Enhanced Fluorescence. *Nanoscale Adv.* **2024**, *6*, 3410−3425.
(95) Pipolo, S.; Corni, S. Real-time description of the electronic dynamics for a molecule close to a plasmonic nanoparticle. *J. Phys. Chem. C* **2016**, *120*, 28774−28781.
(96) Marsili, M.; Corni, S. Electronic dynamics of a molecular system coupled to a plasmonic nanoparticle combining the polarizable continuum model and many-body perturbation theory. *J. Phys. Chem. C* **2022**, *126*, 8768−8776.
(97) Coccia, E.; Fregoni, J.; Guido, C.; Marsili, M.; Pipolo, S.; Corni, S. Hybrid theoretical models for molecular nanoplasmonics. *J. Chem. Phys.* **2020**, *153*, No. 200901.
(98) Dall'Osto, G.; Marsili, M.; Vanzan, M.; Toffoli, D.; Stener, M.; Corni, S.; Coccia, E. Peeking into the Femtosecond Hot-Carrier Dynamics Reveals Unexpected Mechanisms in Plasmonic Photocatalysis. *J. Am. Chem. Soc.* **2024**, *146*, 2208−2218.

https://doi.org/10.1021/acs.jpcc.4c04002
J. Phys. Chem. C XXXX, XXX, XXX−XXX

IV. Atomistic Multiscale Modeling of Colloidal Plasmonic Nanoparticles

ACS PHYSICAL CHEMISTRY Au
AN OPEN ACCESS JOURNAL OF THE AMERICAN CHEMICAL SOCIETY

pubs.acs.org/physchemau
Article

Atomistic Multiscale Modeling of Colloidal Plasmonic Nanoparticles

Luca Nicoli, Sveva Sodomaco, Piero Lafiosca, Tommaso Giovannini,* and Chiara Cappelli*

Cite This: https://doi.org/10.1021/acsphyschemau.4c00052
Read Online

ACCESS | Metrics & More | Article Recommendations | Supporting Information

ABSTRACT: A novel fully atomistic multiscale classical approach to model the optical response of solvated real-size plasmonic nanoparticles (NPs) is presented. The model is based on the coupling of the Frequency Dependent Fluctuating Charges and Fluctuating Dipoles (ωFQFμ), specifically designed to describe plasmonic substrates, and the polarizable Fluctuating Charges (FQ) classical force field to model the solvating environment. The resulting ωFQFμ/FQ approach accounts for the interactions between the radiation and the NP, as well as with the surrounding solvent molecules, by incorporating mutual interactions between the plasmonic substrate and solvent. ωFQFμ/FQ is validated against reference TD-DFTB/FQ calculations, demonstrating remarkable accuracy, particularly in reproducing plasmon resonance frequency shifts for structures below the quantum-size limit. The flexibility and reliability of the approach are also demonstrated by simulating the optical response of homogeneous and bimetallic NPs dissolved in pure solvents and solvent mixtures.

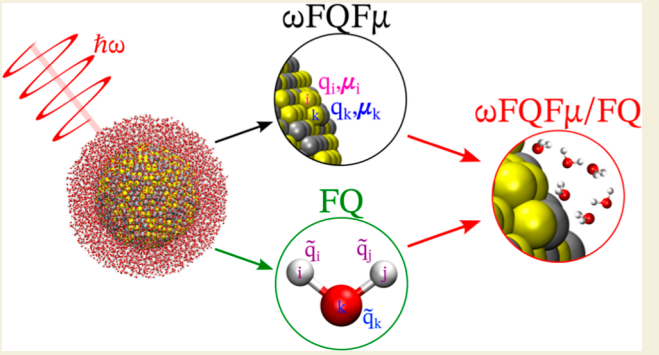

KEYWORDS: *atomistic, solvent effects, silver, gold, alloys, colloids, plasmonics*

1. INTRODUCTION

In the past decades, colloidal nanoparticles (NPs), i.e. NPs dissolved in solution, have gained significant interest due to their applications in many technological contexts, such as sensing,[1] biomedical applications,[2] optoelectronics,[3] and energy conversion.[4] By choosing different precursors, reducing agents, solvents, and capping agents, nanostructured materials can be synthesized with a fine control of shape and size.[5] Size, shape, chemical composition, and the solvent can indeed affect the plasmon resonance frequency (PRF), i.e. the maximum of the NP absorption spectrum.[6] Such a feature is the basis of a particular class of sensors, which exploit the shift of the PRF upon change of the local refractive index (RI) of the solvent in which the plasmonic NPs are dissolved. Such devices have been widely employed in biosensing,[7,8] where maximizing the induced PRF shift as a function of RI is crucial to enhance sensitivity.[1,9]

Rationalizing solvent effects on the PRF of colloidal NPs is particularly challenging from a theoretical point of view. In fact, the optical properties of colloidal NPs result from the interplay of complex phenomena originating under the action of the external electric field, such as the appearance of a localized surface plasmon (LSP) excitation and the polarization of the solvent electron cloud. Solvent effects on PRFs result from a delicate balance between NP-solvent electrostatic (and polarization) interactions, charge-transfer effects, and the possible alteration of the plasmon decaying channels.[10]

In principle, a proper description of all possible NP-solvent effects would require an ab initio treatment of the whole system. However, first principle approaches become rapidly unfeasible due to their unfavorable scaling as a function of the system's size, thus hindering the simulation of realistic systems. For these reasons, commonly exploited theoretical approaches to simulate plasmonic colloidal NPs are rooted in classical physics,[11−15] generally making use of the classical Mie theory,[11] the Boundary Element Method (BEM),[12] the Discrete Dipole Approximation (DDA),[13,16] and the Finite Difference Time Domain (FDTD).[14] However, all these approaches are based on approximated descriptions of both the NP and the solvent, which is generally modeled as a continuum dielectric characterized by its specific permittivity ε. In addition, such approaches do not retain the atomistic nature of the system.

In this paper, we propose a novel multiscale method where both the plasmonic NP and the solvent are treated at full atomistic level. In particular, we employ the fully atomistic electromagnetic model called Frequency Dependent Fluctuating Charges Fluctuating Dipoles (ωFQFμ)[17] to describe the

Received: July 2, 2024
Revised: August 28, 2024
Accepted: August 28, 2024

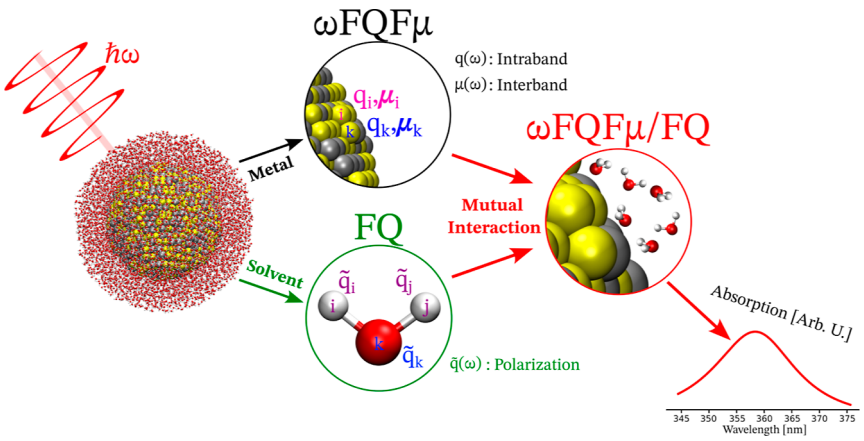

Figure 1. Pictorial view of the multiscale scheme employed to develop ωFQFμ/FQ.

optical response of plasmonic NPs. Such a model is remarkably versatile and can be applied to NPs of any shape[17] and chemical composition,[18] even at the quantum size limit (<5 nm).[17] The solvent is modeled employing the polarizable Fluctuating Charges (FQ) force field,[19−21] which is specifically designed to model the polarization of the electron cloud of molecular systems. For this reason, it has been widely exploited in the context of computational spectroscopy of solvated systems.[22−25]

The two approaches, ωFQFμ and FQ, are coupled in a multiscale fashion so that the resulting ωFQFμ/FQ model accounts for the mutual electrostatic interaction between the solvent and the plasmonic NP, allowing for the modeling of the optical properties of generic colloidal plasmonic NPs. ωFQFμ/FQ is also coupled to classical molecular dynamics (MD) simulations, which are exploited to sample the NP-solvent phase space. Therefore, differently from previous methods,[11−14] the dynamical aspects of the solvation phenomenon, which are crucial to properly model solvent effects on spectroscopy, are taken into account.[22,24,26]

Note that, if solvent molecules are not adsorbed on the surface of the NP, the main solvent effect on plasmonic properties is the local RI variation of the medium surrounding the nanomaterial. This leads to a modification of the local optical field, generally causing a PRF redshift.[10,27] Such effect is harnessed in many colorimetric-sensors for the detection of specific biomolecular analytes.[7,8,11,28−35] In this work, we model the physical processes that lead to plasmon shift upon change of the local RI of the embedding medium.

The paper is organized as follows: first, the novel ωFQFμ/FQ approach is presented after the theoretical foundations of ωFQFμ and FQ methods are recalled. Then, the computational protocol is presented and ωFQFμ/FQ is validated in comparison with reference Time-Dependent Density Functional Tight Binding/Fluctuating Charges (TD-DFTB/FQ[36]) results. The versatility and robustness of the approach are demonstrated by studying real-size homogeneous and bimetallic NPs dissolved in pure solvent or solvent mixtures. A summary and the main conclusions of the work end the manuscript.

2. METHODS

2.1. Theoretical Model

In this section, ωFQFμ and FQ are briefly recalled and the ωFQFμ/FQ approach for modeling the optical properties of colloidal plasmonic NPs is presented (see Figure 1).

2.1.1. Plasmonic Nanoparticle: the Atomistic-Electromagnetic ωFQFμ Model. ωFQFμ models the plasmonic NP atomistically. Each atom is endowed with a set of complex frequency-dependent atom-centered charges $\mathbf{q}(\omega)$ (ωFQs), and dipoles $\boldsymbol{\mu}(\omega)$ (ωFμs) (see Figure 1), accounting for intraband and interband mechanisms, respectively. Charges are obtained by solving the following equation of motion, obtained by modulating a Drude-like conduction mechanics with quantum tunneling[37,38]

$$-i\omega q_i(\omega) = \sum_j \left(\frac{A_j n_j (1 - f_{ji}(l_{ij}))}{1/\tau_j - i\omega} + \frac{A_i n_i (1 - f_{ij}(l_{ij}))}{1/\tau_i - i\omega} \right) \frac{\phi_i(\omega) - \phi_j(\omega)}{l_{ij}} \quad (1)$$

In eq 1 A_i, n_i, and τ_i are the atomic effective area, the electron density, and the relaxation time associated with the intraband scattering events of the i-th atom, respectively. Quantum tunneling effects are expressed in terms of a Fermi-like damping function $f_{ij}(l_{ij})$, which exponentially damps the charge exchange between the atoms (l_{ij} is the distance between i-th and j-th atoms). $\phi_i(\omega)$ is the chemical potential of i-th atom, which reads

$$\phi_i(\omega) = V_i^q(\omega) + V_i^\mu(\omega) + V_i^{ext}(\omega) \quad (2)$$

where V_i^{ext} is the electric potential associated with the optical radiation, whereas V_i^q and V_i^μ are the electric potentials induced by charges and dipoles on the i-th atomic site (see ref 17 for more details).

The plasmonic properties of alkali metals and graphene in the Pauli-blocking regime are correctly described by ωFQs which properly models intraband mechanisms.[37−40] However, when the interband absorption energy threshold is comparable to the plasmon resonance frequency (PRF), such as in noble metal nanoparticles, interband transitions become relevant to the decaying mechanism.[41] To model this process, an additional complex frequency-dependent dipole $\boldsymbol{\mu}(\omega)$ is assigned to each atom

$$\boldsymbol{\mu}_i(\omega) = \alpha_i^{IB}(\omega)\mathbf{E}_i^{tot}(\omega) \quad (3)$$

$$\boldsymbol{\mu}_i(\omega) = \alpha_i^{IB}(\omega)[\mathbf{E}_i^q(\omega) + \mathbf{E}_i^\mu(\omega) + \mathbf{E}_i^{ext}(\omega)] \quad (4)$$

where $\alpha_i^{IB}(\omega)$ is the interband frequency-dependent polarizability of the i-th atom, and $\mathbf{E}_i^{tot}(\omega)$ is the total electric field acting on the i-th dipole, accounting for charge−dipole ($\mathbf{E}^q$), dipole−dipole ($\mathbf{E}^\mu$), and

https://doi.org/10.1021/acsphyschemau.4c00052
ACS Phys. Chem Au XXXX, XXX, XXX−XXX

dipole-field ($\mathbf{E}^{\mathrm{ext}}$) interactions (see ref 17 for more details). For homogeneous materials, $\alpha_i^{\mathrm{IB}}(\omega)$ is determined from the frequency-dependent bulk-permittivity, whereas in the case of multimetallic systems, the interband polarizability of the i-th atom is expressed as a function of the local composition of the system.[17,18]

The ωFQFμ charge−dipole coupled equations can be recast in the following set of complex linear equations

$$\begin{pmatrix} \mathbf{A}(\omega)\mathbf{T}^{\mathrm{qq}} - \mathbf{Z}(\omega) & \mathbf{A}(\omega)\mathbf{T}^{\mathrm{q}\mu} \\ \mathbf{T}^{\mu\mathrm{q}} & \mathbf{T}^{\mu\mu} - \mathbf{Z}^{\mathrm{IB}}(\omega) \end{pmatrix} \begin{pmatrix} \mathbf{q} \\ \boldsymbol{\mu} \end{pmatrix} = \begin{pmatrix} -\mathbf{A}(\omega)\mathbf{V}^{\mathrm{ext}} \\ -\mathbf{E}^{\mathrm{ext}} \end{pmatrix} \tag{5}$$

where $\mathbf{A}(\omega)$ is a frequency-dependent matrix containing NP chemical and geometrical parameters, while $\mathbf{Z}(\omega)$, and $\mathbf{Z}^{\mathrm{IB}}(\omega)$ are diagonal matrices. $\mathbf{T}^{\mathrm{qq}}$, $\mathbf{T}^{\mathrm{q}\mu}$, $\mathbf{T}^{\mu\mathrm{q}}$ and $\mathbf{T}^{\mu\mu}$ are charge−charge, charge−dipole, dipole-charge, and dipole−dipole interaction kernels, respectively (see ref 42 for more details).

When the linear system in eq 5 is solved, charges and dipoles modeling the optical intra- and interband response of the plasmonic NP are obtained. From such variables, the NP complex polarizability and the absorption cross-section $\sigma^{\mathrm{abs}}(\omega)$ can be computed (see refs 17 and 18 for further details about the ωFQFμ model).

2.1.2. Solvent: the Fluctuating Charges Model (FQ). The physics governing the optical response of solvent systems is utterly different from that of plasmonic materials. When external electric fields are applied, solvent molecules might experience several phenomena ranging from electronic transitions to molecular rovibrations depending on the external field frequency. In the following, we focus only on solvents that are transparent in the spectral region where the plasmonic nanostructure absorbs light. Note that this is generally the case for noble metal nanoparticles, whose PRF falls within the visible range (400−700 nm).[43,44] In this way, the external fields exciting the plasmons have energies lower than those of the electronic transitions of the solvent molecules but sufficiently high to quench rovibrational effects completely. Thus, the interaction with the external field only yields the polarization of the solvent's electron cloud. This is modeled by using the Fluctuating Charges (FQ) force field,[19−21] which has been extensively used in computational quantum chemistry for the modeling of molecules in solution.[22,24,45] Within FQ, each solvent atom is endowed with a charge $\tilde{\mathbf{q}}$ whose value is not fixed but can vary as a response to the external electric potential (see Figure 1). Such charge fluctuation is governed by the electronegativity equalization principle (EEP),[46,47] which states that at equilibrium, each atom has the same electronegativity, i.e. the negative of the chemical potential, as reported by Parr.[48] The FQ energy, i.e. the energy required to create a partial charge on each atom is generally written as a second-order Taylor expansion in the charges. For a polyatomic system, this can be written as[19]

$$U(\tilde{\mathbf{q}}) = \sum_{\alpha,i} \left(\chi_{\alpha i}\tilde{q}_{\alpha i} + \frac{1}{2}\eta_{\alpha i}\tilde{q}_{\alpha i}^{\,2} + \tilde{V}_{\alpha i}^{\mathrm{tot}}\tilde{q}_{\alpha i} \right) + \sum_{\beta,k<\alpha,i} \tilde{q}_{\beta k} T_{\beta k,\alpha i}^{\tilde{q}\tilde{q}} \tilde{q}_{\alpha i} \tag{6}$$

where Greek and Roman indices run over molecules and atoms, respectively. $\chi_{\alpha i}$ is the electronegativity of the i-th atom of the α-th molecule, and $\mathbf{T}^{\tilde{q}\tilde{q}}$ is the charge−charge interaction kernel[42] of which the diagonal elements $\eta_{\alpha i}$ are chemical hardnesses, representing self-interaction polarization term. Both electronegativity and chemical hardness are well rooted in Conceptual Density Functional Theory[49] and are the only free parameters defining the model. Moreover, $\tilde{\mathbf{V}}^{\mathrm{tot}}$ is the total external electric potential on each atomic site, which in the FQ case is the potential associated with the external optical field ($\tilde{\mathbf{V}}^{\mathrm{tot}} = \tilde{\mathbf{V}}^{\mathrm{ext}}$). To constrain the charge of each molecule Q_α^{tot} to a constant, a set of Lagrange multipliers λ_α is exploited. The energy functional in eq 6 thus becomes

$$F(\tilde{\mathbf{q}}, \boldsymbol{\lambda}) = U(\tilde{\mathbf{q}}) + \sum_\alpha \lambda_\alpha \left(\sum_i (\tilde{q}_{\alpha i}) - Q_\alpha^{tot} \right) \tag{7}$$

From the minimization of eq 7 with respect to the variables ($\tilde{\mathbf{q}}$ and $\boldsymbol{\lambda}$), the FQ polarization equations are obtained, implying that the electronic degrees of freedom of the solvent instantaneously rearrange without energy dissipation.[19] Such an approximation is also valid for optical fields in the visible range and for transparent solvents.[22,23,S0] When the total electric field is monochromatic at frequency ω, the FQ polarization equations in the frequency domain read as follows (see Section S1.1 in the Supporting Information, for further details)

$$\begin{pmatrix} \mathbf{T}^{\tilde{q}\tilde{q}} & \mathbf{1} \\ \mathbf{1}^t & \mathbf{0} \end{pmatrix} \begin{pmatrix} \tilde{\mathbf{q}}(\omega) \\ \boldsymbol{\lambda}(\omega) \end{pmatrix} = \begin{pmatrix} -\tilde{\mathbf{V}}^{\mathrm{ext}}(\omega) \\ 0 \end{pmatrix} \tag{8}$$

where $\mathbf{1}$ is a rectangular matrix containing the blocks associated with the Lagrange multipliers. By solving eq 8, the atom-centered FQ charges, modeling the instantaneous polarization of the electronic cloud of the solvent under the application of an external monochromatic field, are obtained.

2.1.3. Optical Response of a Plasmonic Nanoparticle in Solution: The ωFQFμ/FQ Model. ωFQFμ for describing the nanostructure's response and FQ for modeling solvent polarization are coupled in a multiscale fashion. In the resulting ωFQFμ/FQ approach, mutual polarization effects between the solvent and the metal NP are introduced (see Figure 1). To this end, we include the solvent-induced electric potential $\mathbf{V}^{\tilde{q}}(\omega)$ and electric field $\mathbf{E}^{\tilde{q}}(\omega)$ acting on the NP's charges $\mathbf{q}(\omega)$ and dipoles $\boldsymbol{\mu}(\omega)$ respectively. Thus, the total chemical potential and field (eq 2 and eq 4, respectively) acting on each atomic site now read

$$\phi_i(\omega) = V_i^q(\omega) + V_i^\mu(\omega) + V_i^{\tilde{q}}(\omega) + V_i^{\mathrm{ext}}(\omega) \tag{9}$$

$$\mathbf{E}_i^{\mathrm{tot}}(\omega) = \mathbf{E}_i^q(\omega) + \mathbf{E}_i^\mu(\omega) + \mathbf{E}_i^{\tilde{q}}(\omega) + \mathbf{E}_i^{\mathrm{ext}}(\omega) \tag{10}$$

The electric potential and field induced by the FQ solvent charges $\tilde{\mathbf{q}}(\omega)$ on the NP's atomic sites read

$$V_i^{\tilde{q}}(\omega) = \sum_{\alpha,k} T_{i,\alpha k}^{q\tilde{q}} \tilde{q}_{\alpha k}(\omega) \tag{11}$$

$$\mathbf{E}_i^{\tilde{q}}(\omega) = \sum_{\alpha,k} \mathbf{T}_{i,\alpha k}^{\mu\tilde{q}} \tilde{q}_{\alpha k}(\omega) \tag{12}$$

$\mathbf{T}^{q\tilde{q}}$ and $\mathbf{T}^{\mu\tilde{q}}$ are the Coulomb interaction kernels between the FQ solvent charges and ωFQFμ plasmonic charges and dipoles respectively, i.e.

$$T_{ij}^{q\tilde{q}} = \frac{1}{|\mathbf{r}_{ij}|} \tag{13}$$

$$\mathbf{T}_{ij}^{\mu\tilde{q}} = \nabla_{r_i} T_{ij}^{q\tilde{q}} \tag{14}$$

where $\mathbf{r}_{ij}$ is the distance between atoms i and j.

To account for mutual polarization effects, the total potential $\tilde{\mathbf{V}}^{\mathrm{tot}}$ acting on the solvent atomic sites includes the potential generated by the NP's charges $\tilde{\mathbf{V}}^q(\omega)$ and dipoles $\tilde{\mathbf{V}}^\mu(\omega)$

$$\tilde{V}_{\alpha i}^{\mathrm{tot}}(\omega) = \tilde{V}_{\alpha i}^q(\omega) + \tilde{V}_{\alpha i}^\mu(\omega) \tag{15}$$

where the electric potential and field induced by the ωFQFμ charges and dipoles on the i-th solvent atom of the α-th molecule read

$$\tilde{V}_{\alpha i}^q(\omega) = \sum_k T_{\alpha i,k}^{\tilde{q}q} q_k(\omega) \tag{16}$$

$$\tilde{V}_{\alpha i}^\mu(\omega) = \sum_k \mathbf{T}_{\alpha i,k}^{\tilde{q}\mu} \boldsymbol{\mu}_k(\omega) \tag{17}$$

Note that in eq 15 we neglect local field effects (i.e., $\tilde{V}_{\alpha i}^{\mathrm{ext}}(\omega) = 0$). The coupled ωFQFμ and FQ equations can thus be recast in a linear system defining the ωFQFμ/FQ master equations

https://doi.org/10.1021/acsphyschemau.4c00052
ACS Phys. Chem Au XXXX, XXX, XXX−XXX

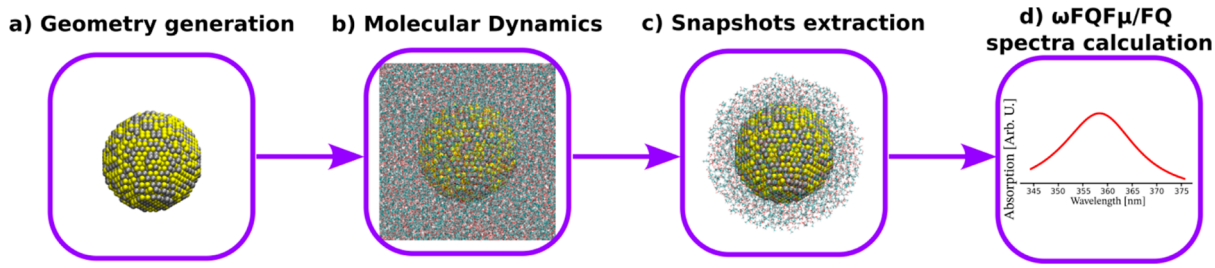

Figure 2. Graphical scheme of the computational protocol employed to compute ωFQFμ/FQ absorption spectra of colloidal plasmonic NPs (see also Sections S2.1, S2.2, S2.4, and S2.3 in the Supporting Information).

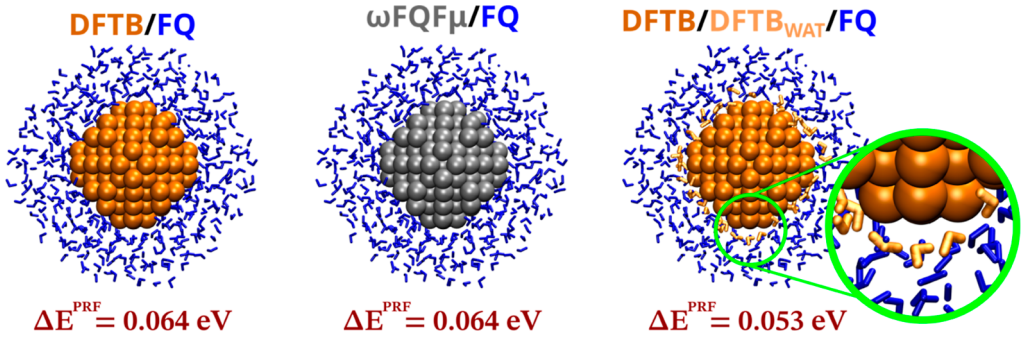

Figure 3. Vacuo-to-water PRF shifts (in eV) computed by using DFTB/FQ, ωFQFμ/FQ, and DFT/DFTB$_{WAT}$/FQ levels of theory. A graphical depiction of the structure used for each calculation is presented and the elements are colored according to the level of theory used (orange-DFTB, gray-ωFQFμ, blue-FQ). In the green inset a zoom of the DFTB/DFTB$_{WAT}$/FQ structure is reported to highlight the presence of water molecules treated at the DFTB level of theory (orange).

$$\begin{pmatrix} \mathbf{A}(\omega)\mathbf{T}^{qq} - \mathbf{Z}(\omega) & \mathbf{A}(\omega)\mathbf{T}^{q\mu} & \mathbf{A}(\omega)\mathbf{T}^{q\tilde{q}} & \mathbf{0} \\ \mathbf{T}^{\mu q} & \mathbf{T}^{\mu\mu} - \mathbf{Z}^{IB}(\omega) & \mathbf{T}^{\mu\tilde{q}} & \mathbf{0} \\ \mathbf{T}^{\tilde{q}q} & \mathbf{T}^{\tilde{q}\mu} & \mathbf{T}^{\tilde{q}\tilde{q}} & \mathbf{1} \\ \mathbf{0} & \mathbf{0} & \mathbf{I}^{t} & \mathbf{0} \end{pmatrix} \begin{pmatrix} \mathbf{q} \\ \boldsymbol{\mu} \\ \tilde{\mathbf{q}} \\ \lambda \end{pmatrix} = \begin{pmatrix} -\mathbf{A}(\omega)\mathbf{V}^{ext}(\omega) \\ -\mathbf{E}^{ext}(\omega) \\ 0 \\ 0 \end{pmatrix} \tag{18}$$

By solving eq 18, the charges and dipoles defining the response of the nanostructure as modified by the presence of the solvent are obtained. This allows the simulation of the optical response of plasmonic substrates with arbitrary shape and chemical composition embedded in a generic solvent or solvent mixture (see Section S1.2 in the Supporting Information).

2.2. Computational Protocol

In this work, we apply ωFQFμ/FQ to the calculation of the absorption cross-section of plasmonic nanoparticles in solution. To reproduce the experimental PRF shift induced by solvent effects, the dynamic nature of the solvation phenomena needs to be properly described. To this end, we adapt the protocol designed for molecular systems in solution[22] to the specific case of colloidal plasmonic NPs.

The protocol can be divided into four main steps (see Figure 2).

2.2.1. Geometry Generation. The geometry of isolated plasmonic NPs is generated by using an in-house code that employs the Atomic Simulation Environment (ASE) Python module v. 3.17[51] (see Figure 2a and Section S2.1 in the Supporting Information).

2.2.2. Molecular Dynamics. The nanostructure is solvated. To sample the NP-solvent phase-space, we perform a classical Molecular Dynamics (MD) simulation of the solvated colloidal system by using the GROMACS software package (version 2020.4) and a suitable force-field[52] (see Figure 2b and Section S2.2 in the Supporting Information).

2.2.3. Extraction of Structures. From the MD trajectory, we extract 25 uncorrelated representative structures of the whole system. The number of structures ensures convergence of the spectral signal (see Section S2.4.2 in the Supporting Information). For each structure, we retain all solvent molecules that are at most 15 Å from the NP surface, resulting in a spherical droplet (see Figure 2c and Section S2.4.1 in the Supporting Information).

2.2.4. ωFQFμ/FQ Spectral Calculations. For each spherical droplet, absorption cross sections are computed at the ωFQFμ/FQ level. The overall spectroscopic response is then recovered as the average over all structures (see Figure 2d and Section S2.3 in the Supporting Information). All ωFQFμ/FQ calculations are performed by employing a stand-alone Fortran 95 package.

3. RESULTS AND DISCUSSION

In this section, ωFQFμ/FQ is applied to compute the absorption properties of noble metal NPs in solution. First, the model is validated by reproducing reference data. Then, it is employed to study solvent effects on realistic homogeneous and bimetallic NPs dissolved in a pure solvent or a solvent mixture, showcasing the potential and flexibility of the approach.

3.1. Model Validation

The ωFQFμ/FQ approach is validated against vacuo-to-water PRF shifts of a small silver spherical-like cluster composed of 164 atoms (Ag_{164}). ωFQFμ/FQ values are compared to polarizable Time-Dependent Density Functional Tight Binding/Fluctuating Charges (TD-DFTB/FQ) calculations.[36] The advantageous computational scaling of TD-DFTB/FQ, which is reached through the approximation of two-electron interactions, makes it capable of handling larger systems than Time-Dependent Density Functional Theory-based methods (TD-DFT) while preserving accuracy.[36] The initial geometry of Ag_{164} is taken from ref 53: from that structure, MD

https://doi.org/10.1021/acsphyschemau.4c00052
ACS Phys. Chem Au XXXX, XXX, XXX−XXX

simulations in aqueous solution are run, a single random snapshot is extracted and cut in a spherical droplet containing water (WAT) molecules within 10 Å from the surface of the NP, resulting in a total number of 807 water molecules. Such distance is chosen to account for the most relevant NP-water interactions (see Section S2.4.1 in the Supporting Information). The absorption spectrum of Ag_{164} in vacuo (i.e., by removing all water molecules from the snapshot) and in aqueous solution (Ag_{164}/WAT_{807}) are computed by using ωFQFμ and DFTB, and ωFQFμ/FQ and DFTB/FQ, respectively (see Section S2.5 in the Supporting Information for more details on the DFTB/FQ calculations). To evaluate quantum effects at the NP-solvent interface, we also performed DFTB/DFTB$_{WAT}$/FQ calculations, where the first solvation shell is treated at the DFTB level of theory (109 water molecules), whereas the remaining 698 WAT molecules are described at the FQ level. ωFQFμ parameters are recovered from ref 17. The FQ WAT molecules are modeled by using the parameters reported in ref 19 (WAT_1, see Table S1 in Section S2.3 in the Supporting Information). Note that additional calculations were performed by using the FQ parameters reported in refs 54−56 (see Section S3 in the Supporting Information).

In Figure 3, we report the PRF shifts ($\Delta E^{PRF} = E^{VAC} - E^{WAT}$) in eV calculated at the DFTB/FQ level (panel A), ωFQFμ/FQ (panel B), and DFTB/DFTB$_{WAT}$/FQ (panel C).

All methods predict a very similar vacuo-to-water PRF redshift. The sign of the shift is expected due to the increase of the refractive index of the NP surrounding medium, as also supported by experimental observations.[57,58] Notably, the hybrid DFTB/FQ and the fully classical ωFQFμ/FQ approaches predict the same solvatochromic shift (64 meV). This is particularly remarkable because the dimension of the studied NP falls within the quantum size region, where quantum effects are expected to play a major role. Our results highlight the accuracy of ωFQFμ in describing such structures.[59] When the first solvation shell of water molecules is described at the DFTB level (DFTB/DFTB$_{WAT}$/FQ), the predicted solvatochromic shift decreases by ∼10 meV (53 meV). Such reduction can be attributed to the inclusion of purely quantum NP-solvent interactions, mainly related to Pauli repulsion effects,[36,60,61] which are not taken into account by both DFTB/FQ and ωFQFμ/FQ. Remarkably, the computational cost associated with ωFQFμ/FQ is negligible as compared to DFTB-based methods (see Table S4 in the Supporting Information). Indeed, the favorable computational scaling of ωFQFμ/FQ provides a substantial 99.4% speed-up of the calculation with respect to DFTB/FQ, thus representing an effective, reliable, and cost-effective alternative to state-of-the-art ab initio methods.

3.2. Homogeneous Colloidal NPs

The favorable computational scaling of ωFQFμ/FQ opens up to computing the plasmonic response of large NPs in solution. We first consider homogeneous silver and gold spherical NPs (diameter = 5 nm, 3851 atoms) in aqueous solution, as modeled by using the WAT_1 parametrization.[19] The average number of WAT molecules in the FQ region is 6464 (19,392 atoms). Computed absorption cross sections both in vacuo (VAC) and in water (WAT) are plotted in Figure 4A,B, respectively, together with the corresponding vacuo-to-water PRF shifts ($\Delta\lambda$, in nm). The spectra of both systems are characterized by a main plasmonic band centered at about 360 nm (Ag NPs) and 570 nm (Au NPs). Au peaks are broader than Ag bands, in agreement with previous observations.[62,63] In the studied region (300−800 nm), the spectra of Au systems are also characterized by the presence of a broad and intense band associated with interband absorption.[17] When dissolved in solution, the main spectral features are maintained. However, we note that the plasmonic peak increases in intensity and slightly redshifts, in line with experimental data.[9,57,58,64] For Ag, ωFQFμ/FQ predicts a red-shift of the plasmonic peak larger than Au NPs, again in agreement with experiments.[9,57,58,64] Such shift is due to the refractive index sensitivity (RIS) of the LSP, a quantity that is commonly exploited in plasmonic colorimetric sensors.[30,31,65,66] RIS is generally expressed as $\Delta\lambda$ (in nm) over refractive index unit—$\Delta\lambda$(nm)/RIU.

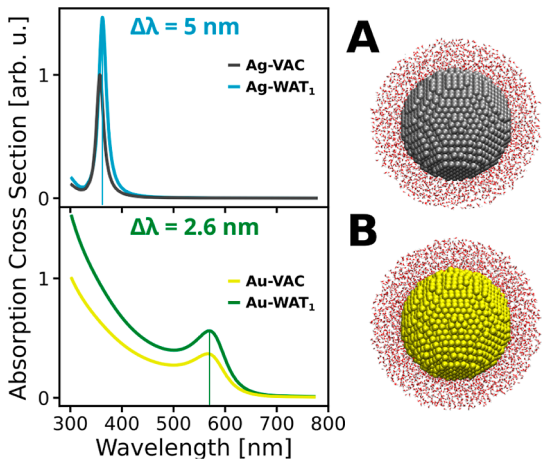

Figure 4. ωFQFμ/FQ absorption spectra of (A) Ag_{3851} and (B) Au_{3851} in vacuo (VAC) and water (WAT_1). $\Delta\lambda$ is the vacuo-to-water solvatochromic shift in nm. All spectra are normalized to the corresponding maximum in vacuo.

The computed ωFQFμ/FQ RIS values are 15.0 nm/RIU for Ag and 7.9 nm/RIU for Au, while the experimentally measured RIS are 120−160 nm/RIU (Ag) and 70 nm/RIU (Au).[30,31,65,66] Therefore, ωFQFμ/FQ absolute RIS values are systematically lower than experimental ones for Ag and Au NPs, however ωFQFμ/FQ can nicely reproduce the experimental Ag/Au ratio (∼2). The discrepancy can be related to the FQ parameters employed for modeling water, which have not been specifically tuned to describe solvated NPs.[19] Nevertheless, although experimental absolute RIS values are underestimated by a factor of 10, the capability of ωFQFμ/FQ to match the Ag/Au sensitivity ratio is a remarkable feature of the model, which can be used to rationalize the optical behavior of plasmonic nanostructures with high RIS, with potential applications in sensor design.

3.3. Au@Ag core−shell Colloidal NPs

By taking advantage of the favorable computational scaling of ωFQFμ/FQ, its atomistic nature, and its capability of correctly reproducing Ag/Au RI sensitivity ratio, the model is challenged to optimize the sensitivity of Au@Ag core−shell spherical NPs. In fact, colorimetric sensors exploiting the PRF shift of noble metals upon change of the local refractive index (RI) are widely used in biosensing.[7,8,11,28−35] Among the various substrates used for this technology, gold−silver core−shell (Au@Ag) NPs are the most employed[67−72] due to their high RIS.[11,72] By studying such structures, we aim to showcase the

https://doi.org/10.1021/acsphyschemau.4c00052
ACS Phys. Chem Au XXXX, XXX, XXX−XXX

potentialities of ωFQFμ/FQ, open up to colorimetric LSP sensor design.

We first consider spherical Au@Ag core−shell NPs (diameter = 5 nm, 3851 atoms) characterized by an Au core of increasing size (d_{Au} = 2, 3, and 4 nm−see Figure 5A−C), in

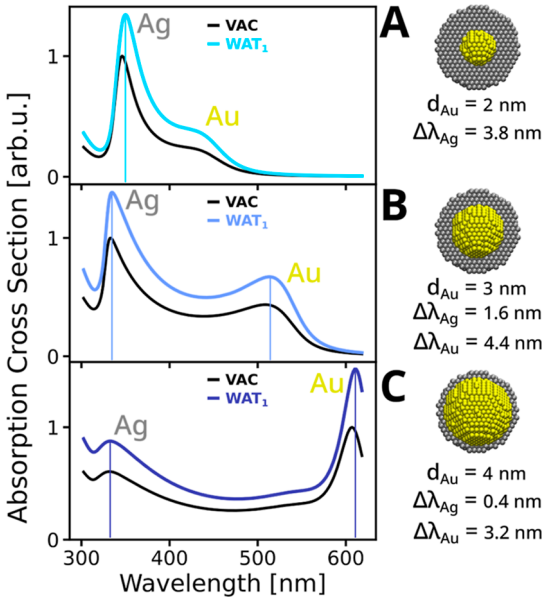

Figure 5. ωFQFμ/FQ absorption spectra of core−shell Au@Ag spherical NPs in vacuo (VAC) and in aqueous solution (WAT_1) as a function of the diameter of the Au core (d_{Au}: (A) 2.0 nm, (B) 3.0 nm and (C) 4.0 nm). The solvatochromic shifts of "Ag" ($\Delta\lambda_{Ag}$) and "Au" ($\Delta\lambda_{Au}$) peaks are reported in nm. All spectra are normalized to the maximum in vacuo.

aqueous solution. To sample the NP-solvent phase space, we perform a classical MD simulation of a single Ag NP in the aqueous solution. We then construct the Ag@Au core−shell bimetallic NP by properly substituting the metal atoms after the MD snapshot's extraction, which is a physically consistent procedure due to the almost equal lattice constants of the two metals.[73] On average, 6464 water molecules are considered in the FQ region and modeled employing the WAT_1 parametrization.[19]

In Figure 5, ωFQFμ/FQ absorption spectra of Au@Ag core−shell NPs in vacuo (black) and water (blue) are reported. For all structures, absorption spectra in vacuo and solution feature two main bands at short (∼350 nm) and long wavelengths (>400 nm), in agreement with previous theoretical and experimental observations.[11,12,74,75] Such peaks are located in the spectral region of the plasmon bands of pure Ag and Au spheres (see Figure 4A,B). For this reason, we call them "Ag" and "Au" peaks, respectively. Their position and intensity strongly depend on the diameter of the Au core both in the gas phase and solution. In particular, by first focusing on vacuo results, for Au-core thickness of 1 nm (Figure 5A), the "Ag" peak, located around 346 nm, dominates the computed spectrum, while the "Au" band appears as a shoulder. By increasing the Au-core size, the "Ag" peak slightly blueshifts of about 10 nm while decreasing in intensity. On the contrary, the "Au" peak largely redshifts of about 150 nm, and significantly increases in intensity, becoming dominant for Au-core diameters of 4 nm (1 nm Ag-shell thickness). Including the solvent redshifts both "Ag" and "Au" peaks and increases their intensity. The shift differs for each peak and each Au-core diameter. In particular, all "Ag" peaks show lower solvatochromic shifts as compared to pure Ag spheres ($\Delta\lambda$ = 5.0 nm see Figure 4A), and increasing the Au-core size reduces the redshift of the "Ag" peak from $\Delta\lambda_{Ag}$ = 3.8 nm (d_{Au} = 2 nm) to $\Delta\lambda_{Ag}$ = 0.4 nm (d_{Au} = 4 nm). The shift of the "Au" peak is generally larger (e.g., $\Delta\lambda_{Au}$ = 4.4 nm for d_{Au} = 2 nm) than that of a pure Au sphere ($\Delta\lambda$ = 2.6 nm, see Figure 4B). This suggests that for small NPs ($d \sim 5$ nm), the "Au" peak RIS can be increased by coating the NP with an Ag layer. Remarkably, our findings align with previous theoretical and experimental observations.[11,69,72]

To showcase more potentialities of ωFQFμ/FQ, we now move to study the effect of alloying the Ag shell on the refractive index sensitivity, for which an atomistic picture is essential.[18] Note that, to the best of our knowledge, the use of atomistic modeling in this field has received only a little attention.[11,12,76]

We consider a substantially more complex system composed of a spherical Au@Ag core−shell bimetallic NP (see Figure 6)

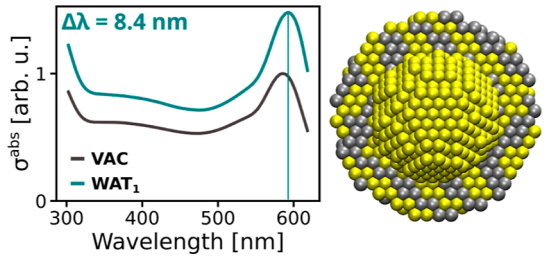

Figure 6. ωFQFμ/FQ absorption cross section (σ^{abs}) of core−shell Au@Ag spherical NP with an Au core diameter of 3 nm and featuring an alloyed (50% Au/Ag) external layer of 1 nm (see right panel) in vacuo (VAC) and aqueous solution (WAT_1). $\Delta\lambda$ indicates the solvatochromic shift (in nm). All spectra are normalized to the maximum in vacuo.

of 5 nm of diameter (3851 atoms) with an Au core of diameter (d_{Au}) of 3 nm, and featuring a 50% Ag 50%Au random bimetallic layer of 1 nm. Such NP is solvated in aqueous solution, exploiting the same procedure discussed above. Figure 6, shows computed ωFQFμ/FQ absorption cross-section (σ^{abs}) both in vacuo and water. The computed spectrum substantially deviates from the corresponding perfect core−shell system (Figure 5B). In fact, the "Au" peak is shifted at higher wavelengths (∼600 nm) and dominates the spectrum, while the "Ag" peak disappears in a dim spectral feature between 350 and 500 nm. Remarkably, the computed PRF shift of the gold peak ($\Delta\lambda_{Au}$) is 8.4 nm, almost double the original Au@Ag core−shell structure ($\Delta\lambda_{Au}$ = 4.4 nm, see Figure 5B), and more than three times than a pure Au sphere of the same dimensions ($\Delta\lambda$ = 2.6 nm, see Figure 4). Remarkably, the same trend is also obtained for the computed ωFQFμ/FQ RIS sensitivity, which reaches 25.5 nm/RIU. The obtained results thus suggest that the alloying of the Ag shell of an Au@Ag core−shell can potentially improve the refractive index sensitivity of the system by almost a factor of 2.

To finally showcase the flexibility of ωFQFμ/FQ, we solvate the NP in a 1:1 water−ethanol mixture (WAT-ETH). The even more complex chemical nature of this system enforces the need for a fully atomistic model to simulate its optical properties. To the best of our knowledge, ωFQFμ/FQ is the first fully atomistic model capable of calculating the response of

https://doi.org/10.1021/acsphyschemau.4c00052
ACS Phys. Chem Au XXXX, XXX, XXX−XXX

a generic multimetallic plasmonic NP embedded in a multicomponent solvent.

To sample the NP-solvent phase space, we perform a classical MD simulation of a single Ag NP in the WAT-ETH mixture. We then construct the Ag@Au core−shell bimetallic NP by properly substituting the metal atoms after the MD snapshot extraction. The FQ parametrization employed for the water molecules is WAT_1, while for ethanol we exploit the parameters proposed in ref 56 (see Table S1 in the Supporting Information). On average 1800 ETH and 1218 WAT molecules are included in the spherically shaped snapshot (i.e., 19,854 atoms in total).

In Figure 7, the absorption spectrum of the complex bimetallic Au/Ag NP both in vacuo (VAC) and solvated in the

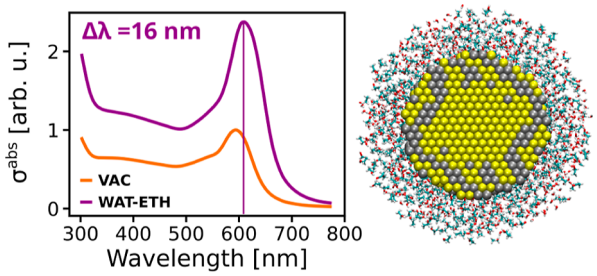

Figure 7. ωFQFμ/FQ absorption cross section (σ^{abs}) of core−shell Au@Ag spherical NP with an Au core diameter of 3 nm and featuring an alloyed (50% Au/Ag) external layer of 1 nm (see right panel) in vacuo (VAC) and a 1:1 water−ethanol mixture (WAT-ETH). The vacuo-to-mixture solvatochromic shift is given in nm. All spectra are normalized to the maximum in vacuo.

1:1 water−ethanol mixture (WAT-ETH) is graphically depicted, together with the corresponding computed PRF shift ($\Delta\lambda$ in nm). Notably, absorption spectra both in vacuo and in solution present a sharp peak around 600 nm which can be assigned to the Au plasmonic dipolar band, and a shoulder at about 350−400 nm associated with the Ag plasmonic absorption. Solvent effects provided by the WAT-ETH mixture lead to a huge enhancement of the peak absorption (almost twice that in vacuo), which is also red-shifted by 16 nm. Considering a refractive index for the WAT-ETH mixture of 1.36,[77] a computed RIS of about 44.0 nm/RIU is obtained. Such a value is almost twice that obtained in pure water, highlighting a nontrivial RIS dependence on the solvent composition.

4. SUMMARY AND CONCLUSIONS

We have presented a novel fully atomistic multiscale classical model, named ωFQFμ/FQ, which is capable of simulating the optical properties of real-size plasmonic colloidal nanoparticles (NPs) of a generic chemical nature. ωFQFμ/FQ is a multiscale model based on the mutual electrostatic interaction between the solvent and the NP. More specifically, the interaction of the plasmonic substrate with the external optical field is modeled employing ωFQFμ,[17,18] where each atom is endowed with a frequency-dependent charge and dipole, modeling intraband and interband plasmon decaying mechanisms, respectively. The solvent environment is considered transparent to the optical radiation and its instantaneous polarization is modeled through the polarizable FQ force field.[19−21]

ωFQFμ/FQ has been challenged to reproduce reference TD-DFTB/FQ values, showing an almost perfect match with the TD-DFTB/FQ vacuo-to-water plasmon resonance frequency (PRF) shift of a small silver cluster (Ag_{164}), with a substantial 99.4% speed-up of the calculation. Then, we have showcased the capabilities of ωFQFμ/FQ by simulating the optical properties of real-size homogeneous Ag and Au spherical NPs (∼5 nm of diameter, 3851 metal atoms with 6464 water molecules), highlighting how the computed ratio between the refractive index sensitivities of Au and Ag NPs matches the experiments. Remarkably, ωFQFμ/FQ can also be used to study the sensitivity of colorimetric LSP sensors, as demonstrated by the chemical substitution of Au atoms in Au@Ag core−shell NPs, which can potentially enhance the sensitivity by a factor 2−3. Finally, the flexibility of ωFQFμ/FQ is validated by simulating the absorption spectrum of a bimetallic Ag/Au NP solvated in a 1:1 water−ethanol mixture. Remarkably, the model can be applied to any solvent or solvent mixtures, including green solvents,[78] pending a reliable parametrization of the FQ force field.[56] Our results are particularly promising; however, it is important to mention that ωFQFμ/FQ have been validated on a small data set, due to the limited computational studies dealing with colloidal plasmonic nanostructures.

It is worth noting that, in ωFQFμ/FQ, the nanostructure-solvent interactions are limited to electrostatics and polarization. Thus, purely quantum effects, such as Chemical Interface Damping (CID)[10,79,80] or Pauli repulsion effects, are neglected. However, for noncovalently bonded molecules, as in the case of solvents, CID effect on plasmonic response is generally negligible.[79,81] The extension of ωFQFμ/FQ to consider CID effects will be the topic of future communications.

In conclusion, ωFQFμ/FQ is the first fully atomistic classical model capable of providing a platform for the calculation of LSP shifts of plasmonic NPs with the accuracy of ab initio methodologies for systems in the quantum confinement size region, but with a computational cost that consents its application to realistic-sized colloidal NPs. Such a development can potentially pave the way for future in-silico rational design of colorimetric sensors.

■ ASSOCIATED CONTENT

Supporting Information

The Supporting Information is available free of charge at https://pubs.acs.org/doi/10.1021/acsphyschemau.4c00052.

Details on ωFQFμ/FQ, computational details, convergence of ωFQFμ/FQ spectra as a function of the radius of the solvent droplet and number of snapshots, MD analysis for spherical NPs (diameter = 5 nm) in solution (PDF)

■ AUTHOR INFORMATION

Corresponding Authors

Tommaso Giovannini − *Department of Physics, University of Rome Tor Vergata, 00133 Rome, Italy;* orcid.org/0000-0002-5637-2853; Email: tommaso.giovannini@uniroma2.it

Chiara Cappelli − *Scuola Normale Superiore, 56126 Pisa, Italy;* orcid.org/0000-0002-4872-4505; Email: chiara.cappelli@sns.it

https://doi.org/10.1021/acsphyschemau.4c00052
ACS Phys. Chem Au XXXX, XXX, XXX−XXX

Authors

Luca Nicoli − *Scuola Normale Superiore, 56126 Pisa, Italy;* orcid.org/0000-0002-4808-3381

Sveva Sodomaco − *Scuola Normale Superiore, 56126 Pisa, Italy*

Piero Lafiosca − *Scuola Normale Superiore, 56126 Pisa, Italy;* orcid.org/0000-0002-3967-0736

Complete contact information is available at: https://pubs.acs.org/10.1021/acsphyschemau.4c00052

Author Contributions

CRediT: **Luca Nicoli** data curation, formal analysis, investigation, methodology, software, validation, visualization, writing - original draft; **Sveva Sodomaco** data curation, formal analysis, investigation, methodology, validation, visualization, writing - original draft; **Piero Lafiosca** data curation, formal analysis, investigation, methodology, software, validation, writing - original draft; **Tommaso Giovannini** conceptualization, formal analysis, methodology, project administration, software, supervision, writing - review & editing; **Chiara Cappelli** conceptualization, formal analysis, funding acquisition, methodology, project administration, resources, supervision, writing - review & editing.

Notes

The authors declare no competing financial interest.

■ ACKNOWLEDGMENTS

We gratefully acknowledge the Center for High-Performance Computing (CHPC) at SNS for providing the computational infrastructure.

■ REFERENCES

(1) Mayer, K. M.; Hafner, J. H. Localized surface plasmon resonance sensors. *Chem. Rev.* **2011**, *111*, 3828−3857.

(2) McNamara, K.; Tofail, S. A. Nanoparticles in biomedical applications. *Adv. Phys. X* **2017**, *2*, 54−88.

(3) Dutta, A.; Medda, A.; Patra, A. Recent advances and perspectives on colloidal semiconductor nanoplatelets for optoelectronic applications. *J. Phys. Chem. C* **2021**, *125*, 20−30.

(4) Hu, X.; Li, G.; Yu, J. C. Design, fabrication, and modification of nanostructured semiconductor materials for environmental and energy applications. *Langmuir* **2010**, *26*, 3031−3039.

(5) Yang, P.; Zheng, J.; Xu, Y.; Zhang, Q.; Jiang, L. Colloidal synthesis and applications of plasmonic metal nanoparticles. *Adv. Mater.* **2016**, *28*, 10508−10517.

(6) Chen, H.; Shao, L.; Woo, K. C.; Ming, T.; Lin, H.-Q.; Wang, J. Shape-dependent refractive index sensitivities of gold nanocrystals with the same plasmon resonance wavelength. *J. Phys. Chem. C* **2009**, *113*, 17691−17697.

(7) Lee, J.-H.; Kim, B.-C.; Oh, B.-K.; Choi, J.-W. Highly sensitive localized surface plasmon resonance immunosensor for label-free detection of HIV-1. *Nanomedicine* **2013**, *9*, 1018−1026.

(8) Kim, J.; Oh, S. Y.; Shukla, S.; Hong, S. B.; Heo, N. S.; Bajpai, V.; Chun, H. S.; Jo, C. H.; Choi, B. G.; Huh, Y. S.; et al. Heteroassembled gold nanoparticles with sandwich-immunoassay LSPR chip format for rapid and sensitive detection of hepatitis B virus surface antigen (HBsAg). *Biosens. Bioelectron.* **2018**, *107*, 118−122.

(9) Chen, H.; Kou, X.; Yang, Z.; Ni, W.; Wang, J. Shape-and size-dependent refractive index sensitivity of gold nanoparticles. *Langmuir* **2008**, *24*, 5233−5237.

(10) Foerster, B.; Joplin, A.; Kaefer, K.; Celiksoy, S.; Link, S.; Sönnichsen, C. Chemical interface damping depends on electrons reaching the surface. *ACS Nano* **2017**, *11*, 2886−2893.

(11) Steinbrück, A.; Stranik, O.; Csaki, A.; Fritzsche, W. Sensoric potential of gold−silver core−shell nanoparticles. *Anal. Bioanal. Chem.* **2011**, *401*, 1241−1249.

(12) Szántó, G.; Csarnovics, I.; Bonyár, A. Numerical investigation of the refractive index sensitivity of Au/Ag core-shell nanostructures for sensing applications. *Sens. Bio-Sens. Res.* **2021**, *32*, 100414.

(13) Hu, Y.; Zhang, A.-Q.; Li, H.-J.; Qian, D.-J.; Chen, M. Synthesis, study, and discrete dipole approximation simulation of Ag-Au bimetallic nanostructures. *Nanoscale Res. Lett.* **2016**, *11*, 209.

(14) Hsiao, A.; Gartia, M. R.; Chang, T.-W.; Wang, X.; Khumwan, P.; Liu, G. L. Colorimetric plasmon resonance microfluidics on nanohole array sensors. *Sens. Bio-Sens. Res.* **2015**, *5*, 24−32.

(15) Yamada, A. Computational Analyses of Plasmonics of a Silver Nanoparticle in a Vacuum and in a Water Solution by Classical Electronic and Molecular Dynamics Simulations. *J. Phys. Chem. A* **2022**, *126*, 4762−4771.

(16) Ross, M. B.; Ku, J. C.; Lee, B.; Mirkin, C. A.; Schatz, G. C. Plasmonic metallurgy enabled by DNA. *Adv. Mater.* **2016**, *28*, 2790−2794.

(17) Giovannini, T.; Bonatti, L.; Lafiosca, P.; Nicoli, L.; Castagnola, M.; Illobre, P. G.; Corni, S.; Cappelli, C. Do we really need quantum mechanics to describe plasmonic properties of metal nanostructures? *ACS Photonics* **2022**, *9*, 3025−3034.

(18) Nicoli, L.; Lafiosca, P.; Grobas Illobre, P.; Bonatti, L.; Giovannini, T.; Cappelli, C. Fully atomistic modeling of plasmonic bimetallic nanoparticles: nanoalloys and core-shell systems. *Front. Photonics* **2023**, *4*, 1199598.

(19) Rick, S. W.; Stuart, S. J.; Berne, B. J. Dynamical fluctuating charge force fields: Application to liquid water. *J. Chem. Phys.* **1994**, *101*, 6141−6156.

(20) Rick, S. W.; Stuart, S. J.; Bader, J. S.; Berne, B. Fluctuating charge force fields for aqueous solutions. *J. Mol. Liq.* **1995**, *65*−*66*, 31−40.

(21) Rick, S. W.; Berne, B. Dynamical fluctuating charge force fields: the aqueous solvation of amides. *J. Am. Chem. Soc.* **1996**, *118*, 672−679.

(22) Giovannini, T.; Egidi, F.; Cappelli, C. Molecular spectroscopy of aqueous solutions: a theoretical perspective. *Chem. Soc. Rev.* **2020**, *49*, 5664−5677.

(23) Giovannini, T.; Egidi, F.; Cappelli, C. Theory and algorithms for chiroptical properties and spectroscopies of aqueous systems. *Phys. Chem. Chem. Phys.* **2020**, *22*, 22864−22879.

(24) Gómez, S.; Giovannini, T.; Cappelli, C. Multiple facets of modeling electronic absorption spectra of systems in solution. *ACS Phys. Chem. Au* **2023**, *3*, 1−16.

(25) Giovannini, T.; Cappelli, C. Continuum vs. atomistic approaches to computational spectroscopy of solvated systems. *Chem. Commun.* **2023**, *59*, 5644−5660.

(26) Mennucci, B.; Corni, S. Multiscale modelling of photoinduced processes in composite systems. *Nat. Rev. Chem* **2019**, *3*, 315−330.

(27) Xia, Y.; Halas, N. J. Shape-controlled synthesis and surface plasmonic properties of metallic nanostructures. *MRS Bull.* **2005**, *30*, 338−348.

(28) Loiseau, A.; Zhang, L.; Hu, D.; Salmain, M.; Mazouzi, Y.; Flack, R.; Liedberg, B.; Boujday, S. Core−shell gold/silver nanoparticles for localized surface plasmon resonance-based naked-eye toxin biosensing. *ACS Appl. Mater. Interfaces* **2019**, *11*, 46462−46471.

(29) Piliarik, M.; Šípová, H.; Kvasnička, P.; Galler, N.; Krenn, J. R.; Homola, J. High-resolution biosensor based on localized surface plasmons. *Opt. Express* **2012**, *20*, 672−680.

(30) Mock, J. J.; Smith, D. R.; Schultz, S. Local refractive index dependence of plasmon resonance spectra from individual nanoparticles. *Nano Lett.* **2003**, *3*, 485−491.

(31) Underwood, S.; Mulvaney, P. Effect of the solution refractive index on the color of gold colloids. *Langmuir* **1994**, *10*, 3427−3430.

(32) Rycenga, M.; Cobley, C. M.; Zeng, J.; Li, W.; Moran, C. H.; Zhang, Q.; Qin, D.; Xia, Y. Controlling the synthesis and assembly of silver nanostructures for plasmonic applications. *Chem. Rev.* **2011**, *111*, 3669−3712.

(33) Haes, A. J.; Van Duyne, R. P. A unified view of propagating and localized surface plasmon resonance biosensors. *Anal. Bioanal. Chem.* **2004**, *379*, 920−930.
(34) Anker, J. N.; Hall, W. P.; Lyandres, O.; Shah, N. C.; Zhao, J.; Van Duyne, R. P. Biosensing with plasmonic nanosensors. *Nat. Mater.* **2008**, *7*, 442−453.
(35) Stewart, M. E.; Anderton, C. R.; Thompson, L. B.; Maria, J.; Gray, S. K.; Rogers, J. A.; Nuzzo, R. G. Nanostructured plasmonic sensors. *Chem. Rev.* **2008**, *108*, 494−521.
(36) Lafiosca, P.; Gómez, S.; Giovannini, T.; Cappelli, C. Absorption properties of large complex molecular systems: the DFTB/fluctuating charge approach. *J. Chem. Theory Comput.* **2022**, *18*, 1765−1779.
(37) Giovannini, T.; Rosa, M.; Corni, S.; Cappelli, C. A classical picture of subnanometer junctions: an atomistic Drude approach to nanoplasmonics. *Nanoscale* **2019**, *11*, 6004−6015.
(38) Giovannini, T.; Bonatti, L.; Polini, M.; Cappelli, C. Graphene plasmonics: Fully atomistic approach for realistic structures. *J. Phys. Chem. Lett.* **2020**, *11*, 7595−7602.
(39) Bonatti, L.; Nicoli, L.; Giovannini, T.; Cappelli, C. In silico design of graphene plasmonic hot-spots. *Nanoscale Adv.* **2022**, *4*, 2294−2302.
(40) Bonatti, L.; Gil, G.; Giovannini, T.; Corni, S.; Cappelli, C. Plasmonic resonances of metal nanoparticles: atomistic vs. Continuum approaches. *Front. Chem.* **2020**, *8*, 340.
(41) Maier, S. A., et al. *Plasmonics: Fundamentals and Applications*; Springer, 2007; Vol. *1*.
(42) Giovannini, T.; Puglisi, A.; Ambrosetti, M.; Cappelli, C. Polarizable QM/MM approach with fluctuating charges and fluctuating dipoles: the QM/FQFμ model. *J. Chem. Theory Comput.* **2019**, *15*, 2233−2245.
(43) Litjens, R. A.; Quickenden, T. I.; Freeman, C. G. Visible and near-ultraviolet absorption spectrum of liquid water. *Appl. Opt.* **1999**, *38*, 1216−1223.
(44) Sani, E.; Dell'Oro, A. Spectral optical constants of ethanol and isopropanol from ultraviolet to far infrared. *Opt. Mater.* **2016**, *60*, 137−141.
(45) Nicoli, L.; Giovannini, T.; Cappelli, C. Assessing the quality of QM/MM approaches to describe vacuo-to-water solvatochromic shifts. *J. Chem. Phys.* **2022**, *157*..
(46) Mortier, W. J.; Van Genechten, K.; Gasteiger, J. Electronegativity equalization: application and parametrization. *J. Am. Chem. Soc.* **1985**, *107*, 829−835.
(47) Sanderson, R. An interpretation of bond lengths and a classification of bonds. *Science* **1951**, *114*, 670−672.
(48) Parr, R. G. Density functional theory. *Annu. Rev. Phys. Chem.* **1983**, *34*, 631−656.
(49) Geerlings, P.; De Proft, F.; Langenaeker, W. Conceptual density functional theory. *Chem. Rev.* **2003**, *103*, 1793−1874.
(50) Cappelli, C. Integrated QM/polarizable MM/continuum approaches to model chiroptical properties of strongly interacting solute−solvent systems. *Int. J. Quantum Chem.* **2016**, *116*, 1532−1542.
(51) Larsen, A. H.; et al. The atomic simulation environment—a Python library for working with atoms. *J. Phys.: Condens. Matter* **2017**, *29*, 273002.
(52) Abraham, M. J.; Murtola, T.; Schulz, R.; Páll, S.; Smith, J. C.; Hess, B.; Lindahl, E. GROMACS: High performance molecular simulations through multi-level parallelism from laptops to supercomputers. *SoftwareX* **2015**, *1−2*, 19−25.
(53) Liu, Z.; Alkan, F.; Aikens, C. M. TD-DFTB study of optical properties of silver nanoparticle homodimers and heterodimers. *J. Chem. Phys.* **2020**, *153*, 144711.
(54) Carnimeo, I.; Cappelli, C.; Barone, V. Analytical gradients for MP 2, double hybrid functionals, and TD-DFT with polarizable embedding described by fluctuating charges. *J. Comput. Chem.* **2015**, *36*, 2271−2290.
(55) Giovannini, T.; Lafiosca, P.; Chandramouli, B.; Barone, V.; Cappelli, C. Effective yet reliable computation of hyperfine coupling constants in solution by a QM/MM approach: Interplay between electrostatics and non-electrostatic effects. *J. Chem. Phys.* **2019**, *150*, 124102.
(56) Ambrosetti, M.; Skoko, S.; Giovannini, T.; Cappelli, C. Quantum mechanics/fluctuating charge protocol to compute solvatochromic shifts. *J. Chem. Theory Comput.* **2021**, *17*, 7146−7156.
(57) Zhang, C.; Sun, L.-D.; Yan, C.-H. Noble metal plasmonic nanostructure related chromisms. *Inorg. Chem. Front.* **2016**, *3*, 203−217.
(58) Lee, Y. H.; Chen, H.; Xu, Q.-H.; Wang, J. Refractive index sensitivities of noble metal nanocrystals: the effects of multipolar plasmon resonances and the metal type. *J. Phys. Chem. C* **2011**, *115*, 7997−8004.
(59) Liebsch, A. Surface-plasmon dispersion and size dependence of Mie resonance: silver versus simple metals. *Phys. Rev. B* **1993**, *48*, 11317−11328.
(60) Giovannini, T.; Ambrosetti, M.; Cappelli, C. Quantum confinement effects on solvatochromic shifts of molecular solutes. *J. Phys. Chem. Lett.* **2019**, *10*, 5823−5829.
(61) Amovilli, C.; Floris, F. M. On the effect of solute-solvent Pauli repulsion on n → π^* transition for acrolein in water solution. *Phys. Chem. Liq.* **2020**, *58*, 281−289.
(62) Hottin, J.; Wijaya, E.; Hay, L.; Maricot, S.; Bouazaoui, M.; Vilcot, J.-P. Comparison of gold and silver/gold bimetallic surface for highly sensitive near-infrared SPR sensor at 1550 nm. *Plasmonics* **2013**, *8*, 619−624.
(63) Dengler, S.; Kübel, C.; Schwenke, A.; Ritt, G.; Eberle, B. Near- and off-resonant optical limiting properties of gold−silver alloy nanoparticles for intense nanosecond laser pulses. *J. Opt.* **2012**, *14*, 075203.
(64) Ghosh, S. K.; Nath, S.; Kundu, S.; Esumi, K.; Pal, T. Solvent and ligand effects on the localized surface plasmon resonance (LSPR) of gold colloids. *J. Phys. Chem. B* **2004**, *108*, 13963−13971.
(65) Malinsky, M. D.; Kelly, K. L.; Schatz, G. C.; Van Duyne, R. P. Chain length dependence and sensing capabilities of the localized surface plasmon resonance of silver nanoparticles chemically modified with alkanethiol self-assembled monolayers. *J. Am. Chem. Soc.* **2001**, *123*, 1471−1482.
(66) Nath, N.; Chilkoti, A. Label free colorimetric biosensing using nanoparticles. *J. Fluoresc.* **2004**, *14*, 377−389.
(67) Mao, K.; Yang, Z.; Li, J.; Zhou, X.; Li, X.; Hu, J. A novel colorimetric biosensor based on non-aggregated Au@ Ag core−shell nanoparticles for methamphetamine and cocaine detection. *Talanta* **2017**, *175*, 338−346.
(68) Dong, P.; Wu, Y.; Guo, W.; Di, J. Plasmonic biosensor based on triangular Au/Ag and Au/Ag/Au core/shell nanoprisms onto indium tin oxide glass. *Plasmonics* **2013**, *8*, 1577−1583.
(69) Sun, L.; Li, Q.; Tang, W.; Di, J.; Wu, Y. The use of gold-silver core-shell nanorods self-assembled on a glass substrate can substantially improve the performance of plasmonic affinity biosensors. *Microchim. Acta* **2014**, *181*, 1991−1997.
(70) Hao, J.; Xiong, B.; Cheng, X.; He, Y.; Yeung, E. S. High-throughput sulfide sensing with colorimetric analysis of single Au−Ag core−shell nanoparticles. *Anal. Chem.* **2014**, *86*, 4663−4667.
(71) Guo, Y.; Wu, J.; Li, J.; Ju, H. A plasmonic colorimetric strategy for biosensing through enzyme guided growth of silver nanoparticles on gold nanostars. *Biosens. Bioelectron.* **2016**, *78*, 267−273.
(72) Fu, Q.; Zhang, D.; Yi, M.; Wang, X.; Chen, Y.; Wang, P.; Ming, H. Effect of shell thickness on a Au−Ag core−shell nanorods-based plasmonic nano-sensor. *J. Opt.* **2012**, *14*, 085001.
(73) Haynes, W. *CRC Handbook of Chemistry and Physics*; CRC Press: Boca Raton, 2014.
(74) Chen, Y.; Wu, H.; Li, Z.; Wang, P.; Yang, L.; Fang, Y. The study of surface plasmon in Au/Ag core/shell compound nanoparticles. *Plasmonics* **2012**, *7*, 509−513.
(75) Peña-Rodríguez, O.; Pal, U. Au@ Ag core−shell nanoparticles: efficient all-plasmonic Fano-resonance generators. *Nanoscale* **2011**, *3*, 3609−3612.
(76) Ma, Y.-W.; Zhang, L.-H.; Wu, Z.-W.; Yi, M.-F.; Zhang, J.; Jian, G.-S. The study of tunable local surface plasmon resonances on Au-Ag

https://doi.org/10.1021/acsphyschemau.4c00052
ACS Phys. Chem Au XXXX, XXX, XXX−XXX

and Ag-Au core-shell alloy nanostructure particles with DDA method. *Plasmonics* **2015**, *10*, 1791−1800.
(77) Oelke, W.; Arnold, R. The Refractive Indices of Alcohol-Water Mixture at 25 °C. In *Proceedings of the Iowa Academy of Science*, **1936**; pp 175−176.
(78) Atilhan, M.; Aparicio, S. Molecular dynamics simulations of metal nanoparticles in deep eutectic solvents. *J. Phys. Chem. C* **2018**, *122*, 18029−18039.
(79) Foerster, B.; Spata, V. A.; Carter, E. A.; Sönnichsen, C.; Link, S. Plasmon damping depends on the chemical nature of the nanoparticle interface. *Sci. Adv.* **2019**, *5*, No. eaav0704.
(80) Lee, S. A.; Link, S. Chemical interface damping of surface plasmon resonances. *Acc. Chem. Res.* **2021**, *54*, 1950−1960.
(81) Douglas-Gallardo, O. A.; Berdakin, M.; Sánchez, C. G. Atomistic insights into chemical interface damping of surface plasmon excitations in silver nanoclusters. *J. Phys. Chem. C* **2016**, *120*, 24389−24399.

https://doi.org/10.1021/acsphyschemau.4c00052
ACS Phys. Chem Au XXXX, XXX, XXX−XXX

V. QM/Classical Modeling of Surface Enhanced Raman Scattering Based on Atomistic Electromagnetic Models

JCTC Journal of Chemical Theory and Computation

pubs.acs.org/JCTC Article

QM/Classical Modeling of Surface Enhanced Raman Scattering Based on Atomistic Electromagnetic Models

Piero Lafiosca, Luca Nicoli, Luca Bonatti, Tommaso Giovannini,* Stefano Corni, and Chiara Cappelli*

Cite This: J. Chem. Theory Comput. 2023, 19, 3616−3633 Read Online

ACCESS | Metrics & More | Article Recommendations | Supporting Information

ABSTRACT: We present quantum mechanics (QM)/frequency dependent fluctuating charge (QM/ωFQ) and fluctuating dipoles (QM/ωFQFμ) multiscale approaches to model surface-enhanced Raman scattering spectra of molecular systems adsorbed on plasmonic nanostructures. The methods are based on a QM/classical partitioning of the system, where the plasmonic substrate is treated by means of the atomistic electromagnetic models ωFQ and ωFQFμ, which are able to describe in a unique fashion and at the same level of accuracy the plasmonic properties of noble metal nanostructures and graphene-based materials. Such methods are based on classical physics, i.e. Drude conduction theory, classical electrodynamics, and atomistic polarizability to account for interband transitions, by also including an ad-hoc phenomenological correction to describe quantum tunneling. QM/ωFQ and QM/ωFQFμ are thus applied to selected test cases, for which computed results are compared with available experiments, showing the robustness and reliability of both approaches.

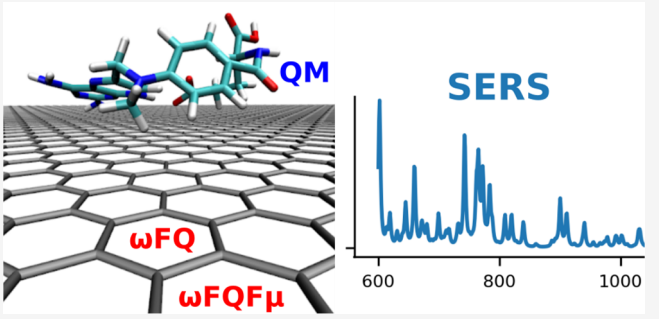

1. INTRODUCTION

Surface-enhanced Raman scattering (SERS) takes advantage of the giant enhancement of the Raman scattering cross section of a target molecule in the proximity of plasmonic nanostructured materials.[1] Enhancement factors (i.e., the ratio between the Raman intensity for the nanoaggregate and the isolated/solvated target molecule) can reach values up to 10^{10-11},[2−4] thus allowing single molecule detection, down to a submolecular resolution.[5] For these reasons, SERS has gained popularity and is widely used in a plethora of applications[6−11] because it inherits the general advantages of classical Raman spectroscopy, solves its main weakness, consisting of generally low scattering amplitudes, and add, possibly, spatial resolution on the nanometer scale and below.[12−14] From the physicochemical point of view, it is generally accepted[3,15−17] that SERS enhancement results from the combination of two factors: the so-called electromagnetic (EM) effect (yielding enhancements up to 10^{7-8}), which is caused by the excitation of surface plasmons in the substrate, which leads to a strong induced electric field in its proximity, and the so-called chemical (CT) enhancement, for which a holistic theoretical explanation is still missing. CT is associated with 10^{2-3} enhancement factors and is mainly ascribed to charge-transfer excitations between the analyte and the substrate.

Metal nanostructures, such as metal nanoparticles (NPs), have been the most used substrates for SERS because they provide highly confined plasmons and huge enhanced electric field on their surfaces,[15,18−24] also thanks to a substantial advancement in experimental techniques for manipulating the nanoscale.[25−29] Indeed, specific morphological arrangements can be designed, giving rise to hot-spots, i.e. regions in space where the electric field is extremely confined and enhanced.[5,12,13,30] Recently, there has been increasing interest in designing novel substrates characterized by high chemical inertness to be used in the investigation of biochemical species. In this context, recent developments of SERS substrates based on carbon allotropes such as graphene and carbon nanotubes (CNTs) are worth being mentioned.[31−33]

A theoretical understanding of the SERS mechanisms can be particularly useful not only for the interpretation of experimental spectra but also for the in-silico design of novel materials and morphologies that can maximize spectral enhancement factors for a specific analyte. For this reason, in the past years, various methodologies have been proposed to simulate SERS signals.[34−46] The huge dimension of typical SERS substrates (tens/hundreds of nanometers) makes a full quantum mechanical (QM) description of the molecule−substrate system unfeasible, although small-size model systems can be exploited to deal with specific features of the SERS phenomenon (mainly related to the CT mechanism).[47−50] To

Received: February 10, 2023
Published: June 6, 2023

solve this problem, multiscale approaches can be used, where the analyte is described at the QM level, while the substrate is treated classically.[34,35,37−41,51−59] In particular, the nanostructured material can be modeled as a continuum medium, defined in terms of its complex-valued permittivity, or by retaining its atomistic nature. Remarkably, in the latter case a precise description of complex geometries, even characterized by geometrical defects, is obtained.[60,61] Note that both approaches neglect CT effects; however, for usual SERS substrates, the EM enhancement is several orders of magnitude higher than the CT.[62]

In this paper, we present QM/ωFQ and QM/ωFQFμ fully atomistic multiscale QM/classical approaches to simulate SERS spectra, where the analyte is treated quantum-mechanically. To describe the nanostructured materials, we exploit a family of atomistic models that we have recently developed, which are able to correctly reproduce experimental and ab initio plasmonic features of metal nanoparticles (ωFQ and ωFQFμ),[61,63] and graphene-based nanostructures (ωFQ).[64] These approaches are based on classical physics and text-book concepts, such as Drude conduction theory, classical electrodynamics, and atomistic polarizability, to account for interband transitions. In addition, ad-hoc phenomenological correction to describe quantum tunneling is included in the model, to deal with nanojunctions and aggregates in which hot-spots may originate. Within ωFQ and ωFQFμ, each atom of the nanostructure is endowed with a frequency-dependent complex-valued charge and supplemented by a complex-valued dipole in ωFQFμ, which responds to the external radiation, thus mimicking the oscillating electron density.

Different from previous classical atomistic approaches,[34−36,42−46,59] Drude conduction, i.e. intraband transitions, is taken into account by means of the equation of motion of the charges placed on each atom, while induced dipoles are included so as to model interband transitions.[61] This permits us to correctly catch the physics underlying the plasmonics of generic *s*, *p*, and *d* metallic systems by also allowing for a physical dissection of the two contributions. Moreover, ωFQ(Fμ) is able to physically account for the quantum tunneling between nearby nanoparticles by exponentially modulating Drude conductance as a function of atom−atom distances, which is particularly relevant for nanoaggregates and nanojunctions, where plasmonic hot-spots are created.[61,63] Finally, it is worth noting that ωFQ is the only atomistic classical approach to date able to physically describe graphene plasmonics in terms of its fundamental physical parameters, such as the Fermi energy, relaxation time, and two-dimensional electron density.[60,64−66]

Here, ωFQ and ωFQFμ are coupled to a density functional theory (DFT) treatment of the QM portion and the resulting QM/ωFQ and QM/ωFQFμ methods are further extended to the calculation of complex molecular polarizabilities through the linear response theory. The robustness of the approaches is showcased through their application to pyridine adsorbed on noble metal NPs. Thanks to the generality of both approaches, we also apply them to the simulation of graphene-enhanced Raman spectroscopy (GERS) by exploiting graphene-based nanostructures as enhancing substrates. For large pristine graphene sheets, the absence of sharp edges is usually connected to the low enhancement factors reported for GERS.[67,68] Nevertheless, suitably engineered graphene-based nanostructures may enhance by several orders of magnitude both the induced electric field and its spatial confinement.[60]

The paper is organized as follows. The first section recalls the theoretical foundations of ωFQ and ωFQFμ and presents their coupling with a DFT Hamiltonian for the ground state and linear response theory. We note that the EM field associated with the induced density in the nanoparticle is neither a purely real nor a purely imaginary perturbation. Therefore, we exploit a general complex linear response formulation. QM/ωFQFμ is then applied to simulate SERS spectra of pyridine adsorbed on different plasmonic substrates (silver, gold, and graphene). Finally, GERS of a widely used anticancer drug, i.e. methotrexate, adsorbed on a graphene disk, is taken as a case study to showcase the potentialities of the method. Summary, conclusions, and future perspectives end the paper.

2. THEORY

2.1. ωFQ and ωFQFμ. ωFQ endows the atoms of the nanostructure with a charge. In the presence of an external monochromatic electric field $\mathbf{E}^{\mathrm{ext}}(\omega)$, the charge can be exchanged with nearest neighbor atoms as a result of Drude conduction[69] and quantum tunnelling effect.[63] For a system composed of N atoms, charges $\mathbf{q}$ can be calculated by solving the following set of linear equations:[68]

$$(\mathbf{A}^q - z(\omega)\mathbf{I})\mathbf{q} = \mathbf{R} \tag{1}$$

where $\mathbf{A}^q$ is a real nonsymmetric matrix, which reads:

$$A_{ij}^q = \sum_{k\neq i}^{N} K_{ik}(T_{kj}^{qq} - T_{ij}^{qq}) \tag{2}$$

$\mathbf{T}^{qq}$ is the charge−charge interaction matrix,[70] while $\mathbf{K}$ is defined as

$$K_{ij} = \begin{cases} [1 - f(r_{ij})]\dfrac{\mathcal{A}_{ij}}{r_{ij}} & \text{if } i \neq j \\ 0 & \text{otherwise} \end{cases} \tag{3}$$

Quantum tunneling effects are taken into account by means of the Fermi damping function $f(r_{ij})$, which exponentially decays as a function of the interatomic distance $r_{ij} = |\mathbf{r}_i - \mathbf{r}_j|$ ($\mathbf{r}_i$ is the position of the i-th atom). $\mathcal{A}_{ij}$ is an effective area connecting atoms i and j. Its value is based on the geometry of the system and has been chosen to best reproduce reference ab initio values.[61,63,64] It is worth noticing that the $\mathbf{A}^q$ matrix only depends on the geometry of the ωFQ system, because it is a function of the interatomic distance r_{ij} only.

The frequency-dependent complex-valued factor $z(\omega)$ in eq 1 is defined as

$$z(\omega) = -\frac{\omega}{2n_0\tau}(\omega\tau + \mathrm{i}) \tag{4}$$

where n_0 is the electron density of the system and τ is the scattering time. The electron density depends on the composition and the morphology of the nanostructure. In general, for 3D systems $n_0 = \frac{\sigma_0/\tau}{m^*}$ where σ_0 is the static conductance of the material and m^* is the effective electron mass, which for metallic systems is usually approximated to 1.[71] For graphene-based structures, this approximation is no longer valid. Therefore, the electronic density can be written as[64,72]

https://doi.org/10.1021/acs.jctc.3c00177
J. Chem. Theory Comput. 2023, 19, 3616−3633

$$n_0^{\text{graphene}} = \frac{n_0}{m^*} = \frac{n_{2D} \cdot a_0}{\sqrt{\pi n_{2D}}/v_F} \tag{5}$$

$$n_{2D} = \alpha \frac{N}{S} \tag{6}$$

where n_{2D} is the 2D numeral electronic density of the system, a_0 is the Bohr radius, v_F is the Fermi velocity, S is the total surface of the graphene system, and α is the fraction of doping electrons per carbon atom. Such a number, and thus graphene plasmonic properties, can be tuned by varying the external gating, which is directly related to the Fermi energy (E_F), which determines the numerical value of n_{2D} (and thus α) by

$$E_F = \hbar v_F \sqrt{\pi n_{2D}} \tag{7}$$

Finally, the right-hand side in eq 1 is defined as[68]

$$R_i = \sum_{j=1}^{N} (V_i^{\text{ext}} - V_j^{\text{ext}}) K_{ij} \tag{8}$$

where V_i^{ext} is the electric potential associated with the external oscillating field evaluated at position $\mathbf{r}_i$, which implies we are assuming the quasistatic approximation to full EM equations.[63]

ωFQ has successfully been applied to the simulation of the plasmonic response of sodium nanostructures and graphene-based materials.[63−65] However, the underlying Drude conduction mechanism is not able to reproduce the plasmonic response of d-metals, as for instance silver and gold nanoparticles, because interband (IB) transitions play an essential role.[73−77] ωFQFμ correctly models such effects.[61] There, each atom is endowed with both an oscillating charge q_i and an oscillating dipole $\boldsymbol{\mu}_i$. The plasmonic response is then assumed to originate from two different mechanisms: the Drude conduction, taken into account by the charges, and the aforementioned IB transitions, which are treated by means of the dipoles, which account for the polarizability of the d-shell. By taking into account both terms, and their interaction, the plasmonic response of metal nanostructures, made by Ag/Au, could be correctly described.[61] The resulting ωFQFμ equation reads:

$$\left[\begin{pmatrix} \mathbf{A}^q & \mathbf{A}^\mu \\ \mathbf{T}^{\mu q} & \mathbf{T}^{\mu\mu} \end{pmatrix} - \begin{pmatrix} z(\omega)\mathbf{I} & 0 \\ 0 & z'(\omega)\mathbf{I} \end{pmatrix}\right]\begin{pmatrix} \mathbf{q} \\ \boldsymbol{\mu} \end{pmatrix} = \begin{pmatrix} \mathbf{R} \\ -\mathbf{E}^{\text{ext}} \end{pmatrix} \tag{9}$$

where $\mathbf{A}^q$, $z(\omega)$, and $\mathbf{R}$ have been already introduced by eq 1. $\mathbf{T}^{\mu q}$ and $\mathbf{T}^{\mu\mu}$ are the dipole−charge and dipole−dipole interaction tensors,[70] whereas $\mathbf{A}^\mu$ and $z'(\omega)$ are defined as follows:

$$A_{ij}^{\mu} = \sum_{k=1}^{N} K_{ij}(T_{kj}^{q\mu} - T_{ij}^{q\mu}) \tag{10}$$

$$z'(\omega) = -\frac{1}{\alpha_{\text{IB}}(\omega)} \tag{11}$$

where $\alpha_{\text{IB}}(\omega)$ is the IB polarizability, which is extracted from the experimental permittivity function (after removing the Drude part, see ref 61 for further details). Similarly to ωFQ, all the frequency-dependent terms are collected into a diagonal shift through the z, z' functions, and the other terms depend on the geometry of the system only.

2.2. Coupling to a QM Hamiltonian. ωFQ and ωFQFμ can be coupled to a QM description of a molecular system in a QM/MM fashion.[78−85] ωFQ and ωFQFμ describe the response to an external oscillating electric field. Thus, they can naturally be translated into a linear response formalism. However, to achieve a physically consistent description of the molecule/substrate system, their interaction needs to be modeled also in the ground state (GS). To this end, the analogous frequency independent force fields, FQ and FQFμ,[70,86−93] can be exploited. In the following, we first briefly recall FQ and FQFμ for the GS. Then, we present the linear response formalism for the novel QM/ωFQ(Fμ) approaches.

2.2.1. Description of the Ground State. The total energy of a two-layer QM/FQ(Fμ) system can be written as

$$\mathcal{E} = E_{\text{QM}} + E_{\text{QM/FQ(F}\mu\text{)}} + E_{\text{FQ(F}\mu\text{)}} \tag{12}$$

where E_{QM} and $E_{\text{FQ(F}\mu\text{)}}$ are the self-energies of the QM and FQ(Fμ) portions, whereas $E_{\text{QM/FQ(F}\mu\text{)}}$ indicates their interaction energy. The latter term is described as the electrostatic interaction energy between the QM charge distribution and the classical fluctuating multipoles of the FQ or FQFμ force fields:[70]

$$E_{\text{QM/FQ}} = \sum_{p=1}^{N} q_p V^{\text{QM}}(\mathbf{r}_p)$$

$$E_{\text{QM/FQF}\mu} = \sum_{p=1}^{N} [q_p V^{\text{QM}}(\mathbf{r}_p) - \boldsymbol{\mu}_p \cdot \mathbf{E}^{\text{QM}}(\mathbf{r}_p)] \tag{13}$$

where the sums run over MM atoms, q_p and $\boldsymbol{\mu}_p$ indicate the p-th FQ and Fμ, which are located at position $\mathbf{r}_p$, while V^{QM} and $\mathbf{E}^{\text{QM}}$ are the electric potential and field generated by the QM portion, respectively.

If we exploit a DFT description of the QM portion, the ground state density can be determined by means of the effective Kohn−Sham (KS) equations, which are expressed in terms of the KS operator h_{KS}. In this work, we use the current implementation of QM/FQ and QM/FQFμ in the Amsterdam Density Functional (ADF) module[94] of the Amsterdam Modeling Suite (AMS) software package.[95] There, the solution of KS equations is performed through a numerical integration scheme, in which the KS operator is built over a grid of points $\mathbf{r}$ in the molecular space of the QM portion, i.e.:

$$h_{\text{KS}}(\mathbf{r}) = h_{\text{KS}}^0(\mathbf{r}) + \sum_{p=1}^{N} q_p T^{(0)}(\mathbf{d}_p)$$

$$h_{\text{KS}}(\mathbf{r}) = h_{\text{KS}}^0(\mathbf{r}) + \sum_{p=1}^{N} (q_p T^{(0)}(\mathbf{d}_p) + \boldsymbol{\mu}_p \cdot \mathbf{T}^{(1)}(\mathbf{d}_p)) \tag{14}$$

In eq 14 $h_{\text{KS}}^0(\mathbf{r})$ indicates the KS operator associated with the isolated QM system, and the QM/FQ and QM/Fμ interaction tensors are introduced. They are defined in terms of the distance $\mathbf{d}_p$ between the p-th atom and the grid point ($\mathbf{d}_p = \mathbf{r} - \mathbf{r}_p$) as follows:

$$T^{(0)}(\mathbf{d}_p) = \frac{1}{d_p}\text{erf}\left(\frac{d_p}{a}\right)$$

$$\mathbf{T}^{(1)}(\mathbf{d}_p) = -\frac{\mathbf{d}_p}{d_p^3}\left[\text{erf}\left(\frac{d_p}{a}\right) - \frac{2d_p}{\sqrt{\pi}\,a}\exp\left(-\frac{d_p^2}{a^2}\right)\right] \tag{15}$$

https://doi.org/10.1021/acs.jctc.3c00177
J. Chem. Theory Comput. 2023, 19, 3616−3633

where $d_p = |\mathbf{d}_p|$ and $a = 0.2$ a.u.[96] Since the molecular grid is constructed independently of the MM portion, in order to avoid numerical instabilities in eq 15, a screened interaction tensor between the QM grid points and the MM positions is considered, by analogy to what is reported in ref 97.

2.2.2. Linear Response Theory and SERS Spectra. By following the approach reported in ref 35, SERS spectral intensities can be evaluated through the frequency-dependent complex polarizability tensor $\overline{\alpha}_{\alpha\beta}(\omega; \omega)$. To this end, the first-order variation of the molecular density under the effect of a time-dependent perturbation is required, which can be accessed by means of the linear response theory. In particular, as a perturbation, we consider a monochromatic uniform electric field $\mathbf{E}^{\text{ext}}(\omega)$, linearly polarized along the direction $\alpha = x, y, z$. The perturbation operator, which acts on the electronic density, can be written as

$$V^{\text{pert}}(\mathbf{r}, \omega) = V^{\text{ext}}(\mathbf{r}, \omega) + V^{\text{loc}}(\mathbf{r}, \omega) \tag{16}$$

where V^{ext} is the electric potential associated with the external field $\mathbf{E}^{\text{ext}}$ and V^{loc} is the local field operator, which takes into account the electric field generated by the plasmonic substrate (PS) as induced by the external field.[38] Within ωFQ(Fμ), the local field operator reads:

$$V^{\text{loc}}_{\omega\text{FQ}}(\mathbf{r}, \omega) = \sum_{p=1}^{N} q_p^{\text{ext}}(\omega) T^{(0)}(\mathbf{d}_p)$$

$$V^{\text{loc}}_{\omega\text{FQF}\mu}(\mathbf{r}, \omega) = \sum_{i=p}^{N} q_p^{\text{ext}}(\omega) T^{(0)}(\mathbf{d}_p) + \boldsymbol{\mu}_p^{\text{ext}}(\omega) \cdot \mathbf{T}^{(1)}(\mathbf{d}_p) \tag{17}$$

$q_p^{\text{ext}}(\omega)$ and $\boldsymbol{\mu}_p^{\text{ext}}(\omega)$ can be calculated from eqs 1 and 9 by using V^{ext} as the source potential. In the following, we use the common notation for identifying the molecular orbitals (MOs): indices i, j for the occupied, a, b for the virtual and r, s, t, u for general MOs; moreover, given a quantity X we will indicate its variation at the first order with respect to the external electric field component α with X^α. Given that, the first order density $\rho^\alpha(\mathbf{r}, \omega)$ can be written as

$$\rho^\alpha(\mathbf{r}, \omega) = \sum_{ia} P^\alpha_{ia}(\omega) \phi_i(\mathbf{r}) \phi_a^*(\mathbf{r}) + P^\alpha_{ai}(\omega) \phi_a(\mathbf{r}) \phi_i^*(\mathbf{r}) \tag{18}$$

where $P^\alpha_{rs}(\omega)$ is the first-order density matrix expressed on the basis of the KS MOs. The nonzero elements of $\mathbf{P}^\alpha(\omega)$ are the off-diagonal ones, which are associated with the occupied-virtual and virtual-occupied MOs. They can be computed through the Time-Dependent Kohn–Sham (TDKS) equations, which read:[98]

$$\left[\begin{pmatrix} \mathbf{A} & \mathbf{B} \\ \mathbf{B}^* & \mathbf{A}^* \end{pmatrix} - (\omega + i\Gamma)\begin{pmatrix} -\mathbf{I} & \mathbf{0} \\ \mathbf{0} & \mathbf{I} \end{pmatrix}\right]\begin{pmatrix} \mathbf{X} \\ \mathbf{Y} \end{pmatrix} = -\begin{pmatrix} \mathbf{Q} \\ \mathbf{Q}^* \end{pmatrix} \tag{19}$$

where $X_{ia} = P^\alpha_{ia}$ and $Y_{ia} = P^\alpha_{ai}$. Also, the phenomenological damping factor Γ, which takes into account the finite lifetime of the QM excited state, is introduced.[99] In addition, the following quantities are defined:

$$A_{ai,bj} = (\varepsilon_a - \varepsilon_i)\delta_{ab}\delta_{ij} + (ai|bj) - c_x(ab|ij) + c_l f^{xc}_{ai,bj} + C^{\text{QM}/\omega\text{FQ(F}\mu)}_{ai,bj}$$

$$B_{ai,bj} = (ai|bj) - c_x(aj|ib) + C^{\text{QM}/\omega\text{FQ(F}\mu)}_{ai,bj}$$

$$Q_{ia} = \langle \phi_i | V^{\alpha,\text{pert}}(\mathrm{r}, \omega) | \phi_a \rangle \tag{20}$$

where ε indicates MO energies, $(rs|tu)$ two-electron integrals, and c_x and c_l define whether a pure ($c_x = 0$) or hybrid ($c_x \neq 0$) DFT functional is exploited. Two additional contributions to TDKS equations arise for QM/ωFQ and QM/ωFQFμ: the local field in the right-hand side (see the definition of $\mathbf{Q}$, and eq 17), and the so-called image field or direct contribution to the left-hand side ($\mathbf{C}^{\text{QM}/\omega\text{FQ(F}\mu)}$).[82] The latter is also introduced in the context of polarizable embedding, such as FQ and FQFμ for nonabsorbing media, and determines the response of the MM variables to the perturbed density. Its expression for both QM/FQ and QM/FQFμ methods can be found elsewhere.[89,96,100] On the other hand, the explicit contribution to the right-hand side is associated with the surface plasmon resonance and is responsible for the EM enhancement mechanism in surface-enhanced properties.

Once eq 19 is solved for the input frequency ω, the frequency-dependent polarizability tensor $\overline{\alpha}_{\alpha\beta}(\omega; \omega')$ is obtained as[101]

$$\overline{\alpha}_{\alpha\beta}(\omega; \omega') = -\text{tr}[\mathbf{H}^\alpha(\omega)\mathbf{P}^\beta(\omega')] \tag{21}$$

where $\mathbf{H}^\alpha(\omega)$ is the dipole matrix of the QM system, which involves both the dipole and the local field operator along the direction α, i.e.:

$$H^\alpha_{rs}(\omega) = \langle \phi_r | \mu_\alpha + V^{\alpha,\text{loc}}(\omega) | \phi_s \rangle \tag{22}$$

From the physical point of view, the presence of the local field operator in eq 22 can be explained by the fact that the total scattered field from the molecule–nanostructures composite system contains two contributions: the scattered field from the molecule and the reflected field, which is generated by the molecule and reflected on the plasmonic nanostructure. In order to calculate Raman intensities, both fields need to be taken into account.[35,37]

Given the frequency-dependent polarizability tensor $\overline{\boldsymbol{\alpha}}(\omega)$, Raman intensities can finally be evaluated by resorting to Placzek's theory of Raman scattering.[102,103] By assuming the perturbation field to be linearly perpendicular-plane polarized and the scattered light to be collected perpendicularly to the incident direction, the Raman intensity associated with the k-th normal mode can be calculated as[104]

$$I^k \propto \frac{(\omega - \omega_k)^4}{\omega_k}\{45[\alpha'_k(\omega; \omega)]^2 + 7[\gamma'_k(\omega; \omega)]^2\} \tag{23}$$

where ω and ω_k are the frequencies of the external field and of the k-th normal mode, respectively, while α' and γ' are the isotropic and anisotropic polarizability derivatives with respect to the k-th normal mode coordinate Q_k, i.e.:

$$[\alpha'_k(\omega; \omega')]^2 = \frac{1}{9}\left|\sum_{i=x,y,z} \frac{\partial \overline{\alpha}_{ii}(\omega; \omega')}{\partial Q_k}\right|^2 \tag{24}$$

https://doi.org/10.1021/acs.jctc.3c00177
J. Chem. Theory Comput. 2023, 19, 3616–3633

$$[\gamma_k'(\omega;\omega')]^2 = \frac{1}{2}\left(\frac{3}{4}\sum_{ij=x,y,z}\left|\frac{\partial\overline{\alpha}_{ij}(\omega;\omega')}{\partial Q_k} + \frac{\partial\overline{\alpha}_{ji}(\omega;\omega')}{\partial Q_k}\right|^2 - 9[\alpha_k'(\omega;\omega')]^2\right) \quad (25)$$

The functional form of eq 23 has been obtained under the assumption that the frequency difference between the incident and scattered light is negligible.[34,104,105] In the general case, the Raman intensity can be calculated as

$$I^k \propto \frac{(\omega-\omega_k)^4}{\omega_k}\{45[\alpha_k'(\omega-\omega_k;\omega)]^2 + 7[\gamma_k'(\omega-\omega_k;\omega)]^2 + 5[\delta_k'(\omega-\omega_k;\omega)]^2\} \quad (26)$$

in which $[\delta'(\omega;\omega')]^2$ is the square of the antisymmetric anisotropy of the polarizability tensor derivative, i.e.:[41]

$$[\delta_k'(\omega;\omega')]^2 = \frac{3}{8}\sum_{ij=x,y,z}\left|\frac{\partial\overline{\alpha}_{ij}(\omega;\omega')}{\partial Q_k} - \frac{\partial\overline{\alpha}_{ji}(\omega;\omega')}{\partial Q_k}\right|^2 \quad (27)$$

In the case in which the incident and scattered frequencies are the same, the latter term is exactly zero and the Raman intensity is reduced to the one reported in eq 23. If the difference between the frequencies is large with respect to the broadness of the plasmonic absorption peak, this approximation may induce some differences in the final computed SERS intensity. In this work, similarly to other approaches,[34,35] we have relied on this approximation, and its implications will be topic of future communications.

3. COMPUTATIONAL DETAILS

Silver and gold NPs' geometries are constructed by using OpenMD.[106] In particular, cuboctahedron (cTO), icosahedron (Ih), and ino-decahedron (i-Dh) morphologies are considered. Graphene disks' (GDs) geometries are generated by using the VMD package[107] by cutting a graphene sheet in a circular shape with radius r and removing dangling bonds, which only marginally affect GDs' plasmonic response.[68] For both metal NPs and GDs, we study SERS signals as a function of the PS size. To this end, we consider GDs with radius $20 \le r \le 160$ Å and metal NPs composed of a maximum of 10179 atoms (see also Tables S2 and S3 in the Supporting Information (SI)). The dipolar plasmon resonance frequency (PRF) of each PS (see Tables S2 and S3 in the SI) varies from 3.64 to 3.42 eV for Ag, and from 2.31 to 2.17 eV for Au. In the case of GDs, the PRF varies from 0.61 to 0.24 eV. In QM/ωFQ(Fμ) calculations, pyridine (PY) is described at the QM level by using BP86 or B3LYP DFT functionals, as coupled with a double−ζ polarized (DZP) or a triple−ζ polarized (TZP) basis set.[108] To simulate Raman/SERS spectra, frequency-dependent polarizabilities $\overline{\alpha}(\omega)$ are calculated[109,110] by setting Γ (see eq 19) to 0.10 eV.[35] The $\overline{\alpha}(\omega)$ geometrical derivatives are obtained by means of a numerical differentiation scheme[111−113] by using a constant step size of 0.001 Å. Similar results are obtained by using a step size of 0.0005 Å (see Figure S1 in the SI). In this first application, normal modes of displacement are calculated on the isolated QM molecule because we expect vibrational frequency shifts induced by the nanostructure to be negligible, as has been shown by previous studies (see for instance refs 35, 40, and 105). Frequency-dependent polarizabilities and SERS spectra are calculated by setting the frequency ω as the PRF of each plasmonic substrate (see Tables S2 and S3 in the SI); moreover, the final SERS spectra are obtained by convoluting raw data with Lorentzian band-shapes (full width at half-maximum (fwhm) of 4 cm^{-1}). The ωFQ parameters for GDs are taken from ref 64, whereas ωFQFμ parameters for silver and gold are taken from ref 61. All QM/ωFQ and QM/ωFQFμ calculations are performed by using a locally modified version of the AMS software.[94,95]

In the following, we evaluate the Raman enhancement associated with the k-th normal mode in terms of the enhancement factor (EF):

$$\mathrm{EF}^k(\omega) = \frac{I^k_{\mathrm{PS}}(\omega)}{I^k_{\mathrm{vac}}(\omega)} \quad (28)$$

where $I^k_{\mathrm{PS}}(\omega)$ and $I^k_{\mathrm{vac}}(\omega)$ are the Raman intensities of the k-th normal mode evaluated for the molecule-PS and the molecule in gas-phase systems, respectively (see eq 23). Since EF clearly depends on the selected normal mode, it is convenient to define a spectrally averaged enhancement factor (AEF) as follows:[49]

$$\mathrm{AEF}(\omega) = \frac{\sum_k I^k_{\mathrm{PS}}(\omega)}{\sum_l I^l_{\mathrm{vac}}(\omega)} \quad (29)$$

where the indices k and l run over the normal modes of the target molecule (in the selected spectral region). As an additional measurement of calculated enhancement, we also introduce the maximum enhancement factor (MEF), i.e.:

$$\mathrm{MEF}(\omega) = \max_k \mathrm{EF}^k(\omega) \quad (30)$$

4. NUMERICAL RESULTS

In this section, we first discuss the capability of QM/ωFQ and QM/ωFQFμ to correctly describe the physicochemical features of the molecule-plasmonic substrates system. To this end, QM/ωFQ and QM/ωFQFμ approaches are first applied to the simulation of SERS spectra of pyridine (PY, see Figure 1a), which has been the first molecular system for which SERS was experimentally observed.[1,18,114] Also, thanks to its small size, PY is a perfect prototype to test our novel approach. PY is adsorbed on two PSs: metal NPs and graphene disks (GDs).

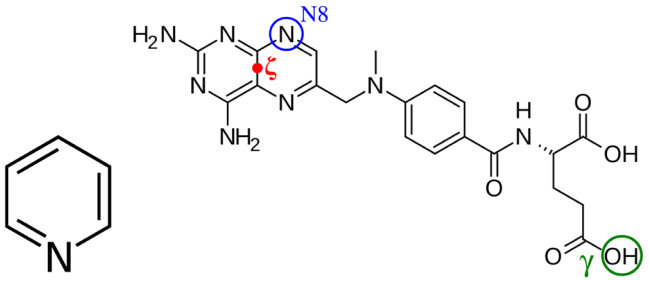

(a) Pyridine (b) Methotrexate

Figure 1. Pyridine (a) and methotrexate (b) molecular structures. In panel b, we highlight the position ζ (red), which indicates the center of MTX aromatic rings, the N8 atom (blue) and the OH (green) of the γ-carboxyl group.

https://doi.org/10.1021/acs.jctc.3c00177
J. Chem. Theory Comput. 2023, 19, 3616−3633

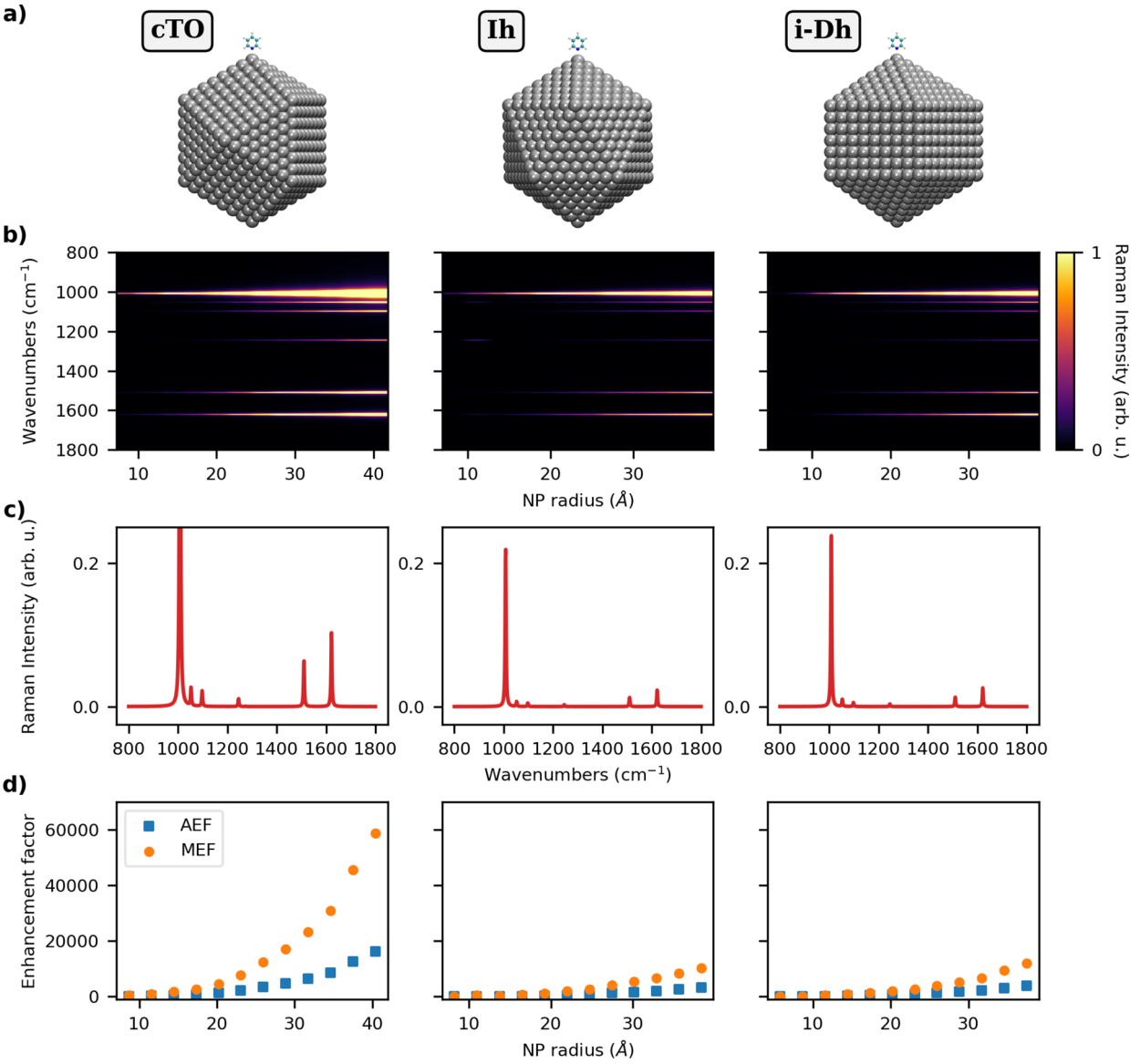

Figure 2. a) Graphical depiction of PY-Ag cTO (left), Ih (middle), and i-Dh (right) systems; (b) color plot of normalized SERS spectra as a function of the NP radius; (c) normalized SERS spectra of PY adsorbed on the largest NP structure for each shape; (d) AEF and MEF as a function of the NP radius. SERS signal is computed at the PRF of each Ag NP (3.54−3.42 eV for cTO; 3.64−3.51 eV for Ih; 3.52−3.42 eV for i-Dh; see also Table S2 in the SI).

We first validate our novel approach by studying the dependence of Raman enhancements on the morphology and the PS chemical composition, the molecule-PS distance, and spatial arrangement. Finally, we present an application of the approach to the simulation of a real-case scenario, i.e. methotrexate (MTX, see Figure 1b), adsorbed on a graphene disk.

4.1. Model Testing. *4.1.1. Metal Nanoparticles. 4.1.1.1. Dependence of Enhancement Factors on the Nanostructure Properties.* In this section, we study how the morphology, the size, and the chemical composition of the PS affect the SERS signal. To this end, PY is adsorbed on silver and gold cTO, Ih, and i-Dh NPs with a radius varying from about 6 to 40 Å (see Figures 2a and 3a and Table S2 in the SI). PY is adsorbed standing on the vertex of each structure along the y axis by setting a distance of 3 Å between the Nitrogen atom and the NP vertex, similarly to previous studies.[35] The results obtained by treating PY at the B3LYP/DZP level of theory are graphically reported in Figures 2 and 3, for Ag and Au NPs, respectively (see Figure S2 in the SI for their analogous calculated at different levels of theory). In particular, in Figures 2b and 3b SERS spectra of the three different configurations as a function of the NP radii are reported, whereas in the corresponding c panels, the dependence of both AEF and MEF on the NP radii is graphically depicted. Note that the introduction of such a screening function guarantees the stability of the results by changing the DFT integration grid (see Figure S3 in the SI).

Let us first discuss the results obtained for Ag NPs. By focusing on Figure 2b, it can be noticed that SERS intensities strongly depend on the NP size, increasing as the NP size increases. The enhancement is not the same for all normal modes. Indeed, the vibrations modulating the components of the electronic polarizability orthogonal to the NP surface are associated with larger SERS intensity, because both the incident radiation and the scattered field benefit from the

https://doi.org/10.1021/acs.jctc.3c00177
J. Chem. Theory Comput. 2023, 19, 3616−3633

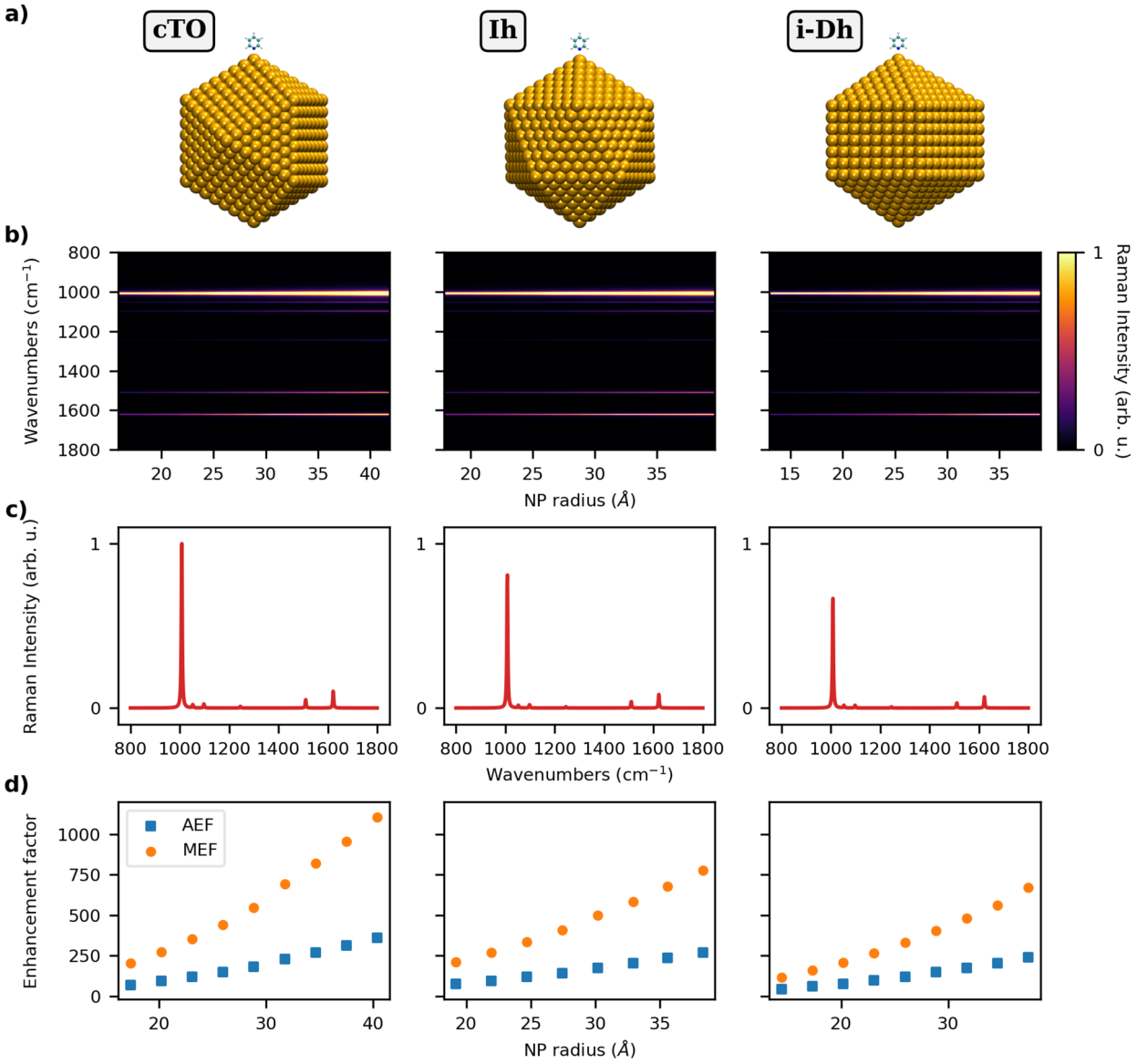

Figure 3. a) Graphical depiction of PY-Au cTO (left), Ih (middle), and i-Dh (right) systems; (b) color plot of normalized SERS spectra as a function of the NP radius (Å); (c) normalized SERS spectra of PY adsorbed on the largest NP structure for each shape; (d) AEF and MEF as a function of the NP radius. SERS signal is computed at the PRF of each Au NP (2.27−2.17 eV for cTO; 2.29−2.21 eV for Ih; 2.31−2.17 eV for i-Dh; see also Table S2 in the SI).

EM enhancement. For instance, this is evident for the ring breathing mode at 1008 cm^{-1} (see Figure S4e in the SI) and the symmetric bending modes of the α-hydrogen atoms at 1510 and 1622 cm^{-1} (see Figure S4n,p in the SI), which are characterized by the largest SERS intensities (see also Figure 2c where SERS spectra for the largest NPs are graphically reported). It is also interesting to note that depending on the morphology of the NPs, a different SERS spectrum can be obtained. In fact, Figure 2b shows that SERS spectra obtained by adsorbing PY on Ag Ih and i-Dh NPs display a significantly different relative intensity patterns as compared to PY on Ag cTO SERS spectrum. This is important to remark, as it shows that the details of the local electric field distribution (such as electric field gradients) are accounted for in the modeling and have a visible effect on SERS spectra. A selection of all enhancement factors of PY adsorbed on selected PS is reported in Table S4 in the SI.

To further analyze such results, Raman enhancements can be quantified in terms of AEF and MEF (see eqs 29 and 30). Their dependence on the NP radius is reported in Figure 2d, which shows that the shape of the NP strongly affects their values. In particular, cTO-based structures yield the largest enhancement factors as compared to the other considered morphologies. Interestingly, for small nanostructures, the most enhanced normal mode is the asymmetric bending of α-hydrogen atoms at 1388 cm^{-1} (see Figure S4l in the SI), while for the largest structures the MEF is associated with the symmetric bending of the same α-hydrogen atoms at 1510 cm^{-1} (see Figure S4n in the SI). In order to rationalize the differences between the three different shapes, we can resort to the so-called E^4 approximation,[15,115] which states that Raman enhancements are proportional to the fourth power of the electric field induced on the NP. Thus, we define Υ^4_{vol} as follows:

https://doi.org/10.1021/acs.jctc.3c00177
J. Chem. Theory Comput. 2023, 19, 3616−3633

$$\Upsilon^4_{vol} = \frac{1}{V}\int_V \frac{|\mathbf{E}^{tot}(\omega)|^4}{|\mathbf{E}^{ext}(\omega)|^4}\mathrm{d}\mathbf{r} \quad (31)$$

where V is the molecular volume, $\mathbf{E}^{tot}(\omega)$ is the total electric field, whereas $\mathbf{E}^{ext}$ is the incident external electric field aligned with NP main axis. $\mathbf{E}^{tot}(\omega)$ is computed on a box, with sides placed at a distance of 1 Å from each PY atom. It is worth remarking that in ωFQFμ the fluctuating multipoles are associated with a spherical Gaussian distribution,[61,68] which is taken into account in the calculation of the electric field intensity.[60] The AEF-Υ^4_{vol} correlation as a function of the NP radius is depicted in Figure 4 for Ag cTO, Ih, and i-Dh

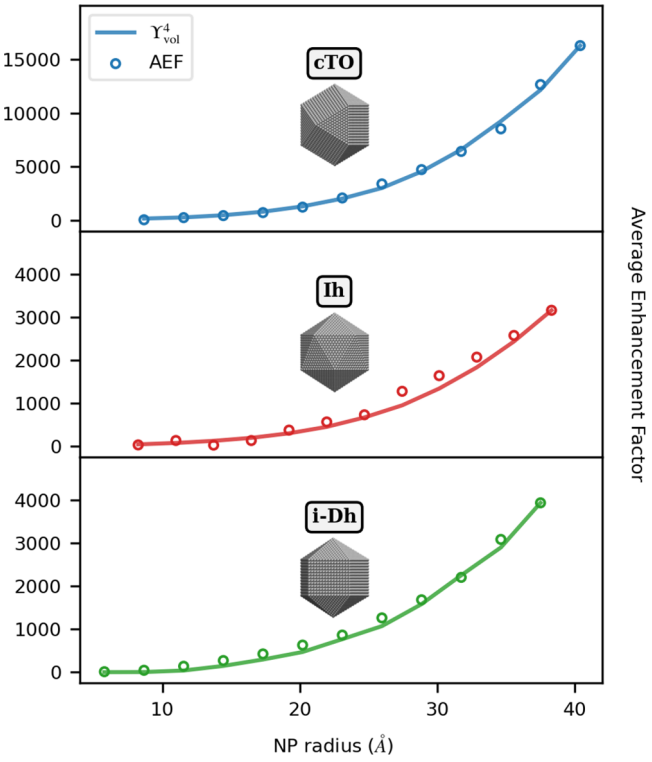

Figure 4. AEF (circles) and normalized Υ^4_{vol} (solid line, see eq 31) for PY-Ag as a function of the NP radius and morphology (cTO, Ih, and i-Dh). The SERS signal is computed at the PRF of each Ag NP (3.54−3.42 eV for cTO; 3.64−3.51 eV for Ih; 3.52−3.42 eV for i-Dh; see also Table S2 in the SI).

substrates. Note that Υ^4_{vol} values are normalized to the largest AEF for each morphology. Absolute AEF and Υ^4_{vol} values are reported in Table S4 in the SI. The two data sets quantitatively differ, probably due to the high inhomogeneity of the electric field in the proximity of the NP surface, in agreement with ref 35.

The agreement between AEF and Υ^4_{vol} is almost perfect, independently of the size and shape of the Ag NPs. Also, we can justify the larger enhancement factors (AEF and MEF) reported in Figure 2c for cTO with respect to Ih and i-Dh arrangements. Indeed, they are due to a greater induced field, as shown in Figure 4. This is not surprising and is in line with the results recently reported by us in ref 61, which highlighted cTO as the most effective morphology to provide near-field enhancement.

A similar analysis can also be performed by modifying the chemical composition of the NPs. To this end, we consider the same NPs shapes, but made of Au atoms (see Figure 3a). As recently reported in ref 61, ωFQFμ predicts a dipolar PRF only for Au NPs with a radius larger than 15 Å (see also Table S2 in the SI). SERS spectra and the AEF/MEF of PY adsorbed on Au cTO, Ih, and i-Dh arrangements as a function of the radius are reported in Figure 3b,c,d, respectively.

Similarly to the Ag case, the most intense SERS signals are associated with the normal modes involving the PY ring (1008 cm^{-1}, see Figure S4e in the SI) and the α-hydrogen atoms (1510 and 1622 cm^{-1}, see Figure S4n,p in the SI, respectively). However, the computed SERS intensities are much lower as compared to the PY-Ag case. By inspecting SERS spectra calculated by considering the largest Au NP (see Figure 3c), we can indeed notice that slight qualitative discrepancies are reported with respect to PY-Ag (see Figure 2c). In fact, the SERS spectra of PY on the selected morphologies are characterized by similar relative intensities between the most intense peaks, and the differences among the three spectra are thus less accentuated than the PY-Ag case.

Computed AEF/MEF indices (see Figure 3d) are also much lower as compared to the PY-Ag case, independent of the NP shape. In this regard, it is worth highlighting that Au PRF is lower than Ag PRF (~2.2 eV vs ~3.5 eV), and this also numerically affects the Raman intensities of the molecule in the gas phase. However, the noticeable decrease of AEF/MEF is primarily due to the fact that the electric field generated by the dipolar plasmon of Au NP is much less intense than for Ag. Therefore, a smaller enhancement of the Raman intensities is observed. This is demonstrated by the numerical values of AEF, and by the fact that the correlation between AEF and Υ^4_{vol} worsens (see Figure S5 in the SI). The reported behavior of Au nanoparticles (see Figure S5 in the SI) has also been previously reported by exploiting other QM/classical approaches.[35]

In case of Au, the E^4 approximation is less accurate, probably because the local field is less intense. In fact, AEF results from the mixing of vibrational normal modes that are enhanced according to different powers of the electric field, up to E^4. When the local field experienced by the molecular system is large, the E^4-dependent vibrational normal modes will dominate the AEF value, thus clearly complying with the E^4 approximation (see Section S1 in the SI for further details).

4.1.1.2. Dependence of AEF on PY-NP Distance. As it has been stated in section 2.2, the local field plays a key role in the enhancement of Raman intensities. In this section, we study how AEF behaves as a function of the distance between the molecule and the PS. As a proof of concept, we consider again the case of PY adsorbed on the largest Ih Ag NP (10179 atoms, radius = 38.30 Å, see Table S2 in the SI), for which we compute the SERS spectrum by increasing the distance d between the Nitrogen atom and the PS tip. QM/ωFQFμ results are reported in Figure 5 for $3 \leq d \leq 10$ Å. Analogous results for Au NP are given in Figure S6 of the SI.

As expected, Figure 5 clearly shows that Raman intensities rapidly decay by increasing d ($\sim d^{-4}$). In particular, AEF decreases from about 1000 at $d = 3$ Å to about 14 at $d = 10$ Å. A similar behavior is observed for MEF. In particular, for $d < 4$ Å, MEF is associated with the symmetric bending of the α-H (1510 cm^{-1}, see Figure S4n in the SI), while for $d \geq 4$ Å the asymmetric bending of the same hydrogens (1098 cm^{-1}, see Figure S4h in the SI) yields the maximum enhancement.

To rationalize these findings, AEF values as a function of d can be compared to the aforementioned E^4 approximation. To this end, we compute the induced electric field in the molecular PY volume as a function of the PY-PS distance.

https://doi.org/10.1021/acs.jctc.3c00177
J. Chem. Theory Comput. 2023, 19, 3616−3633

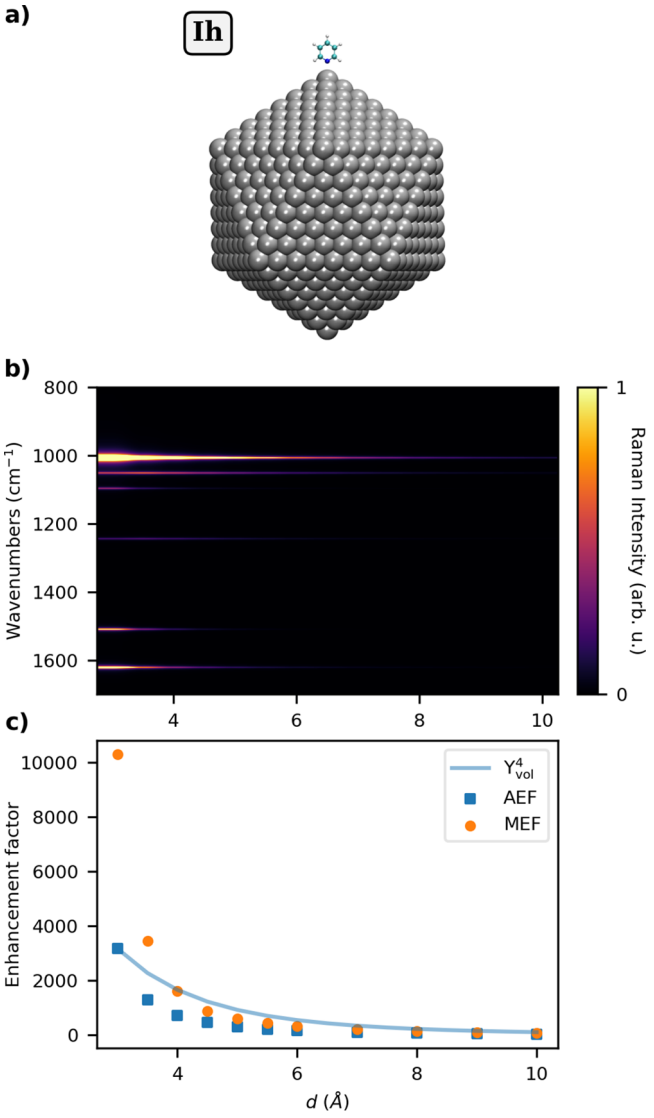

Figure 5. (a) Graphical depiction of PY-Ag_{10179} Ih system; (b) color plot of normalized SERS spectra as a function of the PY-NP distance d (Å); (c) AEF, MEF, and normalized Υ^4_{vol} as a function of d. The SERS signal is computed at the PRF of the Ag NP (3.51 eV, see also Table S2 in the SI).

Such values are graphically depicted in Figure 5c (see Figure S6c in the SI for the Au NP case). As also commented above for Figure 4, both the approximated estimation Υ^4_{vol} and computed AEF rapidly vanish as the distance increases. Indeed, it can be noticed that the curves follow a different trend as a function of the distance, which can be ascribed to the fact that AEF comes from the average of different enhancement factors associated with vibrational normal modes according to different powers of the electric field, up to E^4. Also for Au (see Figure S6c in the SI), small discrepancies are reported, probably related to lower local field effects compared to Ag. Absolute AEF and Υ^4_{vol} values are reported in Table S7 in the SI.

4.1.1.3. Dependence of AEF on Molecule-PS Configuration. In the previous examples, we have discussed how SERS spectra might depend on the NP morphology and chemical nature of the atoms constituting the NP, as well as on the mutual molecule-NP distance. In this section, we discuss how the relative configuration of the molecule-PS system affect the SERS spectrum and enhancement. As a proof of concept, we consider three different PY adsorption positions on Ag_{10179} Ih NP. The most representative points of the icosahedral structure are selected (see Figure 6, bottom): vertex (PY-V, red dot), edge (PY-E, green dot), and face (PY-F, blue dot). In all configurations, PY is adsorbed perpendicularly to the NP surface at a distance of 3 Å, with the nitrogen atom laying closest to the NP. As for the previous cases, the Raman signal is computed by means of eq 23, by irradiating the PY/Ag_{10179} system with an external electric field polarized along the x, y, and z directions. Calculated QM/ωFQFμ SERS spectra are graphically reported in Figure 6, together with the computed Raman spectrum of PY in the gas phase.

As a result of the PY-NP interaction, the Raman spectrum undergoes drastic changes when moving from the in vacuo to the adsorbed case. This can be particularly appreciated by the changes in relative intensities between the two most intense Raman peaks in vacuo, which are associated with the ring breathing (1008 cm^{-1}, see Figure S4e in the SI) and the symmetric bending of the α-H (1053 cm^{-1}, see Figure S4f in the SI), respectively. Indeed, for all the selected absorption sites, the relative intensity of the bending mode (1053 cm^{-1}) decreases with respect to that of the ring breathing mode (1008 cm^{-1}), almost vanishing in the case of PY-V (red). Other major differences for PY-F (blue), PY-E (green), and PY-V (red) are reported, for which the relative intensity between the most intense peaks (1000−1100 cm^{-1}) and the other dominant bands completely differ with respect to the gas phase.

The spatial PY-PS arrangements not only affect the spectral shape but also the enhancement factors. In this respect, AEF for PY-V is 2 orders of magnitude larger than the values computed for both PY-F and PY-E configurations. The same trend is also observed for MEF, which is interestingly associated with different normal modes depending on the relative PY-PS position. In fact, normal modes involving α-H atoms feature the maximum enhancements for all cases (graphically highlighted in Figure 6 with a star): symmetric bending (PY-V case, 1588 cm^{-1}, Figure S4n in the SI), asymmetric bending (PY-F case, 1388 cm^{-1}, Figure S4l in the SI), and out-of-plane vibrations (PY-E, 956 cm^{-1}, Figure S4b in the SI). Such differences are directly related to the relative PY-PS arrangements and are intuitively associated with normal modes providing the largest polarizability variation.

All the reported differences, in both computed SERS spectra and AEF/MEF values, can be related to the inhomogeneity of the electric field induced by the geometrical shape of the Ag NP, which clearly differs by moving for the vertex (PY-V) to a face (PY-F) of the Ih morphology. In fact, the largest changes with respect to the gas-phase spectra/values are predicted for the PY-V configuration (red), for which we observe the largest AEF ($\sim 10^3$) and a drastically different Raman spectrum. Such findings are perfectly explained by the tip effect,[69] which characterizes most plasmonic materials. In fact, in the PY-V configuration, PY is adsorbed to the sharpest region of the Ih NP.

In order to show the effect of the inhomogeneity of the electric field in the surroundings of metal nanoparticles, we have performed additional calculations on the pyridine/Ag_{10179} system in the Ih morphology by changing the relative position of the molecular substrate with respect to the tip of the Ih nanostructure (see Figure S7 in the SI for more details). For each of these configurations, SERS spectra and AEF values

https://doi.org/10.1021/acs.jctc.3c00177
J. Chem. Theory Comput. 2023, 19, 3616−3633

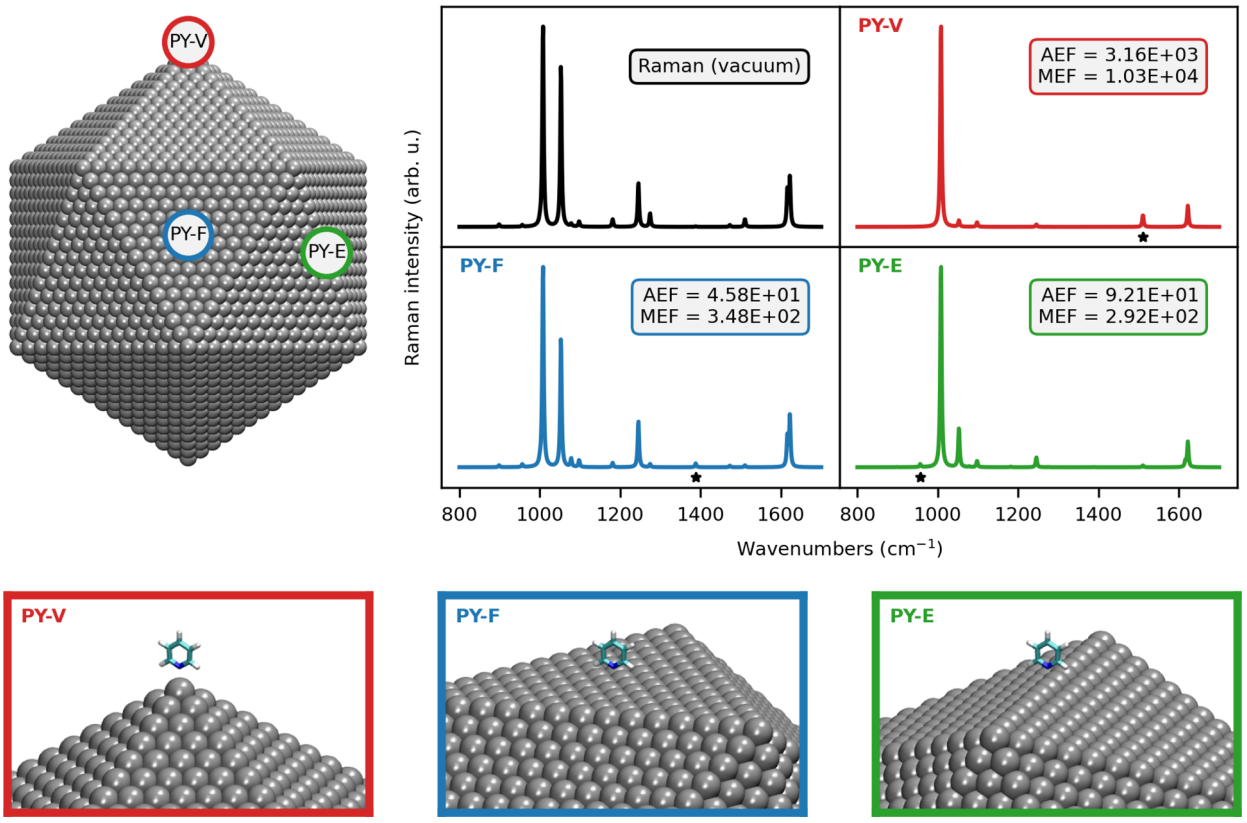

Figure 6. Normalized QM/ωFQFμ PY SERS spectrum as a function of the adsorption site of PY on the Ih Ag_{10179} NP (upper left and bottom panels). AEF and MEF for each configuration are also given. The vibrations associated with the MEF are indicated with a star. The SERS signal is computed at the PRF of the Ag NP (3.51 eV, see also Table S2 in the SI).

have been computed, and the results are reported in Figures S7 and S8.

4.1.1.4. Comparison with Available Experiments. To conclude the discussion, we compare our QM/ωFQFμ calculations with experimental data available in the literature (Figure 7 (a-Ag, b-Au).[116,117] We note that our calculations are based on an ideal representation of experimental conditions. Instead, measured spectra result from the interplay between several effects which are not necessarily accounted for in the modeling, such as solvent effects, the coating of the metal electrode, external bias applied, impurities and the roughness of the metal surface. For these reasons, similarly to previous computational studies,[35] the comparison between our results and experiments may only be qualitative.

Let us first focus on PY SERS on the Ag electrode, for which experimental spectra at different bias potential have been measured (see Figure 7).[116] The experimental spectrum at zero bias (0.00 V) is dominated by two bands at about 1000 and 1050 cm^{-1}, whose relative intensities are inverted at higher voltages (see bottom panels). Remarkably, the same bands are also the most intense in computed QM/ωFQFμ SERS spectra, for all investigated PY-PS configurations. Another relevant feature of experimental SERS spectra is the band at about 1200 cm^{-1}, which only becomes visible by increasing the external bias (see bottom panels in Figure 7). For this reason, such a band has been commonly associated with a CT mechanism. As stated above, QM/ωFQFμ only accounts for the EM mechanism. Remarkably, and differently from previous models,[35] our approach is able to predict such a feature, because the 1200 cm^{-1} peak is almost absent in the SERS spectrum of the most intense configuration (PY-V, top panel), thus confirming previous hypotheses assigning that band to CT effects.

Similar qualitative trends hold for the Au substrate. Indeed, the experimental SERS spectrum (which refers to an unbiased electrode) is dominated by the bands at about 1000−1050 cm^{-1}. A similar behavior is observed in the computed spectrum. In addition, the band at about 1200 cm^{-1} is almost absent in both experimental and theoretical SERS spectra.

4.1.2. Graphene Disks. In order to show the versatility of QM/ωFQ(Fμ), here we extend the previous study to PY adsorbed on 2D graphene-based substrates,[118,119] which to this end, is a set of 8 GDs with a radius 20 < r < 160 Å (see also Table S3 in the SI). PY is assumed to be adsorbed on the GD center of mass, parallel to the GD surface at a distance of 3 Å (see Figure 8a). Such a distance is chosen because it is close to the equilibrium PY-GS distance reported in the literature.[120] For each PY-GD, GERS spectra are calculated at the B3LYP/DZP level of theory, and the results are reported in Figure 8b. Note that, in all calculations, E_F = 0.4 eV, according to typical reported Fermi energy values.[121,122] We note, however, that the PRF of graphene-based materials can be tuned by varying the external bias, thus affecting E_F. When applied to GERS, such a feature can be exploited to make the PRF coincide with a molecular excitation of the system under investigation, thus resulting in a pragmatical method to yield resonance Raman assisted by graphene plasmons. Although our approach is general enough to account for such an effect, this is not investigated in this first work.

From the analysis of GERS spectra, we first note that Raman relative intensities are different from those reported in the case of PY-metal NP systems (see Figures 2 and 3), with the

https://doi.org/10.1021/acs.jctc.3c00177
J. Chem. Theory Comput. 2023, 19, 3616−3633

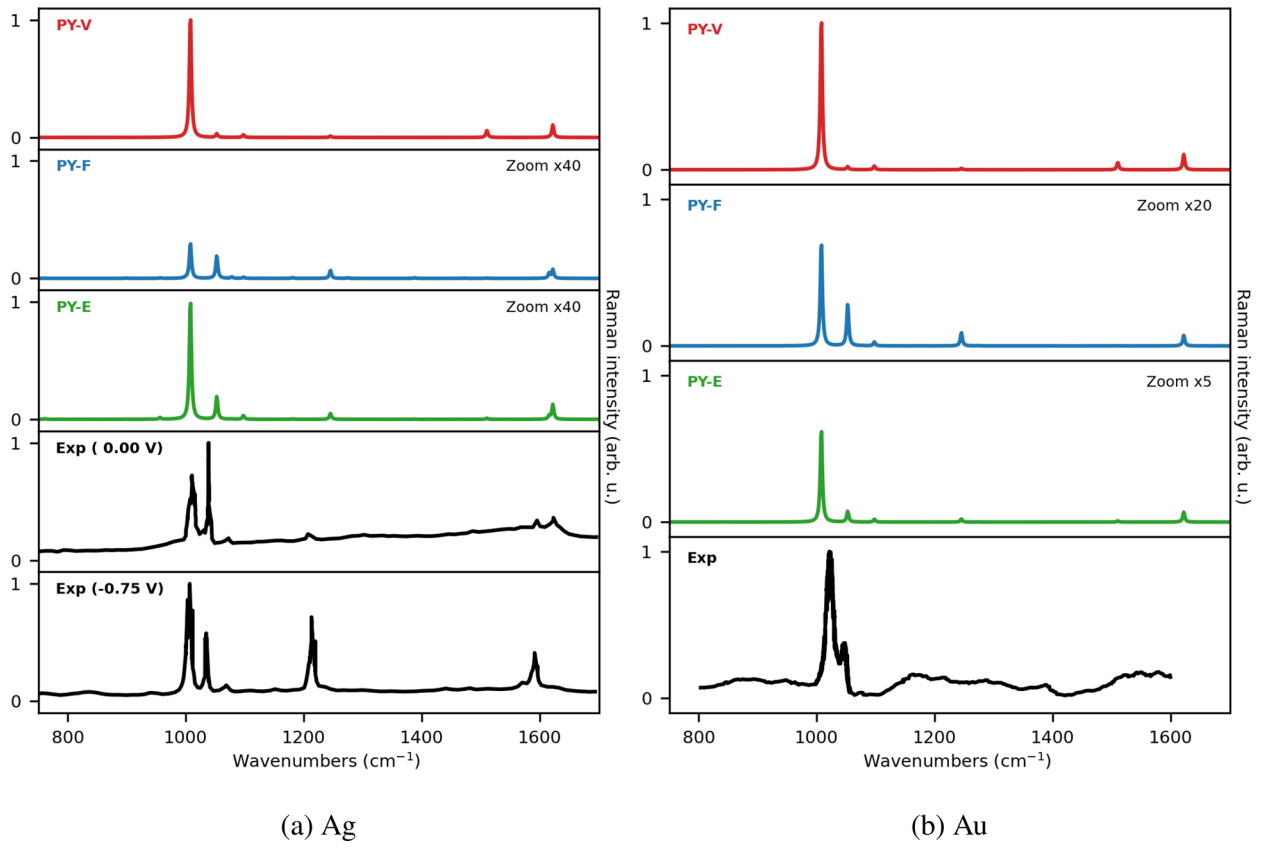

Figure 7. QM/ωFQFμ SERS spectra of PY adsorbed on Ag_{10179} (a) and Au_{10179} (b) Ih NPs (see also Figure 6). Experimental spectra measured for Ag (a, at 0.0 eV and −0.75 eV external bias) and Au (b, at 0.0 eV) electrodes, reproduced from ref 116. (Ag) and 117 (Au) are also reported. The SERS signal is computed at the PRF of the NPs (3.51 eV for Ag; 2.21 eV for Au; see also Table S2 in the SI).

presence of additional peaks. The latter are mainly related to normal modes involving the vibrations of β and γ H atoms of the pyridine ring (1181 and 1274 cm^{-1}, see Figure S4i,k in the SI). This is the result of the PY-GD morphology under investigation. In fact, the parallel configuration of the PY ring with respect to the GD plane allows for a large variation of the polarizability associated with the aforementioned normal modes. Nevertheless, GERS spectra are still dominated by the PY ring breathing and the asymmetric bending of the α hydrogens (1000−1100 cm^{-1}), as already reported for the case of metal NPs. The most relevant dissimilarity between the two substrates is the dependence of GERS spectra on the GD r. In fact, Figure 8 clearly shows that for a large r ($\geq$120 Å) the Raman signal vanishes as compared to for a small r ($\leq$40 Å), thus reporting the opposite trend as compared to metal NPs (see Figures 2b and 3b).

To rationalize this trend, AEF values as a function of r are reported in Figure 8d. Absolute AEF and Υ^4_{vol} values are given in Table S5 in the SI. Different from metal NPs, in this case the two data sets are almost in perfect agreement, even quantitatively. This is related to the absence of inhomogeneities in the induced field at the center of the graphene disk.

A local maximum is observed for r = 40 Å, which rapidly decays for larger r values. As for the metal NPs, the electric field generated by the GD increases with the radius. Therefore, a larger enhancement of the Raman intensity is expected. However, for the specific configuration of the GD system, the electric field is much more intense on the edges (see ref 60). Since the distance between PY (adsorbed on the GD center of mass) and the GD edges increases with r, the enhancement factor and the Raman signal decrease as compared with small r (see Figure 8b). The combination of such effects is responsible for the local maximum in the 40 Å case, in which the electric field at the center of the GD is large enough to substantially increase Raman intensities and therefore PY enhancement factors. Indeed, the trend of AEF as a function of GD r can be explained by means of the Υ^4 approximation, analogously to metal NPs. The correlation between AEF and Υ^4_{vol} is shown by Figure 8d; the agreement is almost perfect, thus justifying the reported behavior in terms of EM enhancement.

We finally remark that our methodology can in principle simulate all possible PY-GD configurations. However, in this work we have restricted the analysis to the selected geometry because it better represents, from the physicochemical point of view, the most favorable configuration of a target molecule adsorbed on a graphene sheet, i.e. far from the edges. Within this picture, in fact, we aim to mimic the common experimental setup that is generally constituted of a graphene substrate with intrinsic dimensions much larger than those considered in this work.[67] We point out that different PY-GD configurations can provide higher enhancements, as we have recently reported in ref 60.

4.2. Increasing the Chromophore Complexity: Methotrexate Adsorbed on Graphene Disks. In this section, we discuss the application of the model to a realistic case, i.e. methotrexate adsorbed on a graphene disk (see Figure 1b for the molecular structure). Differently from PY, MTX is a flexible molecule. Therefore, reliable modeling needs to account for the different conformations. To this end, we perform molecular dynamics (MD) simulations by using

https://doi.org/10.1021/acs.jctc.3c00177
J. Chem. Theory Comput. 2023, 19, 3616−3633

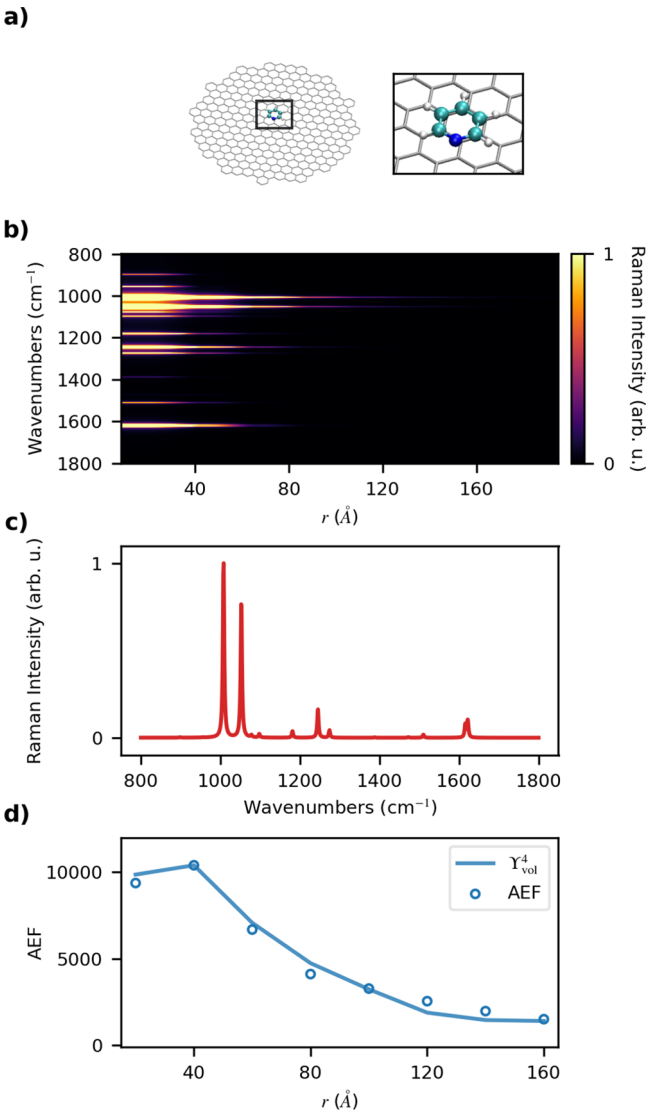

Figure 8. (a) Graphical depiction of the PY-GD system. (b) Color plot of normalized SERS spectra as a function of the GD radius r (Å). (c) Normalized SERS spectra of PY adsorbed on a GD with r = 40 Å, (d) AEF and Υ^4_{vol} as a function of r. The SERS signal is computed at the PRF of each GD (0.61−0.24 eV, see also Table S3 in the SI).

ReaxFF,[123,124] within its dedicated engine[125] in the Amsterdam Modeling Suite (AMS).[95] The ReaxFF force field developed in ref 126, and which has been reported to reliably describe graphene-based systems, is employed.[127] Temperature is maintained at 300 K by using a Nosé−Hoover chain (NHC) thermostat,[128] with a damping constant of 100 fs. In NPT simulations, constant pressure is enforced by using the Martyna−Tobias−Klein barostat with a damping constant of 100 fs.[129] 20 layers of graphite, composed of 50 atoms each, are prepared in a 3-D hexagonal periodic cell with lattice parameters $a = b$ = 12.3 Å and c = 67.1 Å. A 100 ps NPT calculation is then run by imposing a pressure of 1 atm in all directions. At this point, the simulation box is enlarged so that $a = b$ = 62.52 Å and c = 100 Å, and only 10 layers of graphite, formed by 1250 carbon atoms each, are kept. Then a 50 ps NPT simulation is performed by imposing a pressure of 1 atm in the planar directions. No substantial changes in the values of a and b are detected during pressure equilibration. After this, MTX is thermalized in an empty 3-D hexagonal periodic box with lattice parameters $a = b$ = 62.52 Å and c = 100 Å by means of a 62.5 ps NVT simulation. Thermalized MTX is then placed at a distance of ∼10 Å from the equilibrated graphitic surface and a production NVT simulation of 375 ps is performed. After 125 ps, the temperature is equilibrated and the center of the aromatic rings of MTX (ζ-point in Figure 1b) is adsorbed at an average distance of ∼3.42 Å from the first graphitic layer, in agreement with previous studies.[130] Notably, during the adsorption process, we observe the intramolecular hydrogen transfer between the γ-carboxyl group (green circle in Figure 1b) and the N8 atom (blue circle in Figure 1b).

After MTX adsorption, we extract 5000 snapshots from the remaining 250 ps of the production run. MTX geometries are processed by means of the GROMOS[131] clustering approach as it is implemented in the 2020.3 version of the GROMACS[132,133] software. As a result, only two MTX geometries are selected, representing 68.7% (MTX1) and 28.8% (MTX2) of the total configurational space. The two structures are reported in Figure 9b (see also Figure S9 in the SI).

To simulate MTX GERS, we remove the graphitic substrate, and we substitute the first layer by a perfect GD with r = 16 nm (GD16, see Table S3 in the SI) on the center of which MTX is adsorbed. MTX1 and MTX2 Raman (in gas phase) and GERS spectra are finally computed at the B3LYP/DZP level of theory, by setting E_F = 0.4 eV (PRF = 0.24 eV). Spectra are reported in Figure 9a.

MTX1 and MTX2 Raman spectra, both in the gas phase and adsorbed on GD16, qualitatively differ, as they are characterized by a shift in vibrational frequencies, and in relative intensities of the main bands. Indeed, while the MTX1 Raman spectrum is dominated by the presence of intense bands in the low energy region (between 600 and 800 cm^{-1}), the MTX2 spectrum reports diverse intense peaks in the whole considered spectral range. The different MTX1 and MTX2 spectral fingerprints reflect the intrinsic dissimilarity in MTX conformations, as expected from the clustering process. When moving from the gas phase to the adsorbed configuration, both MTX1 and MTX2 Raman spectra are enhanced by an AEF of about 900. However, Raman spectra undergo small qualitative variations. Such findings can be rationalized by considering that the plasmonic electric field generated by the GD is strongly inhomogeneous at the GD edges, while at the GD center it is almost uniform. Therefore, we expect that the electric field felt by each normal mode is essentially uniform, although more intense than in vacuo. To analyze this hypothesis from a quantitative point of view, we compute for both structures the EFs associated with each normal mode (see eq 28), which are graphically depicted in Figure 10a. In particular, for each normal mode, EFs are plotted with a color scale that follows the intensities of the corresponding Raman peak.

Except for a few outliers, all computed EFs are almost equal independent of the normal mode and fall around the AEF (about 900). The normal modes featuring the highest EF are depicted in Figure 10b. However, these modes are associated with rather low-intensity bands. On the contrary, EFs computed for the most intense Raman peaks, which dominate the computed spectra, are almost constant at a value of around 900. As it can be noticed, it is difficult to find a correlation between the most intense normal modes of both conformers because they are localized on separated regions of the MTX structure, independent of the distance with respect to the GD

https://doi.org/10.1021/acs.jctc.3c00177
J. Chem. Theory Comput. 2023, 19, 3616−3633

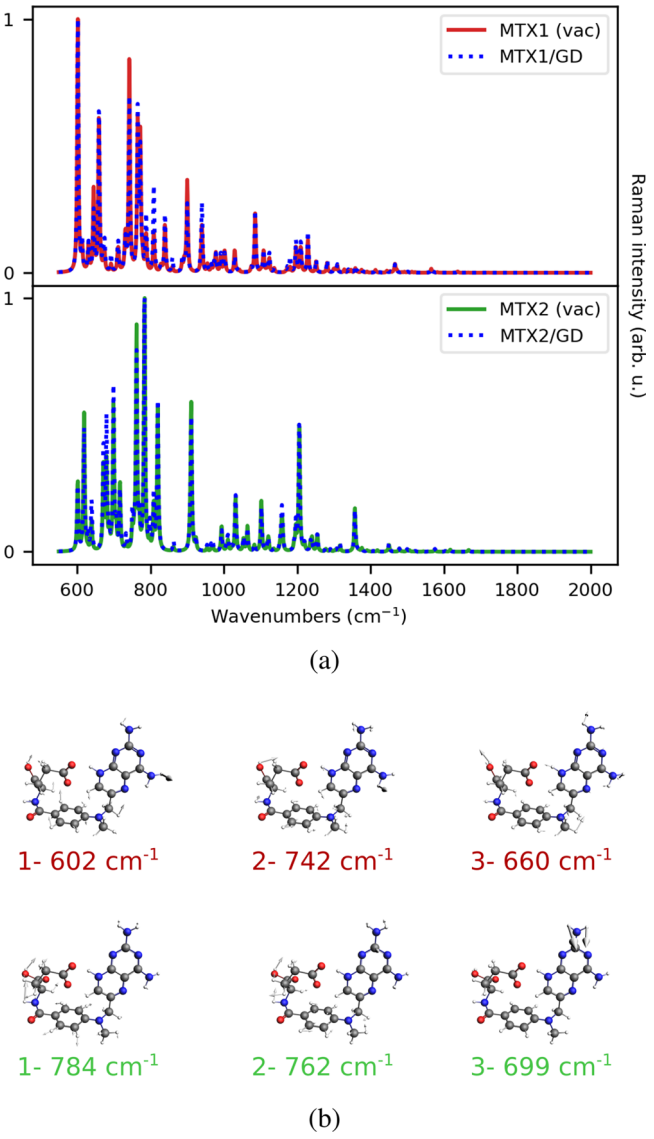

Figure 9. (a) Normalized MTX1 and MTX2 Raman spectra as computed in vacuo (solid line) and adsorbed on GD16 (dashed line). (b) MTX1 and MTX2 normal modes associated with the highest Raman intensities. The Raman signal is computed at GD18 PRF (0.24 eV, see also Table S3 in the SI).

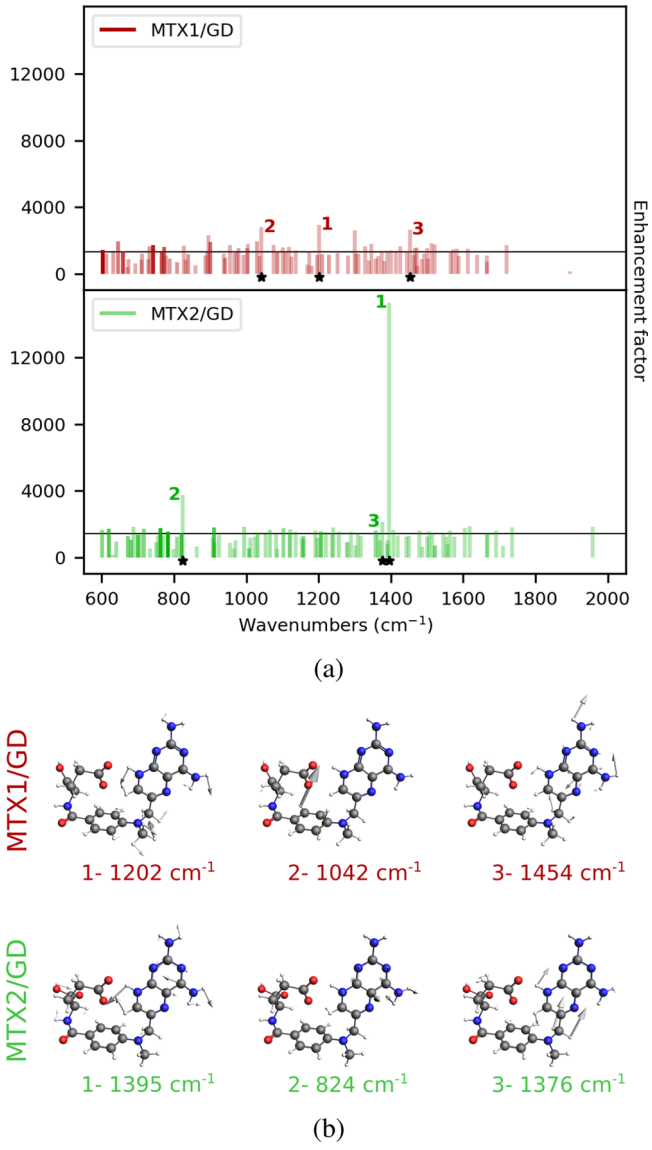

Figure 10. (a) Computed QM/ωFQ MTX1/GD18 (top) and MTX2/GD18 (bottom) normal modes' EFs and AEF reported as horizontal black lines. The darkness of each bar is proportional to the Raman intensity. (b) MTX1 and MTX2 normal modes associated with the largest EFs.

surface. In light of the above discussion, this is not surprising. In fact, the presence of the GD yields an almost uniform increase of the Raman bands as compared to the case in vacuo, without greatly affecting their relative intensities. Thus, the most intense peaks are related to the same normal modes that provide the most intense bands in the gas-phase Raman spectrum.

To conclude the discussion, in Figure 11 we report the MTX/GD16 GERS spectrum as obtained by averaging MTX1 and MTX2 spectra, which are also graphically depicted.

The most important contribution to the Raman spectrum is due to the MTX1 structure (68.7%). Therefore, only the most intense peaks of MTX2 arise noticeably in the averaged spectrum. MTX2 bands, however, drastically affect the final GERS spectrum, which does not present anymore the spectral fingerprints related only to MTX1 or MTX2. Moreover, the final spectrum is particularly noisy, especially in the high-frequency region. This is essentially due to small differences between the vibrational frequencies of the two conformers.

Finally, it is worth pointing out that, for the system under consideration, graphene is able to provide a significant EM enhancement, comparable to specific metal NPs, such as Au surfaces.[134]

5. SUMMARY, CONCLUSIONS, AND FUTURE PERSPECTIVES

In this work, we have presented a new methodology to simulate the Raman spectrum of molecular systems, described at the QM level, adsorbed on plasmonic substrates, treated in terms of ωFQ and ωFQFμ classical atomistic and frequency-dependent force fields. The resulting multiscale approach is particularly versatile because the underlying ωFQ(Fμ) approach is able to accurately describe the plasmonic response of both metallic nanostructures and 2D graphene-based

https://doi.org/10.1021/acs.jctc.3c00177
J. Chem. Theory Comput. 2023, 19, 3616−3633

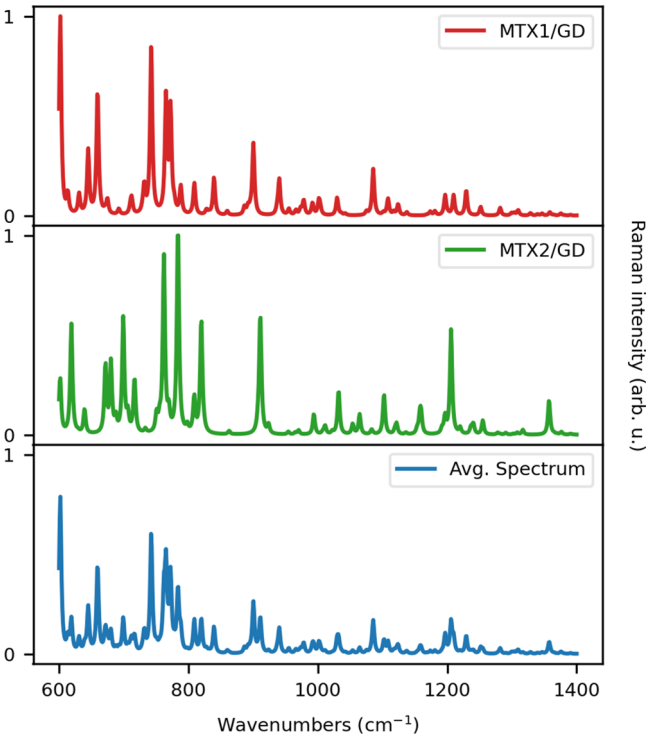

Figure 11. Normalized QM/ωFQFμ GERS spectra of MTX1 and MTX2. The weighted average spectrum is also displayed (bottom panel). The GERS signal is computed at GD18 PRF (0.24 eV, see also Table S3 in the SI).

substrates.[63−65,68] The performance of QM/ωFQ(Fμ) has been tested on PY adsorbed on Ag/Au nanostructures and graphene disks. The enhancement factors of the Raman intensities have been studied as a function of the PS size, the PY-PS distance, and the relative PY-PS orientation, and the qualitative trend has been compared with the E^4 approximation. The largest enhancement has been obtained for silver cTO structures, with an average enhancement factor of about 5000. Such an analysis has allowed confirming that the developed approach is able to correctly describe the EM enhancement in SERS/GERS spectroscopies. Thus, as a final application, we have presented an application of the approach to a realistic case, i.e. methotrexate adsorbed on a graphene disk, for which we also investigate the configurational populations as computed by means of ReaxFF MD simulations. The computed GERS spectrum shows that, although GD is able to enhance the Raman bands by a non-negligible factor of about 900, the GD substrate is not able to discriminate between vibrational normal modes.

Our approach has the potential to become a reliable and efficient tool for the simulation of optical properties of molecular systems adsorbed on plasmonic substrates and might become a viable tool for the experimental design of innovative nanostructured materials able to maximize the enhancement of Raman intensities of a target molecule. To this end, it is worth noting that the current computational bottleneck in QM/ωFQFμ is the cost associated with the solution of ωFQ/ωFQFμ linear systems (see eqs 1 and 9), which can be overcome by resorting to efficient approaches that have been recently tested by some of the authors.[68] In particular, with the aid of on-the-fly iterative techniques, we can largely increase the size of the treatable plasmonic nanostructures, to reach the typical dimensions exploited in real experiments. The latter would also benefit from taking into account the interaction of the molecular system and substrate with a solvating environment.

■ ASSOCIATED CONTENT

Supporting Information

The Supporting Information is available free of charge at https://pubs.acs.org/doi/10.1021/acs.jctc.3c00177.

List of abbreviations introduced in the main text; geometrical details and PRFs on the PS presented in the main text; robustness of the computed EFs with respect to the numerical differentiation step size; Raman spectra of PY-NP composite system with different levels of theory; numerical consistency of the computed SERS spectra and AEF with respect to the DFT integration grid; graphical representation of the isolated PY normal modes computed at the B3LYP/DZP level of theory; EFs for selected PY-PS configurations; absolute AEF and Υ^4_{vol} values for PY adsorbed on Ag NPs and GDs; correlation of AEF and E^4 approximation for Au NPs with respect to the size of the PS; absolute AEF and Υ^4_{vol} values for PY adsorbed on Ag_{10179} in the Ih morphology; correlation of AEF and E^4 approximation for the NPs with respect to the PY-Au distance; AEF and SERS spectra of PY adsorbed on Ag_{10179} in the Ih morphology by changing the relative position of the two moieties; comparison of MTX1 and MTX2 structures; comment on the range of validity of the E^4 approximation with respect to the AEF estimate (PDF)

■ AUTHOR INFORMATION

Corresponding Authors

Tommaso Giovannini − *Scuola Normale Superiore, 56126 Pisa, Italy;* orcid.org/0000-0002-5637-2853; Email: tommaso.giovannini@sns.it

Chiara Cappelli − *Scuola Normale Superiore, 56126 Pisa, Italy; LENS (European Laboratory for Non-Linear Spectroscopy), 50019 Sesto Fiorentino, Italy;* orcid.org/0000-0002-4872-4505; Email: chiara.cappelli@sns.it

Authors

Piero Lafiosca − *Scuola Normale Superiore, 56126 Pisa, Italy;* orcid.org/0000-0002-3967-0736

Luca Nicoli − *Scuola Normale Superiore, 56126 Pisa, Italy;* orcid.org/0000-0002-4808-3381

Luca Bonatti − *Scuola Normale Superiore, 56126 Pisa, Italy*

Stefano Corni − *Dipartimento di Scienze Chimiche, Università di Padova, 35131 Padova, Italy; Istituto di Nanoscienze del Consiglio Nazionale delle Ricerche CNR-NANO, 41125 Modena, Italy;* orcid.org/0000-0001-6707-108X

Complete contact information is available at: https://pubs.acs.org/10.1021/acs.jctc.3c00177

Notes

The authors declare no competing financial interest.

■ ACKNOWLEDGMENTS

This work has received funding from the European Research Council (ERC) under the European Union's Horizon 2020 research and innovation programme (grant agreement No. 818064). S.C. acknowledges funding from EU under the

H2020 grant ProID N. 964363. C.C. acknowledges funding from PNRR MUR project PE0000023-NQSTI. We gratefully acknowledge the Center for High-Performance Computing (CHPC) at SNS for providing the computational infrastructure.

REFERENCES

(1) Fleischmann, M.; Hendra, P. J.; McQuillan, A. J. Raman spectra of pyridine adsorbed at a silver electrode. *Chem. Phys. Lett.* **1974**, *26*, 163−166.
(2) Le Ru, E. C.; Blackie, E.; Meyer, M.; Etchegoin, P. G. Surface enhanced Raman scattering enhancement factors: a comprehensive study. *J. Phys. Chem. C* **2007**, *111*, 13794−13803.
(3) LeRu, E.; Etchegoin, P. *Principles of Surface Enhanced Raman Spectroscopy*; Elsevier, 2009.
(4) Ding, S.-Y.; You, E.-M.; Tian, Z.-Q.; Moskovits, M. Electromagnetic theories of surface-enhanced Raman spectroscopy. *Chem. Soc. Rev.* **2017**, *46*, 4042−4076.
(5) Zrimsek, A. B.; Chiang, N.; Mattei, M.; Zaleski, S.; McAnally, M. O.; Chapman, C. T.; Henry, A.-I.; Schatz, G. C.; Van Duyne, R. P. Single-molecule chemistry with surface-and tip-enhanced Raman spectroscopy. *Chem. Rev.* **2017**, *117*, 7583−7613.
(6) Wang, X.; Shi, W.; She, G.; Mu, L.; Lee, S. High-performance surface-enhanced Raman scattering sensors based on Ag nanoparticles-coated Si nanowire arrays for quantitative detection of pesticides. *Appl. Phys. Lett.* **2010**, *96*, 053104.
(7) Wang, Y.; Wang, Y.; Wang, W.; Sun, K.; Chen, L. Reporter-embedded SERS tags from gold nanorod seeds: selective immobilization of reporter molecules at the tip of nanorods. *ACS Appl. Mater.* **2016**, *8*, 28105−28115.
(8) Zhang, X.; Young, M. A.; Lyandres, O.; Van Duyne, R. P. Rapid detection of an anthrax biomarker by surface-enhanced Raman spectroscopy. *J. Am. Chem. Soc.* **2005**, *127*, 4484−4489.
(9) Jarvis, R. M.; Goodacre, R. Discrimination of bacteria using surface-enhanced Raman spectroscopy. *Anal. Chem.* **2004**, *76*, 40−47.
(10) Huh, Y. S.; Chung, A. J.; Erickson, D. Surface enhanced Raman spectroscopy and its application to molecular and cellular analysis. *Microfluid Nanofluidic* **2009**, *6*, 285−297.
(11) Cailletaud, J.; De Bleye, C.; Dumont, E.; Sacré, P.-Y.; Netchacovitch, L.; Gut, Y.; Boiret, M.; Ginot, Y.-M.; Hubert, P.; Ziemons, E. Critical review of surface-enhanced Raman spectroscopy applications in the pharmaceutical field. *J. Pharm. Biomed. Anal.* **2018**, *147*, 458−472.
(12) Han, X. X.; Rodriguez, R. S.; Haynes, C. L.; Ozaki, Y.; Zhao, B. Surface-enhanced Raman spectroscopy. *Nat. Rev. Methods Primers* **2021**, *1*, 1−17.
(13) Sharma, B.; Frontiera, R. R.; Henry, A.-I.; Ringe, E.; Van Duyne, R. P. SERS: Materials, applications, and the future. *Mater. Today* **2012**, *15*, 16−25.
(14) Le Ru, E. C.; Etchegoin, P. G. Single-molecule surface-enhanced Raman spectroscopy. *Annu. Rev. Phys. Chem.* **2012**, *63*, 65−87.
(15) Langer, J.; Jimenez deAberasturi, D.; Aizpurua, J.; Alvarez-Puebla, R. A.; Auguié, B.; Baumberg, J. J.; Bazan, G. C.; Bell, S. E.; Boisen, A.; Brolo, A. G.; et al. Present and future of surface-enhanced Raman scattering. *ACS Nano* **2020**, *14*, 28−117.
(16) Pilot, R.; Signorini, R.; Durante, C.; Orian, L.; Bhamidipati, M.; Fabris, L. A review on surface-enhanced Raman scattering. *Biosensors* **2019**, *9*, 57.
(17) Zong, C.; Xu, M.; Xu, L.-J.; Wei, T.; Ma, X.; Zheng, X.-S.; Hu, R.; Ren, B. Surface-enhanced Raman spectroscopy for bioanalysis: reliability and challenges. *Chem. Rev.* **2018**, *118*, 4946−4980.
(18) Albrecht, M. G.; Creighton, J. A. Anomalously intense Raman spectra of pyridine at a silver electrode. *J. Am. Chem. Soc.* **1977**, *99*, 5215−5217.
(19) Jeanmaire, D. L.; Van Duyne, R. P. Surface Raman spectroelectrochemistry: Part I. Heterocyclic, aromatic, and aliphatic amines adsorbed on the anodized silver electrode. *J. Electroanal. Chem. Interface Electrochem.* **1977**, *84*, 1−20.
(20) Campion, A.; Kambhampati, P. Surface-enhanced Raman scattering. *Chem. Soc. Rev.* **1998**, *27*, 241−250.
(21) Willets, K. A.; Van Duyne, R. P. Localized surface plasmon resonance spectroscopy and sensing. *Annu. Rev. Phys. Chem.* **2007**, *58*, 267−297.
(22) Alvarez-Puebla, R.; Liz-Marzán, L. M.; García de Abajo, F. J. Light concentration at the nanometer scale. *J. Phys. Chem. Lett.* **2010**, *1*, 2428−2434.
(23) Le Ru, E.; Etchegoin, P. *Principles of Surface-Enhanced Raman Spectroscopy: and related plasmonic effects*; Elsevier, 2008.
(24) Maier, S. A. *Plasmonics: fundamentals and applications*; Springer Science & Business Media, 2007.
(25) Junno, T.; Deppert, K.; Montelius, L.; Samuelson, L. Controlled manipulation of nanoparticles with an atomic force microscope. *Appl. Phys. Lett.* **1995**, *66*, 3627−3629.
(26) Ishida, T.; Murayama, T.; Taketoshi, A.; Haruta, M. Importance of size and contact structure of gold nanoparticles for the genesis of unique catalytic processes. *Chem. Rev.* **2020**, *120*, 464−525.
(27) Sau, T. K.; Rogach, A. L. Nonspherical noble metal nanoparticles: colloid-chemical synthesis and morphology control. *Adv. Mater.* **2010**, *22*, 1781−1804.
(28) Liz-Marzán, L. M. Tailoring surface plasmons through the morphology and assembly of metal nanoparticles. *Langmuir* **2006**, *22*, 32−41.
(29) Grzelczak, M.; Pérez-Juste, J.; Mulvaney, P.; Liz-Marzán, L. M. Shape control in gold nanoparticle synthesis. *Chem. Soc. Rev.* **2008**, *37*, 1783−1791.
(30) Blackie, E. J.; Le Ru, E. C.; Etchegoin, P. G. Single-molecule surface-enhanced Raman spectroscopy of nonresonant molecules. *J. Am. Chem. Soc.* **2009**, *131*, 14466−14472.
(31) Fesenko, O.; Dovbeshko, G.; Dementjev, A.; Karpicz, R.; Kaplas, T.; Svirko, Y. Graphene-enhanced Raman spectroscopy of thymine adsorbed on single-layer graphene. *Nanoscale Res. Lett.* **2015**, *10*, 1−7.
(32) Lai, H.; Xu, F.; Zhang, Y.; Wang, L. Recent progress on graphene-based substrates for surface-enhanced Raman scattering applications. *J. Mater. Chem. B* **2018**, *6*, 4008−4028.
(33) Chen, N.; Xiao, T.-H.; Luo, Z.; Kitahama, Y.; Hiramatsu, K.; Kishimoto, N.; Itoh, T.; Cheng, Z.; Goda, K. Porous carbon nanowire array for surface-enhanced Raman spectroscopy. *Nat. Commun.* **2020**, *11*, 1−8.
(34) Payton, J. L.; Morton, S. M.; Moore, J. E.; Jensen, L. A discrete interaction model/quantum mechanical method for simulating surface-enhanced Raman spectroscopy. *J. Chem. Phys.* **2012**, *136*, 214103.
(35) Payton, J. L.; Morton, S. M.; Moore, J. E.; Jensen, L. A hybrid atomistic electrodynamics−quantum mechanical approach for simulating surface-enhanced Raman scattering. *Acc. Chem. Res.* **2014**, *47*, 88−99.
(36) Hu, Z.; Chulhai, D. V.; Jensen, L. Simulating surface-enhanced hyper-Raman scattering using atomistic electrodynamics-quantum mechanical models. *J. Chem. Theory Comput.* **2016**, *12*, 5968−5978.
(37) Corni, S.; Tomasi, J. Enhanced response properties of a chromophore physisorbed on a metal particle. *J. Chem. Phys.* **2001**, *114*, 3739−3751.
(38) Corni, S.; Tomasi, J. Surface enhanced Raman scattering from a single molecule adsorbed on a metal particle aggregate: A theoretical study. *J. Chem. Phys.* **2002**, *116*, 1156−1164.
(39) Corni, S.; Tomasi, J. Excitation energies of a molecule close to a metal surface. *J. Chem. Phys.* **2002**, *117*, 7266−7278.
(40) Corni, S.; Tomasi, J. Theoretical evaluation of Raman spectra and enhancement factors for a molecule adsorbed on a complex-shaped metal particle. *Chem. Phys. Lett.* **2001**, *342*, 135−140.
(41) Corni, S.; Tomasi, J. Erratum to: Theoretical evaluation of Raman spectra and enhancement factors for a molecule adsorbed on a

https://doi.org/10.1021/acs.jctc.3c00177
J. Chem. Theory Comput. 2023, 19, 3616−3633

complex-shaped metal particle [Chem. Phys. Lett. 342 (2001) 135−140]. *Chem. Phys. Lett.* **2002**, *365*, 552−553.
(42) Chen, R.; Jensen, L. Interpreting the chemical mechanism in SERS using a Raman bond model. *J. Chem. Phys.* **2020**, *152*, 024126.
(43) Chen, R.; Jensen, L. Understanding chemical enhancements of surface-enhanced Raman scattering using a Raman bond model for extended systems. *J. Chem. Phys.* **2022**, *157*, 184705.
(44) Becca, J. C.; Chen, X.; Jensen, L. A discrete interaction model/quantum mechanical method for simulating surface-enhanced Raman spectroscopy in solution. *J. Chem. Phys.* **2021**, *154*, 224705.
(45) Liu, P.; Chulhai, D. V.; Jensen, L. Single-molecule imaging using atomistic near-field tip-enhanced Raman spectroscopy. *ACS Nano* **2017**, *11*, 5094−5102.
(46) Chulhai, D. V.; Chen, X.; Jensen, L. Simulating ensemble-averaged surface-enhanced Raman scattering. *J. Phys. Chem. C* **2016**, *120*, 20833−20842.
(47) Zhao, L.; Jensen, L.; Schatz, G. C. Pyridine- Ag20 cluster: a model system for studying surface-enhanced Raman scattering. *J. Am. Chem. Soc.* **2006**, *128*, 2911−2919.
(48) Jensen, L.; Aikens, C. M.; Schatz, G. C. Electronic structure methods for studying surface-enhanced Raman scattering. *Chem. Soc. Rev.* **2008**, *37*, 1061−1073.
(49) Morton, S. M.; Jensen, L. Understanding the molecule- surface chemical coupling in SERS. *J. Am. Chem. Soc.* **2009**, *131*, 4090−4098.
(50) Morton, S. M.; Silverstein, D. W.; Jensen, L. Theoretical studies of plasmonics using electronic structure methods. *Chem. Rev.* **2011**, *111*, 3962−3994.
(51) Jørgensen, S.; Ratner, M. A.; Mikkelsen, K. V. Heterogeneous solvation: An ab initio approach. *J. Chem. Phys.* **2001**, *115*, 3792−3803.
(52) Neuhauser, D.; Lopata, K. Molecular nanopolaritonics: Cross manipulation of near-field plasmons and molecules. I. Theory and application to junction control. *J. Chem. Phys.* **2007**, *127*, 154715.
(53) Masiello, D. J.; Schatz, G. C. Many-body theory of surface-enhanced Raman scattering. *Phys. Rev. A* **2008**, *78*, 042505.
(54) Vukovic, S.; Corni, S.; Mennucci, B. Fluorescence enhancement of chromophores close to metal nanoparticles. Optimal setup revealed by the polarizable continuum model. *J. Phys. Chem. C* **2009**, *113*, 121−133.
(55) Lopata, K.; Neuhauser, D. Multiscale Maxwell−Schrödinger modeling: A split field finite-difference time-domain approach to molecular nanopolaritonics. *J. Chem. Phys.* **2009**, *130*, 104707.
(56) Arcisauskaite, V.; Kongsted, J.; Hansen, T.; Mikkelsen, K. V. Charge transfer excitation energies in pyridine−silver complexes studied by a QM/MM method. *Chem. Phys. Lett.* **2009**, *470*, 285−288.
(57) Masiello, D. J.; Schatz, G. C. On the linear response and scattering of an interacting molecule-metal system. *J. Chem. Phys.* **2010**, *132*, 064102.
(58) Chen, H.; McMahon, J. M.; Ratner, M. A.; Schatz, G. C. Classical electrodynamics coupled to quantum mechanics for calculation of molecular optical properties: a RT-TDDFT/FDTD approach. *J. Phys. Chem. C* **2010**, *114*, 14384−14392.
(59) Hao, Q.; Morton, S. M.; Wang, B.; Zhao, Y.; Jensen, L.; Jun Huang, T. Tuning surface-enhanced Raman scattering from graphene substrates using the electric field effect and chemical doping. *Appl. Phys. Lett.* **2013**, *102*, 011102.
(60) Bonatti, L.; Nicoli, L.; Giovannini, T.; Cappelli, C. In silico design of graphene plasmonic hot-spots. *Nanoscale Adv.* **2022**, *4*, 2294−2302.
(61) Giovannini, T.; Bonatti, L.; Lafiosca, P.; Nicoli, L.; Castagnola, M.; Illobre, P. G.; Corni, S.; Cappelli, C. Do We Really Need Quantum Mechanics to Describe Plasmonic Properties of Metal Nanostructures? *ACS Photonics* **2022**, *9*, 3025.
(62) Lombardi, J. R.; Birke, R. L.; Lu, T.; Xu, J. Charge-transfer theory of surface enhanced Raman spectroscopy: Herzberg−Teller contributions. *J. Chem. Phys.* **1986**, *84*, 4174−4180.
(63) Giovannini, T.; Rosa, M.; Corni, S.; Cappelli, C. A classical picture of subnanometer junctions: an atomistic Drude approach to nanoplasmonics. *Nanoscale* **2019**, *11*, 6004−6015.
(64) Giovannini, T.; Bonatti, L.; Polini, M.; Cappelli, C. Graphene plasmonics: Fully atomistic approach for realistic structures. *J. Phys. Chem. Lett.* **2020**, *11*, 7595−7602.
(65) Bonatti, L.; Gil, G.; Giovannini, T.; Corni, S.; Cappelli, C. Plasmonic resonances of metal nanoparticles: atomistic vs. Continuum approaches. *Front. Chem.* **2020**, *8*, 340.
(66) Zanotto, S.; Bonatti, L.; Pantano, M. F.; Miseikis, V.; Speranza, G.; Giovannini, T.; Coletti, C.; Cappelli, C.; Tredicucci, A.; Toncelli, A. Strain-Induced Plasmon Confinement in Polycrystalline Graphene. *ACS Photonics* **2023**, *10*, 394.
(67) Barros, E. B.; Dresselhaus, M. S. Theory of Raman enhancement by two-dimensional materials: Applications for graphene-enhanced Raman spectroscopy. *Phys. Rev. B* **2014**, *90*, 035443.
(68) Lafiosca, P.; Giovannini, T.; Benzi, M.; Cappelli, C. Going Beyond the Limits of Classical Atomistic Modeling of Plasmonic Nanostructures. *J. Phys. Chem. C* **2021**, *125*, 23848.
(69) Jackson, J. D. *Classical electrodynamics*; John Wiley & Sons, 1999.
(70) Giovannini, T.; Puglisi, A.; Ambrosetti, M.; Cappelli, C. Polarizable QM/MM approach with fluctuating charges and fluctuating dipoles: the QM/FQFμ model. *J. Chem. Theory Comput.* **2019**, *15*, 2233−2245.
(71) Pelton, M.; Bryant, G. W. *Introduction to metal-nanoparticle plasmonics*; John Wiley & Sons, 2013; Vol. 5.
(72) Castro Neto, A. H.; Guinea, F.; Peres, N. M. R.; Novoselov, K. S.; Geim, A. K. The electronic properties of graphene. *Rev. Mod. Phys.* **2009**, *81*, 109.
(73) Pinchuk, A.; Kreibig, U.; Hilger, A. Optical properties of metallic nanoparticles: influence of interface effects and interband transitions. *Surf. Sci.* **2004**, *557*, 269−280.
(74) Pinchuk, A.; Von Plessen, G.; Kreibig, U. Influence of interband electronic transitions on the optical absorption in metallic nanoparticles. *J. Phys. D: Appl. Phys.* **2004**, *37*, 3133.
(75) Balamurugan, B.; Maruyama, T. Evidence of an enhanced interband absorption in Au nanoparticles: size-dependent electronic structure and optical properties. *Appl. Phys. Lett.* **2005**, *87*, 143105.
(76) Liebsch, A. Surface-plasmon dispersion and size dependence of Mie resonance: silver versus simple metals. *Phys. Rev. B* **1993**, *48*, 11317.
(77) Santiago, E. Y.; Besteiro, L. V.; Kong, X.-T.; Correa-Duarte, M. A.; Wang, Z.; Govorov, A. O. Efficiency of hot-electron generation in plasmonic nanocrystals with complex shapes: surface-induced scattering, hot spots, and interband transitions. *ACS Photonics* **2020**, *7*, 2807−2824.
(78) Warshel, A.; Levitt, M. Theoretical studies of enzymic reactions: dielectric, electrostatic and steric stabilization of the carbonium ion in the reaction of lysozyme. *J. Mol. Biol.* **1976**, *103*, 227−249.
(79) Lin, H.; Truhlar, D. G. QM/MM: what have we learned, where are we, and where do we go from here? *Theor. Chem. Acc.* **2007**, *117*, 185−199.
(80) Senn, H. M.; Thiel, W. QM/MM methods for biomolecular systems. *Angew. Chem., Int. Ed.* **2009**, *48*, 1198−1229.
(81) Mennucci, B.; Corni, S. Multiscale modelling of photoinduced processes in composite systems. *Nat. Rev. Chem.* **2019**, *3*, 315−330.
(82) Morton, S. M.; Jensen, L. A discrete interaction model/quantum mechanical method for describing response properties of molecules adsorbed on metal nanoparticles. *J. Chem. Phys.* **2010**, *133*, 074103.
(83) Guido, C. A.; Rosa, M.; Cammi, R.; Corni, S. An open quantum system theory for polarizable continuum models. *J. Chem. Phys.* **2020**, *152*, 174114.
(84) Coccia, E.; Fregoni, J.; Guido, C.; Marsili, M.; Pipolo, S.; Corni, S. Hybrid theoretical models for molecular nanoplasmonics. *J. Chem. Phys.* **2020**, *153*, 200901.

https://doi.org/10.1021/acs.jctc.3c00177
J. Chem. Theory Comput. 2023, 19, 3616−3633

(85) Corni, S.; Pipolo, S.; Cammi, R. Equation of motion for the solvent polarization apparent charges in the polarizable continuum model: Application to real-time TDDFT. *J. Phys. Chem. A* **2015**, *119*, 5405−5416.
(86) Rick, S. W.; Stuart, S. J.; Bader, J. S.; Berne, B. Fluctuating charge force fields for aqueous solutions. *J. Mol. Liq.* **1995**, *65*, 31−40.
(87) Cappelli, C. Integrated QM/polarizable MM/continuum approaches to model chiroptical properties of strongly interacting solute−solvent systems. *Int. J. Quantum Chem.* **2016**, *116*, 1532−1542.
(88) Giovannini, T.; Egidi, F.; Cappelli, C. Molecular spectroscopy of aqueous solutions: a theoretical perspective. *Chem. Soc. Rev.* **2020**, *49*, 5664−5677.
(89) Giovannini, T.; Egidi, F.; Cappelli, C. Theory and algorithms for chiroptical properties and spectroscopies of aqueous systems. *Phys. Chem. Chem. Phys.* **2020**, *22*, 22864−22879.
(90) Giovannini, T.; Riso, R. R.; Ambrosetti, M.; Puglisi, A.; Cappelli, C. Electronic transitions for a fully polarizable qm/mm approach based on fluctuating charges and fluctuating dipoles: linear and corrected linear response regimes. *J. Chem. Phys.* **2019**, *151*, 174104.
(91) Giovannini, T.; Grazioli, L.; Ambrosetti, M.; Cappelli, C. Calculation of ir spectra with a fully polarizable qm/mm approach based on fluctuating charges and fluctuating dipoles. *J. Chem. Theory Comput.* **2019**, *15*, 5495−5507.
(92) Giovannini, T.; Ambrosetti, M.; Cappelli, C. Quantum confinement effects on solvatochromic shifts of molecular solutes. *J. Phys. Chem. Lett.* **2019**, *10*, 5823−5829.
(93) Marrazzini, G.; Giovannini, T.; Egidi, F.; Cappelli, C. Calculation of linear and non-linear electric response properties of systems in aqueous solution: A polarizable quantum/classical approach with quantum repulsion effects. *J. Chem. Theory Comput.* **2020**, *16*, 6993−7004.
(94) te Velde, G.; Bickelhaupt, F. M.; Baerends, E. J.; Fonseca Guerra, C.; van Gisbergen, S. J. A.; Snijders, J. G.; Ziegler, T. Chemistry with ADF. *J. Comput. Chem.* **2001**, *22*, 931−967.
(95) Baerends, E.; et al. *ADF (version 2020.x)*; Theoretical Chemistry; Vrije Universiteit: Amsterdam, The Netherlands, 2020. http://www.scm.com.
(96) Nicoli, L.; Giovannini, T.; Cappelli, C. Assessing the Quality of QM/MM Approaches to Describe Vacuo-to-water Solvatochromic Shifts. *J. Chem. Phys.* **2022**, *157*, 214101.
(97) Jensen, L.; Van Duijnen, P. T.; Snijders, J. G. A discrete solvent reaction field model within density functional theory. *J. Chem. Phys.* **2003**, *118*, 514−521.
(98) Casida, M. E. *Recent Advances In Density Functional Methods: (Part I)*; World Scientific, 1995; pp 155−192.
(99) Norman, P.; Ruud, K.; Saue, T. *Principles and practices of molecular properties: Theory, modeling, and simulations*; John Wiley & Sons, 2018.
(100) Giovannini, T.; Ambrosetti, M.; Cappelli, C. A polarizable embedding approach to second harmonic generation (SHG) of molecular systems in aqueous solutions. *Theor. Chem. Acc.* **2018**, *137*, 1−11.
(101) Morton, S. M.; Jensen, L. A discrete interaction model/quantum mechanical method to describe the interaction of metal nanoparticles and molecular absorption. *J. Chem. Phys.* **2011**, *135*, 134103.
(102) Placzek, G.; Teller, E. Die Rotationsstruktur der Ramanbanden mehratomiger Moleküle. *Zeitschrift für Physik* **1933**, *81*, 209−258.
(103) Placzek, G. In *Handbuch der Radiologie*; Marx, G., Ed.; Akademische Verlagsgesellschaft: Leipzig, 1934.
(104) Jensen, L.; Zhao, L.; Autschbach, J.; Schatz, G. Theory and method for calculating resonance Raman scattering from resonance polarizability derivatives. *J. Chem. Phys.* **2005**, *123*, 174110.
(105) Corni, S.; Tomasi, J. *Surface-Enhanced Raman Scattering: Physics and Applications*; Springer, 2006; pp 105−123.
(106) Louden, P.; Bhattarai, H.; Neidhart, S.; Lin, T.; Vardeman, C. F., II; Fennell, C. J.; Meineke, M. A.; Kuang, S.; Lamichhane, M.; Michalka, J.; et al. *OPENMD-2.5: molecular dynamics in the open*; OpenMD, 2017. http://openmd.org.
(107) Humphrey, W.; Dalke, A.; Schulten, K. VMD − Visual Molecular Dynamics. *J. Mol. Graphics* **1996**, *14*, 33−38.
(108) Van Lenthe, E.; Baerends, E. J. Optimized Slater-type basis sets for the elements 1−118. *J. Comput. Chem.* **2003**, *24*, 1142−1156.
(109) Van Gisbergen, S.; Snijders, J.; Baerends, E. A density functional theory study of frequency-dependent polarizabilities and Van der Waals dispersion coefficients for polyatomic molecules. *J. Chem. Phys.* **1995**, *103*, 9347−9354.
(110) Van Gisbergen, S.; Snijders, J.; Baerends, E. Implementation of time-dependent density functional response equations. *Comput. Phys. Commun.* **1999**, *118*, 119−138.
(111) Fan, L.; Ziegler, T. Application of density functional theory to infrared absorption intensity calculations on main group molecules. *J. Chem. Phys.* **1992**, *96*, 9005−9012.
(112) Fan, L.; Ziegler, T. Application of density functional theory to infrared absorption intensity calculations on transition-metal carbonyls. *J. Phys. Chem.* **1992**, *96*, 6937−6941.
(113) Van Gisbergen, S.; Snijders, J.; Baerends, E. Application of time-dependent density functional response theory to Raman scattering. *Chem. Phys. Lett.* **1996**, *259*, 599−604.
(114) Van Duyne, R.; Jeanmaire, D. Surface Raman spectroelectochemistry: part1. heterocyclic, aromatic, and aliphatic Amines adsorbed on the anodized silver electrode. *J. Electroanal. Chem.* **1977**, *84*, 1−20.
(115) Le Ru, E.; Etchegoin, P. Rigorous justification of thel El 4 enhancement factor in surface enhanced Raman spectroscopy. *Chem. Phys. Lett.* **2006**, *423*, 63−66.
(116) Arenas, J. F.; López Tocón, I.; Otero, J. C.; Marcos, J. I. Charge transfer processes in surface-enhanced raman scattering. Franck- condon active vibrations of pyridine. *J. Phys. Chem.* **1996**, *100*, 9254−9261.
(117) Khaing Oo, M. K.; Guo, Y.; Reddy, K.; Liu, J.; Fan, X. Ultrasensitive vapor detection with surface-enhanced Raman scattering-active gold nanoparticle immobilized flow-through multihole capillaries. *Anal. Chem.* **2012**, *84*, 3376−3381.
(118) Dresselhaus, M. S.; Jorio, A.; Hofmann, M.; Dresselhaus, G.; Saito, R. Perspectives on carbon nanotubes and graphene Raman spectroscopy. *Nano Lett.* **2010**, *10*, 751−758.
(119) Ling, X.; Xie, L.; Fang, Y.; Xu, H.; Zhang, H.; Kong, J.; Dresselhaus, M. S.; Zhang, J.; Liu, Z. Can. graphene be used as a substrate for Raman enhancement? *Nano Lett.* **2010**, *10*, 553−561.
(120) Voloshina, E.; Mollenhauer, D.; Chiappisi, L.; Paulus, B. Theoretical study on the adsorption of pyridine derivatives on graphene. *Chem. Phys. Lett.* **2011**, *510*, 220−223.
(121) Kim, J.; Son, H.; Cho, D. J.; Geng, B.; Regan, W.; Shi, S.; Kim, K.; Zettl, A.; Shen, Y.-R.; Wang, F. Electrical control of optical plasmon resonance with graphene. *Nano Lett.* **2012**, *12*, 5598−5602.
(122) Thongrattanasiri, S.; Garcia de Abajo, F. J. Optical field enhancement by strong plasmon interaction in graphene nanostructures. *Phys. Rev. Lett.* **2013**, *110*, 187401.
(123) Van Duin, A. C.; Dasgupta, S.; Lorant, F.; Goddard, W. A. ReaxFF: a reactive force field for hydrocarbons. *J. Phys. Chem. A* **2001**, *105*, 9396−9409.
(124) Chenoweth, K.; Van Duin, A. C.; Goddard, W. A. ReaxFF reactive force field for molecular dynamics simulations of hydrocarbon oxidation. *J. Phys. Chem. A* **2008**, *112*, 1040−1053.
(125) SCM. *ReaxFF 2021.1*; Theoretical Chemistry; Vrije Universiteit: Amsterdam, The Netherlands. http://www.scm.com.
(126) Monti, S.; Corozzi, A.; Fristrup, P.; Joshi, K. L.; Shin, Y. K.; Oelschlaeger, P.; Van Duin, A. C.; Barone, V. Exploring the conformational and reactive dynamics of biomolecules in solution using an extended version of the glycine reactive force field. *Phys. Chem. Chem. Phys.* **2013**, *15*, 15062−15077.
(127) Golkaram, M.; van Duin, A. C. Revealing graphene oxide toxicity mechanisms: A reactive molecular dynamics study. *Mater. Discovery* **2015**, *1*, 54−62.

https://doi.org/10.1021/acs.jctc.3c00177
J. Chem. Theory Comput. 2023, 19, 3616−3633

(128) Martyna, G. J.; Klein, M. L.; Tuckerman, M. Nosé−Hoover chains: The canonical ensemble via continuous dynamics. *J. Chem. Phys.* **1992**, *97*, 2635−2643.
(129) Martyna, G. J.; Tobias, D. J.; Klein, M. L. Constant pressure molecular dynamics algorithms. *J. Chem. Phys.* **1994**, *101*, 4177−4189.
(130) Umadevi, D.; Sastry, G. N. Impact of the chirality and curvature of carbon nanostructures on their interaction with aromatics and amino acids. *ChemPhysChem* **2013**, *14*, 2570−2578.
(131) Daura, X.; Gademann, K.; Jaun, B.; Seebach, D.; Van Gunsteren, W. F.; Mark, A. E. Peptide folding: when simulation meets experiment. *Angew. Chem., Int. Ed.* **1999**, *38*, 236−240.
(132) Abraham, M. J.; Murtola, T.; Schulz, R.; Páll, S.; Smith, J. C.; Hess, B.; Lindahl, E. GROMACS: High performance molecular simulations through multi-level parallelism from laptops to supercomputers. *SoftwareX* **2015**, *1*, 19−25.
(133) Abraham, L.; Hess, B.; Spoel, V. *GROMACS 2020.3 source code*; Zenodo, 2020.
(134) Abdelsalam, M. E.; Bartlett, P. N.; Baumberg, J. J.; Cintra, S.; Kelf, T. A.; Russell, A. E. Electrochemical SERS at a structured gold surface. *Electrochem. Commun.* **2005**, *7*, 740−744.

https://doi.org/10.1021/acs.jctc.3c00177
J. Chem. Theory Comput. 2023, 19, 3616−3633

Chapter 5

Summary, conclusions, and future perspectives

This Thesis has focused on developing a family of classical atomistic electromagnetic multiscale models, referred to as ωMM, aimed at providing a versatile theoretical and computational framework for simulating the optical properties of plasmonic materials. Beginning with the classical atomistic ωFQ model,[24,126,128] originally designed for Drude-like plasmonic materials, this work has extended this model to noble metals, resulting in the ωFQFμ approach ([**Paper I**]). ωFQFμ accounts for interband electron transitions between fully occupied bands, such as metal d orbitals, and partially empty s or p orbitals.

Beyond single-metal systems, we have extended ωFQFμ to multimetallic configurations by generalizing its equations to model bimetallic and alloyed nanostructures ([**Paper II**]).

Furthermore, we have reformulated the ωMM model family to operate within the real-time domain, broadening its capacity to study the time-dependent optical behavior of plasmonic materials ([**Paper III**]).

The original contribution of this Thesis has also included extending ωFQFμ to model the interactions with both non-absorbing ([**Paper IV**]) and absorbing environments ([**Paper V**]) to simulate the physics underlying refractive-index LSPR, and SERS sensors respectively.

The proposed methodologies could still be further developed to capture new physical phenomena relevant to specific experimental contexts. A potential extension would consist of integrating the methodologies discussed in [**Paper IV**], and [**Paper V**] by designing a multiscale model for surface-enhanced effects in solution. This would involve the definition of a multiscale three-layer scheme coupling ωMM , FQ, and QM, thus achieving a fully atomistic classical description of plasmonic substrates in a solvating environment. Such QM/ωMM/FQ model could facilitate the *in-silico* study of plasmonic biosensors, offering experimentalists a computational framework to design and optimize sensors tailored to detect specific biomolecules.[129–134]

Furthermore, the proposed ωMM models could be applied to engineer the plasmonic

characteristics of substrates of experimental interest. For instance, ωMM models could allow the exploration of the electric field morphology in single-atom picocavities within large (tens of nm) metal nanostructures. These systems are inherently multiscale, comprising thousands of atoms while exhibiting electric properties concentrated in extremely confined (single-atom) regions.[135] Given their atomistic nature and computational efficiency, ωMM models could serve as a powerful tool to engineer such technologically critical nanostructures. The models developed in this thesis lay a solid foundation for these advancements, and I hope they will prove to be valuable tools in the hands of engineers and researchers aiming to harness plasmonic properties for innovative applications.

Ringraziamenti

Ora che siete arrivati fino a qui, lo so che non avrete letto tutto tutto (forse neanche io l'ho fatto veramente), vi sorbite pure i miei ultimi pensieri.
Partiamo dall'inizio. Ho iniziato questo dottorato carico di aspettative e con una forte motivazione a rimanere in ricerca. Negli anni, questa motivazione e passione sono completamente svanite.
Quindi, questa tesi marca l'inizio e contestualmente la fine della mia carriera in accademia.
Chiudendosi questo capitolo, è quindi bene guardarsi indietro e tirare le somme. Anche se questo dottorato non mi ha lasciato una strada ben delineata da seguire e questo, come sempre, fa sentire un po' persi, sono comunque molto felice del periodo che ho vissuto. Vorrei ringraziare tutti quanti hanno preso parte a questo mio pezzo di vita, e dentro di me lo faccio. Qui mi limiterò solo alle "formalità".
Ringrazio la Prof.ssa Cappelli per tutte le possibilità che mi ha dato e che mi hanno concesso di crescere scientificamente, ma forse ancor di più per il suo lato umano, che mi ha sempre fatto sentire accolto e supportato.
Ovviamente ringrazio Tommaso, che è stato un ottimo mentore oltre che essere diventato un caro amico. Sono queste le cose che ritengo più di valore di questo dottorato.
Ringrazio tutti gli amici del gruppo di ricerca, non vi nomino ma vi penso, ed in particolare tutti quelli che hanno condiviso lo spirito della ω-room con me. Entrare tardi ed uscire presto dall'ufficio con voi è stato edificante.
Ringrazio anche tutti gli altri amici che hanno reso speciale la mia permanenza a Pisa.
Infine, voglio ringraziare la mia famiglia per il costante ed incondizionato supporto che ho ricevuto in questi anni. Sono molto fortunato ad avervi.

Luca

Bibliography

[1] Mayer, K. M. and Hafner, J. H. *Chem. Rev.*, 111(6):3828–3857, **2011**.

[2] Motl, N., Smith, A., DeSantis, C. and Skrabalak, S. *Chem. Soc. Rev.*, 43(11):3823–3834, **2014**.

[3] Zhang, X., Chen, Y. L., Liu, R.-S. and Tsai, D. P. *Rep. Prog. Phys.*, 76(4):046401, **2013**.

[4] Zhang, Z. *Plasmonic Photocatalysis: Principles and Applications*. Springer Nature, **2022**.

[5] Atwater, H. A. and Polman, A. *Nat. Mater*, 9(3):205–213, **2010**.

[6] Ai, B., Fan, Z. and Wong, Z. J. *Microsyst. Nanoeng.*, 8(1):5, **2022**.

[7] Yu, H., Peng, Y., Yang, Y. and Li, Z.-Y. *Npj Comput. Mater.*, 5(1):45, **2019**.

[8] Link, S., Wang, Z. L. and El-Sayed, M. *J. Phys. Chem. B*, 103(18):3529–3533, **1999**.

[9] Shajari, D., Bahari, A., Gill, P. and Mohseni, M. *Opt. Mater.*, 64:376–383, **2017**.

[10] Jensen, T. R., Duval, M. L., Kelly, K. L., Lazarides, A. A., Schatz, G. C. and Van Duyne, R. P. *J. Phys. Chem. B.*, 103(45):9846–9853, **1999**.

[11] Rossi, T. P., Shegai, T., Erhart, P. and Antosiewicz, T. J. *Nat. Commun.*, 10(1):3336, **2019**.

[12] Amendola, V., Pilot, R., Frasconi, M., Maragò, O. M. and Iatì, M. A. *J. Condens. Matter Phys.*, 29(20):203002, **2017**.

[13] Kasani, S., Curtin, K. and Wu, N. *Nanophotonics*, 8(12):2065–2089, **2019**.

[14] Baseggio, O., Fronzoni, G. and Stener, M. *J. Chem. Phys.*, 143(2):024106, **2015**.

[15] Baseggio, O., De Vetta, M., Fronzoni, G., Stener, M., Sementa, L., Fortunelli, A. and Calzolari, A. *J. Phys. Chem. C*, 120(23):12773–12782, **2016**.

[16] Yabana, K. and Bertsch, G. *Phys. Rev. B*, 54(7):4484, **1996**.

[17] Takimoto, Y., Vila, F. and Rehr, J. *J. Chem. Phys.*, 127(15):154114, **2007**.

[18] Li, X., Govind, N., Isborn, C., DePrince III, A. E. and Lopata, K. *Chem. Rev.*, 120(18):9951–9993, **2020**.

[19] Della Sala, F., Pachter, R. and Sukharev, M. *J. Chem. Phys.*, 157(19):190401, **2022**.

[20] Hohenester, U. and Trügler, A. *Comput. Phys. Commun*, 183(2):370–381, **2012**.

[21] Zeng, Z., Venuthurumilli, P. K. and Xu, X. *ACS Photonics*, 8(5):1489–1496, **2021**.

[22] Farmani, A. *JOSA B*, 36(2):401–407, **2019**.

[23] Jensen, L. L. and Jensen, L. *J. Phys. Chem. C*, 112(40):15697–15703, **2008**.

[24] Giovannini, T., Rosa, M., Corni, S. and Cappelli, C. *Nanoscale*, 11(13):6004–6015, **2019**.

[25] Sørensen, L. K., Gerasimov, V. S., Karpov, S. V. and Ågren, H. *Phys. Chem. Chem. Phys.*, 26(37):24209–24245, **2024**.

[26] Pines, D. *Elementary excitations in solids*. CRC Press, **2018**.

[27] Bohm, D. and Pines, D. *Phys. Rev.*, 82(5):625, **1951**.

[28] Pines, D. and Bohm, D. *Phys. Rev.*, 85(2):338, **1952**.

[29] Bohm, D. and Pines, D. *Phys. Rev.*, 92(3):609, **1953**.

[30] Pines, D. *Rev. Mod. Phys.*, 28(3):184, **1956**.

[31] Madelung, O. *Introduction to solid-state theory*, volume 2. Springer Science & Business Media, **2012**.

[32] Vavrukh, M. and Slobodyan, S. *Condensed Matter Physics*, **2005**.

[33] Finazzi, M. and Ciccacci, F. *Phys. Rev. B Condens. Matter*, 86(3):035428, **2012**.

[34] Andersen, K., Jacobsen, K. W. and Thygesen, K. S. *Phys. Rev. B Condens. Matter*, 86(24):245129, **2012**.

[35] Alpeggiani, F. and Andreani, L. C. *Plasmonics*, 9:965–978, **2014**.

[36] Nguyen, V. H. and Nguyen, B. H. *Adv. Nat. Sci.: Nanosci.*, 6(2):023001, **2015**.

[37] Morchio, G. and Strocchi, F. *Ann. Phys.*, 170(2):310–332, **1986**.

[38] Forestiere, C., Miano, G., Pascale, M. and Tricarico, R. *Phys. Rev. A*, 102(4):043704, **2020**.

[39] Khurgin, J., Bykov, A. Y. and Zayats, A. V. *eLight*, 4(1):15, **2024**.

[40] Maier, S. A. and Atwater, H. A. *J. Appl. Phys.*, 98(1), **2005**.

[41] Mueller, N. S. and Reich, S. *Frontiers in chemistry*, 7:470, **2019**.

[42] Khurgin, J. B. *Nanophotonics*, 9(2):453–471, **2020**.

[43] Khurgin, J. B. *Faraday Discuss.*, 214:35–58, **2019**.

[44] Thèye, M.-L. *Phys. Rev. B*, 2(8):3060, **1970**.

[45] Lawrence, W. and Wilkins, J. *Phys. Rev. B*, 7(6):2317, **1973**.

[46] Ziman, J. M. *Electrons and phonons: the theory of transport phenomena in solids*. Oxford university press, **2001**.

[47] Pines, D. and Nozieres, P. The Theory of Quantum Liquids,. New York City, **1966**.

[48] Uskov, A. V., Protsenko, I. E., Ikhsanov, R. S., Babicheva, V. E., Zhukovsky, S. V., Lavrinenko, A. V., O'Reilly, E. P. and Xu, H. *Nanoscale*, 6(9):4716–4727, **2014**.

[49] Uskov, A. V., Protsenko, I. E., Mortensen, N. A. and O'Reilly, E. P. *Plasmonics*, 9:185–192, **2014**.

[50] Yuan, Z. and Gao, S. *Surf. Sci.*, 602(2):460–464, **2008**.

[51] Khurgin, J., Tsai, W.-Y., Tsai, D. P. and Sun, G. *Acs Photonics*, 4(11):2871–2880, **2017**.

[52] Kreibig, U. and Vollmer, M. *Optical properties of metal clusters*, volume 25. Springer Science & Business Media, **2013**.

[53] Pinchuk, A., Kreibig, U. and Hilger, A. *Surf. Sci.*, 557(1-3):269–280, **2004**.

[54] Pinchuk, A., Von Plessen, G. and Kreibig, U. *J. Phys. D Appl. Phys.*, 37(22):3133, **2004**.

[55] Liebsch, A. *Phys. Rev. B*, 48(15):11317, **1993**.

[56] Chen, H., Ming, T., Zhao, L., Wang, F., Sun, L.-D., Wang, J. and Yan, C.-H. *Nano Today*, 5(5):494–505, **2010**.

[57] Stefancu, A., Halas, N. J., Nordlander, P. and Cortes, E. *Nat. Phys.*, 20(7):1065–1077, **2024**.

[58] Mueller, N. S., Heeg, S. and Reich, S. *Physical Review A*, 94(2):023813, **2016**.

[59] Kneipp, K., Wang, Y., Kneipp, H., Itzkan, I., Dasari, R. R. and Feld, M. S. *Phys. Rev. Lett.*, 76(14):2444, **1996**.

[60] Langer, J., Jimenez de Aberasturi, D., Aizpurua, J., Alvarez-Puebla, R. A., Auguié, B., Baumberg, J. J., Bazan, G. C., Bell, S. E., Boisen, A., Brolo, A. G. *et al. ACS Nano*, 14(1):28–117, **2019**.

[61] Maier, S. A. *et al. Plasmonics: fundamentals and applications*, volume 1. Springer, **2007**.

[62] Lombardi, J. R., Birke, R. L., Lu, T. and Xu, J. *J. Chem. Phys.*, 84(8):4174–4180, **1986**.

[63] Kats, M. A., Yu, N., Genevet, P., Gaburro, Z. and Capasso, F. *Optics express*, 19(22):21748–21753, **2011**.

[64] Link, S. and El-Sayed, M. A. *Annu. Rev. Phys. Chem.*, 54(1):331–366, **2003**.

[65] Kolwas, K. *Plasmonics*, 14(6):1629–1637, **2019**.

[66] Li, L., Hall, M. J. and Wiseman, H. M. *Phys. Rep.*, 759:1–51, **2018**.

[67] Lindblad, G. *Commun. Math. Phys.*, 48:119–130, **1976**.

[68] Gorini, V., Kossakowski, A. and Sudarshan, E. C. G. *J. Math. Phys.*, 17(5):821–825, **1976**.

[69] Trügler, A. *Optical properties of metallic nanoparticles*. Springer, **2011**.

[70] Grigorenko, A. N., Polini, M. and Novoselov, K. *Nat. Photonics*, 6(11):749–758, **2012**.

[71] Garcia de Abajo, F. J. *ACS Photonics*, 1(3):135–152, **2014**.

[72] Agrawal, A., Cho, S. H., Zandi, O., Ghosh, S., Johns, R. W. and Milliron, D. J. *Chem. Rev.*, 118(6):3121–3207, **2018**.

[73] Liu, X. and Swihart, M. T. *Chem. Soc. Rev.*, 43(11):3908–3920, **2014**.

[74] Guler, U., Boltasseva, A. and Shalaev, V. M. *Science*, 344(6181):263–264, **2014**.

[75] Maradudin, A. A., Sambles, J. R. and Barnes, W. L. *Modern plasmonics*. Elsevier, **2014**.

[76] Barbillon, G. Plasmonics and its Applications, **2019**.

[77] Lee, K.-S. and El-Sayed, M. A. *J. Phys. Chem. B*, 110(39):19220–19225, **2006**.

[78] Lee, J.-H., Kim, B.-C., Oh, B.-K. and Choi, J.-W. *Nanomedicine*, 9(7):1018–1026, **2013**.

[79] Kim, J., Oh, S. Y., Shukla, S., Hong, S. B., Heo, N. S., Bajpai, V. K., Chun, H. S., Jo, C.-H., Choi, B. G., Huh, Y. S. *et al. Biosens. Bioelectron.*, 107:118–122, **2018**.

[80] Loiseau, A., Zhang, L., Hu, D., Salmain, M., Mazouzi, Y., Flack, R., Liedberg, B. and Boujday, S. *ACS Appl. Mater. Interfaces*, 11(50):46462–46471, **2019**.

[81] Piliarik, M., Šípová, H., Kvasnička, P., Galler, N., Krenn, J. R. and Homola, J. *Opt. Express*, 20(1):672–680, **2012**.

[82] Anker, J. N., Hall, W. P., Lyandres, O., Shah, N. C., Zhao, J. and Van Duyne, R. P. *Nat. Mater.*, 7(6):442–453, **2008**.

[83] Le Ru, E. C., Blackie, E., Meyer, M. and Etchegoin, P. G. *J. Phys. Chem. C*, 111(37):13794–13803, **2007**.

[84] LeRu, E. and Etchegoin, P. Principles of Surface Enhanced Raman Spectroscopy Elsevier, **2009**.

[85] Ding, S.-Y., You, E.-M., Tian, Z.-Q. and Moskovits, M. *Chem. Soc. Rev.*, 46(13):4042–4076, **2017**.

[86] Zrimsek, A. B., Chiang, N., Mattei, M., Zaleski, S., McAnally, M. O., Chapman, C. T., Henry, A.-I., Schatz, G. C. and Van Duyne, R. P. *Chem. Rev.*, 117(11):7583–7613, **2017**.

[87] Jang, Y. H., Jang, Y. J., Kim, S., Quan, L. N., Chung, K. and Kim, D. H. *Chem. Rev.*, 116(24):14982–15034, **2016**.

[88] Manzhos, S., Giorgi, G., Lüder, J. and Ihara, M. *Adv. Phys.: X*, 6(1):1908848, **2021**.

[89] Ramakrishna, K., Cangi, A., Dornheim, T., Baczewski, A. and Vorberger, J. *Phys. Rev.B*, 103(12):125118, **2021**.

[90] Della Sala, F., Pezzolla, M., D'Agostino, S. and Fabiano, E. *ACS Photonics*, 6(6):1474–1484, **2019**.

[91] Stratmann, R. E., Scuseria, G. E. and Frisch, M. J. *J. Chem. Phys.*, 109(19):8218–8224, **1998**.

[92] Wu, X., Alvarez-Ibarra, A., Salahub, D. R. and de la Lande, A. *Eur. Phys. J. D*, 72:1–11, **2018**.

[93] Giannone, G. and Della Sala, F. *J. Chem. Phys.*, 153(8):084110, **2020**.

[94] Rüger, R., Van Lenthe, E., Heine, T. and Visscher, L. *J. Chem. Phys.*, 144(18):184103, **2016**.

[95] Asadi-Aghbolaghi, N., Ruger, R., Jamshidi, Z. and Visscher, L. *J. Phys. Chem. C*, 124(14):7946–7955, **2020**.

[96] Jamshidi, Z., Asadi-Aghbolaghi, N., Morad, R., Mahmoudi, E., Sen, S., Maaza, M. and Visscher, L. *J. Chem. Phys.*, 156(7):074102, **2022**.

[97] Alkan, F. and Aikens, C. M. *J. Phys. Chem. C*, 122(41):23639–23650, **2018**.

[98] Niehaus, T. A., Suhai, S., Della Sala, F., Lugli, P., Elstner, M., Seifert, G. and Frauenheim, T. *Phys. Rev. B*, 63(8):085108, **2001**.

[99] Zhu, W., Esteban, R., Borisov, A. G., Baumberg, J. J., Nordlander, P., Lezec, H. J., Aizpurua, J. and Crozier, K. B. *Nat. Commun.*, 7(1):11495, **2016**.

[100] Varas, A., García-González, P., Feist, J., García-Vidal, F. and Rubio, A. *Nanophotonics*, 5(3):409–426, **2016**.

[101] Aarons, J., Sarwar, M., Thompsett, D. and Skylaris, C.-K. *J. Chem. Phys.*, 145(22):220901, **2016**.

[102] Iida, K., Noda, M., Ishimura, K. and Nobusada, K. *J. Phys. Chem. A*, 118(47):11317–11322, **2014**.

[103] Bohren, C. F. and Huffman, D. R. *Absorption and scattering of light by small particles*. John Wiley & Sons, **2008**.

[104] Mishchenko, M. I., Travis, L. D. and Lacis, A. A. *Scattering, absorption, and emission of light by small particles*. Cambridge university press, **2002**.

[105] Taflove, A., Hagness, S. C. and Piket-May, M. *The Electrical Engineering Handbook*, 3(629-670):15, **2005**.

[106] Amendola, V. *Phys. Chem. Chem. Phys.*, 18(3):2230–2241, **2016**.

[107] De Abajo, F. G. and Howie, A. *Phys. Rev. B*, 65(11):115418, **2002**.

[108] Corni, S. and Tomasi, J. *J. Chem. Phys.*, 114(8):3739–3751, **2001**.

[109] Marcheselli, J., Chateau, D., Lerouge, F., Baldeck, P., Andraud, C., Parola, S., Baroni, S., Corni, S., Garavelli, M. and Rivalta, I. *J. Chem. Theory Comput.*, 16(6):3807–3815, **2020**.

[110] Hohenester, U. and Krenn, J. *Phys. Rev. B Condens. Matter*, 72(19):195429, **2005**.

[111] Dall'Osto, G., Gil, G., Pipolo, S. and Corni, S. *J. Chem. Phys.*, 153(18):184114, **2020**.

[112] Hohenester, U. *Phys. Rev. B*, 91(20):205436, **2015**.

[113] Fregoni, J., Haugland, T. S., Pipolo, S., Giovannini, T., Koch, H. and Corni, S. *Nano Lett.*, 21(15):6664–6670, **2021**.

[114] Jensen, L. L. and Jensen, L. *J. Phys. Chem. C*, 113(34):15182–15190, **2009**.

[115] Rinkevicius, Z., Li, X., Sandberg, J. A., Mikkelsen, K. V. and Ågren, H. *J. Chem. Theory Comput.*, 10(3):989–1003, **2014**.

[116] Morton, S. M., Silverstein, D. W. and Jensen, L. *Chem. Rev.*, 111(6):3962–3994, **2011**.

[117] Chen, X., Moore, J. E., Zekarias, M. and Jensen, L. *Nat. Commun.*, 6(1):8921, **2015**.

[118] Zakomirnyi, V. I., Rinkevicius, Z., Baryshnikov, G. V., Sørensen, L. K. and Ågren, H. *J. Phys. Chem. C*, 123(47):28867–28880, **2019**.

[119] Zakomirnyi, V. I., Rasskazov, I. L., Sørensen, L. K., Carney, P. S., Rinkevicius, Z. and Ågren, H. *Phys. Chem. Chem. Phys.*, 22(24):13467–13473, **2020**.

[120] Morton, S. M. and Jensen, L. *J. Chem. Phys.*, 133(7):074103, **2010**.

[121] Morton, S. M. and Jensen, L. *J. Chem. Phys.*, 135(13):134103, **2011**.

[122] Payton, J. L., Morton, S. M., Moore, J. E. and Jensen, L. *J. Chem. Phys.*, 136(21):214103, **2012**.

[123] Payton, J. L., Morton, S. M., Moore, J. E. and Jensen, L. *Acc. Chem. Res.*, 47(1):88–99, **2014**.

[124] Bade, W. *J. Chem. Phys.*, 27(6):1280–1284, **1957**.

[125] Giovannini, T., Bonatti, L., Polini, M. and Cappelli, C. *J. Phys. Chem. Lett.*, 11(18):7595–7602, **2020**.

[126] Bonatti, L., Nicoli, L., Giovannini, T. and Cappelli, C. *Nanoscale Adv.*, 4(10):2294–2302, **2022**.

[127] Zanotto, S., Bonatti, L., Pantano, M. F., Miseikis, V., Speranza, G., Giovannini, T., Coletti, C., Cappelli, C., Tredicucci, A. and Toncelli, A. *ACS Photonics*, 10(2):394–400, **2023**.

[128] Bonatti, L., Gil, G., Giovannini, T., Corni, S. and Cappelli, C. *Front. Chem.*, 8:340, **2020**.

[129] Huang, S., Pandey, R., Barman, I., Kong, J. and Dresselhaus, M. *ACS Photonics*, 5(8):2978–2982, **2018**.

[130] Seo, G., Lee, G., Kim, M. J., Baek, S.-H., Choi, M., Ku, K. B., Lee, C.-S., Jun, S., Park, D., Kim, H. G. *et al. ACS Nano*, 14(4):5135–5142, **2020**.

[131] Sanchez, J. E., Jaramillo, S. A., Settles, E., Salazar, J. J. V., Lehr, A., Gonzalez, J., Aranda, C. R., Navarro-Contreras, H. R., Raniere, M. O., Harvey, M. *et al. RSC Adv.*, 11(41):25788–25794, **2021**.

[132] Zhang, F., Wang, X., Zhang, T., Zhang, Z., Gao, X. and Li, Y. *J. Phys. Chem. Lett.*, 14:88–94, **2022**.

[133] Zhang, K., Wang, Z., Liu, H., Perea-López, N., Ranasinghe, J. C., Bepete, G., Minns, A. M., Rossi, R. M., Lindner, S. E., Huang, S. X. *et al. ACS Photonics*, 9(9):2963–2972, **2022**.

[134] Silvestri, A., Zayas-Arrabal, J., Vera-Hidalgo, M., Di Silvio, D., Wetzl, C., Martinez-Moro, M., Zurutuza, A., Torres, E., Centeno, A., Maestre, A. *et al. Nanoscale*, **2023**.

[135] Baumberg, J. J. *Nano Lett.*, 22(14):5859–5865, **2022**.